HAL
open science

Détection in-situ de la réactivité à l'interface métal-peinture : exemple de revêtements anti-corrosion en base zinc peints

Thomas Sanchez

To cite this version:

Thomas Sanchez. Détection in-situ de la réactivité à l'interface métal-peinture : exemple de revêtements anti-corrosion en base zinc peints. Chimie théorique et/ou physique. Université Paris sciences et lettres, 2020. Français. NNT : 2020UPSLC030 . tel-03648428

HAL Id: tel-03648428

https://pastel.hal.science/tel-03648428

Submitted on 21 Apr 2022

HAL is a multi-disciplinary open access archive for the deposit and dissemination of scientific research documents, whether they are published or not. The documents may come from teaching and research institutions in France or abroad, or from public or private research centers.

L'archive ouverte pluridisciplinaire **HAL**, est destinée au dépôt et à la diffusion de documents scientifiques de niveau recherche, publiés ou non, émanant des établissements d'enseignement et de recherche français ou étrangers, des laboratoires publics ou privés.

PSL UNIVERSITÉ PARIS

THÈSE DE DOCTORAT
DE L'UNIVERSITÉ PSL

Préparée à L'Ecole Nationale Supérieure de Chimie de Paris

In-situ probing of buried metal-polymer interface stability: example of painted Zn-based anti-corrosion coatings

Soutenue par

Thomas Sanchez

Le 14 décembre 2020

Ecole doctorale n° 388

Ecole doctorale de Chimie Physique et Chimie Analytique de Paris-Centre

Spécialité

Physico-Chimie

Composition du jury :

Laurent, THOUIN DR, ENS Paris	*Président du jury*
Marjorie, OLIVIER Professeur, UMONS	*Rapporteur*
Tomas, PROSEK CR, UCT Praha	*Rapporteur*
Santiago, GARCIA Associate Professor, TU Delft	*Examinateur*
Jolanta, SWIATOWSKA DR, ENSCP	*Codirectrice de thèse*
Polina, VOLOVITCH MCF, ENSCP	*Directrice de thèse*

Sanchez Thomas
Doctorant Safran Landing Systems
PSL Research Institute
IRCP, équipes I2E et PCS

22 Clos du Goujet,
03630, Desertines,
France
0626577910
tomsnch@gmail.com

Recherche de poste : ingénieur-docteur

Formation

- **Déc. 2020** : Doctorat CIFRE en chimie-physique analytique (ED 388)
- **Juillet 2016** : Diplôme d'ingénieur Grenoble-INP Phelma
  Majeur matériaux, spécialisation en électrochimie pour l'énergie et corrosion
- **2012-13** : Classe Préparatoire PC* au lycée Masséna, Nice
- **2012** : 17e place française aux Olympiades Internationales de Physique

Expériences professionnelles

- **2016 – 2020** : Ingénieur de recherche, Safran Landing Systems
  Doctorant Institut de Recherche de Chimie Paris (CIFRE)
  Etude des mécanismes de formation et de dégradation de nouveaux revêtements anti-corrosion pour l'aéronautique.
  Expertise en XPS, GD-OES, Nanosonde Auger et électrochimie locale
- **Février – Juillet 2016** : Stagiaire recherche à l'IRCP-PCS
  Etude d'enrichissement chimique dans les couches ultra fines d'oxyde sur monocristal d'acier inoxydable FeCrNiMo(100) en enceinte ultra haut vide
  Formation en AFM ainsi que STM et XPS en ultra haut vide.
- **Mai – Août 2015** : Stage R&D chez Maizières Research ArcelorMittal France
  Etude de corrosion des nouveaux revêtements métalliques et de délamination de peinture sur des aciers plats pour l'industrie automobile
  Expériences avec une sonde de Kelvin et des tests de corrosion accélérés.

Compétences personnelles

- Anglais courant (C1)
- Allemand élémentaire

Activités extra-professionnelles :

- Président de l'association des thésards de chimie paris (ATCP 2017-2019)
- Encadrant de plongée-sous-marine depuis plus de 6 ans,
  Coordinateur de formation pour l'association sportive de Paris Sorbonne Université.
  Préparation du diplôme de moniteur fédéral de plongée agréé (MF1 FFESSM). Expérience pédagogique, de management et d'encadrement.

Annexe de CV

Formations suivies

- Summer School: Multifunctional Smart Coatings and Surfaces, Aveiro, Portugal: 24-28 Juillet 2017
- Graduate Course Eurocorr 2017 : 1-3 Septembre 2017
- Formation “GD-OES users” par la société Horiba, 20-23 Février 2018
- Graduate Course ETCC 2018 : Life-Cycle-Analysis in polymer coatings, Juin 2018
- Formation “Traitement d'images sous ImageJ et les nouveaux logiciels FIJI et ICY : bases conceptuelles et pratiques” CNRS Formations, 1-4 Avril 2019

Présentations en conférences internationales

- Poster en Summer-School à Aveiro, le 24-28 Juillet 2017
  Degradation at metal-polymer interfaces: quantitative approach for in situ studies

- Oral EUROCORR 2017 & 20th ICC, Prague, Septembre 2017 : abstract n° 96707
  Organic coatings delamination from Zn-Ni coated steel

- Poster ETCC 2018, Amsterdam, Juin 2018 : Abstract n° ETCC18-331
  Development of model system for intelligent screening of conversion coatings

- Oral EUROCORR 2018, Krakow, Septembre 2018 : abstract n° 110777
  Effect of the surface chemistry and morphology of passivated ZnNi on the epoxy paint adherence

- Oral EIS 2019, Lège-Cap-Ferret, June 2019 : abstract n° 190189
  Development of model system for intelligent screening of conversion coatings

Articles

3 article publiés

- “*New experimental approach for 2 intelligent screening of buried metal-oxide polymer interfaces via local electrochemistry: example of undamaged model epoxy-coated Zn alloys*”, T. Sanchez, S. Gillet, V. Shkirskiy, V. Vivier, J. Echouard, J. Swiatowska, P. Volovitch, Electrochimica Acta.

- “*Conversion coating distribution on rough surface analyzed by combined surface analytical techniques*”, T. Sanchez, S. Zanna, A. Seyeux, M. La Haye, P. Volovitch, P. Marcus, J. Swiatowska, Applied Surface Sciences

- “*Detection and quantification of defect evolution at buried metal-oxide-polymer interface on rough substrate by local impedance mapping*”, T. Sanchez, K. Kurchavova, V. Shkirskiy, V. Vivier, J. Swiatowska, P. Volovitch, Electrochimica Acta

Expériences additionnelles

- Encadrement d’un stagiaire de M1 sur le sujet de thèse : Avril - Juillet 2017
- Encadrement de TP-Projets étudiants à l’ENSCP : 2A 4j, 1A 7j : Avril - Mai 2017
- Monitorat en TP Chimie-Physique Analytique à l’ENSCP : chaque année sur 3 ans.
- Encadrement de 2 stagiaires de M1 : Mai - Août 2018

Acknowledgments

Aujourd'hui que j'achève cette expérience que fut ma thèse, et contrairement à mon habitude, je vais tenter de rester concis dans cette série de remerciements.

Je tiens tout d'abord à remercier Polina Volovitch, ma directrice de thèse, qui m'a offert la chance de réaliser l'ensemble de ces travaux et de vivre toutes ces expériences. Son investissement m'ont permis de grandir et d'apprendre, tant sur le plan scientifique que managérial et humain. Je voudrais tout particulièrement la remercier pour l'immense confiance qu'elle a placée en moi ; j'ai eu, de son fait, la liberté de travailler librement et d'accéder à l'ensemble des techniques, connaissances dont j'ai eu envie et/ou besoin au cours de ces dernières années. J'ai pu, ainsi, m'entourer de personnes exceptionnelles qui m'ont soutenu et appris et à qui je tiens à exprimer toute ma gratitude !

Je remercie Jolanta Swiatowska, ma co-directrice de thèse, pour la liberté qu'elle m'a offert ainsi que pour ses conseils avisés.

Bien évidemment, Jacques Echouard, mon encadrant de thèse industriel côté Safran Landing Systems ! Un homme de savoir, avec un parler fort distingué (je vais te ca**** la gu**** ?) si l'on puit dire. Pour ton soutien en dépit des vagues, pour ces longs appels à te faire passer pour un vendeur de pizza alors que je ne connaissais pas encore ta voix … Pour ta sérénité face à l'adversité aussi, je me tiens aujourd'hui fier de pouvoir me dire ton collègue, de dire que nous avons réussi !

Je profite de ces quelques mots pour remercier l'ensemble des personnes de Chimie Paristech ! Profs, élèves, thésards etc. Tous vous citer serait de trop, mais bien évidemment mes collègues proches, de l'équipe PCS : Sandrine, avec qui j'ai eu la chance de partager un bureau de longs mois durant, Antoine, Frédéric, évidemment Dimitri. M. Marcus, vous m'avez un jour donné la chance d'évoluer au sein de votre équipe et je vous en serai éternellement reconnaissant ; en espérant avoir su regagner votre confiance.

Je remercie l'équipe DM&P de Safran ainsi que mes collègues de Bidos, Gaëlle, l'odeur de tes cannelés me donne encore aujourd'hui l'eau à la bouche !

Je dois évidemment tout à mon équipe à CPT, M. Viacheslav, pour son enseignement dans mes débuts, Alina, Diego et Peng aussi ! Je ne saurais comment vous remercier les autres, surtout M. Junsoo Han, notre futur gourou si ce n'est plus, une légende vivante chez les doctorants et un maître dans l'art du café !

Cyril, Palouille, évidemment que vous êtes les meilleurs et je ne sais comment j'aurais traversé ces épreuves sans vous !

Mélou ; pour la fin comme toujours, je crois qu'il nous reste une bouteille à ouvrir ensemble, sûrement de nombreuses à venir !

J'oublie et je saute trop de monde ; l'ATCP, L'ASP6 et bien évidemment ma famille et mes colocs … Camille qui a su égayer et illuminer mon monde de sa chevelure dorée telle un rayon de soleil !

Merci !

PhD thesis
In situ probing of buried metal-polymer interface stability: example of painted Zn-based anti-corrosion coatings

List of figures

Chapter 1

Fig. 1.1. Superposition of Pourbaix diagrams of iron and water stability domain at 298 K. Calculated for soluble species concentration of 10^{-3} M. No common domain exists between water stability domain (area between two dashed lines) and metallic iron. Adapted from [1]

Fig. 1.2. Scheme of steel oxidation mechanism in humid environment. Adapted from [2]

Fig. 1.3. Scheme of galvanic coupling between zinc and iron in humid condition. Adapted from [11]

Fig. 1.4. Compilation of several polarization tests illustrating the cathodic and anodic inhibition of chromates on: **a** AA2024-T3 in 1M NaCl exposed to 10^{-3} M and 10−4 M $Na_2Cr_2O_7$, **b** 2205 duplex stainless steel in 1M NaCl and Na2CrO4 varying from 0 to 0.5M124 and **c** Zinc in acid rain solution exposed to 0, 10, and 50 ppm of $SrCrO_4$ (reproduced from [15]).

Fig. 1.5. Schematic illustrations of the different inhibition scenarios associated with Cr(VI) compounds in: **a** aqueous solution, or when a morphological defect occurs; **b** in the presence of a Sr–Cr-based primer, or **c** a Cr(VI) conversion coating, with a particular emphasis on the self-healing and barrier properties (reproduced from [15]).

Fig. 1.6. Effect of pigments on the path of the aggressive agents and the active properties of pigments with regard to the interfacial reactions and passivation of pores in the organic coating and effect of multi-layered structure on the geometry of the pores and the barrier properties of the coating (from [18])

Fig. 1.7. Scheme of typical corrosion protection system (conversion coating thickness is not respected)

Fig. 1.8. SEM observation of an electrogalvanized steel after phosphating in ZnMnNi PCC bath. Adapted from [37]

Fig. 1.9. An illustration of (a) TCC coating formation during immersion time, the vertical arrows show the forces due to surface tension, acting along the direction parallel to the interface; the horizontal arrows indicate the normal tension perpendicular to the zinc substrate due to the agitation; the black arrows show the force due to the internal pressure of the formed bubbles. The reaction layer is the area between the substrate and the bulk treatment solution, in which during the TCC process the deposition reactions are taking place. (b) A schematic illustration of the ultimate morphology of the formed TCC layer. Adapted from [60]

Fig. 1.10. TEM cross section of TCC and composition line scan. Adapted from [53]

Fig. 1.11. Generation of underpaint reactivity via water and active species diffusion to the interface

Fig. 1.12. General scheme of anodic undermining mechanism

Fig. 1.13. Anodic undermining mechanism in the case of a down to steel scratch on galvanized steel. Adapted from [71]

Fig. 1.14. General scheme of cathodic delamination mechanism

Fig. 1.15. Potentiodynamic polarization curve for steel in aerated 0.5 M NaCl. Adapted from [19]

Fig. 1.16. General scheme of (a) osmotic and (b) mechanical blistering mechanism

Fig. 1.17. Temperature and humidity variation during a one-week cycle of the VDA 233-102 test. Adapted from [88]

Fig. 1.18. Observations in the vicinity of scribed regions on painted steel panels in SST. Adapted from [82]

Fig. 1.19. Optical microscopy observation of painted system after 1000 h immersion test. Adapted from [91]

Fig. 1.20. Schematic description of the cross-hatched test. Adapted from [93]

Fig. 1.21. OCP curve for 2% PNI coated aluminium in 5% NaCl solution for 48h. Adapted from [102]

Fig. 1.22. EIS response of steel coated with epoxy primer immersed in NaCl at 50 °C, adapted from [102]

Fig. 1.23. Typical equivalent circuit for EIS of coated metals. (a) general model of coating; (b) and (c) models with two time-constants in series and in parallel, respectively; (d) and (e) models with two time-constants and characteristics of Warburg impedance; (f) model with Warburg impedance, adapted from [102]

Fig. 1.24. Equivalent circuit for a coated metal with corrosion at defects of the surface and underneath blisters. Reproduced from [64]

Fig. 1.25. Simulated EIS spectra in Bode representation of the equivalent circuit presented in **Fig. 1.24**. Simulated values: R_Ω = 100 Ω.cm² ; C_C = 4.10^{-9} F.cm^{-2} ; R_C = 10^5 Ω.cm² ; C_{dl} = 2.10^{-6} F.cm^{-2} ; R_P = 2.10^3 Ω.cm² ; C_{dlp} = 5.10^{-8} F.cm^{-2} ; R_{CTp} = 9.10^{-4} F.cm^2

Fig. 1.26. EIS in Bode representation of melamine polyester polymer coated galvanized steel with phosphate conversion coating in immersion in 0.5 M NaCl solution. (a) Impedance modulus and (b) phase angle. Reproduced from [115]

Fig. 1.27. Schematic representation of time constant distribution (a) normal to the surface and (b) along the surface, adapted from [121]

Fig. 1.28. Illustration of a kelvin probe facing a metallic surface

Fig. 1.29. Scheme of the SKP measurement principle

Fig. 1.30. Scheme of the delamination process on polymer coated zinc, adapted from [128]

Fig. 1.31. Potential profiles for different delamination times. The accelerated ageing was performed by deposition of 0.5 M NaCl electrolyte in the defect. The atmosphere was saturated with water to prevent from evaporation. Reproduced from [130]

Fig. 1.32. SKP mapping of painted and corroded sample with a down to steel scratch after 24 month of outdoor corrosion testing. Optical image, topography of the surface and potential mappings are presented, Reproduced from [71]

Fig. 1.33. Scheme of the Local Electrochemical Impedance measurement principle. WE, CE and Ref indicates the working electrode, counter electrode and reference electrode of a 3-electrodes electrochemical setup, respectively. E1 and E2 represent the potential values at the dual probe surfaces. The electrical connections are not shown

Fig. 1.34. LEI Mappings at 5 Hz performed on scarified samples after 0, 20, 30, 50 days of salt spray exposure, respectively. Adapted from [140]

Fig. 1.35. Nyquist representation of LEIS of epoxy coated carbon steel immersed in sat. Ca(OH)2. Spectra aquisition above the center of the scratch. Adapted from [141]

Fig. 1.36. Scheme of pH sensing response of underpaint reactivity from active coating. Reproduced from [149]

Fig. 1.37. Photographs of epoxy coated magnesium before and after 20 hours of immersion in 0.5 M NaCl. The polymer coating contains phenolphthalein. Reproduced from [150]

Chapter 2

Fig. 2.1. Schematic work procedure; polymer coating ageing measurement
Fig. 2.2. Schematic representation of the in situ measurement setup
Fig. 2.3. Photography of the initial setup for LEIM and TLM measurement
Fig. 2.4. 3D representations of the designed electrochemical cell for LEIM and TLM coupling
Fig. 2.5. Example of an optical microscopy of degraded industrial painted system, blister apparition
Fig. 2.6. Schematic description of the blister observation by TLM with grazing light
Fig. 2.7. Example of initial representation of blistered surface obtained in situ under an electrolyte layer by TLM and treated binary representation evidenced the presence of blisters
Fig. 2.8. Example of in situ TLM observation of painted sample during cathodic polarization after 0.5 and 3 hours, on the left and right sides, respectively
Fig. 2.9. Schematic of the model defect in PVB polymer coating
Fig. 2.10. TLM observations of the cathodic delamination on ZnNi w/o passivation in the presence of NaCl and $NaHCO_3$. The diameter of the initial defect (in red) is 2 mm
Fig. 2.11. Examples of LEIM on bare ZnNi at different times of the delamination in the vicinity of the defect
Fig. 2.12. Examples of anodic delamination kinetics detected by LEIM on samples coated with PVB model coating
Fig. 2.13. TLM observation of PVB coated Zn HDG after 4h of immersion in 0.01 M NaCl in the presence of phenolphthalein
Fig. 2.14. Schematic representation of the surface characterization methodology
Fig. 2.15. Observation of coated sample at polymer coating (left) and substrate (right) surface
Fig. 2.16. Photography of the anti-vibration setup for Keyence 3D microscope
Fig. 2.17. Schematic representation of the electron-matter "interaction pear" [7]
Fig. 2.18. Schematic representation of an SEM
Fig. 2.19. Principle of XPS [12]
Fig. 2.20. Probability of a photoelectron to reach the surface in function of its depth emission d [14]
Fig. 2.21. Schematic representation of GD-OES principle
Fig. 2.22. Schematic of secondary ions emission principle
Fig. 2.23. Scheme of the in-depth secondary ion profiling by ToF-SIMS principle, adapted from [23]
Fig. 2.24. Auger electron emission principle

Chapter 3

Fig. 3.1. Schematic representation of **(a)** chemical bonding in cured DGEBA-TETA epoxy resin (adapted from Bernassau *et al.* [53]) and **(b)** epoxy degradation induced by interfacial pH increase.

Fig. 3.2. Schematic description of the AC-DC-AC procedure cycle used in the study.

Fig. 3.3. ATR-IR spectra (a, b) and evolution of peaks intensities with time (c, d) of the epoxy polymer over Zn HDG in the low wavelength region. **(a)** after 100 h of immersion and **(b)** after 7 AC-DC-AC cycles compared with the initial spectra of as coated epoxy polymer as indicated; **(c)** average evolution of the OH peaks intensities corresponding to "free -OH" and "total -OH" as a function of immersion time (see text for definition) and **(d)** average evolution of epoxy characteristic peaks (Table 1) intensities as a function of immersion time. Dashed line in **(c)** corresponds to the exponential fitting with Eq. 3 of the peaks intensities (A) *vs* immersion time (t).

Fig. 3.4. Evolution of average contact angle values on the model epoxy surface **(a)** in humid atmosphere (over 95%) and immersion in 10 mM NaCl water as indicated, **(b)** in modified AC-DC-AC ageing test.

Fig. 3.5. Examples of optical images of the epoxy coating on Zn after **(a)** 50 h and **(b)** 75 h of immersion in a 10 mM NaCl electrolyte by *in situ* Time Lapse Microscopy. Image **(c)** represents a 3D image composition (see text for details).

Fig. 3.6. Typical EIS spectra **(a)** and evolution of average low frequency electrochemical impedance modulus **(b, c)** of model epoxy coated Zn at different immersion times (example after 1 and 72 h of immersion time) in a 10 mM NaCl aqueous solution. **(a, b)** during immersion and **(c)** under modified AC-DC-AC degradation procedure

Fig. 3.7. Typical EIS responses of **(a)** uncoated and **(b)** model epoxy coated Zn alloy samples of type 1 and 2 in a 10 mM NaCl solution and **(c)** average evolution of the low frequency electrochemical impedance modulus over modified AC-DC-AC aging procedure for samples of type 1 and 2.

Fig. 3.8. *In situ* Time Lapse Microscopy observation after 5 AC-DC-AC test cycles for epoxy coated Zn alloy samples of type 1 **(a)** and type 2 **(b)**.

Fig. 3.9. *in situ* TLM **(a, c)** and LEIM maps **(b, d)** of the Zn alloy sample of type 1 covered with model epoxy after 4 AC-DC cycles **(a, b)** and with strong epoxy primer after 10 AC-DC cycle **(c, d)**. The areas mapped by LEIM are delimited in TLM images by squares.

Fig. 3.10. Schematic description of the metal-polymer interface degradation in the proposed accelerated test. During immersion, water and aggressive species diffuse through the polymer and reach the metal-polymer interface **(a)**. In function of weak **(b)** or strong **(c)** stability of the metal-oxide-polymer interface, the underpaint reactivity under polarization leads to different intensity of cathodic reaction and to different EIS response (Type 1 or Type 2) respectively. Finally, hydroxides and peroxides generated at the interface diffuse through the coating and degrade the polymer **(d)**.

Chapter 4

Fig. 4.1. Scheme illustrating the methodological approach used to describe in-depth chemical characterization of thin coatings on rough substrates.

Fig 4.2. Example of high resolution XPS spectra for: the reference Zn(OH)2 sample: **(a)** Zn 2p, **(b)** Zn LMM Auger, **(c)** Cr 2p region with Zn Auger peaks ; and for Cr(III) passivated ZnNi sample: **(d)** Zn 2p, **(e)** Zn LMM Auger, **(f)** Cr 2p region with Zn Auger peaks.

Fig 4.3. (a) ToF-SIMS secondary ion depth profiles (ZnO^- CrO^- and Ni_2^-) on passivated ZnNi surface, **(b)** Average ToF-SIMS ZnO^- to $CrO2^-$ ion ratio profile. And GD-OES elemental depth profiles (Cr, Zn, O, Ni, C, Fe) on passivated ZnNi alloy: **(c)** high energy argon plasma, **(d)** low power argon plasma

Fig 4.4. Schematic representation of the generated model defect: **(a)** 2mm anode with GD-OES, **(b)** 30 µm oxygen ion source with ToF-SIMS; and optical micrographs of the defects by Keyence high resolution 3D microscope: **(c)** 2 mm crater produced by GD-OES, **(d)** Grid of 49 defects produced by ToF-SIMS. High magnification optical microscopy comparison of sputtered and unsputtered regions **(e)** of GD-OES 2 mm defect, **(f)** of ToF-SIMS defect

Fig 4.5. Examples of high resolution XPS spectra in the middle of the GD-OES crater: **(a)** Zn 2p, **(b)** Zn LMM Auger, **(c)** Cr 2p region with Zn Auger peaks ; and in the middle of the grid of 49 defects produced by ToF-SIMS: **(d)** Zn 2p, **(e)** Zn LMM Auger, **(f)** Cr 2p region with Zn Auger peaks.

Fig 4.6. SEM images and Nano Auger elemental profiles in the vicinity of the 2 mm diameter sputtered area generated by GD-OES. **(a)** General view showing sputtered and not-sputtered zones, **(b)** magnification showing an example of the zone selected for AES profiling inside the defect (valley-type zones are shown with black circles while hill-type are shown by white circles). **(c)** Example of in-depth chemical profiling of chromium and nickel on intact unsputtered surface, **(d)** Example of in-depth chemical profiling of chromium and nickel in the valley-type zones inside the crater, **(e)** Example of in-depth chemical profiling of chromium and nickel on the hill-type zones of the crater.

Fig 4.7. SEM images and Nano Auger elemental profiles in the vicinity of the sputtered area generated by ToF-SIMS. **(a)** General view showing sputtered and non-sputtered zones, **(b)** magnification showing an example of the zone selected for AES profiling inside the defect (valley-type zones are shown with black circles while hill-type are shown by white circles). **(c)** Example of in-depth chemical profiling of chromium and nickel in the valley-type zones inside the crater, **(d)** Example of in-depth chemical profiling of chromium and nickel on the hill-type zones of the crater.

Chapter 5

Fig. 5.1. (a) Cross sectional and (b-c) top view schematics of model systems for the parameters definition. Linear dimension (*d*) and depth (0.8×*h*, where *h* is the initial conversion coating thickness) of an individual defect as well as the grid size (*N*×*N*) and the considered linear defect size (*D)* are shown.

Fig. 5.2. Examples of 3D-microscopy images and corresponding topographic profiles of surfaces with defect in conversion coating produced by (a) GD-OES (2 mm crater, sample B) and (b) ToF-SIMS (grid of 49 craters, sample C). The imaging is made before polymer coating

Fig. 5.3. Schematic representation of one ageing cycle (a). Examples of (b) OCP evolution during the relaxation stage and (c) potentiostatic current evolution during cathodic polarization for different cycles as indicated. One cycle is composed of 15 minutes of cathodic polarization under E=– 1.5 V vs. Ag/AgCl, 15 minutes of OCP stabilization and 30 minutes of LEI mapping at OCP.

Fig. 5.4. Time Lapse Microscopy images of samples A, B and C (D_0 = 3.8, 1.8 and 0.8 mm, respectively) at the beginning of the first and in the beginning of the fourth degradation cycles.

Fig. 5.5. Examples of (a) OCP evolution during the relaxation stage and (b) potentiostatic current evolution during cathodic polarization for different cycles as indicated.

Fig. 5.6. Total charge, exchanged during cathodic polarization stage of the degradation cycle, as a function of the cycle number (a-b) for samples from two different batches and as a function of the estimated area of the active zone (attributed to damaged oxide-polymer interface) (c). The initial dimension of the defect zone D_0 is indicated.

Fig. 5.7. LEIM maps of the local impedance modulus, |Z| in the vicinity of the defects for samples A, B and C (D_0 = 3.8, 1.8 and 0.8 mm, respectively) at the first (a) and fourth (b) degradation cycles as indicated.

Fig. 5.8. Maps of the gradient of the local impedance modulus, Grad |Z|, in the vicinity of the defects for samples A, B and C (D_0 = 3.8, 1.8 and 0.8 mm, respectively) at the first (a) and fourth (b) degradation cycles. All the values are normalized by the value of the maximum of gradient through the map.

Fig. 5.9. Evolution of the LEIM measured size of the defects with degradation cycling for sample A (D_0 = 3.8, black squares) and B (D_0=1.8 mm, red circles). All the values are normalized by the value of the maximum of gradient through the map.

Fig. 5.10. Optical images of the systems with the defects in conversion coating with different initial area as indicated after 7 degradation cycles. a) general appearance of the defect, b) higher resolution 3D decomposition of the polymer surface and the metal-polymer interface as indicated.

List of tables

Table 1.1. Morphological characteristics and Cr(VI) content in several types of TCC studied in [62]
Table 2.1. Gravimetric measurement of coated Zn HDG samples with model epoxy coating
Table 2.2. List of studied samples during the PhD thesis
Table 2.3. Comparison of surface techniques characteristics
Table 3.1. Attribution of ATR-IR peak positions to characteristic groups of DGEBA-TETA epoxy resin
Table 4.1. Peak assignment and fitting parameters used for the decomposition of XPS core level spectra of model $Zn(OH)_2$ reference sample
Table 4.2. Peak assignment and fitting parameters used for the decomposition of XPS core level spectra of trivalent conversion coating on ZnNi substrate sample
Table 5.1. Description of defects in conversion coatings of studied samples. Parameters defined in the text and in **Fig. 5.1**
Table 5.2. Summary of the detection capacity of different technics for the model systems for various size of defects in the conversion coating

Table of contents

In situ probing of buried metal-polymer interface stability: example of painted Zn-based anti-corrosion coatings 1
List of figures 2
Chapter 1 2
Chapter 2 4
Chapter 3 5
Chapter 4 6
Chapter 5 7
List of tables 8
Table des matières 9
Chapter 1: Introduction and State of the Art 15
Introduction 15
State of the Art 18
1.Basics of corrosion protection of metallic materials 18
1.1. “Active” corrosion protection 20
1.1.1. Sacrificial protection 20
1.1.2. Protection by corrosion inhibitors 20
1.2. “Passive” corrosion protection 22
1.3. Structure of typical painted anticorrosion system 23
2.Introduction to conversion coatings at zinc-polymer interface 25
2.1. Thick (micrometric) phosphate conversion coatings 25
2.2. Thin chromates conversion coatings (CCC) 25
2.3. Trivalent Chromium Conversion (TCC) as an alternative to chromate conversion 26
3.Possible degradation mechanisms of metal-polymer interface in humid environment 30
3.1. Anodic undermining 31
3.2. Cathodic delamination: 32
3.3. Blistering 34
4.Experimental approaches to access interface stability in painted systems 35
4.1. Accelerated degradation tests 35
4.1.1. Atmospheric corrosion and salt spray tests 35
4.1.2. Immersion test 37
4.1.3. Electrochemical tests 38

1 4.2. Electrochemical survey of the degradation of the system metal-polymer 39
2 4.2.1. Open Circuit Potential measurement 39
3 4.2.2. Electrochemical impedance spectroscopy 40
4 4.3. Localized measurement of stability and degradation in painted systems 44
5 4.3.1. Scanning Kelvin Probe (SKP) 44
6 4.3.2. Scanning Vibrating Electrode Technique (SVET) 47
7 4.3.3. Local Electrochemical Impedance Spectroscopy / Mapping (LEIS-LEIM) 48
8 4.3.4. Time Lapse Microscopy (TLM) 51
9 5.Difficulties of chemical characterization of metal-oxide-polymer interfaces 53
10 5.1. Ex situ chemical characterization of evolving metal-oxide-polymer interfaces 53
11 5.2. In situ chemical characterization of evolving metal-polymer and oxide-polymer interfaces ... 54
12 6.Conclusion of the state of the art 56
13 **Chapter 2: Experimental strategy & methodology 65**
14 1.Substrate materials 65
15 1.1. Model samples 65
16 1.2. Electrodeposited Zn alloy and conversion coating 65
17 2.Proposed polymer coating 66
18 2.1. Optimizing procedure of model epoxy polymer 66
19 2.2. Tests used for selection of model systems for LEIM-TLM studies 67
20 2.3. Recapitulative of used combinations substrate-polymer 68
21 3.Methodologies for in situ reactivity measurement. 70
22 3.1. LEIM and TLM combination in one experiment for underpaint reactivity studies 70
23 3.2. LEIM details and LEIM cell adaptation for combination with TLM 71
24 3.3. TLM adaptation for distinguishing gas bubbles and surface inhomogeneity and for optical
25 detection of degradation on non-transparent thick paint 73
26 3.4. Verification of LEIM-TLM coupling for PVB coated systems aged in humidity chamber 76
27 4.Combination of characterization technics for ex situ observations 80
28 4.1. Strategy of the chemical characterization of conversion coating layer 80
29 4.2. High resolution 3D-Microscopy 82
30 5.Principles of conventional methods used for ex situ characterizations 84
31 5.1. Scanning Electron Microscopy and Electron Dispersion Spectroscopy (SEM-EDS) 84
32 5.2. X-ray photoelectron spectroscopy (XPS) 85
33 5.3. Glow Discharge Optical Emission Spectroscopy (GD-OES) 87

5.4. Time of Flight Secondary Ion Mass Spectrometry (ToF-SIMS) 88
5.5. Nano-probe Auger Emission Spectroscopy 90
Chapter 3: New experimental approach for intelligent screening of buried metal-oxide-polymer interfaces via local electrochemistry: example of undamaged model epoxy-coated Zn alloys 95
Abstract 97
Highlights 97
1.Introduction 98
2.Materials and methods 101
2.1. Materials 101
2.1.1. Substrates preparation 101
2.1.2. Epoxy coating 101
2.2. Polymer characterization 103
2.3. Degradation procedures 104
2.4. Electrochemical characterization and Time Lapse Microscopy 104
3.Results 106
3.1. Stability of the epoxy coating on Zn substrate during immersion 106
3.2. Stability of the epoxy coating on Zn substrate under AC-DC-AC cycling 110
3.3. Zn alloy/oxide/model epoxy interface evolution under modified AC-DC-AC test 110
3.4. Spatial distribution of underpaint reactivity 112
4.Discussion 114
4.1. Speculative degradation mechanism of model epoxy 114
4.2. Applicability of the modified AC-DC-AC protocol to discriminate conversion coatings ... 114
4.3. Physical interpretation of LEIM on undamaged coated samples 116
5.Conclusions 117
Chapter 4: Conversion coating distribution on rough surface analyzed by combining surface analytical techniques 123
Abstract 125
Highlights: 125
1.Introduction 126
2.Experimental 128
2.1. Materials 128
2.1.1. Zn-Ni alloy with chromium conversion coating 128
2.1.2. Model $Zn(OH)_2$ ALD layer 128
2.2. Morphological and chemical characterizations 128

2.2.1. Morphological characterization 128
2.2.2. Chemical characterization of the thin oxide layer 129
2.2.3. XPS 129
2.2.4. ToF-SIMS and GD-OES 129
2.2.5. Nano Auger 130
3.Results and discussion 132
3.1. Surface composition of ZnNi alloy with conversion layer 132
3.1.1. $Zn(OH)_2$ reference sample 132
3.1.2. Surface atomic composition of the conversion coating 132
3.1.3. Chemical composition of the conversion coating by ToF-SIMS and GD-OES depth profiles 134
3.2. Chemical characterization of the interface conversion coating / substrate alloy 137
3.2.1. Crater generation 137
3.2.2. Surface morphology and distribution of the conversion coating in the sputtered areas 137
3.2.3. Chemical composition near the conversion coating/substrate interface 139
3.2.4. Local chemistry distribution in sputtered area from Nano Auger 141
3.3. Discussion: feasibility of thin layers characterization on rough substrates 144
4.Conclusion 145
Chapter 5: Analytical limits of LEIM to detect and quantify defects evolution at buried metal-oxide-polymer interface on rough substrates 151
Abstract 153
Highlights 153
1.Introduction 154
2.Experimental 156
2.1. Materials 156
2.1.1. Substrate 156
2.1.2. Model defects generation and initial characterization 156
2.1.3. Types of defects 157
2.1.4. Polymer coating 158
2.2. Electrochemical set up and degradation procedure 159
2.3. Electrochemical impedance 159
2.4. Optical characterization 160

3.Results 161
3.1. Optical surface evolution during cycling 161
3.2. Electrochemical characterizations 161
3.3. Electrochemical impedance spectroscopy 165
3.4. Detection and quantification of the underpaint defects in conversion coating by LEIM . 166
3.5. Ex situ optical observations in the vicinity of the defect after cycling 170
4.Discussion: LEIM detection of nanometer depth defects in conversion coating on rough surface 173
5.Conclusion 175
Chapter 6: Conclusions & Perspectives 184
Conclusions 184
Perspectives 187

Chapter 1: Introduction and State of the Art

Introduction

Zinc-based electrodeposited coatings are often used for sacrificial protection of steel. To ensure longer service life, in many applications, such as construction, automotive, electronics and aerospace industries, the sacrificial protection offered by metallic coating is combined with barrier protection by application of polymer coatings (paints), isolating the metallic surfaces from the aggressive environment.

To ensure good paint adherence on the metallic substrate, and enhance the corrosion resistance of the systems, conversion coatings (CC) are used on metallic alloys prior to painting. Conversion coatings are thin layers of inorganic (oxides, phosphates …) or organic (sol-gel) species. The corrosion protection systems built upon this strategy have then a multi-layered structure: substrate/sacrificial-metallic-coating/conversion-coating/polymer-coating.

Although this multi-layered structure is aimed to be stable in corrosive conditions, the complexity of the multi-layered structure makes it susceptible to multiple types of degradation. Because of non-negligible polymer permeability and possible localized adhesion loss, accumulation of liquid water at the interface is possible. The presence of water at metal-polymer interface can then degrade the system and lead to blistering or underpaint corrosion; whose initiation and development are highly difficult to detect. Understanding the degradation mechanisms and the measurement of degradation kinetics in such systems is still challenging. The task is even more complex for rough substrates, like electrodeposited zinc-based substrates, under thick polymer coatings.

In this PhD thesis, a new methodology able to correlate the effect of thin conversion coatings with the stability of metal-oxide-polymer in immersion condition was proposed. It consisted in the combination of in situ reactivity measurement by local electrochemical impedance mapping and time lapse microscopy with ex situ chemical and morphological analysis by surface characterization technics. The main objective of the work was to answer the following question:

"How to quantify in situ the evolution of local stability of initially undamaged buried metal-oxide-polymer interface in immersion condition?"

To answer this question, three different analytical steps were suggested:

- Propose a model system permitting underpaint reactivity measurement and a combination of technics for localized underpaint reactivity assessment.
- Define the analytical limits of the techniques employed for the model system.
- Validate the proposed methodology for intelligent screening of conversion coatings on zinc-based substrates with well-known conversion coating.

A secondary objective of this PhD was to permit the correlation between the chemistry of a conversion coating on a rough substrate and the stability of the painted system. It was hence necessary to propose a novel approach for the chemical characterization of thin conversion coatings on rough substrates.

The manuscript is organized in **six chapters.**

The first chapter ("Introduction and State of the Art") includes this introduction followed by the state of the art relevant to this work. This brief literature review leads to the main questions answered in the PhD thesis. For this, the principles of corrosion protection by multi-layered coating systems as well as their typical failure mechanisms are introduced first. Specific sections focalize on the reactivity assessment in painted systems, including accelerated ageing, and in situ reactivity measurement including local electrochemical measurement. Analytical methods for conversion coatings chemical characterization and their difficulties for applications on rough substrates are also presented. This literature review allowed to ask some questions and propose the experimental strategy presented in the following chapters.

The second chapter, ("Experimental Strategy and Methodology") shortly presents the materials and the combination of experimental techniques used in this work. The proposed setup for combined in situ local electrochemical mapping (LEIM) and optical time lapse microscopy (TLM) used to characterize the reactivity at buried interface is detailed. The preliminary work for the methodological verification of the proposed setup on the application to well-known system galvanized steel – polyvinyl butyral (PVB) are presented. The application of PVB as a model polymer for the degradation study in immersion conditions is also questioned and the necessity to develop an alternative model polymer coating is shown. Some details of the development of a model epoxy-based polymer are also given. The list of studied systems is presented. Finally, the combination of surface analytical technics used for 3D characterization of conversion coating and principles of the used surface analytical techniques are briefly introduced.

The third chapter ("A new system for intelligent screening of buried interfaces: local electrochemistry characterization of undamaged model epoxy-coated Zn alloys") presents the methodological approach proposed for the *in situ* accelerated study of the stability of initially intact buried metal-oxide-polymer interfaces in immersion condition. The method includes a specific electrochemical ageing protocol and an application of model epoxy-polymer stable under this protocol, associated with local electrochemical impedance mapping and time lapse microscopy. No preliminary local damage in order to initiate localized reactivity at metal-oxide-polymer was performed so that the methodology allowed to obtain the true response of the sample protected by coating. On the example of a zinc-based alloy coated with trivalent chromium conversion coating, it was demonstrated that the proposed methodology is able to discriminate more and less stable conversion coatings with similar composition, which were barely distinguishable by EIS without the use of the model polymer.

The fourth chapter ("Conversion coating distribution on rough surface analyzed by combining surface analytical techniques") covers a methodological approach allowing chemical description of thin conversion coating on rough electrodeposited substrates, including buried metal-oxide interface. The presented methodology first allows the generation of homogenous nanometric thinning of the conversion coating

on a substrate with micrometric roughness via the use of low energy argon plasma sputtering by GD-OES technique. The homogeneity of the sputtering in the model defect was verified by Auger nano-probe. The in-depth quantitative chemical composition was obtained by XPS characterization inside the GD-OES crater. The sputtering homogeneity of both GD-OES and ToF-SIMS on rough surfaces is compared.

The fifth chapter ("Analytical limits of LEIM to detect and quantify defects in thin oxide layers, and their evolution at buried metal-oxide-polymer interface on rough substrates") details the ability of the proposed methodology (**chapter 3**) to detect nanometric thinning in trivalent chromium conversion coating (**chapter 4**) at metal-oxide-polymer interface. The influence of the lateral size and distribution of model defects in the conversion coating on the stability of the painted systems is presented. The most interesting material result is that for trivalent chromium conversion coatings, local thinning on rough substrates need to have a critical size to affect significantly the underpaint reactivity.

The sixth chapter, conclusion and perspectives, summarizes the general conclusions brought to light by this work and covers a summary of the proposed methodologies of the thesis. Some perspectives concerning the improvement and the adaptability of the proposed methodologies are presented.

State of the Art

This chapter introduces the bases about metal-oxide-polymer interface on painted metallic substrates and reviews the state of the art in the characterization of these buried interfaces. For this aim, first, the corrosion protection strategies of steel are briefly reviewed in **section 1** and several types of conversion coatings necessary for polymer adhesion on metallic substrates are described in **section 2**. Then, some typical degradation mechanisms considered in the literature for multi-layered painted systems are described in **section 3**. Finally, the existing methodologies used for the stability assessment of painted systems are briefly reviewed. A particular accent is put on the in situ probing of the reactivity at buried interfaces and the methods of analysis of the interface chemistry in **sections 4 and 5** respectively. The chapter 1 ends up with a short summary revealing the scientific questions relevant for reactivity measurements at buried metal-oxide-polymer interfaces. These questions caused the subject of the PhD and justified the methodological development realized in it. The following chapters will respond the selected questions, but each chapter is presented in a form of scientific publication which can be read independently and contains a more specific bibliographical introduction.

1. Basics of corrosion protection of metallic materials

Corrosion is a natural process describing the gradual destruction of materials, usually metals, by electrochemical or chemical reaction with their environment. For metallic materials, it consists in the oxidation of metals (M^0) into more stable in selected conditions oxidized species (M^{n+}) which could be present in the form of oxides, hydroxides, soluble species and complexes, etc. For iron, this oxidation process is thermodynamically favorable in presence of water, as illustrated by Pourbaix diagram, with lines drawn representing solubility limits of 0.001 molar concentration for the soluble species (**Fig. 1.1**). This means that corrosion of iron in the presence of water is nearly impossible to stop. Some would say “Trying to prevent corrosion from happening is like playing against god, or in this specific case thermodynamics; you run to inevitable doom, but you do it with fancy and expensive technologies so it’s okay” [1]. Hence, corrosion protection consists in limiting and/or preventing degradation.

[1] R. Nogueira, Corrosion introduction lecture, Grenoble INP Phelma (2013)

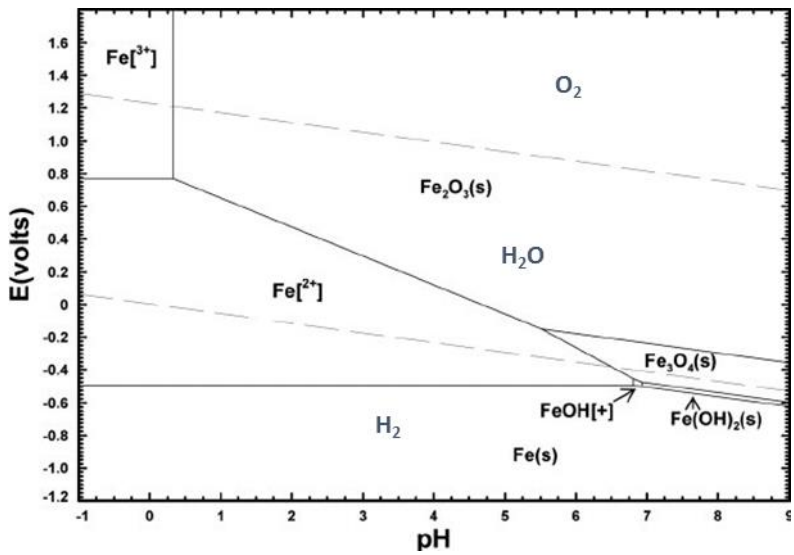

Figure 1.1: Superposition of Pourbaix diagrams of iron and water stability domain at 298 K. Calculated for soluble species concentration of 10^{-3}M. No common domain exists between water stability domain (area between two dashed lines) and metallic iron. Adapted from [1]

To choose an anticorrosion strategy, first the corrosion mechanism should be considered. A simplified scheme of steel corrosion is shown in **Figure 1.2**, representing the separation of anodic and cathodic sites in the corrosion process of iron.

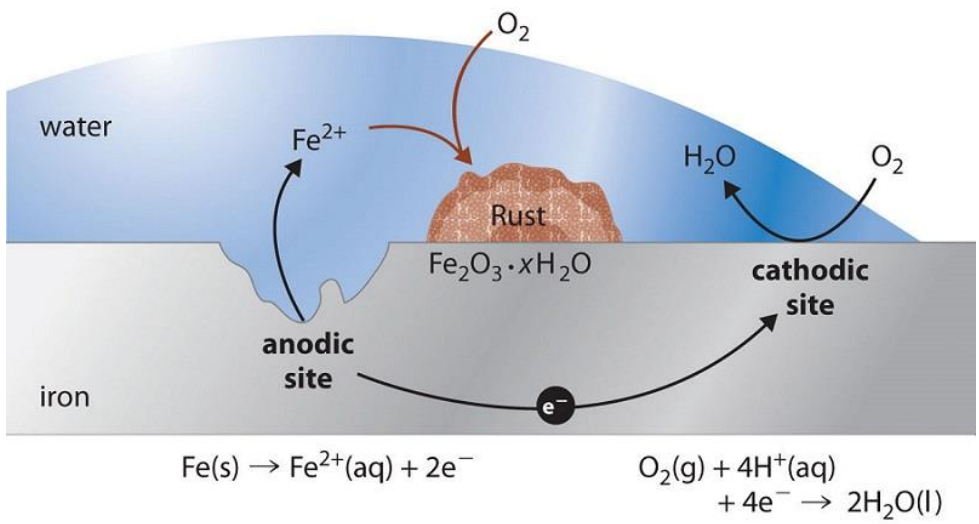

Figure 1.2: Scheme of steel oxidation mechanism in humid environment. Adapted from [2]

According to this schema, to prevent corrosion one should slow or modify the elementary steps of the process: reduce mass and/or charge transfer by a barrier layer or modify the reaction sequence by introducing another active element as described below.

1.1. "Active" corrosion protection

Active corrosion protection consists in employing a chemically or electrochemically active substance in contact with steel which will modify the mechanisms of the reaction. This can be achieved by a sacrificial protection by more active metals or by implication of corrosion inhibitors.

1.1.1. Sacrificial protection

Sacrificial protection consists in the connection of the metal to protect to a more active metal which will dissolve anodically and suppress anodic reactions of the protected metal. **Figure 1.3** shows schematically the galvanic coupling appearing during cathodic protection of steel in contact with zinc (for instance cut edge of zinc coated steel): zinc acting as an anode and protected steel (iron) on which cathodic reaction occurs. Sacrificial metallic coatings represent one of the most used ways to protect steel. Zinc and cadmium were traditionally widely used for galvanic protection of steels thanks to their anodic behavior compared to iron (steel) in the galvanic series [3]. For Zn or Cd coated steel, while the coating is undamaged, it corrodes slower than steel [4,5]. If the coating is damaged and steel is exposed, it is preferentially oxidized and acts as an anode in the galvanic coupling [6]. Nowadays, Zn and Cd coatings are more and more replaced by alloys containing Al, Mg, Zn-Al-Mg [7,8] or by the Zn-Ni alloys [9] respectively in many applications including automotive, building industry, aerospace and pre-painted markets [10].

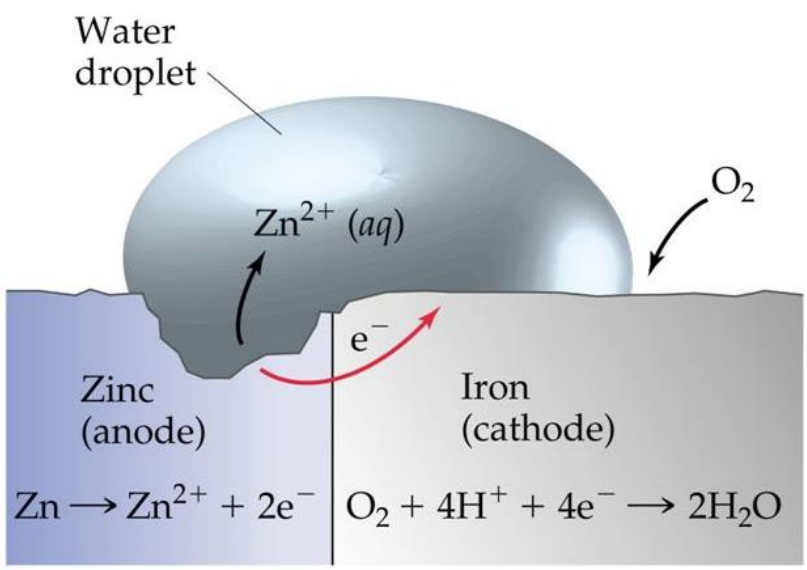

Figure 1.3: Scheme of galvanic coupling between zinc and iron in humid condition. Adapted from [11]

1.1.2. Protection by corrosion inhibitors

Active corrosion protection can be also achieved via application of corrosion inhibitors: organic or inorganic species which modifies the reaction path without modification of the reaction products. The inhibitors added in enough low concentrations significantly reduce corrosion rates. Different classifications of inhibitors were proposed in the literature. In function of their effect on the anodic or cathodic partial reactions, the inhibitors can be classified as anodic, cathodic, or mix-type. Different types of inhibition mechanisms [12] were proposed in the literature, among which:

- Adsorption of organic molecules on the metal forming a monolayer protective film limiting the access of aggressive species to the surface;
- Formation of a thin passive oxide film on the metallic surface;
- Reaction with aggressive species in the media (pH buffering, etc.) to reduce the aggressivity of the media preventing or slowing the reactions on the metallic surface.

Among numerous groups of corrosion inhibitors, hexavalent chromium was for a long time by far the most used. Its popularity was related not only to its relatively low cost, but also to the remarkable corrosion resistance persistent over a very wide range of pH and concentrations [13,14]. A particularity of Cr(VI) inhibitors is that, unlike many other inhibitors, they can act on both, anodic and cathodic reactions (**Fig. 1.4**) [15].

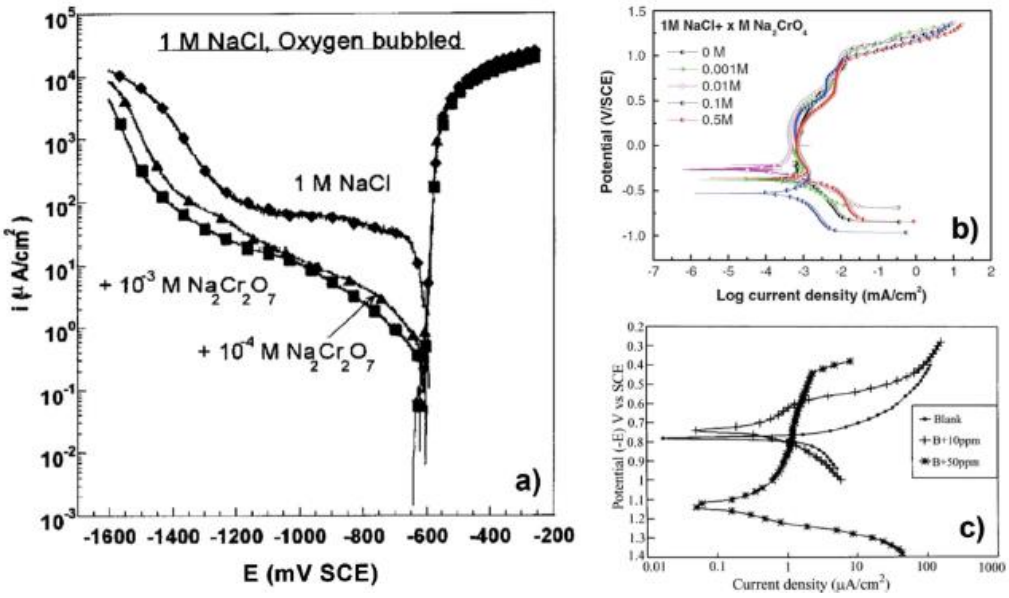

*Figure 1.4: Compilation of several polarization tests illustrating the cathodic and anodic inhibition of chromates on: **a** AA2024-T3 in 1M NaCl exposed to 10−3 M and 10−4 M Na2Cr2O7, **b** 2205 duplex stainless steel in 1M NaCl and Na2CrO4 varying from 0 to 0.5M124 and **c** Zinc in acid rain solution exposed to 0, 10, and 50 ppm of SrCrO4 (reproduced from [15]).*

Because chromate ions (CrO_4^{2-}) are highly soluble, they easily leach into the electrolyte (and move to so called "active sites") and undergo cathodic reduction (coupled to anodic metal dissolution) to form an adherent chromium oxide (Cr_2O_3) film. The latter can block the reaction rates given its relative insolubility in aqueous environments in a large pH spectrum, and its adherence to the underlying metal [16]. Different mechanisms of protection by chromates, revealed in the literature, are schematically illustrated in **Figure 1.5**.

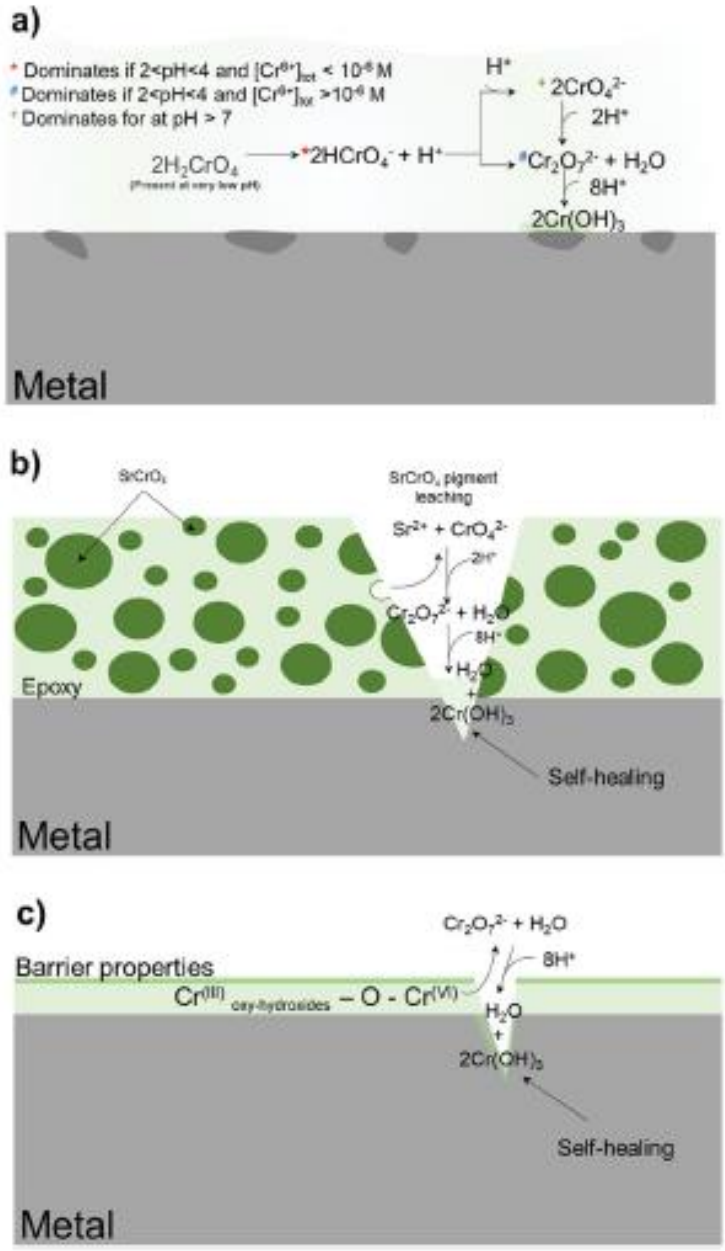

*Figure 1.5: Schematic illustrations of the different inhibition scenarios associated with Cr(VI) compounds in: **a** aqueous solution, or when a morphological defect occurs; **b** in the presence of a Sr–Cr-based primer, or **c** a Cr(VI) conversion coating, with a particular emphasis on the self-healing and barrier properties (reproduced from [15]).*

1.2. "Passive" corrosion protection

Also called "barrier protection", it is ensured by a protective layer (coating) formed on the metallic surface, usually with a polymer structure formed by organic molecules (paint, lacquer, …), aiming to isolate the metal from the environment. In reality, the composition of organic coatings is very complex. The

review of formulation is out of the scope of this work, however a good introduction to the chemistry of coatings can be found in [17]. Other than binder and hardener, paints contain multiple additives and dispersed pigments, thus they eventually show some permeability; moreover, the permeability will depend on the multi-layered structure of the paint [18].The effect of pigments and of the layered structure on the permeability of paints is schematically illustrated in **Figure 1.6**.

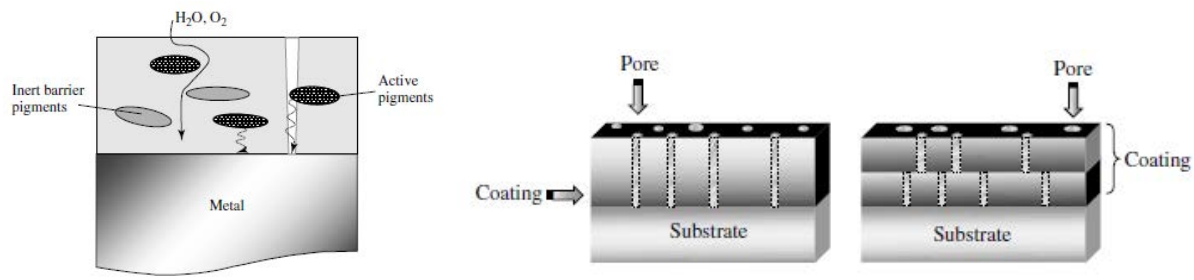

Figure 1.6: Effect of pigments on the path of the aggressive agents and the active properties of pigments with regard to the interfacial reactions and passivation of pores in the organic coating and effect of multi-layered structure on the geometry of the pores and the barrier properties of the coating (from [18])

A more appropriate way to describe the effect of barrier protection would be delay the exposure to water and limit the diffusion of oxygen and other aggressive species to the metallic surface [19,20].

1.3. Structure of typical painted anticorrosion system

In industrial applications coatings are applied not only for anticorrosion but for many other functions, resulting in enough complex and multi-layered structures [21]. Anticorrosion protection of steel is often performed by combining different modes of protection (active and passive protections) in multi-layered systems as schematically described in **Figure 1.7**.

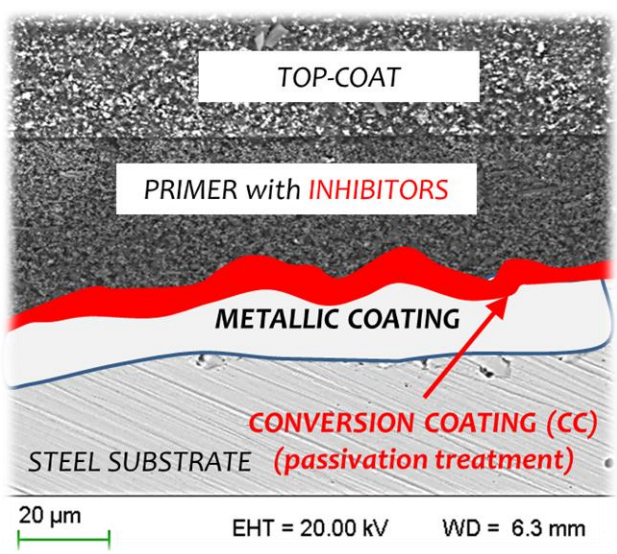

Figure 1.7: Scheme of typical corrosion protection system (conversion coating thickness is not respected)

The first layer, "metallic coating", is often a zinc-based alloy, produced by either electrochemical or hot dip processes. Its role is to ensure a sacrificial protection of the steel on cut edges and in the case of a failure in the protection system.

To provide good barrier effect, an organic polymer should adhere to the metallic surface. To ensure good polymer adherence, the surface should be able to create covalent bonds [22]. This can be achieved by the "conversion" of the metallic surface into an oxidized state, forming insoluble oxide or/and inorganic salts (phosphates, titanates, etc.) The conversion coating is hence an inorganic oxide layer of varying thickness from 10 nm up to several µm, depending on the type of conversion applied [23]. Its role is to limit the corrosion rate of the metallic coating and to ensure a good paint adherence [24].

The first paint layer, the "primer", is essential in the corrosion protection mechanism: it is often epoxy based and ensures good barrier protection by its low porosity and low hydrophilicity. It also contains pigments, including corrosion inhibitors, allowing active corrosion protection [24]. Epoxy resins can form good barriers for water; however, they are known to be chemically unstable under UV irradiation.

The next layer of the corrosion protection system, the "top-coat", forms an additional barrier protection and protects the system from UV but also from mechanical solicitations such as wear and scratching.

According to the literature, well optimized conversion coatings seems to be a key parameter improving the overall stability of the complete painted systems [25,26,27]. The next section will briefly introduce these conversion coatings, with a particular stress put on chromium-based conversion coatings.

2. Introduction to conversion coatings at zinc-polymer interface

As previously noted, for painted Zn-based coated steel, the overall paint adherence is mainly ensured by conversion coatings (CC). These coatings have been extensively studied in the literature and their efficiency was demonstrated for most types of conversions [28,29,30]. Multiple formulations of conversion coatings exist, and different mechanisms can lead to the conversion of the metallic surface into an oxidized surface, such as chemical dissolution-precipitation sequence (phosphate, chromate conversion coatings, etc.), electrochemical processes (anodized layers) or physical processes (sol-gel conversion coating, plasma processes,…). The obtained layers are usually classified as thick (thickness of 1 µm and above) or thin (thickness from several nanometers to several hundred nanometers). A recent review of CC can be found in [27]. In the present chapter only several established classes of CC selected among the most used for zinc alloys coated steel are described. Other formulations of thin CC for Zn based substrates, in particular based on Zr, Ti, Ce [31,32,33], have been developed in recent decades however their review is out of scope of the present manuscript.

2.1. Thick (micrometric) phosphate conversion coatings

Phosphate conversion coatings (PCC) with typical thickness of 1-2 µm can be applied on a wide range of materials such as zinc, iron and magnesium [34,35] and not only on the flat surfaces but also on rough industrial substrates. PCC are rough due to the dispersion of PCC grains on the surface, as shown on an example of SEM observation of PCC treated surface in **Figure 1.8**. This high roughness allows excellent adherence of polymer coatings to the substrate [36].Despite their excellent adherence, this type of conversion coatings is highly porous and its distribution on the surface is not every time homogeneous, which can limit corrosion protection of the substrate [37,38].

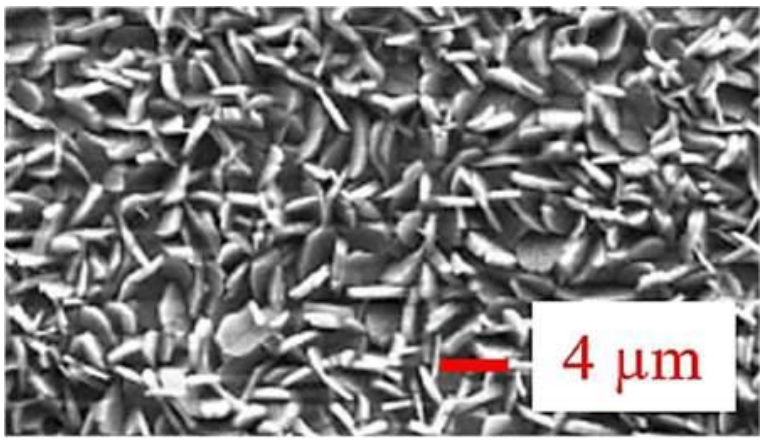

Figure 1.8: SEM observation of an electrogalvanized steel after phosphating in ZnMnNi PCC bath. Adapted from [37]

2.2. Thin chromates conversion coatings (CCC)

Historically, chromate conversion coatings (CCC) have been among the most used conversion coatings on zinc and aluminum alloys as they provide excellent corrosion protection and adhesion for polymer

coatings [39,40]. CCC are usually formed in a bath containing combinations of chromic acid H_2CrO_4, chromium salts such as sodium chromate or dichromate, and additional acids like phosphoric acid H_3PO_4 [41]. The formation of CCC is considered to be thermodynamically favorable since Cr(VI) species are strong oxidants. It is usually described by a 2-step deposition mechanism presented in reactions (1-2):

- Anodic dissolution of the substrate:

$$Zn \rightarrow Zn^{2+} + 2e^- \quad \textbf{(1.1)}$$

- Reduction of Cr(VI) species from pH = 2:

$$CrO_4^{2-} + 5H^+ + 3e^- \rightarrow Cr(OH)_3 + H_2O \quad \textbf{(1.2a)}$$

Or

$$Cr_2O_7^{2-} + 8H^+ + 6e^- \rightarrow Cr_2O_3.H_2O + 3H_2O \quad \textbf{(1.2b)}$$

The resulting CC thickness is in order of 100 nm, in addition, during CC formation Cr(VI) species are trapped inside the conversion layer and can be released "on request" in case of exposure to humid environment or creation of a defect in the conversion layer. These soluble Cr(VI) species promote further corrosion protection ensuring so called "self-healing" properties of CCC [42,43].

Despite their universality and excellent usage properties, chromates were proved to be genotoxic and carcinogen [44] and since 2006, European legislation tries to tackle hexavalent chromium via Registration, Evaluation, Authorization and Restriction of Chemicals (REACh) and Restriction of the use of certain Hazardous Substances (RoHS) [45]. According to these legislations, the application of Cr(VI) compounds will be banned by 2022 in Europe in most industrial application. Among the commercially available alternatives considered for chromate replacement and trivalent chromium conversion coatings were developed. These CC are briefly introduced in the next section.

2.3. Trivalent Chromium Conversion (TCC) as an alternative to chromate conversion

Trivalent chromium passivation was studied as a replacement of Cr(VI) conversion layers since more than 50 years. First attempts to develop trivalent conversion coatings (TCC) were performed in the early 1950s; in these works, the conversion solutions were based on chromates conversion bath with reducing additives to reduce most Cr(VI) into Cr(III) species [46,47]. However, the resulting concentration in Cr(VI) species in the bath and in the conversion coating was still not negligible in such processes. In the early 1980s, trivalent chromium passivation bath formulations containing either fluorides or zirconium additives were proposed [48,49]. More recently proposed formulations of TCC for zinc-based substrates incorporate transition metal ions such as Co(II), Ni(II) and Fe(II), which are expected to enhance corrosion resistance of the coating and control the surface appearance (coloration, brightness, …) [50,51,52].

Compared to CCC, TCC are thinner (mean thickness is around 20-30 nm). The thickness of a passive layer in TCC was shown to increase with the treatment duration, however the best corrosion resistance was achieved not with the highest but with an optimum TCC thickness because of possible dehydration voids and cracking in thick passivation films [53]. Compared to CCC, TCC were shown to be able to protect undamaged zinc panels from corrosion as efficient as CCC do in both immersion tests and atmospheric corrosion [54]. One of the advantages of trivalent chromium conversion coating compared to chromates

conversion coating is their stability at high temperature [55]. These specific characteristics gives TCC a high compatibility with electrogalvanized steels if the relief baking step in the production process is used to prevent hydrogen embrittlement [56].

TCC are largely studied on Al alloys [57,58,59]. Studies are less common for Zn substrates. Although the detailed mechanism of TCC is not well established on zinc substrate, is it commonly accepted that Cr(III) species are not strong enough oxidizing agents to initiate the conversion process. In TCC, nitrates are often added to play this role [50]. A description of the deposition mechanism of Co containing TCC was recently proposed by Hesamedini et al. (**Figure 1.9**), highlighting the co-deposition of cobalt and chromium species and the presence of zinc hydroxides in varying ratios in function of the type of complexing and oxidizing agents in the conversion bath [60].

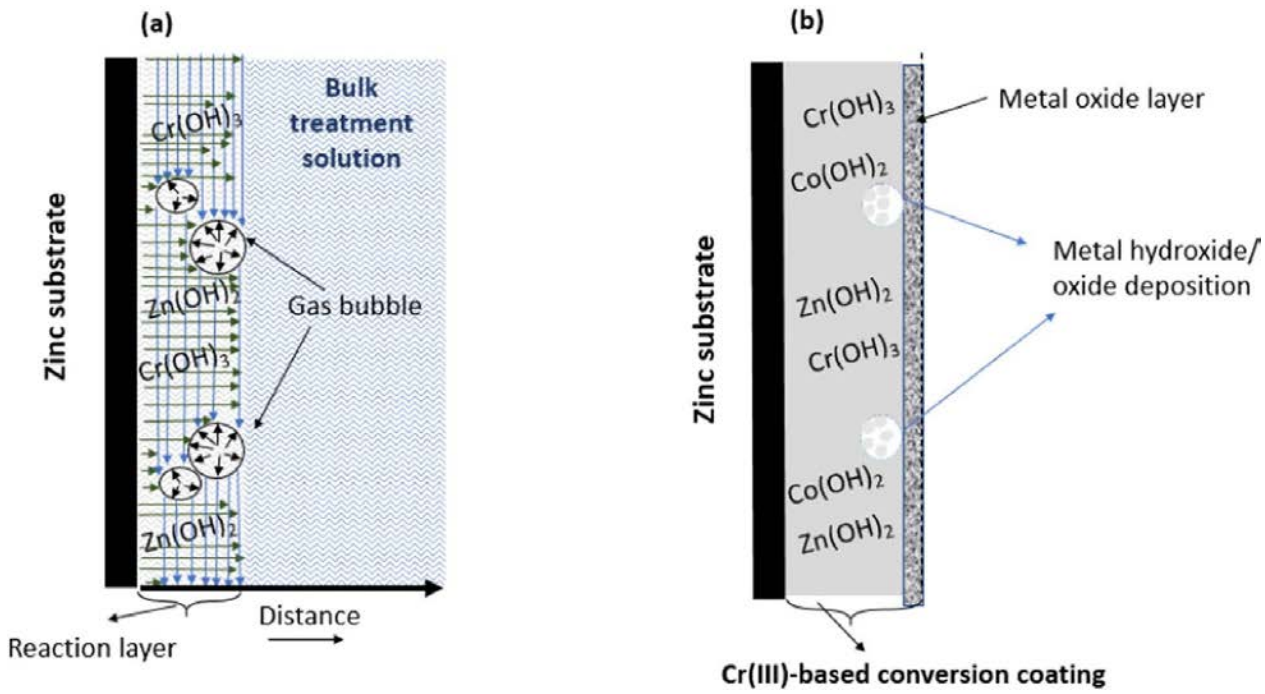

Figure 1.9: An illustration of (a) TCC coating formation during immersion time, the vertical arrows show the forces due to surface tension, acting along the direction parallel to the interface; the horizontal arrows indicate the normal tension perpendicular to the zinc substrate due to the agitation; the black arrows show the force due to the internal pressure of the formed bubbles. The reaction layer is the area between the substrate and the bulk treatment solution, in which during the TCC process the deposition reactions are taking place. (b) A schematic illustration of the ultimate morphology of the formed TCC layer. Adapted from [60]

The structure and composition of such TCC on zinc plates steel were characterized by TEM cross-section observation and high-resolution EDS technique to provide in-depth composition of the coated zinc nickel (**Figure 1.10**). The results correlate with the schematic description presented in **Figure 1.9**.

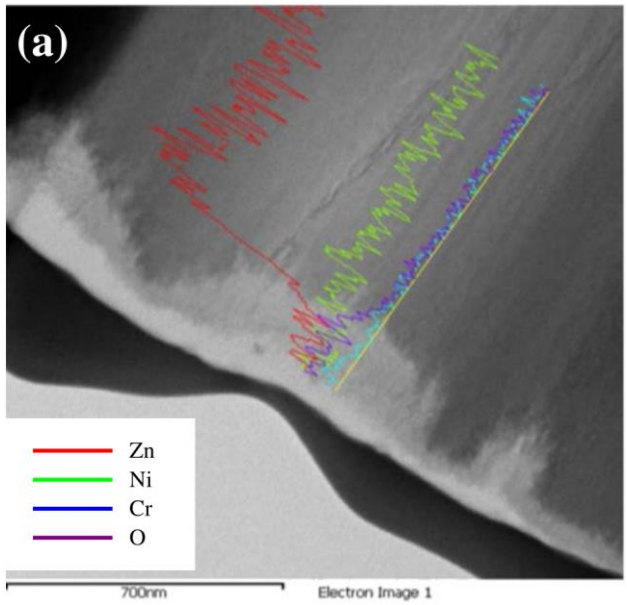

Figure 1.10: TEM cross section of TCC and composition line scan. Adapted from [53]

Similarly, TCC improved corrosion resistance of electroplated Zn–Ni alloys [53,61]. In this works, the formed layer showed lower Ni content that in pristine ZnNi alloy and the conversion coating was mainly composed of Cr_2O_3, ZnO and NiO. Morphological, compositional and structural characterization of several types of TCC and different substrates were made in [62]. The obtained TCC characteristics are summarized in Table 1.1. From the data presented in this table, one can note that TCC can present some cracks as well as traces of Cr(VI).

Table 1.1: Morphological characteristics and Cr(VI) content in several types of TCC studied in [62].

	Morphology	Thickness (nm)	[CrVI] (dpc ug/m2)	Application	Other
Organic CrIII w Co	Gen. smooth, occ. cracks	Zn 100-400	<0.1	Std Zn yellow alternative, generally with seal, 'clear' alloy.	ZnO in film., no spinnel. Co reduces heat variation
Inorganic CrIII wo Co	ibid.	Alloy 70-200 function of alloy	<0.02 or nd	Alloy tie coat. With ZnFe and seal. With ZnNi as clear.	Ibid. Alloy sensitive ([Fe], [Ni]).
Inorganic CrIII w Co	ibid.	Alloy 70-200 function of [Co] and dense?		Lower corrosion req'ts (blue). Improved corrosion resistance with seal.	Low T app.
Phosphate CrIII	Rough, dense crack pattern	Zn trace Fe 40-80 nm. ZnFe 80-200 nm	<0.1	Black coatings.	Low T app.
Organic Seal	Low rms, inorganic nano particles	800-1500	0	Improve corrosion resistance. Can be integrated with lubricant	
Inorganic Seal			0	Interiors, when low cost needed, and with fluid compatibility issues.	

More technical information about technical parameters of TCC on Zn, ZnFe and ZnNi plated steel panels can be found in [61]. The literature about the important aspects of TCC, including their corrosion performance, the methods employed to study composition, morphology, and corrosion resistance and the

impact of process parameters and passivating bath composition on the microstructure and properties of the obtained layers was also recently reviewed in [63].

Although numerous works made in the research laboratories and in industry demonstrated good anticorrosion action of TCC for traditional Zn alloys and good initial adhesion of epoxy based paints to these substrates treated by TCC, the stability of the metal-TCC-polymer interfaces steel needs to be optimized, in particular taking into account that, as previously mentioned, conventional substrates are more and more replaced by new alloys.

The optimization of the durability of metal-conversion coating-polymer combination requires a good understanding of the interface processes during degradation and the development of methods, able to detect and help to understand degradation processes in reasonable time scale, in order to reduce time to market of new materials.

The next sections will review the existing knowledge about degradation of metal-oxide-polymer interfaces (section 3), the methods for interfacial reactivity measurement (section 4) and the state of the art in the characterization of such interfaces (section 5).

3. Possible degradation mechanisms of metal-polymer interface in humid environment

This section briefly summarizes the theoretical degradation mechanisms proposed in the literature to describe degradation of painted systems. The experimental works leading to the proposed degradation mechanisms of painted systems being reviewed several times, in particular, in early work of Leidheiser et al. (1982, [19]) and more recently review of Grundmeyer et al. (2007, [64]), this section doesn't aim to present the experimental proofs of these general degradation mechanisms. The main objective is to explain the terminology and introduce the problematics for the next sections.

The origin of the instability of painted metals in humid environments is attributed to the imperfect barrier effect of polymer coatings, resulting in water access to the interface. The "loss of adhesion of a coating when wet" phenomenon was for the first time highlighted by Funke et al. [65]. As water penetrates the polymer and reaches the interface, a liquid accumulation under the paint (**Figure 1.11**) makes possible electrochemical and chemical dissolution. The substrate and conversion coating react with the electrolyte and underpaint reactivity increases with time, leading to the metal-polymer interface disbondment and delamination of the polymer coating from the metallic substrate [66]. Finally, the fraction of unprotected substrate increases which eventually accelerates the degradation of the whole system [67,68].

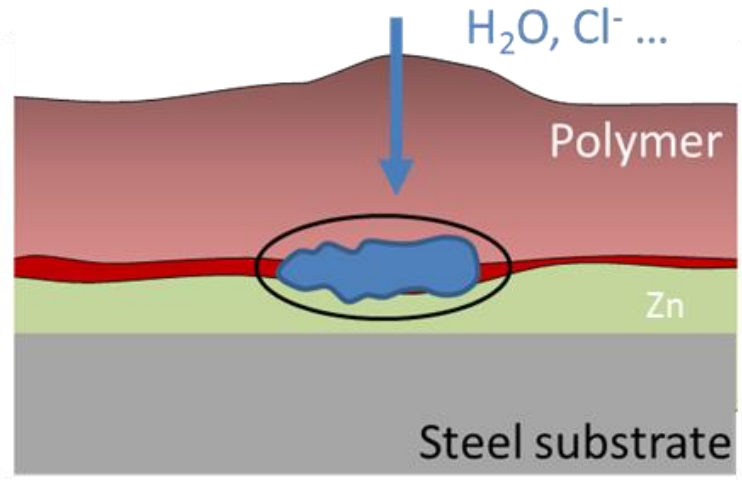

Figure 1.11: Generation of underpaint reactivity via water and active species diffusion to the interface

In the literature <u>six specific types of disbondment at buried metal-polymer interfaces are usually named: blistering, early rusting, flash rusting, anodic undermining, cathodic delamination and filiform corrosion.</u> In this work, we only focus on underpaint degradation leading to a loss of adhesion, hence early rusting and flash rusting mechanism will not be presented. Filiform corrosion at buried interfaces being a specific type of anodic undermining where the degradation progresses in the thread-like filaments which are not common for zinc substrates, it won't be detailed as well. The following sections will describe the degradation mechanisms relevant to zinc-based substrates at initial states of degradation of metal-oxide-polymer interface.

3.1. Anodic undermining

Anodic undermining represents the type of underpaint degradation resulting from a galvanic coupling between the zones ascribed to the center and to the front of the disbonded area under the polymer coating; in that case, the driving force for the separation between metal and paint is driven by the anodic dissolution of the metal (**Figure 1.12**).

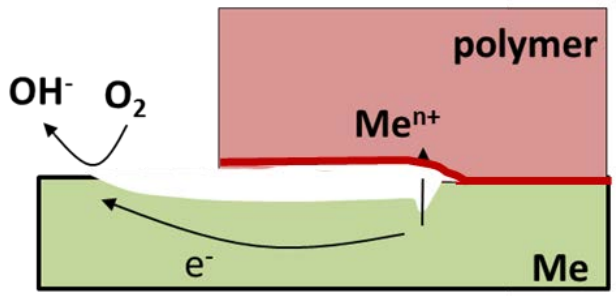

Figure 1.12: General scheme of anodic undermining mechanism

In neutral environments containing dissolved oxygen, the corrosion rate of zinc and steel is defined by the cathodic reaction, which is the oxygen reduction reaction (ORR). The degradation mechanism can be written as follows:

- Anodic dissolution of the metal (delamination edge):

$$Me \rightarrow Me^{n+} + ne^{-} \quad \textbf{(1.3)}$$

- Cathodic ORR ("open area"):

$$\frac{1}{2}O_2 + H_2O + 2e^{-} \rightarrow 2OH^{-} \quad \textbf{(1.4)}$$

The anodic undermining is characteristic for stable conversion coatings with strong adhesion between the conversion coating and the polymer coating; it was shown that it often results in an undamaged conversion coating detected at the polymer coating lower surface in the vicinity of the delamination edge [69,70].

In the case of relatively thin metallic coatings used as sacrificial anodes for steel protection, the anodic undermining occurs at a higher rate than on plain metallic surfaces because the anodic dissolution is forced to progress in the horizontal direction. This phenomenon can be further accelerated by the presence of defects in the sacrificial coatings (such as down to steel scratches) because of the galvanic coupling between the steel surface and the sacrificial metallic coating as described in the **Figure 1.13**.

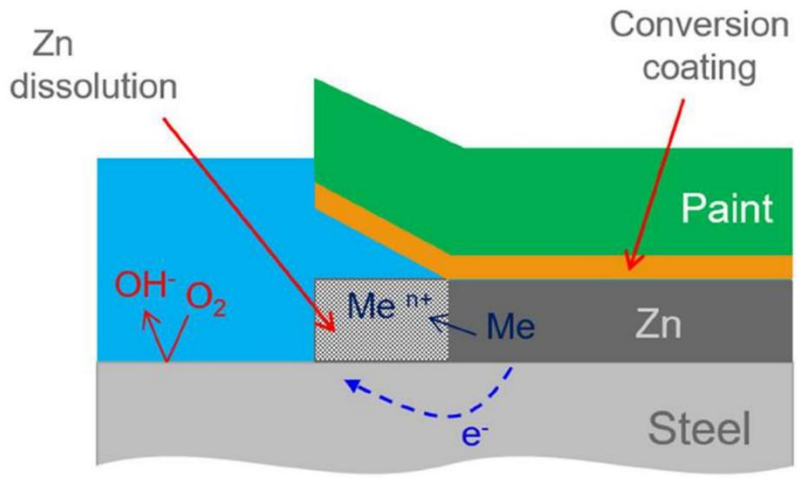

Figure 1.13: Anodic undermining mechanism in the case of a down to steel scratch on galvanized steel. Adapted from [71]

3.2. Cathodic delamination:

Cathodic delamination is the counterpart mechanism of anodic undermining in which the driving force for the interface degradation comes from cathodic reaction. Usually, degradation results from a local alkalization of the media in the vicinity of the metal-oxide-polymer interface (**Figure 1.14**), leading to the dissolution of conversion coating and hence to a disbondment between the metal and the polymer [72,73]. Cathodic delamination at buried interface can either result from cathodic polarization of the metal in the case of cathodic protection or from the galvanic coupling between the center and the front of the defect at metal-polymer interface.

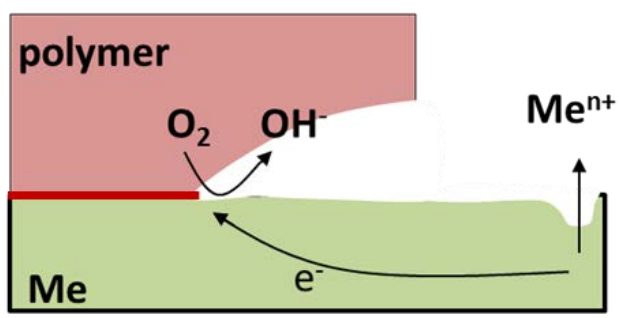

Figure 14: General scheme of cathodic delamination mechanism

The degradation mechanism can be written as follows:

- Anodic dissolution of the metal ("open area"):

$$Me \rightarrow Me^{n+} + ne^- \quad \textbf{(1.3)}$$

- Cathodic ORR (delamination edge):

$$\frac{1}{2}O_2 + H_2O + 2e^- \rightarrow 2OH^- \quad \textbf{(1.4)}$$

A general mechanism of cathodic delamination was proposed by Leidheiser and Kendig [74], describing the following steps:

1. Penetration of water, ions and oxygen
2. Development of a low-resistance pathway between the bulk and the substrate
3. Anodic reaction taking place on the steel surface
4. Cathodic reaction also taking place on the steel surface, and leading to some delamination
5. As a consequence of the anodic and cathodic reactions proceeding in a confined environment, the ion concentration increases, corrosion products precipitate on the metal surface
6. Precipitation of the corrosion products cause a drop of pH at the corrosion site (anodic)
7. A difference in acidity develops between the anodic and cathodic areas, pH being higher in the cathodic areas

As for anodic undermining, it is commonly admitted that the degradation rate in the presence of air is limited by the ORR [75]. In the case of weak adherent polymer (PVB) on galvanized steel, recent studies have shown that the cathodic delamination rate was limited by the diffusion of counter-ions (cations) to the delamination edge, which are necessary to allow the electroneutrality of the electrolyte [76].

As cathodic delamination occurs, the underpaint media becomes highly alkaline. Previous studies have reported local pH values reaching pH 14 [77]. In such conditions, many metallic oxides could form soluble complexes and the degradation of the metal-oxide-polymer interface is often explained by the dissolution of the oxide layer (or conversion coating) [78].

In the case of external cathodic polarization at sufficiently low potential, the proton reduction reaction cannot be neglected. As shown on the polarization curve of uncoated steel in 0.5 M NaCl solution, the proton reduction reaction is clearly the dominant process for potential below -1 V vs HSE (**Figure 1.15**). One should note however that the absolute value of the potential should be taken with caution for polymer coated metals. Indeed, a significant difference can exist between the applied potential and the potential taking place at the solid/liquid interface. This difference is not easy to evaluate in practice.

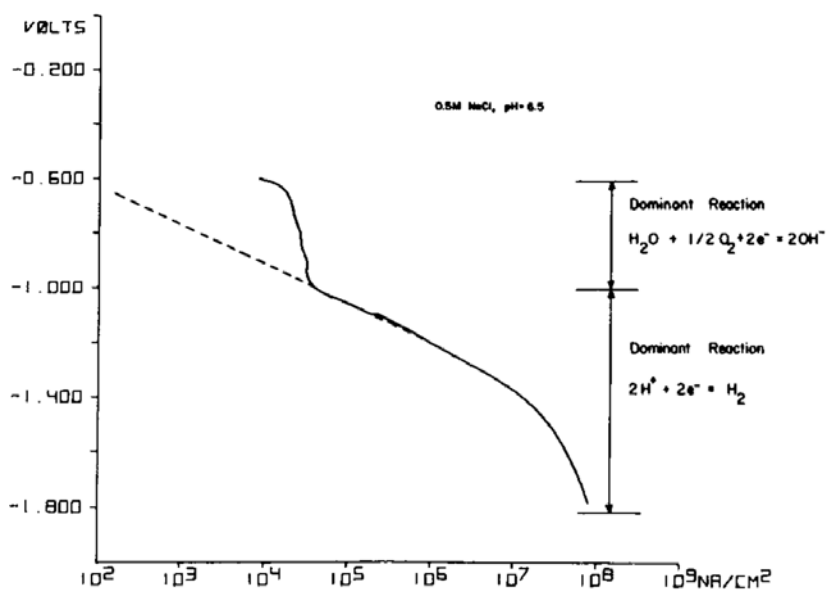

Figure 1.15: Potentiodynamic polarization curve for steel in aerated 0.5 M NaCl. Adapted from [19]

3.3. Blistering

"Blistering is one of the first signs of the breakdown in the protective nature of the coating. The blisters are local regions where the coating has lost adherence from the substrate and where water may accumulate, and corrosion may begin." [19] Blistering can be induced by mechanical or osmotic driving forces (**Figure 1.16**).

Mechanical blistering can be induced by the formation of voluminous corrosion products at the metal-polymer interface which will pressurize the polymer until the disbondment occurs. This mechanical pressure can also be induced by hydrogen evolution during cathodic polarization (**Fig. 1.16 b**) [69].

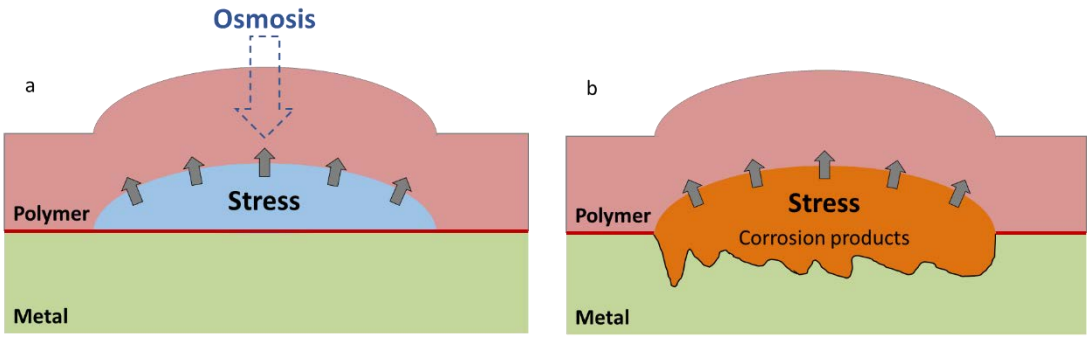

Figure 1.16: General scheme of (a) osmotic and (b) mechanical blistering mechanism

Osmotic blistering mechanism (**Fig. 1.16 a**) is related to a concentration gradient of soluble species between the metal-polymer interface and the environment [79]. As noted here-above, polymer coatings can be described as permeable membrane which allow water to flow. Thus, if soluble species (inorganic salts, corrosion products, solvent traces…) are present at the metal-polymer interface, the dilution of the media will tend to increase and force the water to flow through the paint. It was reported that the osmotic pressure inside a blister can reach about 2500 kPa, which is approximately two orders of magnitude higher than the yield strength of common organic coatings (10-50 kPa) [19].

In summary, ***the presence of a pre-existing weak points at the metal-oxide-polymer interface serves very often as an initiation of polymer disbondment (delamination)*** [80,81]. *This means that when the attempts are made to understand degradation mechanisms in concrete systems, particular attention should be payed to the characterization of the initial damage of the interface and its evolution during environmental exposure. For this purpose,* ***localized characterization of the chemistry and localized measurement of electrochemical reactivity at the interface seem to be the most relevant****.*

The next section will overview the methods proposed for the stability characterization of metal-oxide-polymer systems with a particular interest to local techniques.

4. Experimental approaches to access interface stability in painted systems

This section reviews the experimental approaches, used to describe stability of painted metals in humid environments. These approaches have different objectives and deliver complementary information. The current section reviews two types of experimental approaches: accelerated corrosion tests and electrochemical techniques. Accelerated corrosion tests are initially designed for quality control and materials ranking. In situ monitoring and localized analysis in climatic tests is possible but still challenging and the results of accelerated climatic test are rarely studied in depth in order to access degradation mechanisms. Electrochemical tests in contrast aim to study corrosion mechanisms. Moreover, they allow the in situ survey of the system evolution and localized characterization. Special attention will be payed to the detection of localized electrochemical reactivity by electrochemical technics.

4.1. Accelerated degradation tests

Polymer coated metals are designed for long service life, it is hence very important to be able to evaluate their long-term stability. To accelerate materials qualification, accelerated corrosion testing has been in development since 1930s and is nowadays a key step in the corrosion control and the assessment of organic coatings properties [82,83]. For instance, some structural parts in automotive construction are qualified “corrosion proof” for more than 25 years by manufacturers. It is unlikely to allow a 25-year delay between the development of new materials and their application in industrial processes. Moreover, even if manufacturers could afford this R&D delay, new materials could not be accurately tested for a 25-year period, for instance in field exposure, and still be representative of the environment and the constraints of real in-service application. Moreover, a rapid qualification is necessary for production lines in order to ensure the quality control. Accelerated corrosion tests are hence essential for the development of new materials in terms of anti-corrosion properties and surface treatments.

The most important requirement for accelerated laboratory test is that the test should be meaningful, *i.e.* that it simulates the relative ranking of material, and that it reveals similar failure modes than the ones observed in field exposure. Although a “perfect” accelerated test cannot be established because accelerating the corrosion phenomenon changes its mechanism by nature, recent work comparing field exposure and new accelerated tests were able to show correlations between the failure modes and therefore the existence of “relevant” accelerated corrosion tests depending on the desired limiting phenomenon. Another approach is to corroborate different corrosion tests, such as correlation between salt fog exposure, long immersion test and electrochemical procedures [84]. The following sections will detail some types of accelerated corrosion tests used in steel, automotive and aerospace industry.

4.1.1. Atmospheric corrosion and salt spray tests

The first accelerated atmospheric corrosion test was published in 1939. It consisted in the exposure of the samples in a hermetic chamber in which saline aqueous solution (5 wt.% NaCl) was continuously sprayed on the samples at 35 °C [85]. This type of tests is called continuous salt spray test (SST); it is now

one of the most widely used types of test for corrosion assessment. Recent developments in SST proposed to vary the composition of the sprayed solution in order to fit different environment and promote better correlation with "real" corrosion mechanism of samples [86].

In the automotive industry, accelerated corrosion tests were extensively developed in the last decade and this development resulted in complex sequences of cycling weathering conditions alternating salt spray, humidity, drying, heat and cold [87,88]. **Figure 1.17** presents an example of such a test used in the automotive industry: the "new VDA" accelerated test [88].

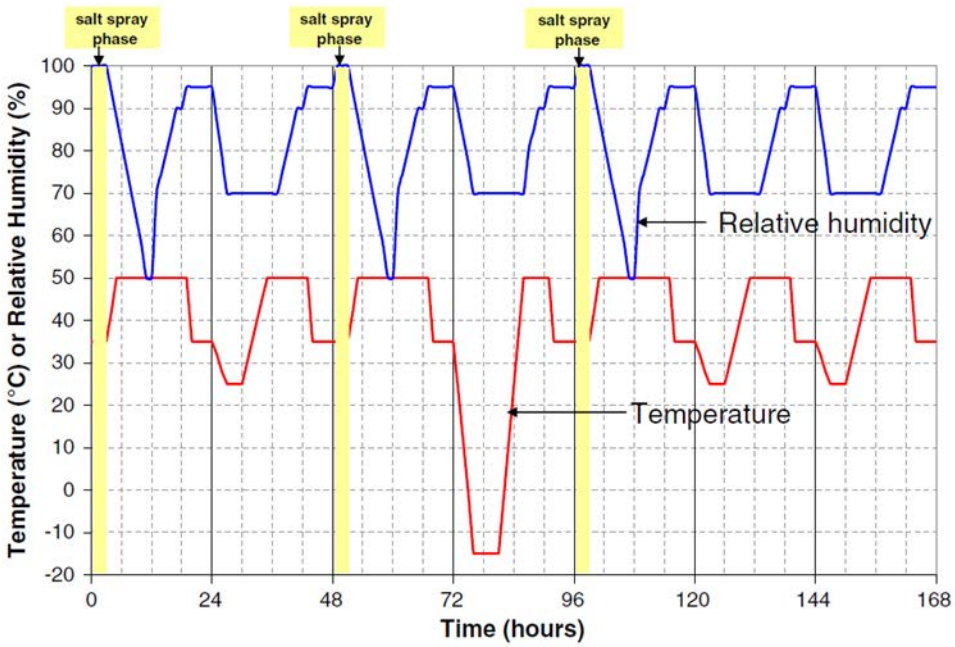

Figure 1.17: Temperature and humidity variation during a one-week cycle of the VDA 233-102 test. Adapted from [88]

For steel coated by zinc alloys it was demonstrated that cyclic climatic tests can better describe degradation mechanisms relevant to atmospheric corrosion than continuous SST [83].

Salt spray test application to the polymer coated substrate with an artificially introduced defect in the coating (scratch in the polymer down to the metal or even down to the steel substrate for galvanized steels) is extensively used to assess the capacity of a painted system to limit delamination and eventually to verify self-healing properties of the system. A standard way is a cross scratch in the polymer prior to SST. The observation of the vicinity of the defect and the evaluation of the delaminated distance from the scratch center after the test is routinely used to compare different materials; blistering far from the scribe can also be observed as shown in **Figure 1.18**.

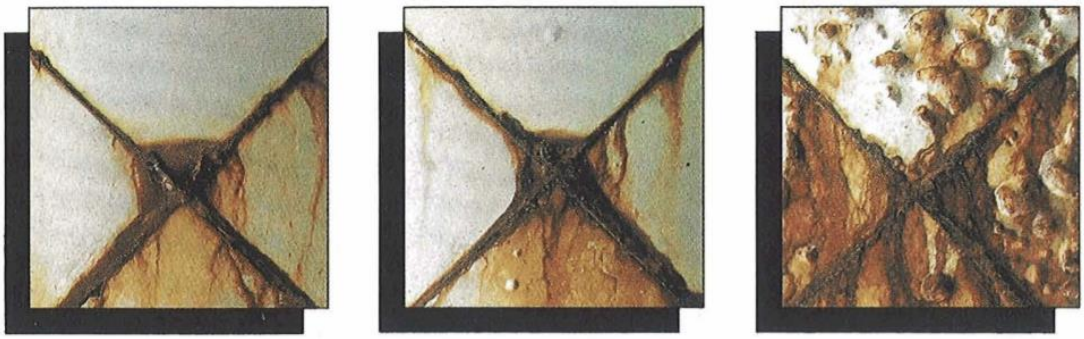

Figure 1.18: Observations in the vicinity of scribed regions on painted steel panels in SST. Adapted from [82]

4.1.2. Immersion test

Long term immersion tests in distilled or demineralized water are often used to evaluate the paint stability and paint adherence to the substrate. Indeed, with water immersion, various degradation phenomena can be observed, such as: paint discoloration, staining, formation of blisters, swelling, adhesion loss, softening, or hardening. These parameters can be evaluated visually or via appropriate physical tests along the test. Immersion test application to coated metals in order to assess paint adherence were first published in the 1980s [89]. The most often observed phenomenon in these tests is blistering, often attributed to osmotic blistering. It is usually evaluated with standardized methods by optical photography and visual observations [90]. An example of optical microscopy observation of paint blistering is shown in **Figure 1.19**.

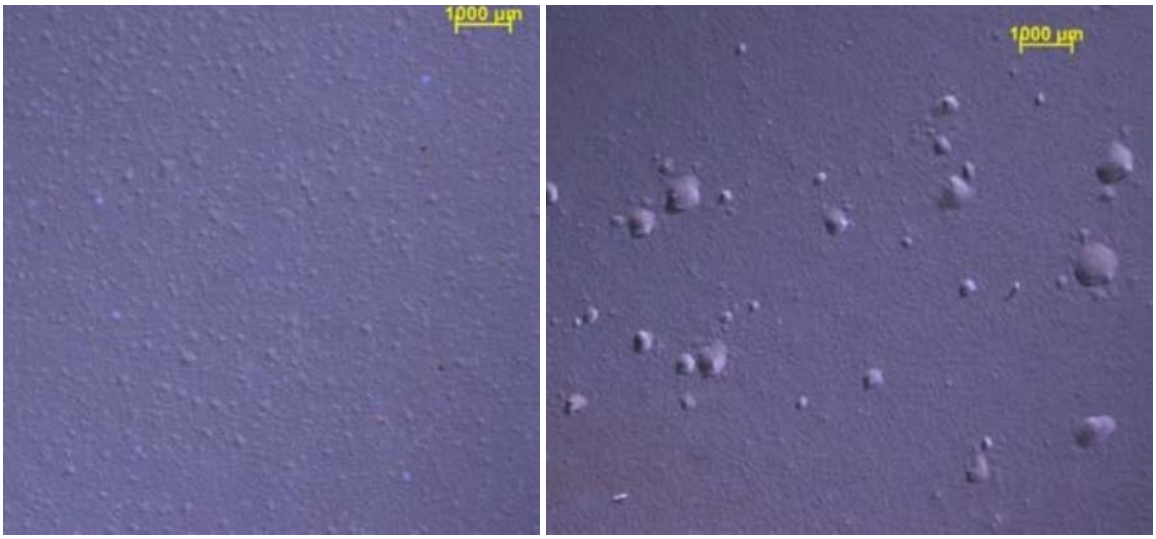

Figure 1.19: Optical microscopy observation of painted system after 1000 h immersion test. Adapted from [91].

In addition to immersion test combined with the observation of blistering, a semi-quantitative assessment of polymer coating adherence can be obtained from the adherence test on the samples with preliminary cross hatch on the polymer [92]. The paint adherence to the substrate is evaluated by cross cutting the polymer and evaluation of the polymer fraction removed with an adhesive tape (**Figure 1.20**).

The remaining coating in the tested area after the adhesive test removing is compared to standardized results and provide semi-quantitative information on the adherence of the polymer coating on the substrate [92].

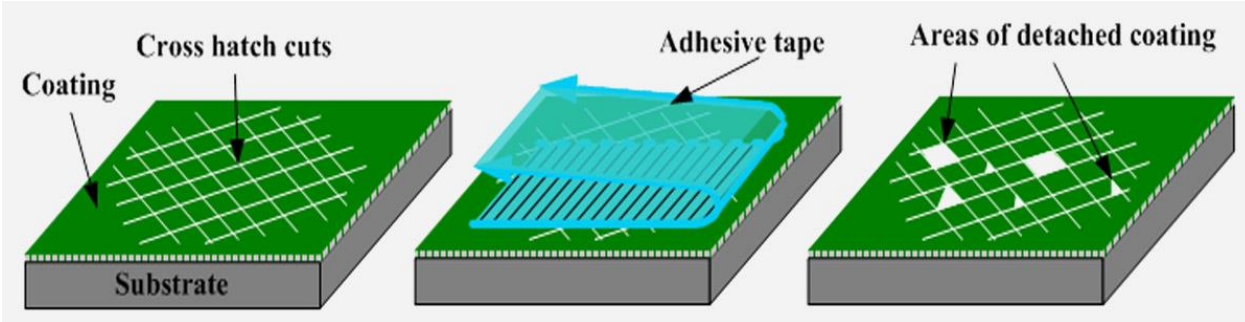

Figure 1.20: Schematic description of the cross-hatched test. Adapted from [93].

4.1.3. Electrochemical tests

As detailed here-above, the degradation mechanisms of painted systems are related to the electrochemical behavior of the buried interface. Hence it is possible to electrochemically accelerate anodic undermining and cathodic delamination by polarizing the sample via applied polarization.

One of the first electrochemical assessment of coated system was published in 1996, it consisted in 24 h cathodic polarization at -1.050 V vs SCE in 0.5 M NaCl aqueous solution at ambient temperature of scribed painted carbon steel [94]. The results of this test were correlated to long-term exposure in SST (up to 1200 hours) by comparing the surface appearance, results of pull-back test and electrochemical impedance spectroscopy. This technique, REAP (Rapid Electrochemical Assessment of Paint), is still used to this day, promoted by potentiostat manufacturers and considered by the ASTM [95,96].

For an undamaged coated surface, in addition to long term immersion, AC-DC-AC accelerated electrochemical degradation procedure via alternating cathodic polarization (DC) and EIS measurement at open circuit potential (AC) [84,97] is often used. Depending on the potential of the cathodic polarization during AC-DC-AC procedure, it can either be used to assess the polymer coating properties [98], or to study the underpaint reactivity and delamination [99]. The application of cathodic potential promotes the disbondment initiation at metal-polymer interface and its propagation [100]. At potentials more cathodic than -1 V/SHE, both the oxygen reduction and the water reduction can occur [101] thus leading to an increase of OH^- concentration at the buried metal-polymer interface. In the case of large cathodic over-potential, high local pH, peroxides and free radicals can also damage the polymer matrix; the polarization conditions should then be chosen carefully for each system. The cathodic reactivity is localized in delaminated areas and/or zones of the interface with weaker adherence.

$$\mathbf{O_2 + 2\,H_2O + 2\,e^- \rightarrow H_2O_2 + 2\,OH^-} \qquad \textbf{(1.5.a)}$$

$$\mathbf{H_2O_2 + 2\,e^- \rightarrow 2\,OH^-} \qquad \textbf{(1.5.b)}$$

$$\mathbf{2\,H_2O + 2\,e^- \rightarrow H_2 + 2\,OH^-} \qquad \textbf{(1.6)}$$

As described here-above, painted systems present various ageing behavior and can degrade in many ways at every interface and in each layer: metal, conversion coating and paint.

A non-exhaustive review of the existing electrochemical techniques and methodologies applied to the characterization of painted systems is presented in the next sections.

4.2. Electrochemical survey of the degradation of the system metal-polymer

Electrochemical measurement technologies permit fast measurements with simple instruments. These tools allow quantitative or semi-quantitative evaluation of the degradation rate and hence permit the evaluation of corrosion protection. Among the most used in situ technics are the measurements of open circuit potential (OCP), linear polarization resistance (LPR), electrochemical noise (EN) and electrochemical impedance spectroscopy (EIS) [102]. Some of them will be detailed below.

4.2.1. Open Circuit Potential measurement

It was earlier demonstrated that the potential of coated metals is more noble (positive) than the potential of bare metal. As such, the OCP evolution during immersion of the sample allows to measure the time required for the electrolyte to penetrate the polymer coating by observing the steep decrease in the OCP value [103]. Then, the evolution of the OCP can be related to underpaint phenomena like oxidation and passivation of the coated metal [104,105].

An example of OCP evolution of an aluminum alloy specimen coated with 2 wt.% polyaniline (PANI) epoxy coating during immersion in 5 % NaCl solution is provided in **Figure 1.21**. The drop in the OCP after 6-12 hours of immersion corresponds to the accumulation of water at the metal-polymer interface. The increase in the potential between 20 and 48 hours of immersion was attributed to the change of the protection mechanism of the painted system: from barrier protection of the organic coating to ionic resistance due via the formation of an oxide layer (passivation) at the metal-polymer interface.

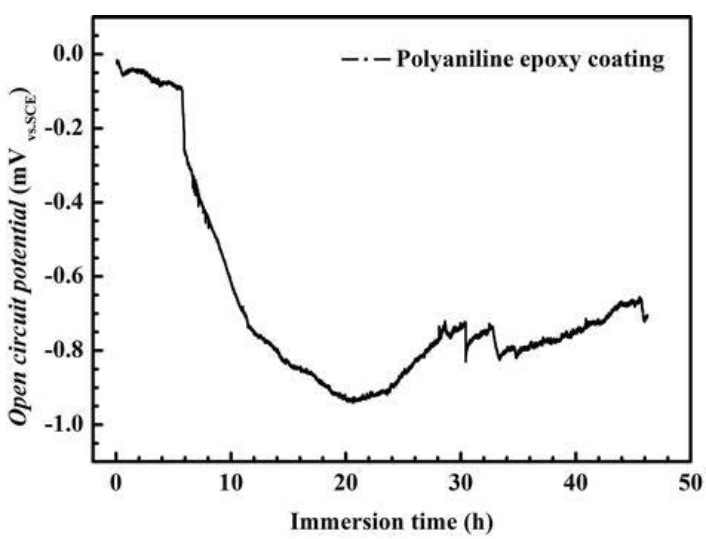

Figure 21: OCP curve for 2% PNI coated aluminium in 5% NaCl solution for 48h. Adapted from [102]

4.2.2. Electrochemical impedance spectroscopy

Electrochemical impedance spectroscopy (EIS) is one of the most used in situ techniques to study the polymer ageing during immersion [106,107,108]. It is a non-destructive technique providing immediate information on the degradation state of the painted system such as the properties of the polymer coating and/or the underpaint interface. The principle relies on the application of a sinusoidal potential excitation and the measurement of the induced current; the electrochemical impedance Z is the complex number obtained by the ratio of potential V and current I at the selected frequency ω as described by the Ohm law.

$$Z(\omega) = \frac{V(\omega)}{I(\omega)} = \frac{V_0 \sin(\omega t)}{I_0 \sin(\omega t + \varphi)} \quad \textbf{(7)}$$

Electrochemical impedance spectra are acquired by calculating Z at various frequencies ω.

An example of the evolution of the EIS modulus in Bode representation of epoxy coated steel over 28 days of immersion in 0.5 NaCl aqueous solution is provided in **Figure 1.22**. The degradation is visible from the decrease of the impedance modulus in low frequency domain.

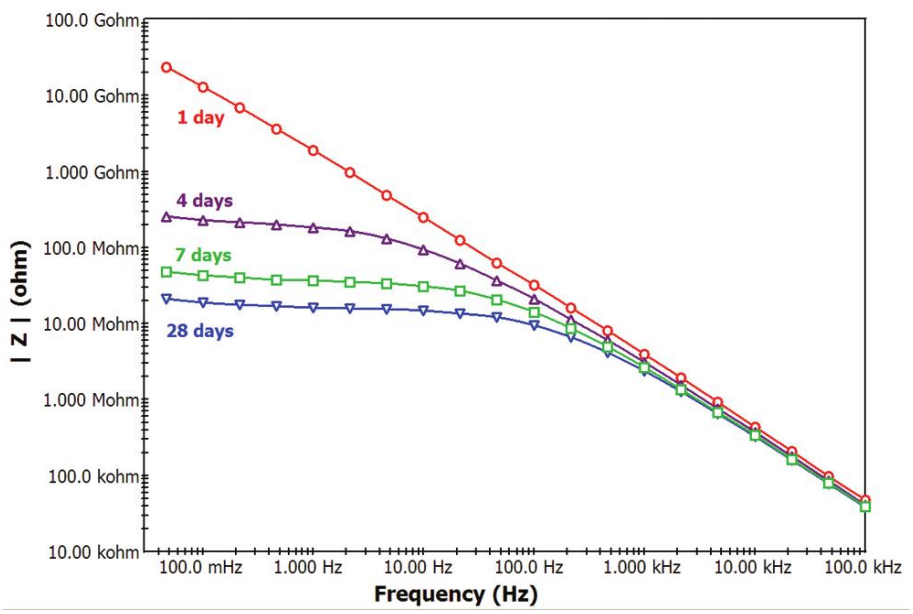

Figure 1.22: EIS response of steel coated with epoxy primer immersed in NaCl at 50 °C, adapted from [102]

For more detailed analysis, the EIS spectra should be fitted. The possibility of fitting electrochemical impedance spectra with various equivalent circuit models, all describing different systems or stages of degradation (**Figure 1.23**) [109], is one of the great interests of using EIS to mechanistic description of the degrading system. The following electrical circuits can be considered:

- Intact polymer coating can be described as a dielectric (**Fig. 1.23.a**, **Fig. 22**, day 1))

- When water penetrates the coating and reaches metal-polymer interface, the double layer at electrolyte-metal interface is observed by the apparition of a second time constant (**Fig. 1.23.b** and **c**)
- In most cases, diffusion processes are involved, either of oxygen or of aggressive ions involved in the metal-polymer interface degradation, so a Warburg constant is required to fit the spectrum.

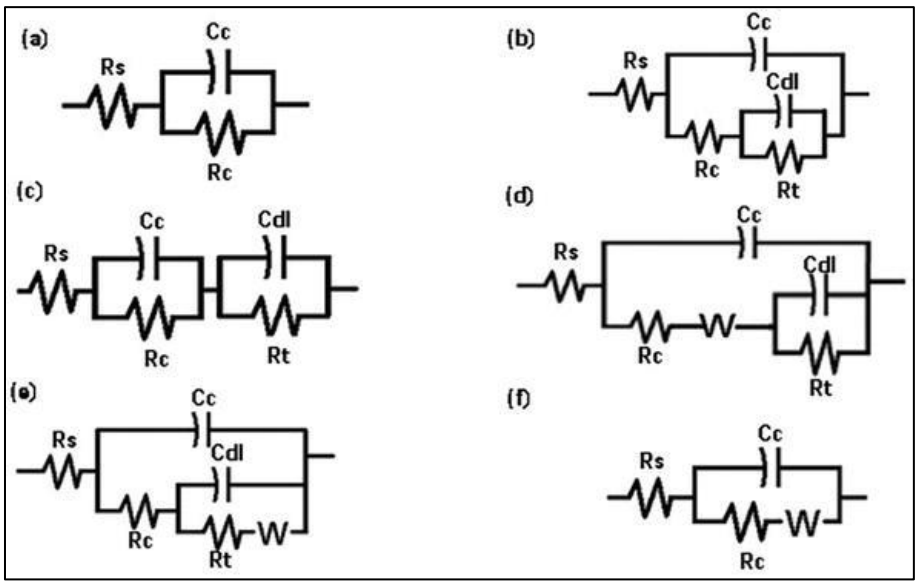

Figure 1.23: Typical equivalent circuit for EIS of coated metals. (a) general model of coating; (b) and (c) models with two time-constants in series and in parallel, respectively; (d) and (e) models with two time-constants and characteristics of Warburg impedance; (f) model with Warburg impedance, adapted from [102]

The parameters, obtained from fitting, can deliver quantitative evaluation of coating degradation. According to the evolution of the capacitance of the polymer coating (Cc), the water uptake evolution can be followed using the Brasher and Kingsbury equation:

$$\Phi = \frac{K \log \left({}^{C_t}/_{C_0} \right)}{\log \left(\varepsilon_w \right)} \qquad \textbf{(1.8)}$$

where Φ is the volume fraction of the water in the polymer, C_t and C_0 are the capacitances of the coating after an immersion duration t and as coated, respectively, and ε_w is the dielectric constant of the water at working temperature.

Although this equation was proposed in 1950, it has some limitations and often renders different values from the ones expected from the other measurements, such as gravimetry [110]. Recent development in the EIS field, including modelling, have permitted to obtain more accurate and quantitative information on the water uptake evolution [111]. Several works combined EIS and infrared measurement to quantify water uptake into the polymer (see for instance [112]).

In addition to water uptake, physical structure of the polymer coating can be assessed by EIS and could be correlated to its glass transition temperature variation, *i.e.* the plasticization of the polymer coating during immersion [113].

The study of the electrochemical impedance spectra can also relate information on the buried metal-oxide-polymer interface. The evolution of the C_{dl} corresponding to the metal-electrolyte interface double layer can be modelled as a simple planar capacitor.

$$C = \frac{S\,\varepsilon_0}{d} \tag{1.9}$$

Hence the variation of the capacitor value simply depends on the metallic surface in contact exposed to the electrolyte, *i.e.* the degraded metal-polymer interface [114].
An illustration of equivalent circuit and the description of the system in the case of corrosion inside a blister and a scratch in the paint is provided in **Figure 1.24**.

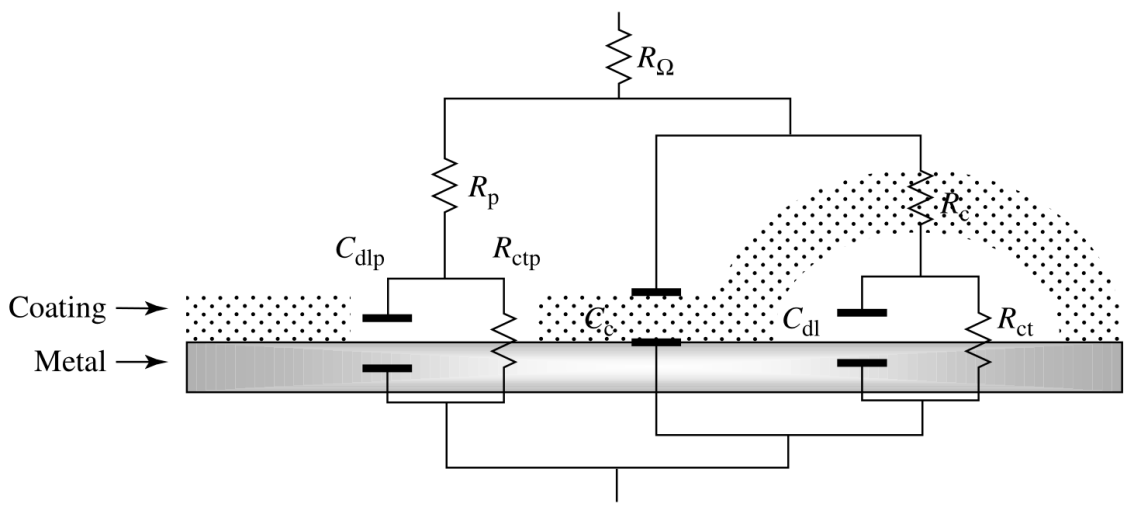

Figure 1.24: Equivalent circuit for a coated metal with corrosion at defects of the surface and underneath blisters. Reproduced from [64]

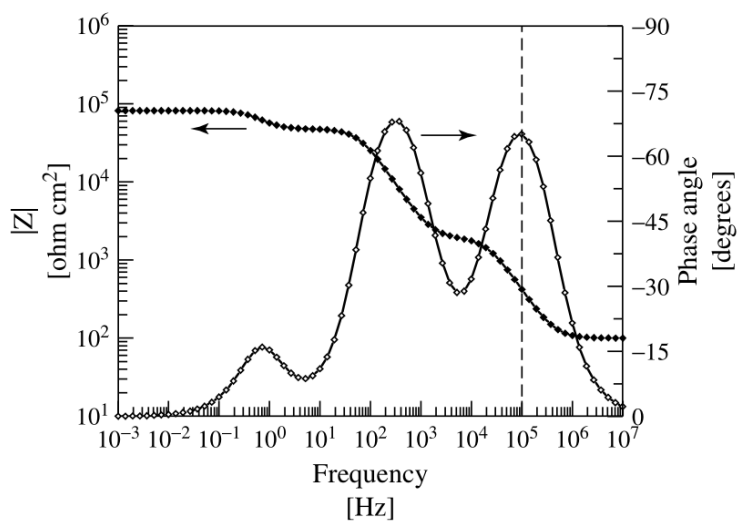

*Figure 1.25: Simulated EIS spectra in Bode representation of the equivalent circuit presented in **Fig. 1.24**. Simulated values: R_Ω = 100 Ω.cm² ; C_C = 4.10^{-9} F.cm^{-2} ; R_C = 10^5 Ω.cm² ; C_{dl} = 2.10^{-6} F.cm^{-2} ; R_P = 2.10^3 Ω.cm² ; C_{dlp} = 5.10^{-8} F.cm^{-2} ; R_{CTp} = 9.10^{-4} F.cm^2*

On the simulated spectra (**Fig. 1.25**) the three contributions of the undamaged polymer coating, the corrosion in damaged coating and the corrosion in the blister can be observed at respectively about 10^5 Hz, 10^2 Hz and 10^0 Hz. On the basis of these simulated curves, one can extrapolate this simple analysis on EIS spectra and identify the processes occurring at metal-oxide-polymer interface during the degradation of the sample.

Despite the apparent simplicity of EIS analysis, real samples often show much more complicated spectra with superimposition of the time-constants of the contributions and inhomogeneity at the interfaces. For instance, **Figure 1.26** shows the EIS of melamine polyester coated HDG Zn surfaces after phosphating treatment at different immersion time in 0.5 M NaCl solution [115]. Following the principles cited hereabove, one should expect to observe three contribution on the impedance spectra: the polymer coating, the conversion coating and the charge transfer. In reality, frequency response of the system is much more complicated and time constants cannot be distinguished from one another.

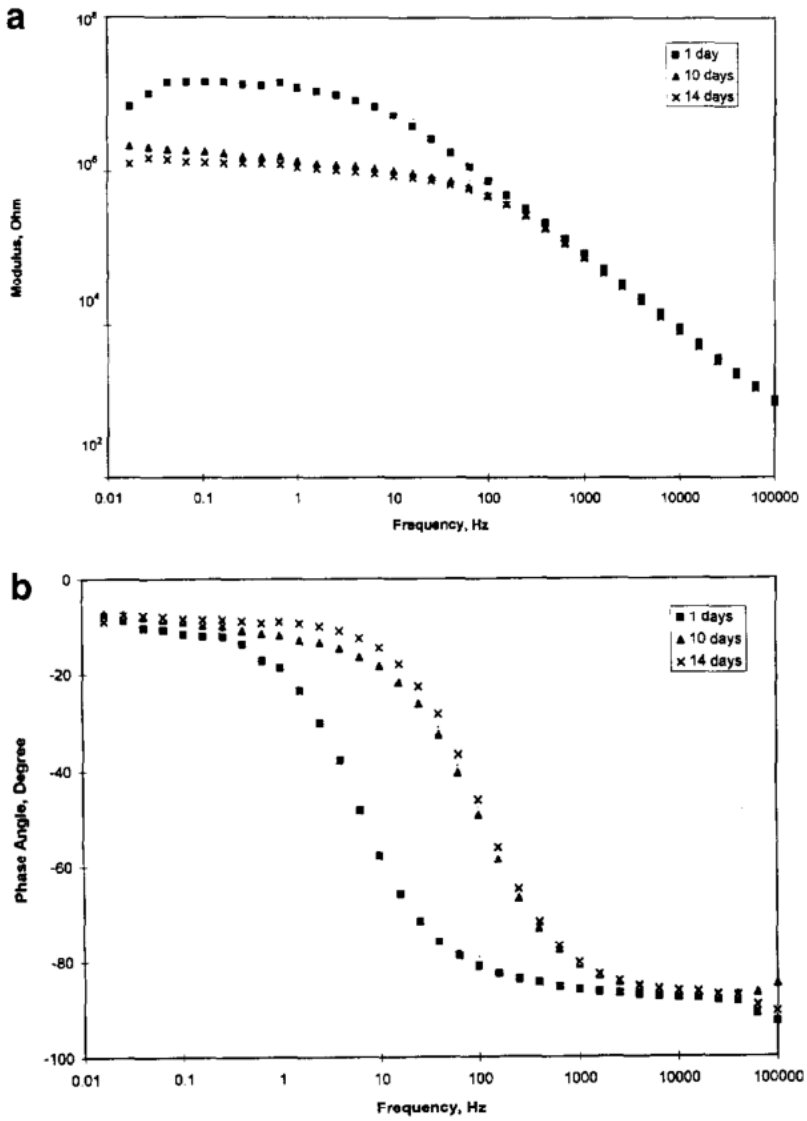

Figure 1.26: EIS in Bode representation of melamine polyester polymer coated galvanized steel with phosphate conversion coating in immersion in 0.5 M NaCl solution. (a) Impedance modulus and (b) phase angle. Reproduced from [115].

In electrochemical impedance spectroscopy fitting, a Constant Phase Element (CPE) is often used instead of a capacitor in equivalent electrical circuit. CPE is used to model the non-ideal capacitance of the polymer coating and of the double layer; it describes a heterogeneous behavior of the capacitance or a dispersion in frequency of the capacitance values. This dispersion can be related to:

- A non-uniform current distribution [116,117]
- The porosity of the electrode-electrolyte interface [118]
- The heterogeneity and the surface roughness [119,120]

To summarize, the CPE behavior is related to a distribution of time constants as presented in **Figure 1.27**; among them, two main types of distributions can be distinguished: a 2D distribution along the interface (b) and a 3D distribution combining 2D distribution and a dispersion normal to the surface (a).

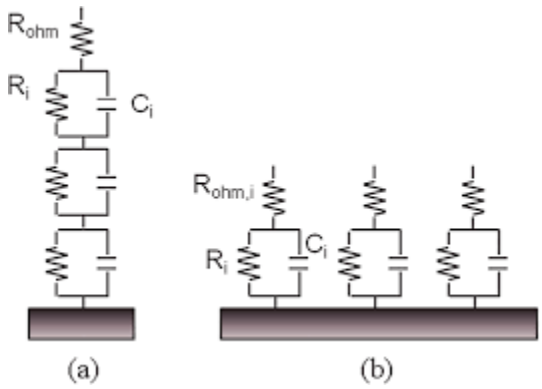

Figure 1.27: Schematic representation of time constant distribution (a) normal to the surface and (b) along the surface, adapted from [121]

The use of CPE was studied to describe the inhomogeneities of painted systems, for the distribution of polymer coating properties [122], degraded areas at metal-oxide-polymer interface [123] and of water uptake in the polymer coating [124,125].

The EIS technique allows to describe the heterogeneous processes occurring during ageing of painted systems, however, it does not permit to localize them as well as to distinguish between 2D and 3D distributions of defects. For that purpose and for the identification of the processes, the use of local techniques combined to EIS is required.

4.3. Localized measurement of stability and degradation in painted systems

4.3.1. Scanning Kelvin Probe (SKP)

SKP is one of the most used localized technics for polymer coated metals studies in atmospheric corrosion. Is was theorized by Lord Kelvin in 1898; in the 1930s, the first Kelvin Probe technique was developed [126]. SKP is a non-destructive technique used to measure the contact potential difference (CPD) between the probe and the metallic surface of a sample. The principle is illustrated below.

As the probe and the sample are held parallel to each other, the two facing surfaces form a capacitor (**Figure 1.28**). By electrically connecting the probe to the sample, electrons can flow between the sample and the probe to equilibrate the Fermi levels; the difference between the work functions Φ_1 and Φ_2 of both surfaces is the CDP. It leads to a charging of the capacitor generated by the two surfaces.

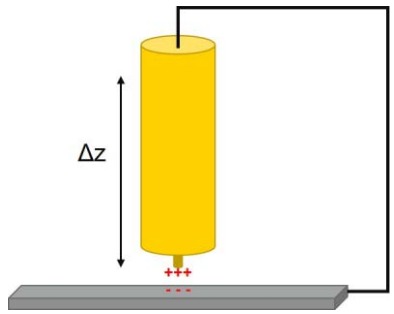

Figure 1.28: Illustration of a kelvin probe facing a metallic surface

During the measurement, the probe tip vibrates at a specific frequency, generating an alternative current at this specific frequency. A DC voltage is applied between the probe and the sample to counterbalance the CDP, the value of the CDP is obtained by varying the DC component until the alternating current provoked by the oscillation of the probe is nullified, *i.e.* when the charge of the capacitor is nullified [127]. **Figure 1.29** shows a descriptive scheme of this measurement process.

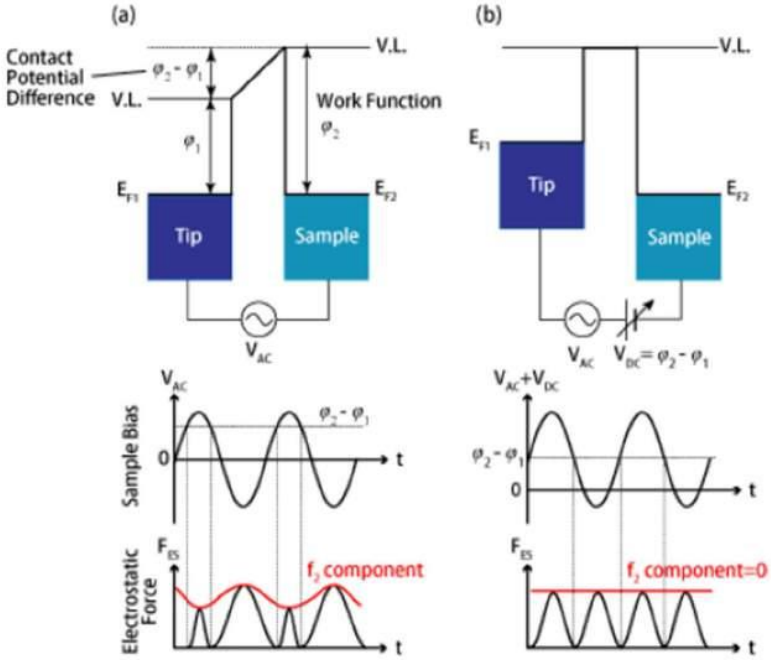

Figure 1.29: Scheme of the SKP measurement principle

SKP is one of the most common local tools for painted systems characterization. As shown here-above, the potential of a metallic substrate varies whether it is coated by paint or not, and in function of the water penetration in this polymer coating. Hence, SKP mapping was proposed to observe the potential distribution around defects in polymer coating during ageing of the system [128].

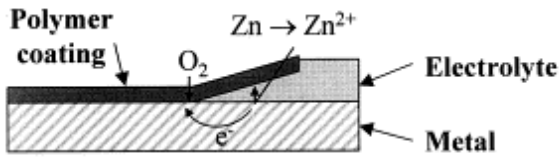

Figure 1.30: Scheme of the delamination process on polymer coated zinc, adapted from [128]

As the system degrades, the polymer peels off from the metallic surface, increasing the size of the defect with time; this process is called delamination (**Figure 1.30**). The advance of the delamination edge was correlated in [129] with the advance of the threshold value for the increase in the surface potential measured by SKP. This is illustrated by the SKP potential lines evolution over delamination of a weak polymer coated on zinc [130] in **Figure 1.31**.

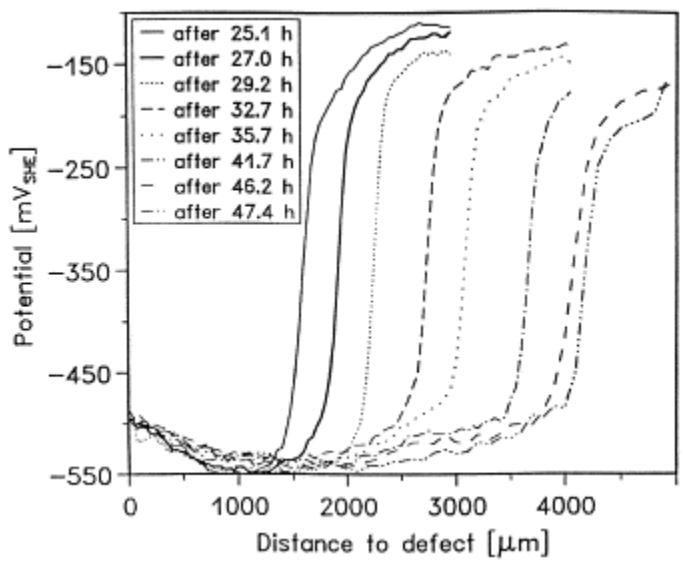

Figure 1.31: Potential profiles for different delamination times. The accelerated ageing was performed by deposition of 0.5 M NaCl electrolyte in the defect. The atmosphere was saturated with water to prevent from evaporation. Reproduced from [130]

The development of such a local quantitative technique for the measurement of delamination front position permitted to study the kinetics of metal-polymer adhesion loss from an initial defect [129]. The obtained kinetics permitted to formulate a hypothesis concerning the delamination mechanism and the influence of various aggressive species, such as carbon dioxide present in air, on the delamination mechanism [131,132].

In more recent work, SKP combined with optical microscopy permitted to describe the degradation of scratched Zn samples and the evolution of the metal-oxide-polymer interface [133]. The SKP measurements on scratched galvanized steel with thick polymer coating blistered after accelerated corrosion test evidenced the existence of connections linking the blisters found far from the scratch with each other and to the initial defect in the polymer coating [71], as illustrated in **Figure 1.32**. The potential distribution in the vicinity of the scratch shown in the figure demonstrates the areas of lower potential under the paint between blisters and in the path linked to the scribe.

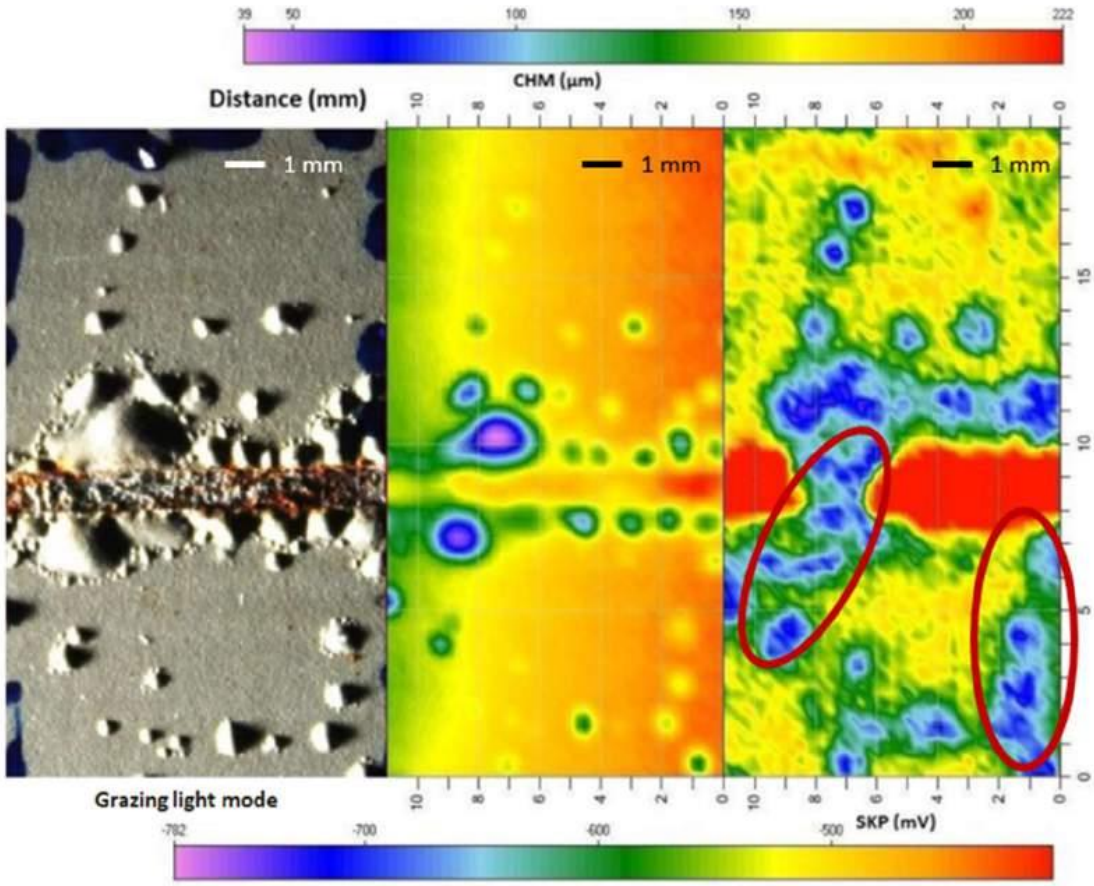

Figure 1.32: SKP mapping of painted and corroded sample with a down to steel scratch after 24 month of outdoor corrosion testing. Optical image, topography of the surface and potential mappings are presented, Reproduced from [71]

Despite its ability to measure electrochemical processes underneath organic coatings in situ, *one of the main drawbacks of SKP technique is the impossibility to perform in situ measurement of systems in immersion condition*.

4.3.2. Scanning Vibrating Electrode Technique (SVET)

Scanning vibrating electrode technics (SVET) is a non-destructive technique measuring the local currents associated with the sample surface. Its principle is based on the vibration of a probe perpendicular to the surface, resulting in the measurement of an AC signal because of the crossing of the equipotential lines in the solution. This signal is then related to local current in function of the conductivity of the solution.

SVET was first applied to investigate local corrosion processes at metallic surfaces in 1990s [134]. Its interest in the study of galvanic coupling under immersion is unraveled. However, *for painted systems, the application of SVET is limited to the systems with significant defects in the polymer and can be used mainly for the evaluation of the evolution in the defect*. Indeed, in the case of an intact coating, either the local current is negligible, or it might not be detected by SVET because the micro-galvanic couplings occur below

the polymer coating surface [135]. For this reason, the interest of SVET in the study of buried metal-oxide-polymer interface seems irrelevant.

4.3.3. Local Electrochemical Impedance Spectroscopy / Mapping (LEIS-LEIM)

Local Electrochemical Impedance Spectroscopy (LEIS) is the evolution of EIS designed for local measurements. It permits to measure the local contribution of the electrochemical impedance. Based on the same principle, the phenomena involved in the analysis of EIS and SEI are identical. The measurement principle of local electrochemical impedance relies on a similar principle than the SVET from which the technique was first derivated [136]. The use of a dual microelectrode in the vicinity of the working electrode (the sample surface) was later proposed by Isaacs [137] to measure the local contribution of the current during the AC perturbation induced by EIS measurement [138]. A schematic description of the LEI measurement principle is provided in **Figure 1.33**.

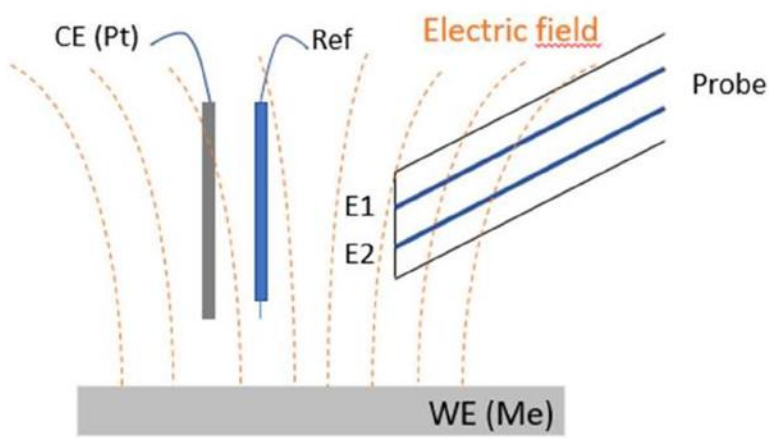

Figure 1.33: Scheme of the Local Electrochemical Impedance measurement principle. WE, CE and Ref indicates the working electrode, counter electrode and reference electrode of a 3-electrodes electrochemical setup, respectively. E1 and E2 represent the potential values at the dual probe surfaces. The electrical connections are not shown.

In this configuration, the local current density normal to the sample surface (i_{loc}) is calculated from the potential difference between the two micro electrodes of the dual probe:

$$i_{loc} = \frac{\Delta V_{probe}\,\sigma}{d} \tag{1.10}$$

where ΔV_{probe} is the potential difference between the two micro electrodes, σ is the conductivity of the electrolyte in the vicinity of the dual probe, and d is the distance between the two micro electrodes. The local impedance is defined as follow:

$$z(\omega) = \frac{V(\omega) - \Phi ref}{i_{loc}(\Phi)} = \frac{V(\omega)}{\Delta V_{probe}(\omega)}\,\frac{d}{\sigma} \tag{1.11}$$

where V(ω) -Φref represents the AC potential difference between the WE surface and the reference electrode in the bulk of the solution.

As EIS, LEI is a powerful tool for the exploration of painted systems with spatial resolution, allowing to distinguish localized reactivity at metal-oxide-polymer interface [139].
The technique was applied to painted substrates after scarification of the polymer coating and salt spray exposure to enhance delamination mechanism.

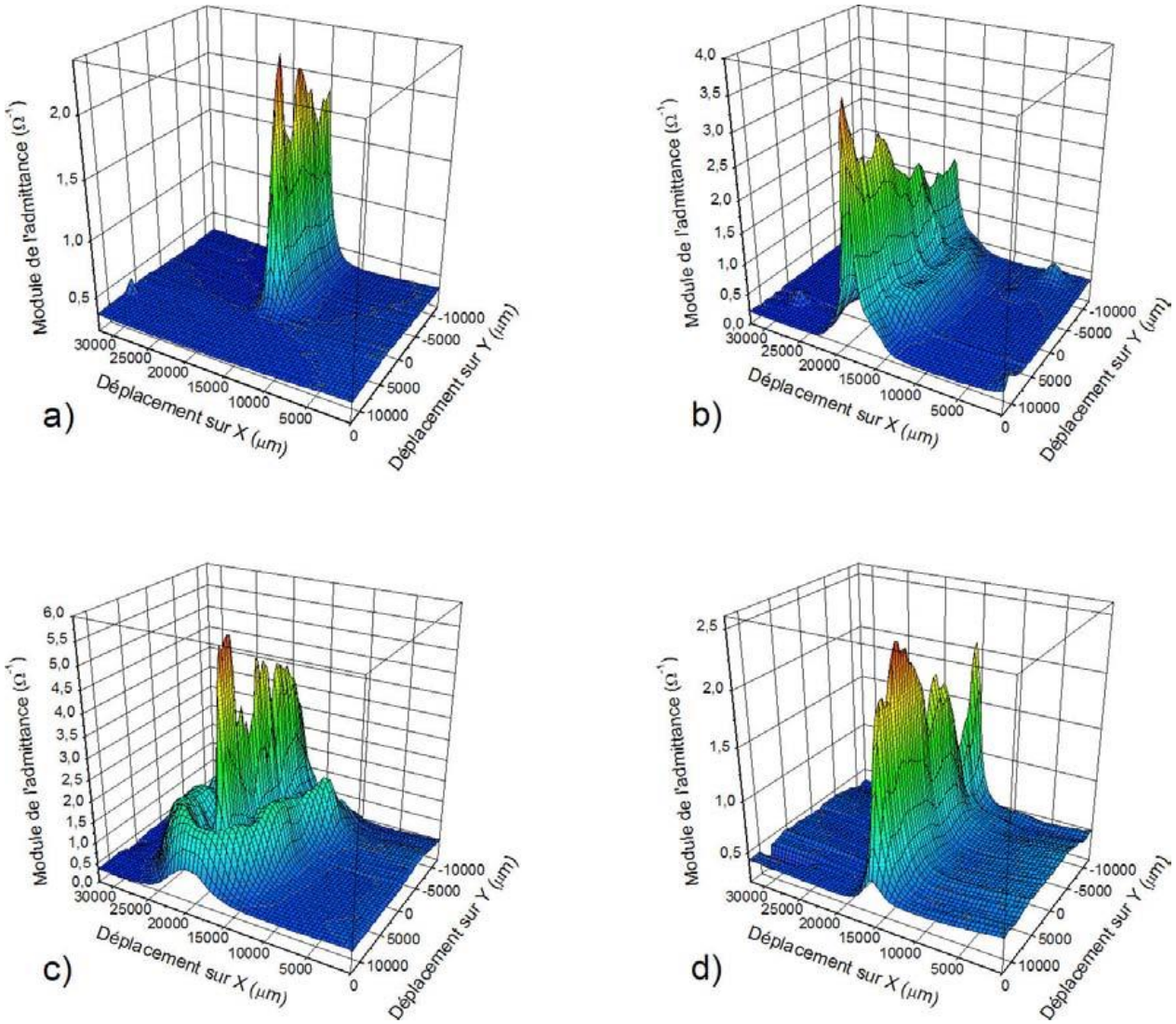

Figure 1.34: LEI Mappings at 5 Hz performed on scarified samples after 0, 20, 30, 50 days of salt spray exposure, respectively. Adapted from [140]

Figure 1.34 illustrates LEIM evolution near a scarification in epoxy-vinylic coated steel surface with ageing time in SST. The advancement of higher reactivity area near the initial defect after different times of SST is detected. This advancement in the first 30 days (**c**) was attributed to the increase of the delaminated area around the initial defect.

Recent work has studied the electrochemical behavior of scratched epoxy coated carbon steel in immersion by LEIS (**Figure 1.35**). The analysis of the LEIS spectra acquired in the center of the scratches demonstrated initial decrease and following increase of the associated resistance, which was interpreted in terms of the evolution of the iron oxide layer in the scratch. The latter permitted to propose a degradation mechanism of this scratched painted systems and explain the influence of chlorides concentration on the passivation of steel in the defect [141].

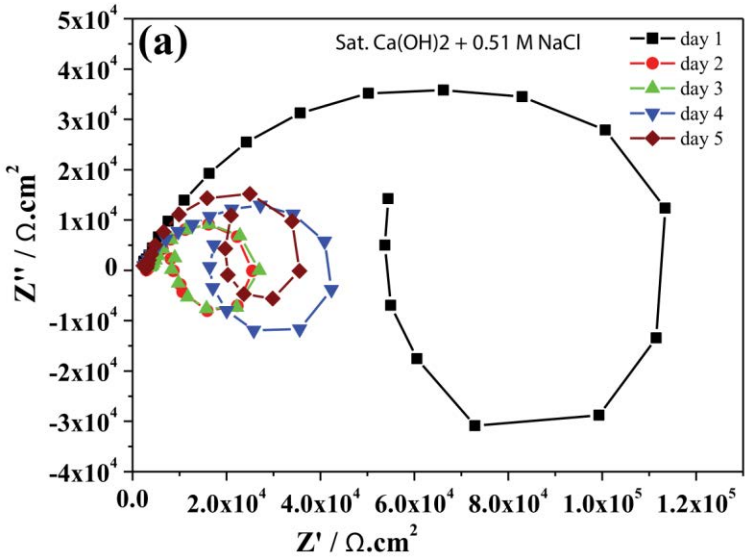

Figure 35: Nyquist representation of LEIS of epoxy coated carbon steel immersed in sat. Ca(OH)2. Spectra aquisition above the center of the scratch. Adapted from [141]

In addition to defects in the polymer coating, like scarification or scratches, other groups have proposed to initiate the degradation of buried metal-oxide-polymer coating by application of aggressive species (like concentrated sodium chloride solution drops) on the metal surface prior to paint application [142]. Their results show that reactivity maps performed by SKP and/or LEIM are able to detect the presence of underpaint reactivity with no artificial defect generated in the polymer coating.

Recent development in LEIM demonstrated the ability of the technique to perform quantitative evaluation of the delamination front progression. The front position was accessed via the extremum of the local impedance modulus gradient calculated from LEI maps [143]. This novel LEIM data treatment allows to perform *in situ* quantitative assessment of the localized kinetics of metal-oxide-polymer interface degradation during ageing procedures in immersion condition.

Despite the evident interest of LEI techniques, they have at least two serious complications for the application to real systems. The response of the system being strongly dependent on the distance between the probe and the surface [139] the application can be tricky for rough substrates. Moreover, in case of complex and resistant thick polymer coatings, the use of small local probes can result in very low and noisy electrochemical response, complicating the obtention of correct EIS spectra and their treatment, which can be even impossible for some geometries. These aspects make *the application of the LEIS and LEIM to buried metal-polymer interfaces on rough substrate very challenging* and explain the small quantities of works applying local electrochemistry to buried interfaces on rough substrates.

4.3.4. Time Lapse Microscopy (TLM)

TLM consists of recording image sequences at regular time to observe the evolution of a process over time. The technique is widely used in corrosion by several groups [144,145]. It was recently shown that TLM with in situ optical analysis of the surfaces permitted to obtain complementary information on corrosion processes and correct the appreciation made from EIS results [146].

In the case of polymer coated surfaces, in situ optical microscopy was used to study delamination mechanism from initial defects in the coating [147].

Recent advances in nanocontainer adding to the formulations of the polymer coatings permitted to insert corrosion sensing chemical species in organic coatings. With these advances, some teams have proposed to incorporate phenolphthalein in nano-containers to permit earlier detection of underpaint reactivity [148,149,150]. A description of the proposed methodology is provided in **Figure 1.36**.

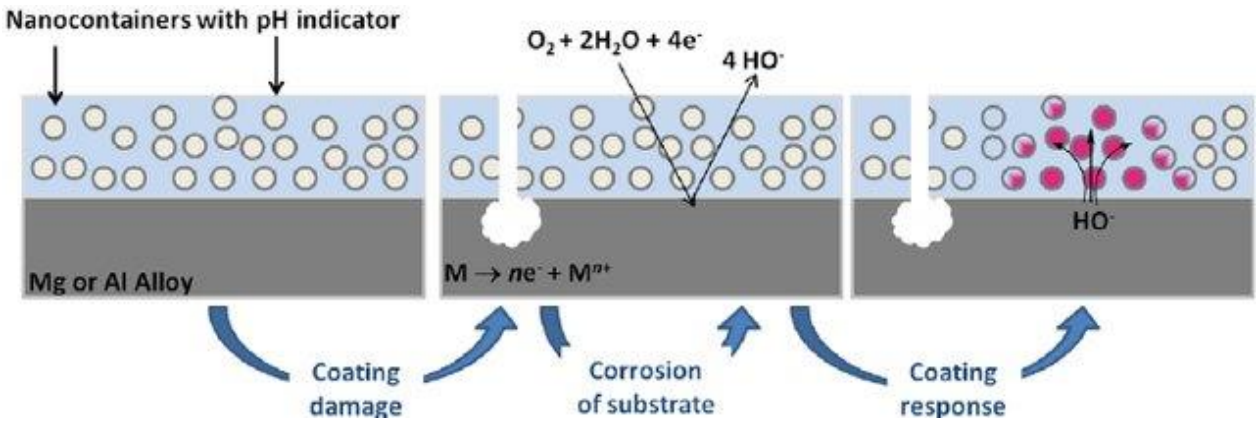

Figure 1.36: Scheme of pH sensing response of underpaint reactivity from active coating. Reproduced from [149]

Coupled with TLM, this technology of "marked" coatings can allow in situ follow-up of the underpaint cathodic reactivity as described in the **Figure 1.37**. On these two photographs, the apparition of blisters in the polymer coating with immersion time is accompanied by coloring of some blisters in pink after 20 hours of immersion, demonstrating the alkalinity increase underneath and therefore confirming strong cathodic reactivity.

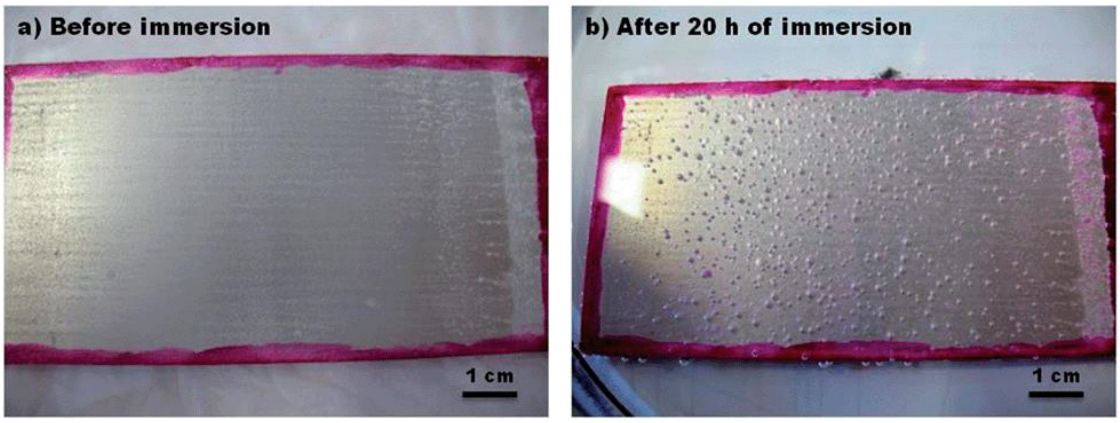

Figure 1.37: Photographs of epoxy coated magnesium before and after 20 hours of immersion in 0.5 M NaCl. The polymer coating contains phenolphthalein. Reproduced from [150]

To sum up the described methodologies, it seems that TLM and LEIS/LEIM are the most interesting techniques to study local reactivity at buried interfaces. However, even if these technics were previously applied to metal-oxide-polymer interfaces, most studies aiming spatially resolved reactivity measurement at buried interface were designed with an initially introduced defect at the metal-polymer interface. Usually, this defect is introduced in the polymer coating in the form of a scratch; in some cases, underpaint reactivity was initiated by deposition of aggressive species at the metallic surface prior to polymer coating. Nonetheless, both ways can modify the chemistry of the interface near the defect. It seems hence that there is a lack of knowledge on the influence of the conversion coating itself on the stability of the metal-conversion-polymer interface in immersion conditions. Moreover, the measurement is complicated for rough substrates, which are common for electrodeposited zinc-based coatings.

In this PhD we will try to fill this lacuna and answer the question:

How to measure in situ and good spatial resolution the electrochemical reactivity at buried rough metal-oxide-polymer interface in immersion condition without initial chemical modification of the system?

The experimental set up proposed to answer this question will be detailed in Chapter 2 Section 3; the methodology itself is detailed in Chapter 3 and the aspects of localization and spatial resolution of the proposed methodology are discussed in Chapter 5.

5. Difficulties of chemical characterization of metal-oxide-polymer interfaces

Understanding chemical and electrochemical degradation mechanisms of metal-oxide-polymer interfaces requires not only to identify the presence of electrochemical reactions, but also to describe the evolution of the chemistry of the whole painted systems during degradation, both in its globality and locally at selected interfaces and hence with good depth resolution and in selected location in which the reactivity is detected and therefore with good lateral resolution.

5.1. Ex situ chemical characterization of evolving metal-oxide-polymer interfaces

Considering nanometer thickness of conversion layers, the high vacuum surface analytical technics such as X-ray photoelectron spectroscopy (XPS), Atomic Force Microscopy (AFM), Time of Flight Secondary Ion Mass Spectrometry (ToF-SIMS), Auger spectroscopy (AES) etc. are often applied first considered for spatial and depth chemical analysis of thin layers on metallic substrates. The principles, interest and analytical limits of these technics will be presented in Chapter 2. These technics were designed for characterization of nanometer thick layers on a flat and clean surface, allowing to measure elemental depth profiling, chemical speciation at selected depth (if combined with sputtering) and/or localized chemical composition with high lateral resolution. Indeed, surface analytical technics were successfully applied for description of uncovered by polymer conversion coatings or for model systems interacting with monolayers of organic molecules [37,54,151,152].

The combination of surface characterization techniques is extensively studied to obtain a complete and accurate description of thin layer chemistry [153,154]. In addition, the coupling between ion beam sputtering and XPS offers a better understanding of the in-depth composition and quantification of the thin oxide layers chemistry [155]. For that matter, recent XPS setup are often equipped with a noble gas ion gun such as argon to perform alternating cycles of sputtering and analysis of the surface [156]. Although this setup allows to perform in-depth chemical description of the thin films, XPS profiling via argon ion gun shows some limitation in the sputtering accuracy [157].

In order to have a better control on the depth of the crater in which the XPS measurement is taken, some groups have shown the powerfulness of the coupling between XPS and ToF-SIMS techniques. The methodology was applied in several studies focusing on conversion coatings and passive films [158,159].

Recently, a group has proposed the use of the couple GD-OES // XPS to obtain a detailed chemical description of the surface chemistry at different depths of a multi-layer system [160,161]. One of the advantages of the GD-OES is its depth resolution with high etching rate[162]; moreover, the argon ions in the plasma are accelerated in the direction normal to the surface of the sample, which could prevent from shadowing effect in the crater generation[163].

Although very important for surface analysis, these <u>high vacuum surface analytical technics have several fundamental limitations for the analysis of conversion coatings on a rough substrate in particular when the coating is buried under a µm-thick polymer layer</u>. These limitations are related to the high vacuum condition and sample preparation (drying, cutting, polishing or ion beam slicing) which can be challenging by itself and can also modify significantly the interface. At the same time, a very limited erosion

depth (nanometric scale) and possible shadowing effect because of the incidence angle during erosion [164,165] significantly restrains the possibility of a correct analysis at depths more than several tens of nm in the direct analysis. Recently proposed GD-OES sputtering could limit shadowing effect, however to our knowledge no work combining GD-OES sputtering and XPS analysis of buried conversion coating was published.

The question ***"How to describe the chemistry of nanometer-thick oxide layer buried under µm-thick polymer coating on rough metallic substrate with good spatial resolution?"*** *hence still requires a solution.*

5.2. In situ chemical characterization of evolving metal-polymer and oxide-polymer interfaces

In situ chemical analysis of the evolution of buried metal-oxide-polymer interfaces is usually approached using model systems formed by thin layer deposition and chemical characterization via combination of Attenuated Total Reflection−Fourier Transform Infrared Spectroscopy (ATR-FTIR) under thin polymer films and Visible−Infrared Sum-Frequency Generation Spectroscopy [166]. Application of ATR-FTIR in the Kretschmann Geometry [167] allowed to approach the interface from the metal side using nanometrically thin model metallic layer deposition. More recent works use these technics individually or in a combination for in situ characterization of such flat thin layer model systems [22,168]. The application of ATR-FTIR and SFG technics is however limited to model systems. For thicker coatings Raman spectroscopy could be of interest. A combination of Raman spectroscopy and spectroscopic ellipsometry was applied to achieve a qualitative information about the polypyrrole/iron interface [169] More recently, metal oxide nanoparticles (MONPs) were proposed to achieve surface enhanced Raman spectroscopy SERS and improve the capacity of Raman spectroscopy to study the interfaces metal oxide-polymer in situ [170].

The developments of the near-ambient pressure XPS (NAPXPS) made possible to perform photoelectron spectroscopy under elevated gas pressures of about 25 mbar [171], however because high-photon fluxes are required, and polymer systems tend to degrade under high-photon fluxes. Recently available lab-based NAPXPS with a conventional Al K α source made possible to study ultrathin polymer films under near-ambient conditions [172,173]

More details about different methodologies proposed to survey degradation processes occurring locally at the metal oxide- polymer hybrid interface, monitored under (near-)ambient conditions, in particular in application for model systems in the initial stages of degradation, can be found in the recent review [174].

Two groups of analytical approaches to the chemistry of metal-oxide-polymer interface were presented in this section.

1) High vacuum surface analytical technics are able ex situ analyze in detail the chemistry of thin oxide layers with excellent spatial resolution but barely applicable in their conventional form for the analysis of rough and often hydrated and buried interfaces. The sample preparation for the analysis by these technics should include cutting, polishing, and drying which can result in significant modification of the system.
2) In situ spectroscopical methods compatible with ambient conditions but in their existing configurations applicable only to thin model systems and not convenient for the interfaces formed on alloyed substrates, which complex chemistry and its distribution at the interface is strongly dependent on their processing, and thick or complex polymers.

Despite of evident fundamental interest of the reviewed previously methodologies, other than previously cited limitations, the most part of both, in situ and ex situ analytical technics, is not adopted to study the rough interfaces. Moreover, in the actual configuration, these technics work in one-point analysis mode and doesn't allow lateral scanning. As previously mentioned, sacrificial coating, developed nowadays, are usually alloyed and hence multi-element (ZnAlMg, ZnAl, ZnNi, etc.). The coating can be also very rough because of their processing (skin pass, electrodeposition, etc.).

The roughness and the chemical complexity of the interface being critical to its durability, the development of new methodological solutions for chemical analysis of buried interfaces formed on rough substrates is still necessary in order to extend the analytical approaches to more complex systems.

The approach proposed to answer this problematic is assessed in Chapter 2 Section 4 and the detailed results are provided in Chapter 4.

6. Conclusion of the state of the art

As mentioned here-above, different contributions and phenomena occur at metal-oxide-polymer interfaces during degradation processes, but many of them contain electrochemical processes. The literature evidenced the importance of conversion coatings and their characteristics (thickness, porosity, self-healing ability) on stability issues of the metal-oxide-polymer interface. EIS and its local variation (LEIS/LEIM) seem to be interesting techniques to detect, localize and describe painted system degradation in immersion condition. However, most studies using these techniques focused either on the metal-polymer interface degradation via the use of weak polymer coatings and initially introduced macroscopic defects, or on the evolution of the global characteristics of the painted system. Little is made in the application of these techniques for detection of the local evolution of initially undamaged polymer systems or the systems in which the chemistry of the interface is not significantly modified around the defect. The effect of conversion coating on the system stability has also never been de-correlated from the effect of polymer coating and initial defect generation. Moreover, the application of LEI technics can be significantly complicated by the roughness of the sample.

This overview led us to the following questions which will be addressed in the next chapters (experimental and results sections) of is PhD thesis:

1. ***How to measure in situ the local reactivity at buried rough metal-oxide-polymer interface under intact polymer with good spatial resolution, in immersion condition?***

2. ***How to de-correlate the effect of nanometric thin oxide conversion coating on the stability of painted systems from the effect of thick polymer layer and the effect of the initial defect usually introduced in previous studies?***

To answer the second question, the important step is to characterize the interface chemistry and morphology and to propose a way to produce a model system in which the chemical evolution in the defect is minimized. A brief review of surface characterization techniques and methodologies demonstrated that accurate chemical description of thin oxide layers is mainly made in the case of model smooth substrates. For rough electrodeposited substrates, although relevant in industrial context, the analytical aspects are still unsolved. For this reason, the correct solution of the second question led us to another question which also will be answered in the results chapters.

3. ***How to describe the surface chemistry of nanometer thick oxide layer on rough electrodeposited substrates? And specifically, how to access buried metal-oxide interface?***

Questions 1 and 2 will be answered in Chapter 3 and 5 while question 3 will be addressed in Chapter 4.

1 References:

1 T. Eisele, K.L. Gabby, Review of reductive leaching of iron by anaerobic bacteria, Mineral Processing and Extractive Metallurgy Review 35 (2012)

2 Total Materia, Corrosion protection of Steel [Online], available on: https://www.totalmateria.com/page.aspx?ID=CheckArticle&site=kts&NM=300, [Accessed on 16/08/2020]

3 D. Thierry, C. Leballeur, N. Larché, Galvanic Series in Sea Water as a Function of Temperature, Oxygen content, and Chlorination, Corrosion 74 (2018), 147-152

4 G.D. Wilcox, Electrodeposited zinc alloy coatings, Corrosion Science 35 (1993), 1251-1258

5 F.C. Porter, Corrosion resistance of zinc and zinc alloys, CRC Press, (1994)

6 X.G. Zhang, Galvanic corrosion of zinc and its alloys, Journal of the Electrochemical Society 143 (1996), 1472

7 M. Dutta, A. K. Halder, S. B. Singh, Morphology and properties of hot dip Zn–Mg and Zn–Mg–Al alloy coatings on steel sheet, Surf. Coat. Technol., 205 (2010) 2578‑2584

8 S. Schuerz, M. Fleischanderl, G.H. Luckeneder, K. Preis, T. Haunschmied, G. Mori, A.C. Kneissl, Corrosion behaviour of Zn–Al–Mg coated steel sheet in sodium chloride- containing environment, Corros. Sci., 51 (2009) 2355‑2363

9 M.S. Chandrasekar, S. Srinivasan, M. Pushpavanam, Properties of Zinc alloy electrodeposits produced from acid and alkaline electrolytes, Journal of Solid State Electrochemistry 13 (2009), 781-789

10 User manual, Metallic coated steel, ArcelorMittal Flat Carbon Europe 19, avenue de la Liberté L-2930 Luxembourg

11 “Handbook of Corrosion Engineering", [Online] Available at www.corrosion-doctors.org, [Accessed on 26/08/2020]

12 C.G. Dariva, A.F. Gallio, Corrosion Inhibitors – Principles, mechanisms and applications, in: Aliofkhazraei, M. (Ed.), Developments in corrosion protection (2014). InTechOpen

13 Kendig, M. W. & Buchheit, R. G. Corrosion inhibition of aluminum and aluminum alloys by soluble chromates, chromate coatings, and chromate-free coating, Corrosion 59, 379–400 (2003)

14 Frankel, G. S. & Mccreery, R. L. Inhibition of Al alloy corrosion by chromates, Electrochem. Soc. Interface 10, 34–38 (2001)

15 Gharbi, O., Thomas, S., Smith, C. et al. Chromate replacement: what does the future hold?. npj Mater Degrad 2, 12 (2018). https://doi.org/10.1038/s41529-018-0034-5

16 P. R. Roberge, Handbook of corrosion engineering, New York: Mc Graw Hill Hand-book (1999)

17 R. Lambourne, (Ed.), Paint and Surface Coatings, Ellis Horwood, Chichester, UK (1987)

18 G. Grundmeier, A. Simões, Corrosion Protection by Organic Coatings, in. Encyclopedia of Electrochemistry: Wiley VHS, (2007) [Online]

19 H. Leidheiser Jr, Corrosion of painted metals – a review, Corrosion 38 (1982), 374-383

20 W. Funke, Problems and progress in organic coatings science and technology, Progress in Organic Coatings 31 (1997), 5-9

21 H. Hintze-Bruening, F. Leroux, Nanocomposite based multifunctional coatings, IntechOpen (2011), [Online] Available at https://www.intechopen.com/books/new-advances-in-vehicular-technology-and-automotive-engineering/nanocomposite-based-multifunctional-coatings, [Accessed on 20/08/2020]

22 P. Taheri, H. Terryn, J.M.C. de Mol, Studying interfacial bonding at buried polymer-zinc interfaces, Progress in Organic Coatings 89 (2015), 323-331

23 N. K. Akafuah, S. Poozesh, A. Salaimeh, G. Patrick, K. Lawler, K. Saito, Evolution of the Automotive Body Coating Process—A Review, Coatings, 24 (2016) 1‑22

24 Twite RL & Bierwagen GP (1998) Review of alternatives to chromate for corrosion protection of aluminum aerospace alloys. Prog. Org. Coatings 33, 91–100

25 W. Funke, Toward a unified view of the mechanism responsible for paint defects by metallic corrosion, Ind. Chem. Prod. Res. Dev. 24 (1985), 343-347

26 K. Ogle, S. Morel, N. Meddahi, An electrochemical study of the delamination of polymer coatings on galvanized steel, Corrosion Science 47 (2005), 2034-2052

27 A.E. Hughes, Conversion Coatings, in Encyclopedia of Interfacial Chemistry, Elsevier,2018,Editor(s): Klaus Wandelt, Pages 108-114, ISBN 9780128098943, https://doi.org/10.1016/B978-0-12-409547-2.13441-9

28 W. Funke, The role of adhesion in corrosion protection by organic coatings, Journal of the oil and colour chemists' association 68 (1985), 229-232

29 G. L. Song, Surface Engineering of light alloys (2010), 3-39

30 A.S.H. Makhlouf, Current and advanced coating technologies for industrial applications, Nanocoatings and Ultra-Thin Films (2011), 3-23

31 T. Lostak, A. Maljusch, B. Klink, S. Krebs, M. Kimpel, J. Flock, S. Schulz, W. Schuhmann, Zr-based conversion layer on Zn-Al-Mg alloy coated steel sheets: insights into the formation mechanism, Electrochim. Acta, 137 (2014) 65‑74

32 O. Lunder, C. Simensen, Y. Yu, K. Nisancioglu, Formation and characterisation of Ti– Zr based conversion layers on AA6060 aluminium, Surf. Coat. Technol., 184 (2004) 278‑290

33 Dabalà M, Ramous E & Magrini M (2004) Corrosion resistance of cerium-based chemical conversion coatings on AA5083 aluminium alloy. Mater. Corros. 55, 381–386

34 K. Ogle, R. Buchheit, Conversion Coatings, in: A.J. Bard, M. Stratmann, J. Frankel (Eds.), Encyclopedia of Electrochemistry, 4, Corrosion and Oxide Films, Wiley-VCH, (2003), 460-495

35 W. Zhou, D. Shan, E.-H. Han, W. Ke, Structure and formation mechanism of phosphate conversion coating on die-cast AZ91D magnesium alloy, Corros. Sci., 50 (2008) 329–337

36 K. Ogle, M. Wolpers, Phosphate conversion coatings, in: S.D. Cramer, B.S. Covino (Eds.), ASM Handbook, 13A, Corrosion: Fundamentals, Testing, and Protection, ASM International, (2003) 712-719

37 I. Van Roy, H. Terryn, G. Goeminne, Study of the phosphating treatment of aluminium surfaces: role of the activating process, Colloids Surf. Physicochem. Eng. Asp., 136 (1998) 89‑96

38 L. Jiang, Application of atomic emission spectroelectrochemistry to the formation and degradation of conversion coatings on galvanized steel (Zn and Zn-Al-Mg)', PhD thesis, Université Pierre et Marie Curie, Paris, 2012

39 A. A. O. Magalhães, B. Tribollet, O. R. Mattos, I. C. P. Margarit, O. E. Barcia, Chromate Conversion Coatings Formation on Zinc Studied by Electrochemical and Electrohydrodynamical Impedances, J. Electrochem. Soc., 150 (2003) B16–B25

40 J. Zhao, R.L. McCreery, G.S. Frankel, *Effects of chromate and chromate conversion coatings on corrosion of aluminum alloy 2024-T3*, Surface and coating technologies 140 (2001), 51-57

41 P. L. Hagans, C. M. Haas, Chromate Conversion Coatings, 5 (1994) 405‑411

42 D. Gilroy, P.J. Eddowes, , F.L. Bentes, *Techniques for assessing the protective properties of chromated conversion coatings—Part II*: Galvanized steel, Metal Finishing 94 (1996), 14-22

43 C.S. Jeffcoate, H.S. Isaacs, A.J. Aldykiewicz, M.P. Ryan, Chromate in conversion coatings: a XANES study of its concentration and mobility, JOCS 147 (2000), 540-547

44 U.S. EPA (1998) Principles of Environmental Impact Assessment Review: Appendix A: Environmental Impact Assessment Checklist

45 European Commission regulation report n°2017/999 - REACH, Official Journal of European Union (2017)

46 D.M. Johnson, Zinc and cadmium passivation bath, US2559878A, (1951)

47 C.V. Bishop, T.J. Foley, J.M. Frank, Coating solutions of trivalent chromim for coating zinc surfaces, United State patent, US4171231A (1979)

48 B. da Fonte Jr., M.C. Mich, Trivalent chromium passivate solution and process for yellow passivate film, US Patent 4.359.345, (1982)

49 D.J. Guhde, D.M Burdt, Coating solutions of trivalent chromium fr coating zinc and cadmium surfaces, US Patent, US4263059A, (1981)

50 V. Dikinis, V. Rezait ˙ e, I. Dem ˙ cenko, A. Seiskis, T. Bernatavi ˇ cius, R. ˇ Sarmaitis, ˇ Trans Inst Metal Finishing, 82, 98 (2004)

51 A. R. D. Sarli, J. D. Culcasi, C. R. Tomachuk, C. I. Elsner, J. M. Ferreira-Jr, I. Costa, Surface & Coatings Technology, 258, 426 (2014)

52 C. R. Tomachuk, C. I. Elsner, A. R. D. Sarli, O. B. Ferraz, Coating Technology, 7, 493 (2010)

53 H.H. Sheu, H.B. Lee, S.Y. Jian, C.Y. Hsu, C.Y. Lee, Investigation on the corrosion resistance of trivalent chromium conversion passivate on electroplated Zn–Ni alloy, Surface and Coatings Technology (2016) 305 241-248, https://doi.org/10.1016/j.surfcoat.2016.08.032

54 X. Zhang, C. van den Bos, W.G. Sloof, A. Hovestad, H. Terryn, J.H.W. de Wit, Comparison of the morphology and corrosion performance of Cr(VI)- and Cr(III)-based conversion coatings on zinc, Surface and Coating Technologies 1999 (2005), 92-104

55 A. Gardner, J. Scharf, Soc. Automot. Eng. (2001) 91, ([Spec. Publ.], SP-1614 DOI: 10.4271/2001-01-0644?)

56 ASM International 2759/9, "Hydrogen embrittlement relief [baking] of steel parts" (2006)

57 Matzdorf C, Kane M & Green J (2002) Corrosion resistant coatings for aluminum and aluminum alloys

58 Dong X, Wang P, Argekar S & Schaefer DW (2010) Structure and composition of trivalent chromium process (TCP) films on Al alloy. Langmuir 26, 10833–41

59 Guo Y & Frankel GS (2012) Characterization of trivalent chromium process coating on AA2024-T3. Surf. Coatings Technol. 206, 3895–3902

60 S. Hesamedini, G. Ecke, A. Bund, Structure and formation of trivalent chromium conversion coatings containing cobalt on zinc plated steel, Journal of the Electrochemical Society 165 (2018), C657-C669

61 Alan Gardner, John Scharf, High Performance Alternative to Hexavalent Chromium Passivation of Plated Zinc and Zinc Alloys, DOI: 10.4271/2001-01-0644

62 Craig V. Bishop, Roland Vogel*, John R. Kochilla, Charlotta Wennefors, Corrosion resistant films from trivalent chrome-based solutions applied to electrodeposited zinc and zinc alloys. In Heat Treating 2003: Proceedings of the 22nd Heat Treating Society Conference and the 2nd International Surface Engineering Congress (ASM International) https://www.asminternational.org/home/-/journal_content/56/10192/CP2003HT355/CONFERENCE-PAPER

63 Hesamedini, S., Bund, A. Trivalent chromium conversion coatings. J Coat Technol Res 16, 623–641 (2019). https://doi.org/10.1007/s11998-019-00210-9

64 G. Grundmeyer, A.M. Simoes, Corrosion protection by organic coatings, In book: Encyclopedia of Electrochemistry (2007), DOI: 10.1002/9783527610426.bard040504

65 W. Funke. Corrosion Control by Coatings, H. Leidheiser, Jr., Editor, Science Press, Princeton, N. J., p. 35 (1979)

66 X.G. Zhang, Under-paint corrosion, Corrosion and electrochemistry of zinc, Chapter 11, Springer Science + Business media, New-York, 1996

67 W. Funke, Towards environmentally acceptable corrosion protection by organic coating, Anti Corrosion (1984), 4-7

68 W. Funke, Problems and progress in organic coatings science and technology, Progress in Organic Coatings 31 (1997), 5-9

69 A. Amirudin, D. Thierry, Corrosion mechanisms of phosphated zinc layers on steel as substrates for automotive coatings, Prog. Org. Coat., 28 (1996) 59‑76

70 P. Marcus, Corrosion Mechanisms in Theory and Practice. CRC Press, 2011

71 P. Tanguy, Impact of the microstructure of ZnAlMg coatings for steel on the formation mechanisms and performance of Cr-free conversion coatings, PhD Thesis (2019)

72 R. A. Dickie. paper presented at Electrochem. Soc. meeting, Minneapolis, Minn., May 1981.

73 O. D. Gonzalez, P. H. Josephic, and R. A. Oriani. J. Electrochem. Soc., Vol. 121, p. 29 (1974)

74 H. Leidheiser Jr., M.W. Kendig, Corrosion (1976), 32-69

75 R. A. Dickie and A. G. Smith. Chem. Tech. 1980, No. 1, p. 31

76 A. Leng, H. Streckel, M. Stratmann, The delamination of polymeric coatings from steel. Part 2: First stage of delamination, effect of type and concentration of cations on delamination, chemical analysis of the interface, Corrosion Science 41 (3) (1999) 579–597

77 J. J. Ritter and J. Kruger. Corrosion Control by Organic Coatings, H. Leidheiser, Jr., Editor, Natl. Assoc. Corrosion Engrs., Houston, Texas, p. 28 (1981)

78 Pourbaix, Atlas d'équilibres électrochimiques à 25°C, Gauthier-Villar. Paris, 1963

79 E. Petrie, Osmotic blisters in coatings and adhesives, Met. Finish., (2011) 28–30

80 B. Liu, Y. Wei, W. Chen, L. Hou, C. Guo, Blistering failure analysis of organic coatings on AZ91D Mg-alloy components, Eng. Fail. Anal., 42 (2014) 231‑239

81 D. Greenfield, D. Scantlebury, The protective action of organic coatings on steel: A review, J. Corros. Sci. Eng., 3 (2000)

82 C.H.Simpson, C.J. Ray, .S. Skerry, Accelerated corrosion testing of industrial maintenance paints using a cyclinc cossosion weathering method, Journal of Protective Coatings and Linings (1991)

83 K.R. Baldwin, C.J.E. Smith, Accelerated corrosion tests for aerospace materials: current limitations and future trends, Aircraft Engineering and Aerospace Technology 71 (1999), 239-244

84 M. Poelman, M.G. Olivier, N. Gayarre, J.P. Petitjean, Electrochemical study of different ageing tests for the evaluation of a cataphoretic epoxy primer on aluminium, Progress in Organic Coatings 54 (2005), 55-62

85 ASTM International B 117 – 09 "Standard practices for operating salt spray (fog) apparatus" (2009)

86 SO 9227:2006 "Corrosion tests in artificial atmospheres – Salt spray tests" July 2006

87 Test Method D17 2018, "Corrosion test by automatic change of phases of salt spray, dryig and humidity (ECC1)" Standardization of Renault Automobiles – DMI / Service 65810, revision of October 2007

88 VDA 233-102 "Cyclic corrosion testing of materials and components in automotive construction" June 2013

89 ASTM International D 870 – 15 "Standard practices for testing water resistance of coatings using water immersion" (2020)

90 ASTM International D 714 – 02 "Standard test method for evaluating degree of blistering of paints" (2017)

91 N.B. Salah, Reducing test bias in evaluating reach compliant paint systems, Presentation at AsetsDefense (2016)

92 NF EN ISO 2409:2013 « Peintures et vernis – essais de quadrillage »

93 Test the resistance of coating to separation with cross hatch tester, Presto Testing Instruments [Online] Available at https://www.prestogroup.com/articles/test-the-resistance-of-coating-to-separation-with-cross-hatch-tester/, [Accessed on 20/08/2020]

94 M. Kendig, S. Jeanjaquet, R. Brown, F. Thomas, Rapid electrochemical assessment of paint, Journal of Coatings Technology 68 (1996), 29-47

95 Rapid Electrochemical Assessment of Paint,Gamry [Online], Available at https://www.gamry.com/application-notes/corrosion-coatings/rapid-electrochemical-assessment-of-paint/, [Accessed on 25/08/2020]

96 ASTM International G01.11 "Subcommittee on electrochemical measurement in corrosion testing" (2020)

97 K.N. Allahar, G.P. Bierwagen, V.J. Gelling, *Understanding ac–dc–ac accelerated test results*, Corrosion Science 52 (2010), 1106-1114

98 M. Bethencourt, F.J. Botana, M.J. Cano, R.M. Osuna, M.Marcos, *Lifetime prediction of waterborne acrylic paints with the AC–DC–AC method*, Progress in Organic Coatings 49 (2004), 275-281

99 J. Hollaender, Rapid assessment of food/package interactions by electrochemical impedance spectroscopy (EIS), Food Additives and Contaminants 14 (1997), 617-626

100 R. Montoya, F.R. García-Galván, A. Jiménez-Morales, J.C.Galván, *A cathodic delamination study of coatings with and without mechanical defects*, Corrosion Science 82 (2014), 432-436

101 H. Leidheiser, *Cathodic delamination of polybutadiene from steel: a review*, Journal of Adhesion Science Technology 1 (1987) 79-98

102 F. Meng, L. Liu, Electrochemical evaluation technologies of organic coatings, intechopen (2018) [Online] available on https://www.intechopen.com/books/coatings-and-thin-film-technologies/electrochemical-evaluation-technologies-of-organic-coatings, [Accessed on 10/02/2019]

103 S. Gowri, K. Balakrishnan, The effect of the PVC/CPVC ratio on the corrosion resistance properties of organic coatings, Progress in Organic Coatings 23 (1994), 363-377

104 J.N. Murray, Electrochemical test methods for evaluating organic coatings on metals: an update. Part II: single test parameter measurement, Progress in Organic Coatings 31 (1997), 255-264

105 S Liu, F Meng, Y Li, F Wang, Protective performance of polyaniline-sulfosalicylic acid/epoxy coating for 5083 aluminum, Materials (Basel). (2018), 11-19

106 D. Loveday, P. Peterson, B. Rodger, Evaluation of Organic Coatings with Electrochemical Impedance Spectroscopy, JCT CoatingTech (2005), 22-27

107 A. Amirudin, D. Thierry, Application of electrochemical impedance spectroscopy to study the degradation of polymer-coated metals, Progress in Organic Coatings 26 (1995), 1-28

108 E. Akbarinezhad, M. Bahremandi, H.R. Faridi, F. Rezaei, Another approach for ranking and evaluating organic paint coatings via electrochemical impedance spectroscopy, Corrosion Science 51 (2009), 356-363

109 M. Ates, Review study of electrochemical impedance spectroscopy and equivalent electrical circuits of conducting polymers on carbon surfaces, Progress in Organic Coatings 71 (2011), 1-10

110 C.V. Lacombe, G. Bouvet, D. Trinh, S. Mallarino, S. Touzain, Water uptake in free films and coatings using the Brasher and Kingsbury equation: a possible explanation of the different values obtained by electrochemical Impedance spectroscopy and gravimetry, Electrochimica Acta 231 (2017), 162-170

111 A.S. Nguyen, N. Causse, M.Musiani, M.E. Orazem, N. Pebere, B. Tribollet, V. Vivier, Dtermination of water uptake in organic coatings deposited on 2024 aluminium alloy: Comparison between impedance measurements and gravimetry, Progress in Organic Coatings 112 (2017), 93-100

112 R. VlasakI. Klueppel G. Grundmeier, Electrochimica Acta 52(28):8075-8080 DOI: 10.1016/j.electacta.2007.07.003

113 A. Roggero, L. Villareal, N. Causse, A. Santos, N. Pebere, Correlation between the physical structure of a commercially formulated epoxy paint and its electrochemical impedance response, Progress in Organic Coatings 146 (2020), 105729

114 D.H. van der Weijde, E.P.M. van Westing, J.D.H. de Wit, Electrochemical techniques for delamination studies, Corrosion Science 36 (1994), 643-652

115 N. Tang, W.J. van Ooij, G. Gorecki, Comparative EIS study of pretreatment performance in coated metals, Progress in Organic Coatings 30 (1997), 255-263

116 J. Newman, Frequency dispersion in capacity measurement at a disk electrode, Journal of the Electrochemical Society 117 (1970), 198-203

117 M. Durbha, M.E. Orazem, B. Tribollet, A mathematical model for the radially dependant impedance of a rotating disk electrode, Journal of the Electrochemical Society 146 (1999), 2199-2208

118 H.K. Song, H.Y. Hwang, K.H. Lee, L.H. Dao, The effect f pore size distribution on the frequency dispersion of porous electrodes, Electrochimica Acta 45 (2000), 2241-2257

119 Z. Kerner, T. Pajkossy, Impedance of rough capacitive electrodes: the role of surface disorder, Journal of the Electrochemical Society 448 (1998), 139-142

120 C.H. Kim, S.I. Pyun, J.H. Kim, An investigation of the capacitance dispersion on the fractal carbon electrode with edge and basal orientations, Electrochimica Acta 48 (2003), 3455-3463

121 X.D. Benetton, S. Sevda, K. Vanbroekhoven, D. Pant, The accurate use of impedance analysis for the study of microbial electrochemical systems, Chemical Society Reviews 41 (2012), 7228-7246

122 E.P.M. van Westing, G.M. Ferrari, J.H.W de Wit, The determination of coating performance with impedance measurement-I. Coating polymer properties, Corrosion Science 34 (1993), 1511-1530

123 E.P.M. van Westing, G.M. Ferrari, J.H.W de Wit, The determination of coating performance with impedance measurement-III. in situ determination of loss of adhesion, Corrosion Science 36 (1994), 979-994

124 E.P.M. van Westing, G.M. Ferrari, J.H.W de Wit, The determination of coating performance with impedance measurement-II. in situ determination of loss of adhesion, Corrosion Science 36 (1994), 957-977

125 S. Amand, M. Musiani, M.E. Orazem, N. Pebere, B. Tribollet, V. Vivier, Constant-phase-element behavior caused by inhomogeneous water uptake in anti-corrosion coatings, Electrochimica Acta 87 (2013), 693-700

126 W.A. Zisman, A new method of measuring contact potential differences in metals, Review of Scientific Instruments 3 (1932), 367-370

127 S. Huber, M. Wicinski, A.W. Hassel, Suitability of various materials for probes in scanning kelvin probe measurements, Physical Status Solidity A 215 (2018), 1700952

128 G. Grundmeier, W. Schmidt, M. Stratmann, Corrosion protection by organic coatings: electrochemical mechanism and novel methods of investigation, Electrochimica Acta 45 (2000), 2515-2533

129 M. Stratman, H. Streckel, R. Feser, A new technique able to measure directly the delamination of organic polymer films, Corrosion Science 32 (1991), 467-470

130 A. Leng, H. Streckel, M. Stratmann, Corrosion Science 41 (1999), 599

131 W. Fürbeth, M. Stratman, The delamination of polymeric coatings from electrogalvanized steel – a mechanistic approach. Part 3: delamination kinetics and influence of CO_2, Corrosion Science 43 (2001), 207-227

132 V. Shkirskiy, M. Uebel, A. Maltseva, G. Lefevre, P. Volovitch, M. Rohwerder, Cathodic driven coating delamination suppressed by inhibition of cation migration along ZN/polymer interface in atmospheric CO_2, npj Materials Degradation 3, 2 (2019)

133 A. Nazarov, T. Prosek, D. Thierry, Application of EIS and SKP methods for the study of the zinc/polymer interface, Electrochimica Acta 53 (2008), 7531-7538

134 H.S. Isaacs, Initiation of stress corrosion cracking of sensitized type 304 stainless steel in dilute thiosulfate solution, Journal of the Electrochemical Society 135 (1988), 2180

135 A.C. Bastos, M.C. Quevedo, O.V. Karavai, M.G.S. Ferreira, Review – On the application of Scanning Vibrating Electrode Technique (SVET) to corrosion research, ournal of the Electrochemical Society 164 (2017), 14

136 H.S. Isaacs, M.W. Kendig, Corrosion 36 (1980), 269

137 R.S. Lillard, P.J. Moran, H.S. Isaacs, J. Electrochem. Soc. 139 (1992) 1007

138 F. Zou, D. Thierry, H.S. Isaacs, J. Electrochem. Soc. 144 (1997) 1957

139 V.M. Huang, S.L. Wu, M.E. Orazem, N. Pebere, B. Tribollet, V. Vivier, Local electrochemical impedance spectroscopy: a review and some recent developments, Electrochimica Acta 56 (2011), 8048-8057

140 J-B. Jorcin, E. Aragon, N. Pébère, Delaminated areas beneath organic coating: A local electrochemical impedance approach, Corrosion Science 48 (2006) 1779-1790

141 T. Balusamy, T. Nishimura, Localized electrochemical impedance spectroscopy observation on scratched epoxy coated carbon steel in saturated $Ca(OH)_2$ with various chloride concentration, J Anal Bioanal Tech 7 (2016), http://dx.doi.org/10.4172/2155-9872.1000328

142 G. Williams, and H.N. McMurray, The mechanism of group (I) chloride initiated filiform corrosion on iron, Electrochemical Communications 5 (2003), 871–877

143 V. Shkirskiy, P. Volovitch, V. Vivier, Development of quantitative Local Electrochemical Impedance Mapping: an efficient tool for the evaluation of delamination kinetics, Electrochimica Acta 235 (2017) 442-452

144 J. Sullivan, N. Cooze, C. Gallagher, T. Lewis, T. Prosek, D. Thierry, In situ monitoring of corrosion mechanisms and phosphate inhibitor surface deposition during corrosion of zinc-magnesium-aluminum (ZMA) alloy using novel time-lapse microscopy, Faraday Discussions 180 (2015), 361-379

145 C. Gallagher, N. Cooze, J. Sullivan, P. Dodds, In situ Time-Lapse microscopy to elucidate the corrosion mechanism of Zn-4.8wt.%Al Galvanising metallic coating surface and cut edge, [Conference] Galvatech (2017).

146 P.J. Denissen, S.J. Garcia, Reducing subjectivity in EIS interpretation of corrosion and corrosion inhibition processes by in situ optical analysis, Electrochimica Acta 293 (2019), 514-524

147 M.A. Hernandez, F. Galliano, D. Landolt, Mechanism of cathodic delamination control of zinc-aluminum phosphate pigment in waterborne coatings, Corrosion Science 46 (2004), 2281-2300

148 F. Maia, J. Tedim, A.C. Bastos, M.G.S. Ferreira, M.L. Zeludkevich, Nanocontainer-based corrosion sensing coating, Nanotechnology 41 (2013), 415502

149 C.B. Uzundal, B. Ulgut, Method for visualizing under-coating corrosion using pH indicators before visible damage, Progress in Organic Coatings 122 (2018), 72-78

150 F. Maia, J. Tedim, A.C. Bastos, M.G.S. Ferreira and M.L. Zheludkevich, Active sensing coating for early detection of corrosion processes, RSC Advances 34 (2014), 17780-17786

151 J.E. Devries, Surface Characterization methods – XPS, ToF-SIMS, and SAM a complementary ensemble of tools, Journal of Materials Engineering and Performances 7 (1998), 303-311

152 A.I. Stoica, J. Światowska, A. Romaine, F. Di Franco, J. Qi, D. Mercier, A. Seyeux, S. Zanna, P. Marcus, Influence of post-treatment time of trivalent chromium protection coating on aluminium alloy 2024-T3 on improved corrosion resistance, Surface and Coatings Technology 369 (2019), 186-197

153 Lee HY, Jung WS, Han JG, Seo SM, Kim JH, Bae YH, The synthesis of CrSiN film deposited using magnetron sputtering system. Surf Coat Technol 200 (2005), 1026–1030

154 Bubert H, Grallath E, Quentmeier A, Wielunski M, Borucki L, Comparative investigation on copper oxides by depth profiling using XPS, RBS and GDOES. Fresenius J Anal Chem 353 (1995), 456-463

155 R.E. Galindo, R. Gago, D. Dudy, C. Palacio, Towards nanometric resolution in multilayer depth profiling: a comparative study of RBS, SIMS, XPS and GDOES, Analytical and Bioanalytical Chemistry 386 (2010,) 2725-2740

156 S Oswald, S Baunack, Comparison of depth profiling techniques using ion sputtering from the practical point of view, Thin Solid Films 425 (2003), 9-19

157 S. Oswald, R. Reiche, Binding state information from XPS depth profiling: capabilities and limits, Applide Surface Science 179 (2001), 307-315

158 M. Ely, J. Światowska, A. Seyeux, S. Zanna, P. Marcus, Effect of Post-treatment on Improved Corrosion Behavior of Trivalent Chromium Protection (TCP) Coating Deposited on Aluminium Alloy 2024-T3, Journal of the Electrochemical Society 164 (2017), C276-C284

159 E. Gardin, S. Zanna, A. Seyeux, A. Allion-Maurer, P. Marcus, XPS and ToF-SIMS characterization of the surface oxides on lean duplex stainless steel – Global and Local approaches, Corrosion Science 155 (2019), 121-133

160 D. Mercier, M. Bouttemy, J. Vigneron, P. Chapon, GD-OES and XPS coupling: A new way for the chemical profiling of photovoltaic absorbers, Applied Surface Science 347 (2015), 799-807

161 A. Loubat, S. Béchu, M. Bouttemy, C. Eypert, S. Gaiaschi, Mathieu Frégnaux, D. Aureau, J. Vigneron, N. Simon, P. Chapon, A.M. Gonçalves, A. Etcheberry, Coupling GD-OES and XPS profiling to perform advanced physico-chemical characterizations of III-V layers for photovoltaic applications, Conference WCPEC-7 (2018), 10.1109/PVSC.2018.8547731

162 T. Nelis, R. Payling, Glow Discharge Optical Emission Spectroscopy, Royal Society of Chemistry Cambridge (2004)

163 N. Trigoulet, T. Hashimoto, I.S. Molchan, P. Skeldon, G.E. Thompson, A. Tempez, P. Chapon, Surface topography effect on glow discharge depth profiling analysis, Surface and Interface Analysis 42 (2010), 328-333

164 A.W. Czanderna, T.E. Madey, C.J. Powell, Beam effects, surface topography, and depth profiling in surface analysis, Methods of Surface Characterization, Springer Books, (2002)

165 S. Hoffman, A. Zalar, Depth Profiling with Sample Rotation: Capabilities and Limitations, Surface and Interface Analysis 21 (1994), 304-309

166 Adhikari, N. M.; Premadasa, U. I.; Cimatu, K. L. A. Sum Frequency Generation Vibrational Spectroscopy of Methacrylate-Based Functional Monomers at the Hydrophilic Solid-Liquid Interface. Phys. Chem. Chem. Phys. 2017, 19 (32), 21818−21828

167 M. Öhman, D. Persson, C. Leygraf, In situ ATR-FTIR studies of the aluminium/polymer interface upon exposure to water and electrolyte, Progress in Organic Coatings 57(1):78-88 DOI: 10.1016/j.porgcoat.2006.07.002

168 S. Pletincx, S. Abrahami, J.M.C. Mol, T. Hauffman, H. Terryn, Advanced (in situ) surface analysis of organic coating/metal oxide interractions for corrosion protection of passivated metals, Encyclopedia of interfacial chemistry: Surface Science and Electrochemistry (2018), 1-17

169 Van Schaftinghen, T., Joiret, S., Deslouis, C. & Terryn, H. In situ Raman Spectroscopy and Spectroscopic Ellipsometry study of the iron/Polypyrrole interface. In Passivation of Metals and Semiconductors

170 Lee, N., Schuck, P. J., Nico, P. S. & Gilbert, B. Surface enhanced Raman spectroscopy of organic molecules on magnetite (Fe3O4) nanoparticles. J. Phys.Chem. Lett. 6, 970–974 (2015)

171 Ogletree, D. F., Bluhm, H., Hebenstreit, E. D. & Salmeron, M. Photoelectron spectroscopy under ambient pressure and temperature conditions. Nuclear Instruments and Methods in Physics. Res., Sect. A: Accel., Spectrometers, Detect. Assoc. Equip. 601, 151–160 (2009)

172 Pletincx, S. et al. In situ characterization of the initial effect of water on molecular interactions at the interface of organic/inorganic hybrid systems. Sci. Rep.7, 45123 (2017)

173 Pletincx, S. et al. Unravelling the chemical influence of water on the PMMA/aluminum oxide hybrid interface in situ. Sci. Rep. 7, 13341 (2017)

174 Pletincx, S., Fockaert, L.L.I., Mol, J.M.C. et al. Probing the formation and degradation of chemical interactions from model molecule/metal oxide to buried polymer/metal oxide interfaces. npj Mater Degrad 3, 23 (2019). https://doi.org/10.1038/s41529-019-0085-2

Chapter 2: Experimental strategy & methodology

In the literature review in State of the art, several techniques were employed to investigate the stability of metal-oxide-polymer interfaces. They can be categorized into two main types of study: in situ reactivity measurement and global test after surface characterization. However, in the case of complex industrial systems, the existing tools do not seem to provide a full understanding of the degradation mechanism of painted systems.

The objective of this chapter is to give an overview of the materials and the techniques used in this work. In addition, the proposed methodologies will be explained and justified; the development of specific technical aspects will be detailed. Measurement parameters are given in the experimental section of the respective result chapter and in specific appendix.

1. Substrate materials

1.1. Model samples

Hot Dip Galvanized zinc (Zn HDG) provided by Chemetall was selected as the first model substrate for methodological verification of the designed set up. This substrate was chosen because the delamination studies published in the literature were the most advanced for galvanized steels. It was also used in this work to develop the model epoxy polymer coating on a well-known and controlled substrate.

$Zn(OH)_2$ reference sample used for XPS peak attribution was made in the laboratory. A zinc oxide thin film (few micrometers) reference sample for XPS analysis was prepared by atomic layer deposition (ALD) on silicon wafer with (0001) orientation. It was produced at low temperature (80 °C) following the production procedure of doped ZnO films for semi-conductors. Following the ZnO deposition, the ZnO layer was hydrated during one week in a humid chamber to produce the $Zn(OH)_2$.

1.2. Electrodeposited Zn alloy and conversion coating

The Zn alloy samples used for conversion coatings study were produced by the PhD student on a semi-industrial production line. *During the PhD, the methodologies were applied on three different ZnNi and four conversion coating formulations. For consistency reasons, the manuscript summarizes only the results obtained on a single selected ZnNi and its conversion coating formulation*.

For sample production, first, steel plates of 10 x 15 cm² used as substrates were degreased, grit-blasted and electrodeposition was performed in alkaline 12-16 % Zn-Ni bath for 45 minutes at 3 A/dm². After electrodeposition, samples were rinsed with deionized water for 10 minutes and dipped in trivalent chromium passivation bath then rinsed for 3 minutes in deionized water and dried with pressurized air. Relief-baking of the samples was performed at around 200 °C for 20 h to alleviate hydrogen embrittlement. X-ray fluorescence (XRF) showed that the deposited ZnNi is of 18 ± 2 µm in thickness and is composed of 14 ± 2 %at. in nickel. X-ray diffraction (XRD) showed only the presence of the gamma phase ($Zn_{21}Ni_5$).

Coupons were cut from the central part of each 15 x 10 cm plate to avoid the edge effects that can be observed in electrodeposition process.

2. Proposed polymer coating

Several polymer coatings were tested. A first verification of the methodology coupling LEIM and TLM to study the adhesion loss at metal-polymer interface was performed on the well-known system containing polyvinyl butyral (PVB) polymer. Several tests were also made using polyvinyl acetate polymer. The polymer stability tests (see section 2.2.4) have however demonstrated that PVA dissolves during immersion while PVB degradation in immersion condition starts earlier than the degradation of the substrate and the interface. The PVB polymer was finally used only for the methodological verifications made on the systems degraded in humid chamber, in order to compare the degradation kinetics obtained by LEIM with degradation kinetics obtained previously by SKP for Zn/PVB system [1]. For further studies, in particular in order to be able to study the systems with stronger metal-oxide-interface and hence requiring longer immersions, the use of more stable and adherent coating was necessary. It was proposed to use an epoxy-based polymer because of high relevance of epoxy coatings for Zn-based substrates. The design of the model epoxy polymer is described in the next section.

2.1. Optimizing procedure of model epoxy polymer

In order to fit with the long immersion and cathodic polarization, necessary for stability follow-up of the buried metal-oxide-polymer interface in immersion condition, the proposed model coating was optimized based on some specific characteristics. The coating should have a simple chemistry, be transparent, remain stable during AC-DC-AC ageing procedure, show limited resistivity to permit LEI measurement, and be epoxy based to model epoxy primer coating. The DGEBA-TETA epoxy matrix formulation was selected and met these requirements.

In order to optimize the deposition of the polymer coating, the homogeneity and the thickness of the layer being a key parameter, an observation of the resin-hardener mix behavior was performed. After mixing and stirring, the mix held numerous air bubbles which were not evacuated before the drying of the resin. The presence of air bubbles in the coating could favor water and/or aggressive species accumulation or promote adhesion loss of the coating on the metallic surface. Being able to evacuate these bubbles before coating was necessary. To do so, the viscosity of the mix was reduced by adding chemical grade ethanol before stirring. In these conditions, after stirring, air bubbles were evacuated within 10 minutes and the mix was homogeneous and transparent.

Spin-coating was selected for coating application because of its high reproducibility in terms of both homogeneity and thickness in the case of thin layer deposition. After a few tests of parameters, the rotation speed, duration and acceleration were selected (see **Appendix 2**). The coating thickness was measured with 3D Keyence microscope on ten different locations of the samples and reproducibility was checked on ten different coupons. The result out of 100 measurement was 10 ± 1 µm in thickness.

Gravimetric measurements were performed on coupons before coating, after coating and after reticulation and evaporation of the ethanol solvent. For 5 x 5 cm coupons, although the thickness of the Zn layer was not homogeneous on some samples (see Zn_p_7 on Table 2), the deposition process showed a good reproducibility in terms of mass and thickness of the polymer coating. The detailed procedure is presented in **Appendix 2**.

Table 2.1: Gravimetric measurement of coated Zn HDG samples with model epoxy coating

Masses /g	Before depostion	As Deposited	Post-Baked	Deposited coating	Baked coating	Ethanol Evaporated
Zn_p_1	14.274	14.316	14.314	0.042	0.040	0.002
Zn_p_2	14.279	14.323	14.320	0.044	0.041	0.003
Zn_p_3	14.300	14.346	14.344	0.046	0.043	0.003
Zn_p_4	14.283	14.329	14.326	0.046	0.043	0.003
Zn_p_5	14.246	14.287	14.283	0.041	0.037	0.003
Zn_p_6	14.245	14.287	14.283	0.042	0.038	0.004
Zn_p_7	11.865	11.909	11.904	0.044	0.040	0.004
Mean				0.044	0.040	0.003
Std				0.002	0.002	0.001

2.2. Tests used for selection of model systems for LEIM-TLM studies

The main purpose of this work is to focus on the stability of the metal-oxide-polymer, specifically on paint adherence in immersion conditions. The degradation or initially insufficient adhesion of the polymer coating during the testing procedure could accelerate the degradation of the system and result in misleading conclusions about the underlying material stability. If the paint were not chemically or structurally stable over the immersion and testing procedure, the detected reactivity might not be the response of the hidden interface but only the one of the degrading coating. At the same time, thick industrial epoxy coatings cannot be used because of their high impedance and the presence of various pigments in the paint composition. The high impedance of the coating hinders underpaint reactivity as the current values during impedance measurement are below detection limits. In addition, pigments and corrosion inhibitors present in industrial coatings do not permit to look at the metal-polymer interface by optical means and provoke side electrochemical processes.

The use of a thin model polymer coating seemed hence necessary to avoid external contribution hindering processes at buried interface. In order to make sure that the electrochemical response reveals the stability of the metal-oxide-polymer interface and not the evolution of the polymer itself, knowing the polymer degradation (kinetics and process) is important.

For this reason, *the stability of the selected model systems was also verified from the point of view of the polymer evolution*. The verification of the polymer integrity was performed by combining in situ electrochemical impedance spectroscopy (for detection of reactivity at different interfaces) with ex situ attenuated total reflectance infrared spectroscopy (ATR-IR, for detection of chemical evolution of the system, including both, water adsorption and polymer chain degradation) and contact angle measurement (for the detection and ex situ optical observation of the defects formation in the polymer film), as schematically shown in **Fig. 2.1**. For the polymer testing, the selected polymer was applied on zinc substrate (galvanized steel) and the obtained system was aged in two parallel procedures – in the humid chamber (a hermetic chamber with a source of > 75 % relative humidity (RH) ensured by the presence of saturated NaCl solution) and in immersion in the electrochemical cell (only from the polymer side). Every hour during the ageing process the samples were tested by EIS, ATR-IR and contact angle measurement, as well as optical images where taken, in particular if the changes were visible in one of the characterizations.

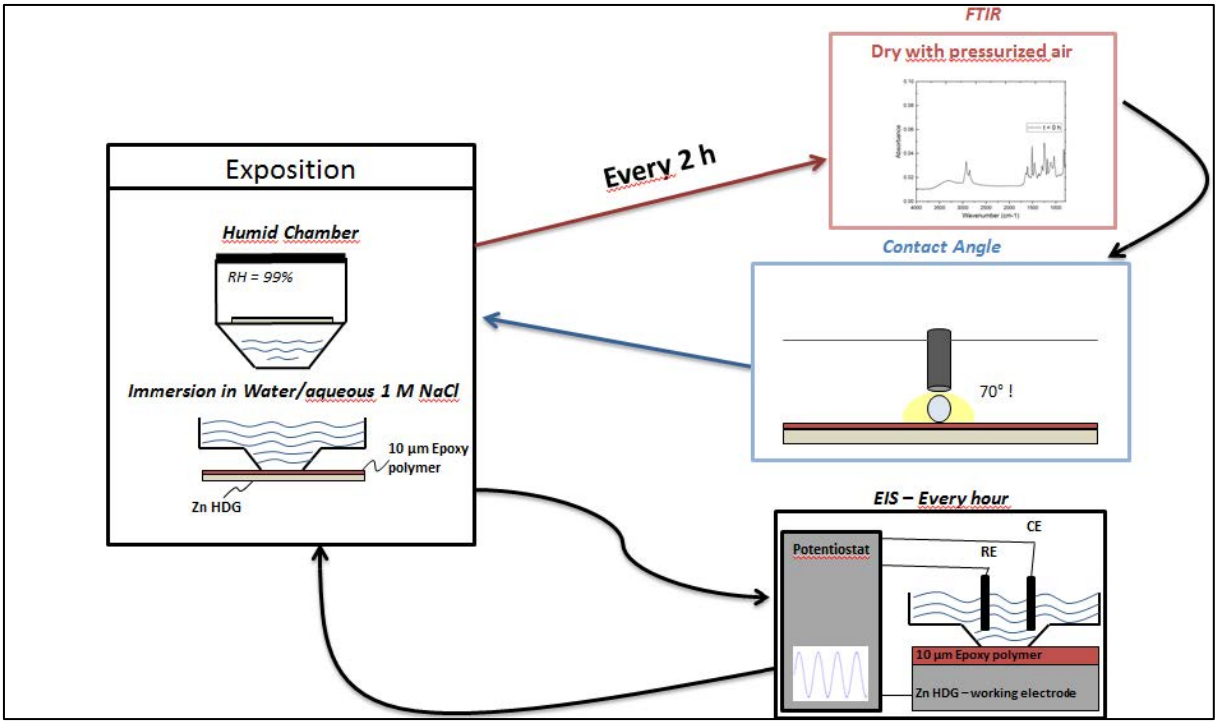

Figure 2.1: Schematic work procedure; polymer coating ageing measurement

The detailed results of the model polymer coating development and stability measurement are presented in the section 3 of this chapter (for PVB coating) and in Chapter 3 (*New experimental approach for intelligent screening of buried metal-oxide-polymer interfaces via local electrochemistry: example of undamaged model epoxy-coated Zn alloys*) for the developed in this work model epoxy coating. The application of model epoxy polymer coating by spin-coating is detailed in **Appendix 2**.

2.3. Recapitulative of used combinations substrate-polymer

The complete list of tested combinations of substrates and polymers and the tests made on the selected combination can be found in **Table 2.2**.

Table 2.2: List of studied samples during the PhD thesis

Substrate	Conversion coating	Polymer coating	Ageing methodology	Tests performed	Nb of samples
Zn HDG	-	PVB	Model defect NaCl droplet	LEIM TLM µ-Raman	10
Zn HDG	-	PVB	Model defect NaHCO3 droplet	LEIM TLM µ-Raman	10
ZnNi	-	PVB	Model defect NaCl droplet	LEIM TLM µ-Raman	5
ZnNi	TCP	PVB	Model defect NaCl droplet	LEIM TLM µ-Raman	5
ZnNi	-	PVB	Model defect NaHCO3 droplet	LEIM TLM	5
ZnNi	TCP	PVB	Model defect NaHCO3 droplet	LEIM TLM	5
ZnNi	-	PVB	Model defect Immersion	LEIM TLM	2
ZnNi	TCP	PVB	Model defect Immersion	LEIM TLM	2
Zn HDG	-	DGEBA-TETA Model epoxy	Intact polymer Immersion	ATR-IR EIS TLM Gravimetry Contact angle	25
Zn HDG	-	DGEBA-TETA Model epoxy	Intact polymer AC-DC-AC	ATR-IR EIS TLM	10
ZnNi	TCP	DGEBA-TETA Model epoxy	Intact polymer AC-DC-AC	ATR-IR EIS TLM	10
ZnNi	TCP	DGEBA-TETA Model epoxy	Intact polymer AC-DC-AC	EIS TLM LEIM	30
ZnNi	TCP	DGEBA-TETA Model epoxy	Intact polymer Degraded TCP (NaOH) AC-DC-AC	EIS TLM LEIM	4
ZnNi	TCP	Industrial Epoxy Primer	Intact polymer AC-DC-AC	EIS TLM	10
ZnNi	TCP	DGEBA-TETA Model epoxy	Intact polymer Degraded TCP (GD-OES defect) AC-DC-AC	EIS TLM LEIM	8
ZnNi	TCP	DGEBA-TETA Model epoxy	Intact polymer Degraded TCP (ToF-SIMS defect) AC-DC-AC	EIS TLM LEIM	4
ZnNi	TCP	-	-	GD-OES ToF-SIMS XPS Nano-AES	50

3. Methodologies for in situ reactivity measurement.

In order to obtain a good understanding of the stability at metal-oxide-polymer interface, and specifically of the paint to substrate adherence loss in contact with liquid, relevant to 1000 h immersion test used for some industries, it was decided to perform in situ reactivity measurement in immersion conditions.

As presented in the previous chapter, depending on the system, the adhesion loss and further degradation of the metal-polymer interface can pass through cathodic and anodic mechanisms, it is hence necessary to detect and distinguish both anodic and cathodic reactivity at buried interface.

In order to answer these problematics, the methodological approach contained several steps:

1) Selection of a method or a combination of methods able to detect reactivity at buried interface
2) Selection of a known model system and verification that the developed methodology gives the results similar to the expected from the literature.
3) Application, development and extension of the methodology to more complex and unknown systems.

The following sections will describe the technical details and problems of the experimental development, made in this work, while the result section will present the results obtained with already optimized methodological approach and experimental set up.

3.1. LEIM and TLM combination in one experiment for underpaint reactivity studies

The objective of this work being to develop a methodology for characterization of immersion stability of metal-polymer interface with initially undamaged polymer coatings and detection of local damage; on the basis of the technics review presented in the state of the art (**Section 4.3**), *local electrochemical impedance spectroscopy and mapping (LEIS and LEIM) were selected as the main technics to detect electrochemical reactivity*. The application of the oscillating potential bends the current lines normal to the sample's surface therefore reducing the signal loss through the polymer and enabling the micro-probe to detect current through the polymer coating. Local electrochemical impedance technics were selected first as the main tool of this work. This technic has however some limitations.

First, the application of LEIM still can be perturbed or even impossible under thick and very insulating polymers and can be also misleading for the systems in which polymer coating contains electrochemically active additives. Moreover, even for thin organic coatings without additives, electrochemical impedance spectroscopy can be unable to detect cathodic reactivity if the cathodic reaction is the oxygen reduction reaction. Indeed, the current reflecting the reaction rate in this case is limited by oxygen diffusion and hence potential independent [2]. The latter is a typical case in aqueous corrosion of iron and galvanized steel [3]. To complete the electrochemical study, *the oxygen reduction reaction was complementary detected by optical time lapse microscopy* (TLM) thanks to local pH increase near the metal-polymer interface as described in the **Chapter 1 Section 4.3**. The use of phenolphthalein indicator was previously proposed as an additive in model transparent coatings [4], however in this work we tested both, the presence of the indicator in the coating and in the solution, the latter being potentially interesting if industrially produced coatings, in which the indicator incorporation is "too late" are tested. Another

interesting application of the TLM in relation to painted system degradation is that *TLM can detect cathodic hydrogen formation in the case when the cathodic reaction is water reduction* (**Eq. 5**). From this point of view, the main difficulty of bubbles detection by TLM can be related to the fact that in direct visual observation under the electrolyte, small gas bubbles could be confounded with the details of surface inhomogeneity. Even if a quantitative approach was not yet made, a partial solution of the problem of this problem was proposed, as described in section 2.1.3.

One of the methodological advantages of these work is in the combination of local electrochemical measurement and in situ TLM in one experiment. **Figure 2.2** represents schematically the set up combining LEI probe and optical camera. The details of the set up are given in the next section.

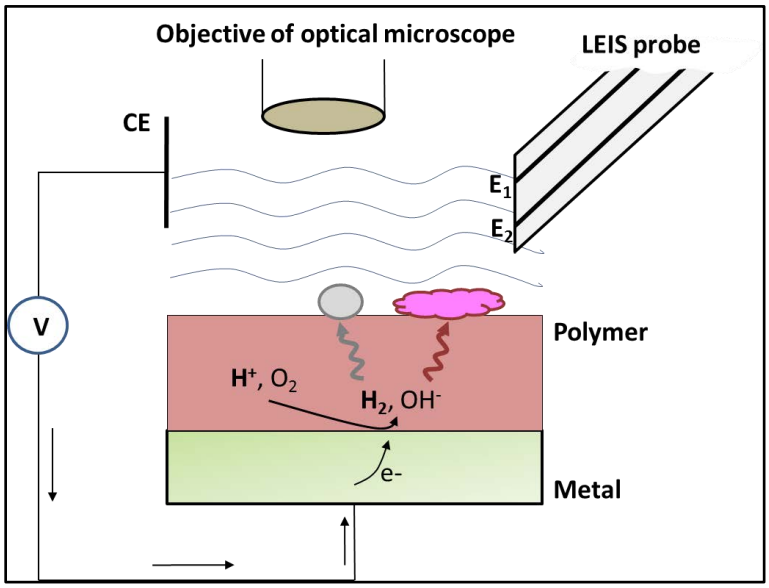

Figure 2.2: Schematic representation of the in situ measurement setup

3.2. LEIM details and LEIM cell adaptation for combination with TLM

LEIM measurement was performed with a home-made setup composed of Solartron Modulab software with auxiliary input and a 3-axis stepper motor-controlled by Sensolytics. A three-electrode configuration was used with the sample as working electrode, an Ag/AgCl electrode as reference and a platinum wire as counter electrode. Impedance measurements are carried out with a homemade local probe composed of two Ag wires of 250 µm diameter in a glass capillary (sealed in two joined capillaries with the distance between the two Ag wires centers d = 1 ± 0.1 mm). The local impedance probes preparation is described in **Appendix 1**. The probe was positioned at 100 ± 25 µm above the WE during the mapping. In these experimental conditions, only the local current density component normal to the sample surface was detected. In such a configuration of the probe and its position, the spatial resolution was around 250-300 µm in diameter. Probes with the Ag wires of 50 µm were also tested, however the probe diameter decrease have a controversial effect which needed to be optimized. Despite the spatial resolution improvement, the sensitivity to low currents decreases and the time of the measurement can

be longer for small probes. For this reason, to study larger areas of polymer coated substrates the selected probe was chosen as a compromise solution.

One of the problems faced during the installation of the setup coupling LEIM and TLM was the congestion of the area above the sample surface and the low amount of electrolyte required to perform HD images by TLM. During preliminary tests, platinum grid was used as a counter electrode and located on one side of the sample (**Fig. 2.3**); although the setup did permit to place the camera on top of the surface, the local impedance mappings appeared distorted in the direction of the counter electrode.

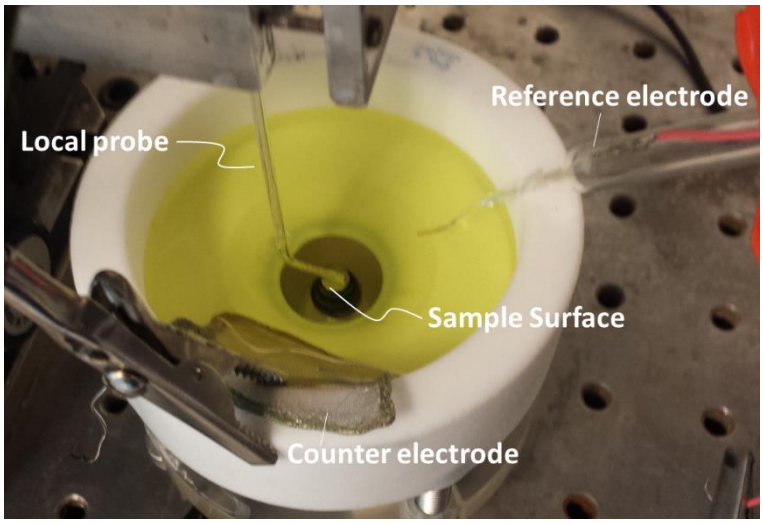

Figure 2.3: Photography of the initial setup for LEIM and TLM measurement

The distortion of the electrochemical impedance mapping in the direction of the counter electrode in the setup described above can be explained by the bending of the current lines towards the CE during potential application. The local current measured by LEIM probe is proportional to ($\varphi_1 - \varphi_2$), the difference in the potential between the two Ag wires. However, φ_1 and φ_2 are correlated to the potential values of the equipotential lines between the working electrode (the sample) and the counter electrode. Or when the distance between WE and CE varies, so does the distance between the equipotential lines. In this case, since the distance between the two Ag wires is fixed, the distortion of the LEIM in the direction of the CE is attributed to the variation of the equipotential distance as a function of the local impedance probe position. A perfect setup would be to get a planar CE projected at an infinite distance in the normal direction of the sample surface, hence the current lines during EIS would be normal to the sample surface.

A compromise was made in the case of our specific setup to enable the presence of the LEIM probe and the HD camera not far above the sample surface: the chosen counter electrode was a 3 cm diameter toroid of platinum wire placed above the sample surface and the cell height was reduced. This choice permitted to obtain a symmetrical distribution of current lines above the sample surface. A specific electrochemical cell geometry was proposed (**Fig. 3**) and 3D-printed in the lab. The cell material was a polylactic acid. The advantage of 3D printed cell is that different cell dimensions could be adopted in function of the sample size.

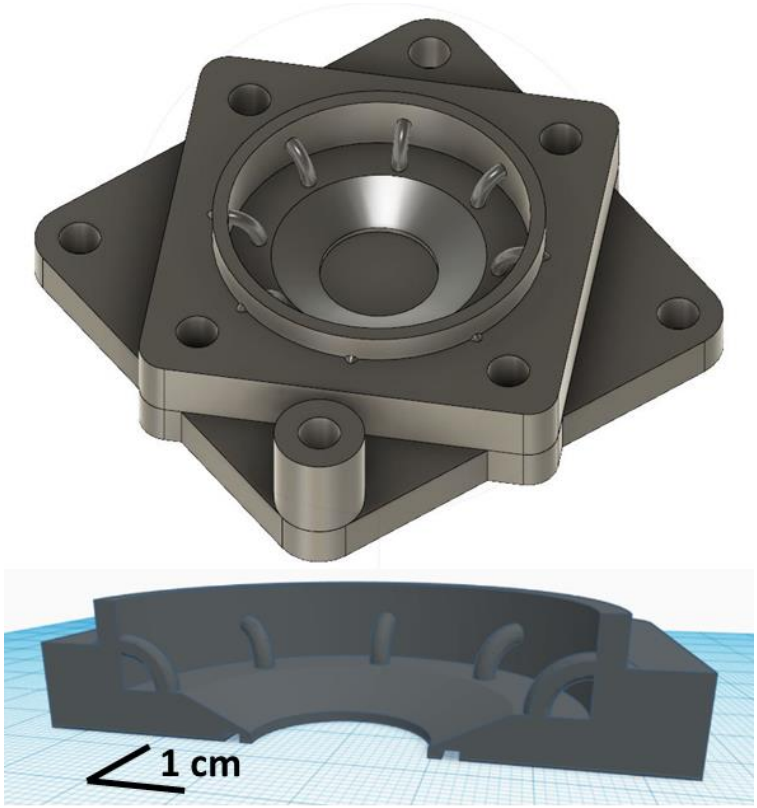

Figure 2.4: 3D representations of the designed electrochemical cell for LEIM and TLM coupling

The proposed LEIM+TLM setup was applied first to a model system for which the behavior was previously well described in the literature: zinc coated substrates without conversion coatings with weak polymer coatings, like polyvinyl butyral (PVB). For this system no specific accelerated ageing was necessary, the system degrading enough rapidly and the substrate corrosion starting in several hours. However, for application to more stable systems, containing conversion coating improving polymer adhesion, very long immersions were necessary to degrade the interface. For slowly degrading systems, the degradation of the metal-oxide-polymer interface was accelerated by cathodic polarization via a specific cycling procedure based on the AC-DC-AC cycling (see results **Chapter 3**).

3.3. TLM adaptation for distinguishing gas bubbles and surface inhomogeneity and for optical detection of degradation on non-transparent thick paint

As mentioned in **section 3.1**, TLM can potentially be interesting to detect pH modification and hydrogen evolution; especially under cathodic polarization condition. However, two limitations of this techniques should be noted:

- Thick and opaque organic coatings hinder buried interface reactivity from optical observation
- Direct view normal to the surface does not allow topographical variation detection like blisters, bubbles, local swelling and surface roughness.

Hence in the case of industrial painted system ageing in immersion conditions, in situ optical microscopy as described previously has a limited interest.

Although EIS is one of the most used technique to detect and study degradation processes of painted systems in situ, it was recently shown that the interpretation of EIS in corrosion protection processes could be biased [5]. The paper highlighted this by combining in situ TLM and EIS for the study of corrosion processes of 2024 aluminium, in the presence of various corrosion inhibitors. Counterintuitively, they demonstrated that the impedance values of the systems could not be directly correlated to the corrosion inhibition efficiency and concluded:" The optical analysis could be used as a complementary technique to clarify electrochemical models for corrosion and inhibitor action."

The previously described set up (**Section 3.2**) was mainly designed to be applied to understand reactivity under the polymer and to be applied under relatively thin and hence not too insulating model polymer. In the prospective to obtain a complete approach to the degradation phenomena at metal-oxide-polymer interface and give a tool to study the above cited cases, optical time lapse microscopy was extended to make it able to distinguish small defect formation on non-transparent thick polymer coatings, initial defects and gas bubbles.

Concerning surface defects, as previously mentioned in **Chapter 1 Section 3**, during immersion test, the most evident process revealing the metal-oxide-polymer interface degradation is the apparition of blisters on the paint surface (**Fig. 2.4**). Micro-blistering is not evident to detect *in situ*, it can be masked by the surface imperfections like initial roughness and can also be confounded with little gas bubbles.

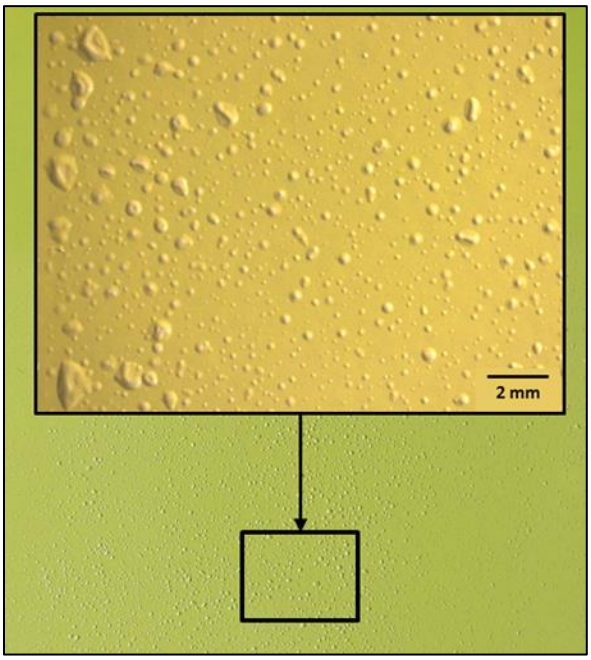

Figure 2.5: Example of an optical microscopy of degraded industrial painted system, blister apparition

The main idea was to use a glass electrochemical cell instead of the PLA 3D-printed cell, and to set a 20° incidence grazing light close to the sample surface. The grazing light permitted to highlight the presence of small inhomogeneities in the height of the paint surface by projecting their shadow on the surface. A graphical illustration of the proposed approach is detailed in **Figure 2.5**: the light source on the left part of the figure illuminates a defect in the paint and projects a shadow on the paint surface (on the right of the figure). The gas bubbles present on the paint surface are less opaque than the paint but the

difference in the refraction angle between H_2 and water should influence the light and therefore project a shadow on the paint surface; in addition, the bubble surface directly exposed to the light is reflective and will present white traces. Hence theoretically, it should be possible to differentiate bubbles from defects on the paint surface.

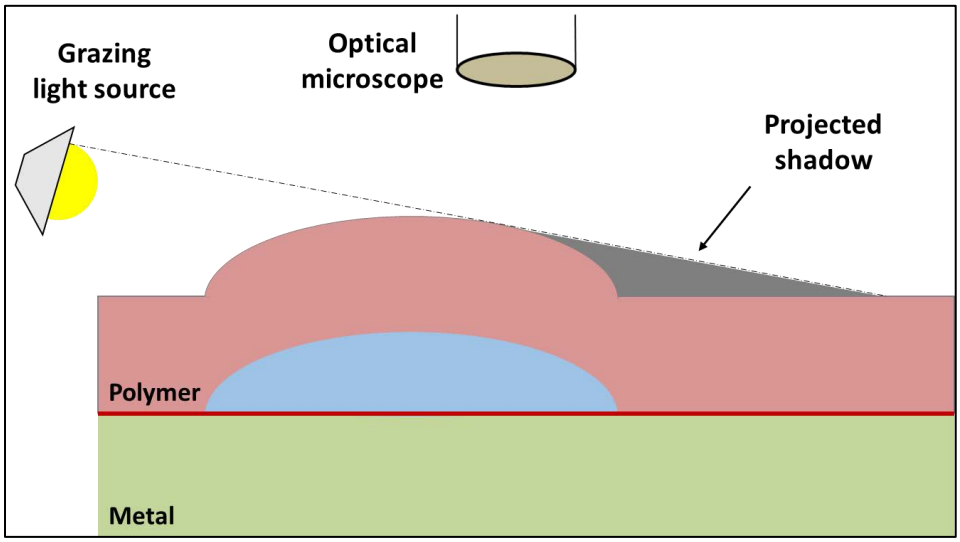

Figure 2.6: Schematic description of the blister observation by TLM with grazing light

The proposed approach is provided in **Figure 2.7**: a painted sample presenting blistering was put in immersion in the presented setup and observe with grazing light. On the image the shadow appears darker than the rest of the painted surface (**Fig. 2.7** on the left). The automated image analysis, performed with FiJi software, permits to binarize the images into defect-shadows and non-degraded surface (**Fig. 2.7** on the right). The analysis consists of background removal using Fourier Transformation Function, followed by a binarization of the image by contrast threshold.
This procedure makes hence possible to automate the quantification of the blisters and/or gas bubbles number, size, distribution on the surface etc.

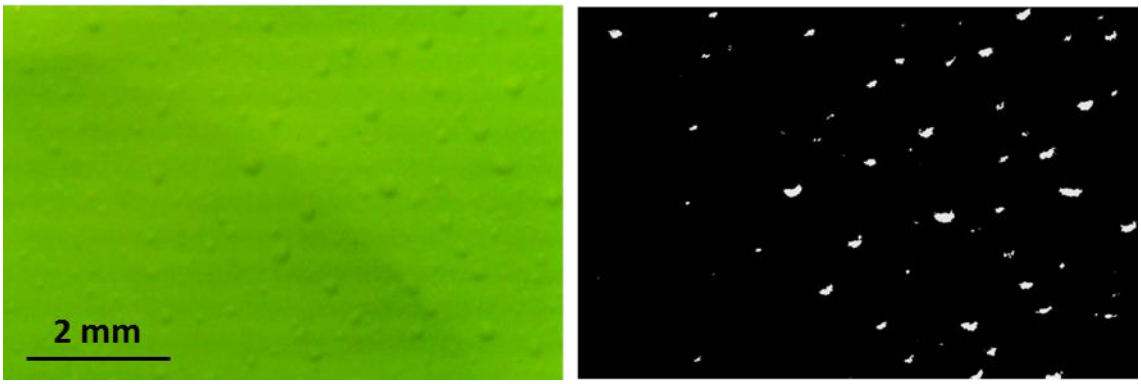

Figure 2.7: Example of initial representation of blistered surface obtained in situ under an electrolyte layer by TLM and treated binary representation evidenced the presence of blisters

An example of *in situ* TLM observations of a painted sample during cathodic polarization test in 0.05 M NaCl solution is presented in **Figure 2.8**. The light source is located at the bottom of the image; hence

the parallel horizontal lines are attributed to light interference. On both images, taken after 0.5 and 3 hours of cathodic polarization, respectively, hydrogen evolution is clearly detected by the presence of various gas bubbles. It can be noticed on the picture that, as related earlier, two major components are observed:

- The bubbles project a shadow in the vertical direction (oriented to the top of the picture)
- The bottom side of the bubbles (directly exposed to light) present a white color due to the light reflection at gas-electrolyte interface

On the observation after 3 hours of cathodic polarization (**Fig. 2.8** on the right), multiple small defects on the paint surface are detected among the bigger gas bubbles. As for the defects observed on the **Fig. 2.7**, a projected shadow on their top side is observed and no white color can be detected on their bottom side. This difference should allow to distinct bubbles from paint surface defects.

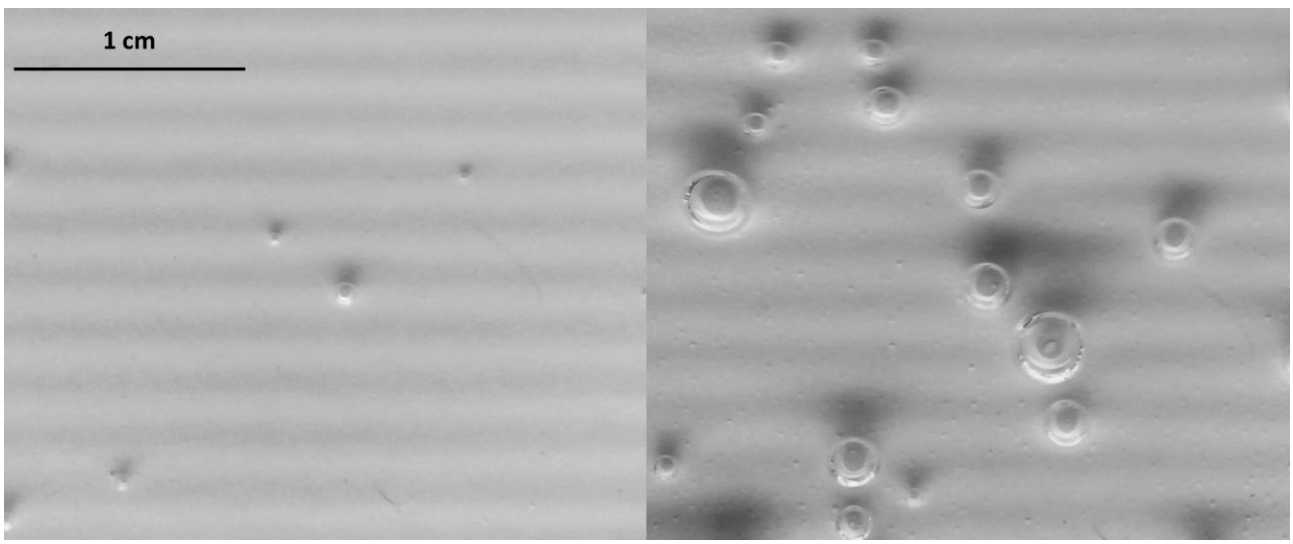

Figure 2.8: Example of in situ TLM observation of painted sample during cathodic polarization after 0.5 and 3 hours, on the left and right sides, respectively

Furthermore, the proposed automated analysis allows to describe the evolution of the defects and/or gas bubbles present at the polymer coating surface.

3.4. Verification of LEIM-TLM coupling for PVB coated systems aged in humidity chamber

A first verification of the methodology coupling LEIM and TLM to study the adhesion loss at metal-polymer interface was performed on the well-known system presented in the previous chapter: delamination of a model PVB from an initial defect.

The geometry of the samples is presented in **Fig. 2.9.**

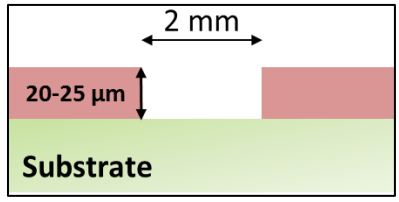

Figure 2.9: Schematic of the model defect in PVB polymer coating

The ageing of the system was performed as such:
The sample was put in a humid chamber with relative humidity of > 75 % at 23-26° C for 24 hours to saturate the polymer with water; then a 5 µL droplet of solution of 0.5 M NaCl was placed in the artificial defect to initiate delamination. Every hour, the droplet was removed from the surface and the sample was placed in the electrochemical cell then immersed in 25 mL of 10 mM NaCl. Optical image (TLM) and LEIM were performed then the sample was removed from the electrochemical cell, a new 5 µL droplet was placed in the artificial defect and the sample was placed in humid chamber for 2 hours before repeating the measurement procedure. The immersion duration during LEIM was approximately 25 minutes.

The application to LEIM and TLM to this system was performed on Zn HDG /PVB and ZnNi /PVB systems. **Figure 2.10** illustrates the cathodic front detection by the color change caused by phenolphthalein incorporated in the coating. **Figure 2.11** illustrates the anodic front development on the same system. Comparing anodic (from LEIM) and cathodic (from TLM) front positions, it was confirmed a clear difference between the two fronts.

In addition, for Zn/PVB system, the delamination kinetics was measured by plotting delaminated depth versus time (see **Fig 2.12** for the anodic kinetics) in –log-log coordinates, assuming the rate in a form of the following equation:

$$D_t - D_0 = kt^{\alpha} \quad \textbf{(2.1)}$$

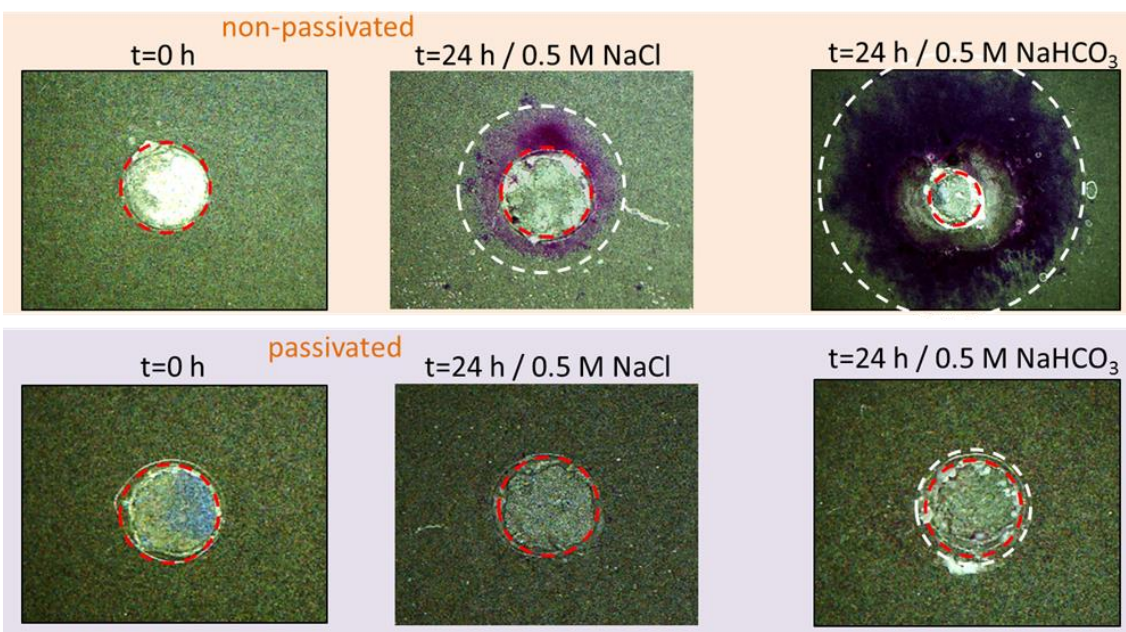

Figure 2.10: TLM observations of the cathodic delamination on ZnNi w/o passivation in the presence of NaCl and $NaHCO_3$. The diameter of the initial defect (in red) is 2 mm

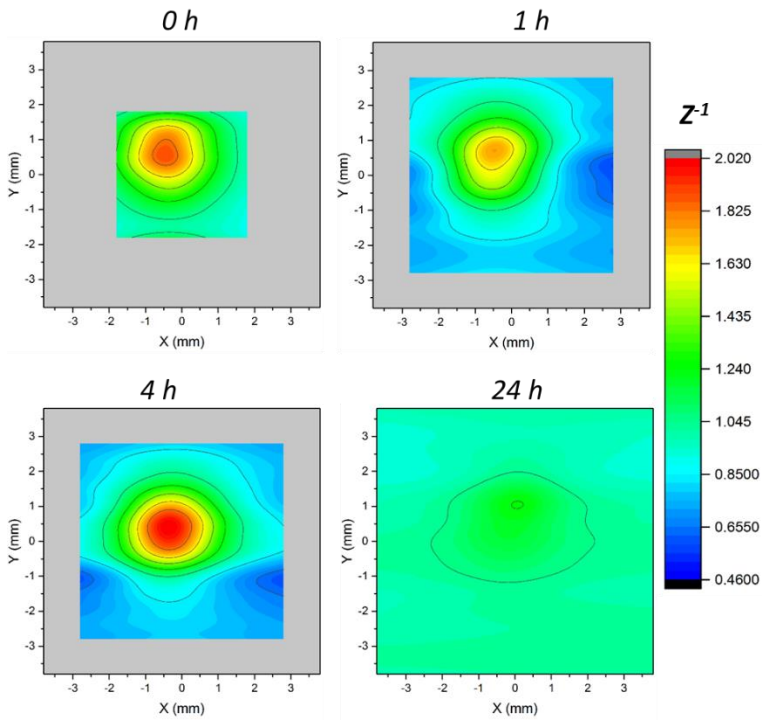

Figure 2.11: Examples of LEIM on bare ZnNi at different times of the delamination in the vicinity of the defect

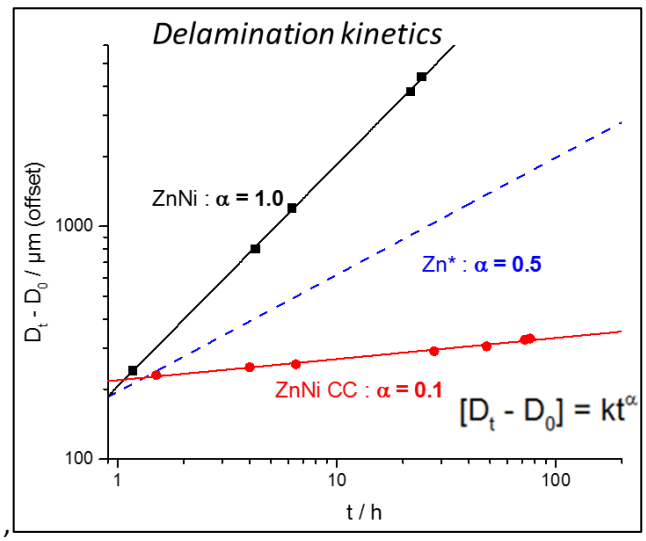

Figure 2.12: Examples of anodic delamination kinetics detected by LEIM on samples coated with PVB model coating

As expected, the slopes obtained from the evolution of cathodic and anodic delamination fronts were different, for instance for Zn in NaCl the slope was 0.5 from the anodic front evolution and 1 from the evolution of the cathodic front. The obtained anodic slopes of α=0.5 for Zn/PVB in environments without carbonates and α=1 in the presence of carbonates were coherent with previous work performed with Scanning Kelvin probe on a similar system degraded in a humid chamber [1]. The application of this methodology to ZnNi without conversion coating revealed a stronger reactivity than on Zn HDG surface and a surface reactivity limiting process (α = 1).

However, an important observation can be made from **Fig. 2.12**: comparing ZnNi substrates with and without conversion coating. *Delamination kinetics of the samples with conversion coating (noted as passivated) is at least 10 times slower than the delamination kinetics of the same substrate without conversion coating even in the case of the application of very weak polymer. The later confirms the necessity to find an accelerating procedure for stability studies of the substrates with conversion coatings*.

More details about the results obtained on PVB coated substrates can be found in **Appendix 4** [6].

An attempt was made to accelerate the process by immersion of PVB coated zinc. TLM in situ permitted to observe color changes related to underpaint cathodic reactivity far from the initial defect, and sometimes even before the delamination process was initiated in the vicinity of the defect. This can be seen as an indication of the existence of water permeability at these locations, implying either polymer degradation or polymer mechanical deadhesion and is a strong evidence of the incompatibility of this weak model polymer for the study of conversion coatings in immersion conditions.

Figure 2.13 shows an example of such TLM observation.

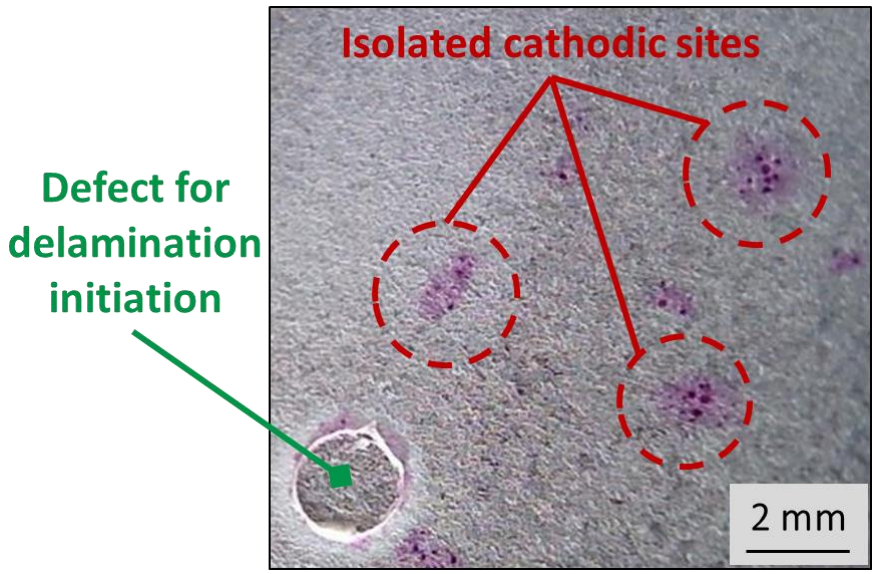

Figure 2.13: TLM observation of PVB coated Zn HDG after 4h of immersion in 0.01 M NaCl in the presence of phenolphthalein

These results demonstrated *that PVB model coating did not sustain these conditions and degraded during this procedure, confirming the necessity to develop a new model polymer coating for studies of conversion coatings*. The development of this coating is detailed in the result section (see **Chapter 3**).

4. Combination of characterization technics for ex situ observations

Two types of ex situ characterizations were made in this work. From one side, the chemistry of the initial system was characterized with surface analytical technics. The difficulty of such a characterization resides on the necessity to characterize a rough substrate. The **first section (3.1.)** of the current chapter introduces and justifies the selected combination of technics in this work in order to describe the chemistry of conversion coating in the nanometric range on rough electrodeposited substrates.

The **second section (3.2.)** describes the 3D optical characterization of the complete system, necessary for a global overview of the system, revealing surface roughness parameters or topography as well as evaluation of the depth of relatively thick (10 µm) polymer coating.

4.1. Strategy of the chemical characterization of conversion coating layer

In order to obtain a good understanding of the interface chemistry of the sample, four main types of surface characterization are often performed on nanometric oxide layers:

1. Top surface chemical description with species identification and quantification on “wide” area
2. Elemental in-depth profiles to describe multilayer systems and interfacial areas
3. In depth chemical description with species identification and quantification
4. Description and profiling with high lateral accuracy to study the homogeneity of the layers.

These can be achieved by combination of multiple technics described in **Table 2.3**. The principles of these technics and their advantages and limitations are more in detail reviewed in the Section 5 of this chapter.

As revealed in **Chapter 1**, the combination of XPS and ToF-SIMS is unparalleled to characterize well-prepared smooth sample surfaces and nanometric oxide layers. However, the ToF-SIMS is highly sensitive to surface roughness because of the low incidence ion gun of the technique. Hence in this work, the combination might not give proper results.

Table 2.3: Comparison of surface techniques characteristics

	GD-OES	ToF-SIMS	XPS	Nano-AES
Depth sensitivity	1 nm	0.1 nm	10 nm	3 nm
Lateral resolution	2 mm	20 µm	400 µm	10 nm
Limit of detection	PPM	PPB	0.10%	1%
Quantification accuracy	-	-	1%	3-5%
Chemical speciation	-	Limited	Yes	Limited
In-depth measurement	Yes	Yes	-	Yes
Sensitivity to surface roughness	Limited	Yes	Limited	Very Limited

For this reason, complementary combinations were selected. The combination of surface analytical technics and their sequence in this work is schematically shown in **Fig. 2.14**. The sequence consisted of initial characterization (step a), crater generation with depth elemental profiling (b or c) and following crater characterization (steps d and e). In the case of rough substrate, the steps surface and depth profile characterization can be performed by XPS and GD-OES (or XPS and ToF-SIMS), respectively. Although the detection limit and the signal-to-noise ratio might be worse than in the case of a smooth surface, results can be conclusive. The localized characterization of the oxide layer can be performed by Auger-microscopy, as selected in this work because of possible roughness of the surface.

To perform a proper XPS measurement at a certain depth of the oxide layer thanks to a crater generation, the sputtering must be as homogeneous as possible over the 400 µm of diameter range of the XPS analysis. Otherwise the result is inconclusive because the analyzed surface represents different depths. The homogeneity of the sputtering in the crater was verified in this work by comparison of depth profiles obtained in unsputtered zones and comparison of depth profiles inside different locations of the GD-OES generated crater was performed with nano-AES technique. For comparison, the same type of experiment was performed with ToF-SIMS sputtering combined with XPS.

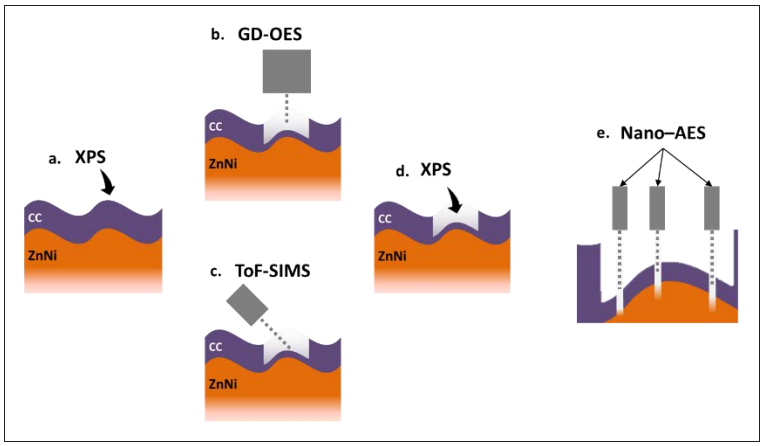

Figure 2.14: Schematic representation of the surface characterization methodology

4.2. High resolution 3D-Microscopy

Observations of the surface were performed using a Keyence VHX-5000 microscope equipped with the VH-Z500T objective allowing for magnification from 500x to 5000x. With 500x magnification and numerical image stabilization, the area of view was of 610 x 457 µm² for a 2000 x 1600 px² image. The microscope as very short depth of field and is equipped with a 3D axis step motor moving system. The setup permitted to perform measurements of the transparent polymer coating thickness with the height difference between the focus on the paint surface and the substrate surface. To do so, the enlightenment conditions were set in accordance as presented on the **Figure 2.15**:

- Coaxial light normal to the surface was used to focus on the substrate (**Fig. 2.15**, on the right)
- Grazing light with low incidence was used to focus on the micro-scratches performed at the paint surface (**Fig. 2.15**, on the left)

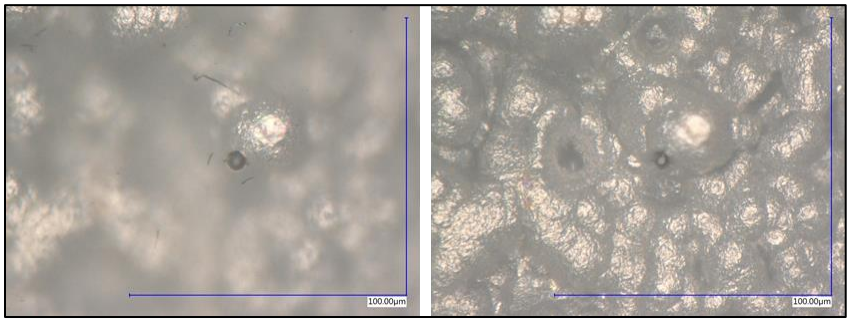

Figure 2.15: Observation of coated sample at polymer coating (left) and substrate (right) surface

In addition to measurement of substrate and paint surfaces, the Keyence microscope permits to perform 3D image composition and extract 8-bit topography mapping of the observed surface. The data could then be processed with Gwidion software to obtain roughness parameters with micrometric accuracy. The protocol for data extraction is provided in **Appendix 3**. The earlier results of the electrodeposited substrate rendered Ra values of 5 µm AND Rz values up to 10 µm.

To be able to perform high resolution images at these magnifications, especially in the case of 3D composition where the lens must move with high accuracy, vibration and movement reduction is a great issue for optical observations. In the beginning of this work, a special anti-vibration table was developed and proposed. The setup is composed of a commercial EMT antivibration mattress designed for washing machine, 5 pads of high-grade silicon and a 4 cm thick aluminum plate (**Fig. 2.16**).

Figure 2.16: Photography of the anti-vibration setup for Keyence 3D microscope

5. Principles of conventional methods used for ex situ characterizations

This section describes some theoretical principles of the characterization technics used in the work. It can be omitted by an experimental reader familiar with these technics.

5.1. Scanning Electron Microscopy and Electron Dispersion Spectroscopy (SEM-EDS)

Scanning Electron Microscopy (SEM) is an electron microscope producing images of a sample surface by scanning the surface with a focused beam of electrons. The electrons interact with the atoms at the sample surface producing various types of electrons emitted from the surface. The low energy electrons (secondary electrons) resulting from inelastic interaction of the electrons permit to obtain images where the contrast is related to the surface roughness. The part of the electron beam reflected by the surface (backscattered electrons) result of an elastic interaction with the atoms of the surface and permit imaging with high sensitivity to the chemistry of the surface. SEM allows observations of the surface of samples as well as primary characterization. The resolution of the analysis depends on both the focusing of the primary electron beam and the type of electrons analyzed described by the electron-matter “interaction pear” (**Figure 2.17**).

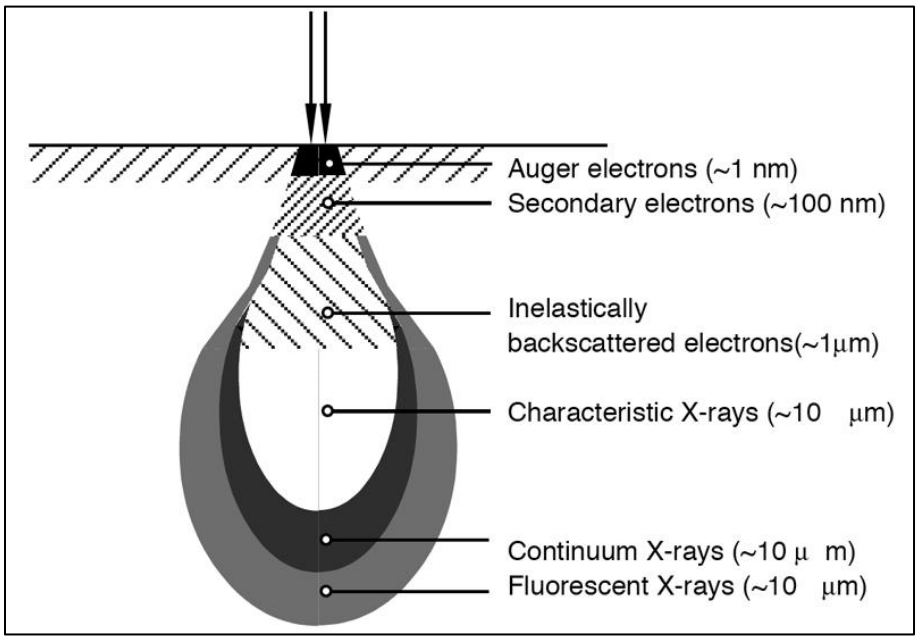

Figure 2.17: Schematic representation of the electron-matter "interaction pear" [7]

In addition, the characterization by SEM permits both an observation of the surface of the samples and the cross-section of complete painted systems. For that purpose, both mechanical polishing the edge of the sample and ionic milling techniques can be used depending on the accuracy. Where mechanical polishing enables a fast surface preparation, two main issues emerge: good accuracy of the position of the cross section is difficult to obtain; the interfaces between different materials, especially at metal-oxide-paint interface, can be disturbed by polishing [8]. On the contrary, ionic milling permits to obtain undamaged interfaces in multi-layer systems with no pollution and a very good accuracy [9].

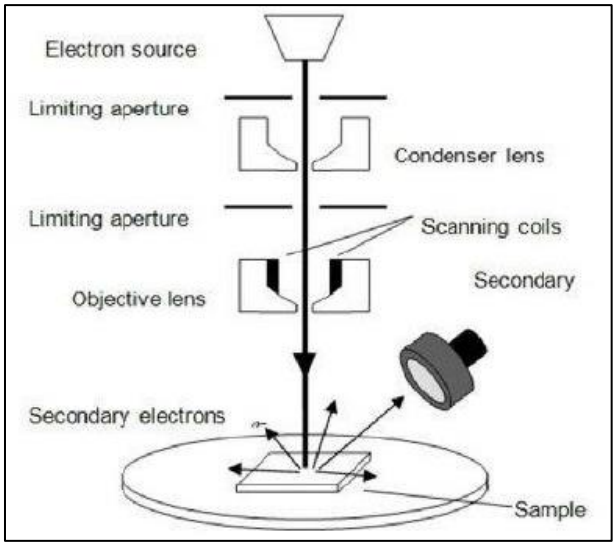

Figure 2.18: Schematic representation of an SEM

In the case of rough surfaces, SEM technique can present a drawback: the detection of the secondary electrons is performed at low take off angle as shown on SEM scheme presented in **Figure 2.18**. The high roughness of the surface can hence be detrimental for a good observation. For that matter, new types of electron detector, such as in-lens detectors, were developed with band-pass filter to obtain higher resolution imaging for both secondary and backscattered electrons [10].

5.2. X-ray photoelectron spectroscopy (XPS)

X-ray photoelectron spectroscopy (XPS), is a characterization technique providing accurate chemical description of the extreme surface (5 - 10 nm in depth). It is a non-destructive technique providing quantitative data analysis. The previous denomination of XPS was ESCA (Electron Spectroscopy for Chemical Analysis) and was developed in 1960 [11] The principle relies on the irradiation of the sample surface with monochromatized X-Ray beam generated by an electron beam bombarding a metallic target; in most cases, the Kα line of aluminum is used (hν = 1486.6 eV). The surface atoms of the irradiated sample are ionized by photoelectric effect and emit photoelectrons during their relaxation. The kinetic energy of the emitted photoelectrons E_k is measured by a hemispherical energy spectrometer. According to the energy conservation relation, we can write:

$$E_{total} = h\nu_{RX} = E_k + E_b\,(ndl) + \varphi_{spectro} \qquad \textbf{(2.2)}$$

Where $h\nu_{RX}$ is the energy of the X-ray source, E_k is the kinetic energy of the emitted electron, $E_b\,(ndl)$ is the binding energy of the original electron in the ndl orbital, and $\varphi_{spectro}$ is the extraction work of the spectrometer. A schematic representation of the XPS principle is shown in **Figure 2.19**.

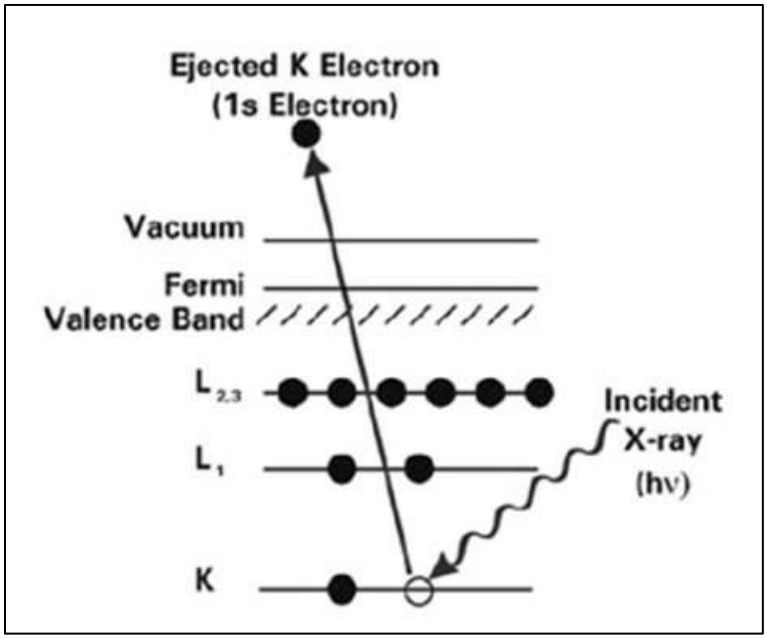

Figure 2.19: Principle of XPS [12]

The number of detected electrons for each binding energy is directly linked to the concentration of the element at the analyzed surface.

The average analysis depth of XPS can be calculated with a Beer-Lambert type exponential decrease relation.

$$\frac{I}{I_0} = \exp\left(\frac{-z}{\lambda \sin(\theta)}\right) \quad \textbf{(2.3)}$$

where I is the intensity of the peak in the XPS spectra, z is the depth, θ is the take-off angle of the emitted electron and λ is the inelastic mean free path of the electron in the matter. The mean free path of the electrons depends on its kinetic energy and the nature of the material. In the case of transition oxides, this length is around 3 nm [13]. It is hence possible to determine the probability for a photoelectron to reach the surface of the sample and to be detected by the XPS.

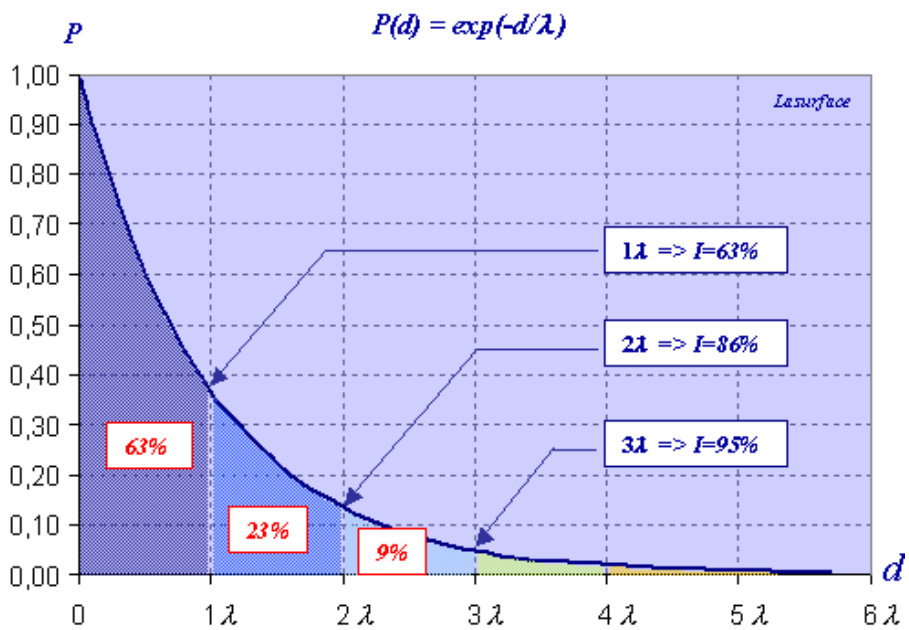

Figure 2.20: Probability of a photoelectron to reach the surface in function of its depth emission d [14]

According to the probability decrease relation illustrated in **Figure 2.20**, 95% of the atoms contributing to the signal in XPS come from less than 3 λ in depth, *i.e.* less than 10 nm. Which makes the XPS a very powerful technique for extreme surface analysis.

According to the exponential decrease relation, the take-off angle of the emitted electrons θ is a key parameter in the determination of the analyzed depth. Hence, in the case of a rough surface, since the photoelectron detector is fixed toward the surface, the electrons detected come with a take-off angle varying between 0 and 90 ° depending on the surface roughness. The analyzed depth of the surface on the sample is therefore not homogeneous and varies between 1 and 10 nm depending on the local orientation of the surface. This heterogeneity was shown to affect XPS characterization in the case of thin oxide layer [15,16] but quantification of the surface composition was still possible.

5.3. Glow Discharge Optical Emission Spectroscopy (GD-OES)

Glow-Discharge Optical Emission Spectroscopy (GD-OES) is a surface analysis technique developed in the seventies based on Grimm type argon plasma source [17] and Rowland design spectrometer [18].

The analyzed samples are placed in a primary vacuum chamber and exposed to a plasma. The surface is sputtered by argon ions accelerated in the plasma; the sputtered atoms are excited in the plasma and, by returning to their initial state, emit characteristic photons. The wavelength of these photons can be calculated using Max Planck's equation:

$$E = \frac{hc}{\lambda} \quad \textbf{(2.4)}$$

where E is the photon energy, corresponding to the transition between orbitals in the sputtered atom, h is the Planck's constant, c is the speed of light and λ is the wavelength.

An optical spectrometer analyzes the emitted photons in the plasma chamber in real time, hence it is possible to identify the elements present in the material at each step of the sputtering and reconstruct elemental in-depth distribution. A schematic principle of GD-OES measurement principle is shown in **Figure 2.21**.

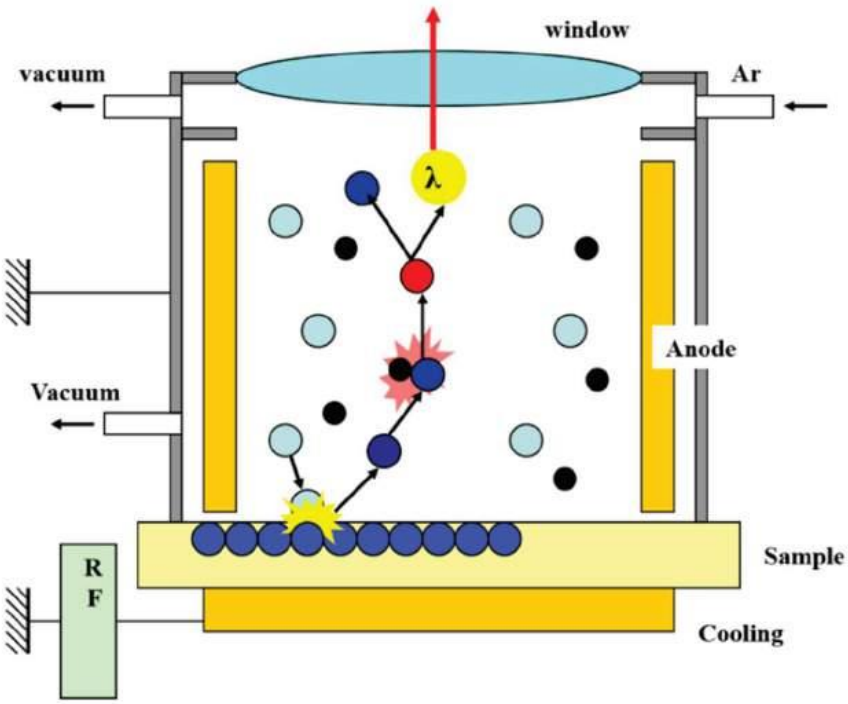

Figure 2.21: Schematic representation of GD-OES principle

Thanks to the real time analysis and argon plasma sputtering, GD-OES technique provides a high sputtering speed: a few micrometers per minute. Still, the depth resolution of GD-OES profiling in the case of well-prepared samples is lower than the nanometer and detection limit of the technique is around the PPM; this makes a powerful and fast technique for the characterization of thin oxide films [19].

Recent development of so-called “ultra-fast sputtering” using argon-oxygen gas mixture in the plasma for GD-OES analysis has permitted to perform in-depth elemental profiling on painted systems and therefore characterize the complete system and see metal-oxide-polymer interfaces [20].

5.4. Time of Flight Secondary Ion Mass Spectrometry (ToF-SIMS)

Time of Flight Secondary Ion Mass Spectrometry (ToF-SIMS) is a surface analysis technique highly sensitive to the extreme surface chemistry. It allows elementary analysis as well as molecular and isotopic identifications of the samples, with a detection limit in the ppb (part per billion) range. Like the GD-OES, ToF-SIMS cannot allow quantitative analysis of the surface chemistry without preliminary calibration.

The operating principle is the one of a mass spectrometer equipped with a time of flight analyzer. A focalized primary ion beam is irradiated on the sample surface; numerous particles are then emitted, including charged species, called “secondary ions” [21]. These ions are the only particles detected by the

ToF-SIMS. The analysis depth of the technique is around 1 nm (1 to 3 atomic monolayers). A schematic of SIMS principle is presented in **Figure 2.22**.

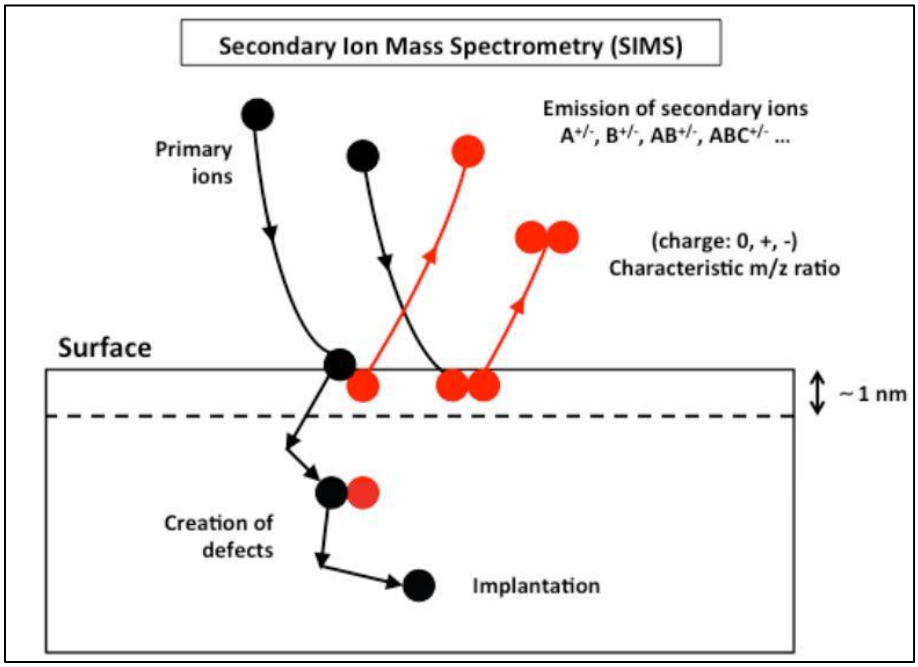

Figure 2.22: Schematic of secondary ions emission principle

The surface analysis by ToF-SIMS returns a mass spectrum revealing species present at the surface. The focalized primary beam can be thinned up to a few hundred nanometers, allowing high resolution cartography of the surface chemistry [22]. In the analysis chamber, another ion beam is used on the surface to permit surface sputtering; hence in-depth secondary ion profiles can be performed by combining both sputtering and primary ion beams in sputtering/analysis successive cycles.

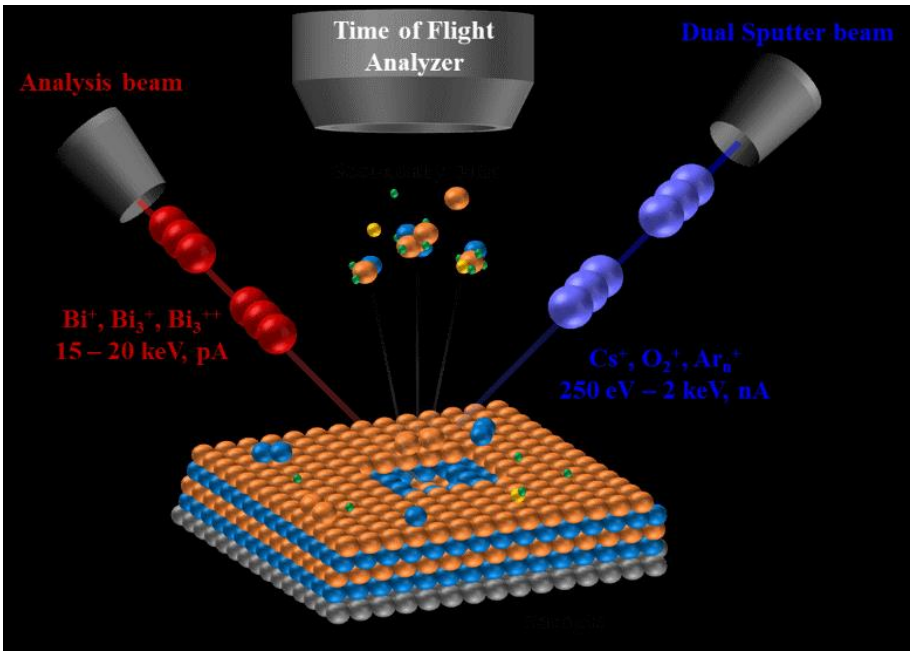

Figure 2.23: Scheme of the in-depth secondary ion profiling by ToF-SIMS principle, adapted from [23]

In order to limit the surface roughness generation during sputtering, both ion guns, sputtering and analysis, are placed to obtain low incidence angle ion beams: 45° [24]. The two are often placed on opposite sides of the analyzed site in a symmetrical way as described in **Figure 2.23**. Such a setup provides unmatched capabilities to the ToF-SIMS technique but rends it much more sensitive to initial surface roughness of the samples [25].

5.5. Nano-probe Auger Emission Spectroscopy

Nano-probe Auger Emission Spectroscopy (Nano-AES) is an extreme surface characterization technique combining the assets of SEM and XPS. Its name is derived from the Auger effect, identified by Pierre Auger, a French physicist. The interest of Auger electron spectroscopy was demonstrated in the late 60s [26]. Its principle relies on the SEM technique: a focalized electron beam irradiates the sample surface, and electrons emitted from the surface are detected in an electron spectrometer like in XPS. However, the electrons of interest in AES are Auger electrons. As the surface is irradiated by the electron beam, atoms of the surface are ionized: a core level electron is then ejected, creating an inner shell vacancy. To fill the energy gap in that level, a higher energy electron is transferred; the energy release from this electron transfer might eject a third electron called Auger electron. A schematic principle of Auger electron generation is presented in **Figure 2.24**. The kinetic energy of this Auger electron allows the identification of the atom and its chemical environment [27].

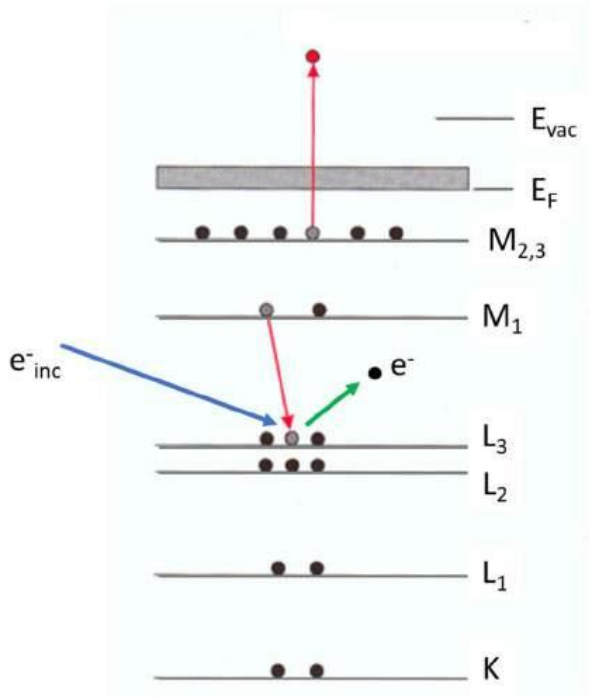

Figure 2.24: Auger electron emission principle

The two great assets in nano-probe Auger electron spectroscopy are its high resolution and the low sensitivity to surface roughness. As described in SEM section by the electron-matter pear interaction (**Figure 2.17**), Auger electrons emitted by the surface are emitted by atoms within the first two nanometers in depth. The focalized electron beam allows a lateral resolution of 10 nm. Hence the analyzed spot in nano-AES corresponds to a 10 nm wide and 2 nm deep volume of the extreme surface [28]. Contrary to other surface characterization techniques detailed here-above, the Auger electrons analyzed in nano-AES technique have a take-off angle close to the normal to the surface thanks to the coaxial cylindrical mirror analyzer (CMA); this specific setup offers a higher sensitivity and reduces the influence of surface roughness on AES [29].

1 References:

1 W. Fürbeth, M. Stratman, The delamination of polymeric coatings from electrogalvanized steel – a mechanistic approach. Part 1: delamination from a defect with intact zinc layer, Corrosion Science 43 (2001) 243-254

2 V. Shkirskiy, A. Krasnova, T. Sanchez, A. Amar, V. Vivier, P. Volovitch, Development of anodic and cathodic blisters at a model Zn/epoxy interface studied using local electrochemical impedance, Electrochemistry Communications 111 (2020), 106633

3 V. Shkirskiy, P. Keil, H. Hintze-Bruening, F. Leroux, P. Volovitch, K. Ogle, Observation of l-cysteine enhanced zinc dissolution during cathodic polarization and its consequences for corrosion rate measurements, Electrochimica Acta 184 (2015), 203-213

4 J. Zhang, G. S. Frankel, Corrosion-Sensing Behavior of an Acrylic-Based Coating System, CORROSION 55 (1999), 957-967

5 P.J. Denissen, S.J. Garcia, Reducing subjectivity in EIS interpretation of corrosion and corrosion inhibition processes by in situ optical analysis, Electrochimica Acta 293 (2019), 514-524

6 T. Sanchez, V. Shkirskiy, J. Swiatowska, P. Volovitch, Organic coatings delamination from Zn-Ni coated steel, Oral presentation, EUROCORR 2017 & 20th ICC, Abstract n° 96707

7 F. Krumeich, Properties of electrons, their interactions with matter and applications in electron microscopy, [Online] Available on: https://www.microscopy.ethz.ch/downloads/Interactions.pdf [Accessed on 15/08/2020]

8 N. Khandekar, Preparation of cross-sections from easel paintings, Studies in conservation 48 (2003), 52-64

9 Ion beam preparation of samples for SEM, application booklet [online], Available on https://downloads.leica-microsystems.com/Leica%20EM%20TIC%203X/Application%20Notes/Application_Booklet_Leica_EM_TIC_3X_EN.pdf [Accessed on 14/08/2020]

10 I. Konvalina, F. Mika, S. Kratki, E.M. Mikmekova, I. Mullerova, In-lens band-pass filter for secondary electrons in ultrahigh resolution SEM, Materials 2019, 212-2307

11 Nobel prize laureates, [online], available on http://www.nobelprize.org/nobel_prizes/physics/laureates/1981/, [Accessed on 10/08/2020]

12 'Thermo Scientific XPS: What is XPS'. [Online]. Available on:https://xpssimplified.com/whatisxps.php. [Accessed on: 12/07/2020]

13 Marcus P, Hinnen C & Olefjord I, Determination of Attenuation Lengths of Photoelectrons in Aluminium and Aluminium Oxide by Angle-dependent X-ray Photoelectron Spectroscopy. Surf. Interface Anal. 20 (1993), 923.

14 Http://www.lasurface.com/xps/imfp.php?lang=fr La surface.

15 Y.L. Yan, M.A. Helfand, C.R. Clayton, Evaluation of the effect of surface roughness on thin film thickness measurement using variable angle XPS, Applied surface science 37 (1989), 395-405

16 L.S. De Bernardez, J Ferron, E.C. Goldberg, R.H. Buitrago, The effect of surface roughness on XPS and AES, Surface Science 139 (1984) 541-548

17 W. Grimm, Spectrochemica Acta 23, Part B (1968), 443

18 ISO 18115:2001(E), 5.311, p.47

19 J. Angeli, A. Bengston, A. Bogaerts, V.P. Hoffman, V.D. Hodoroaba, E. Steers, Glow-discharge optical emission spectrometry: moving towards reliable thin film analysis – a short review, Journal of analytical atomic spectrometry 18 (2003), 670-679

20 P. Chapon, A. Tempez, C. Olivero, T. Nakamura, H. Nakamura, A. Fujimoto, Procédé de mesure par spectrométrie de décharge luminescente d'un échantillon solide organique ou polymère, Europeen Patent EP2434275A1 (2012)

21 NS McIntyre, MJ Graham, Studies of Metal Corrosion and Oxidation Phenomenon Using Secondary Ion Mass Spectroscopy. In Analytical Methods in Corrosion Science and Engineering (Marcus P & Mansfeld FB, eds) (2006), Analytical, pp. 65–102. CRC Press

22 A Seyeux, GS Frankel, N Missert, K Unocic, LH Klein, A Galtayries, P Marcus, ToF-SIMS Imaging Study of the Early Stages of Corrosion in Al-Cu Thin Films. J. Electrochem. Soc. 158 (2011), C165

23 ToF-SIMS description, Rice University [Online], Available on http://simslab.rice.edu/surface-analysis-lab/teaching-activities-resources/time-of-flight-secondary-ion-mass-spectrometry/ [Accessed on 20/08/2020]

24 S. Hoffman, A. Zalar, Depth Profiling with Sample Rotation: Capabilities and Limitations, Surface and Interface Analysis 21 (1994), 304-309

25 J.L.S. Lee, I.S. Gilmore, I.W. Fletcher, M.P. Seah, Topography and field effects in the quantitative analysis of conductive surfaces using ToF-SIMS, Applied Surface Science 255 (2008), 1560-1563

26 R.P. Gunawardane, C.R. Arumainayagam, Auger Electron Spectroscopy, Online Course,Department of Chemistry, Wellesley College, Wellesley, MA 02481, U.S.A, [Online] Available at https://www.wellesley.edu/sites/default/files/assets/departments/chemistry/files/2006_auger.pdf [Accessed on 20/08/2020]

27 N.S. Bishena, Auger electron spectroscopy as a tool for electronic and chemical information, Energy conservation in buildings (1991), 413-419

28 E. Martinez, P. Yadav, M. Bouttemy, O. Renault, L. Borowik, F. Bertin, A. Etcheberry, A. Chabli, Scanning Auger microscopy for high lateral and depth elemental sensitivity, Journal of electron spectroscopy and related phenomena 191 (2013), 86-91

29 S.N. Raman, D.F. Paul, J.S. Hammond, K.D. Bomben, Auger electron spectroscopy and its application to nanotechnology, Microscopy Today 19 (2011), 12-15

Chapter 3

New experimental approach for intelligent screening of buried metal-oxide-polymer interfaces via local electrochemistry: Example of undamaged model epoxy-coated Zn alloys

Thomas Sanchez, Simon Gillet, Viacheslav Shkirskiy, Vincent Vivier, Jaques Echouard, Jolanta Światowska, Polina Volovitch

The content of this chapter was published in Electrochimica Acta

https://doi.org/10.1016/j.electacta.2020.137411

The content of the chapter corresponds tothe publication before peer review and corrections

1

Chapter 3: New experimental approach for intelligent screening of buried metal-oxide-polymer interfaces via local electrochemistry: example of undamaged model epoxy-coated Zn alloys

As shown in Chapter 1, localized studies on degradation kinetics of metal-oxide-polymer interfaces used model PVB coating and atmospheric ageing. However, these conditions cannot be applied neither to substrates with conversion coatings ensuing slower degradation rate, nor to immersion conditions. The current chapter introduces a new experimental strategy aiming to access the stability of buried interfaces in presence of conversion coatings in immersion conditions.

Abstract

A new simple experimental approach is proposed for *in situ* mechanistic studies of the underpaint stability of metal-oxide-polymer interface under immersion. It allows an intelligent screening and fast ranking of conversion coatings on Zn alloys designed for further application of organic coatings. The approach is based on the application of a simple electrochemical aging protocol to the samples preliminary coated with a model epoxy-polymer. The latter is enough thin to allow local electrochemical impedance measurement and stable under this protocol, as revealed by attenuated total reflectance infrared spectroscopy (ATR-IR) and electrochemical impedance spectroscopy (EIS). The interface stability and degradation modes characterization are accessed via combined EIS, local electrochemical impedance spectroscopy and mapping (LEIS and LEIM) and time lapse microscopy (TLM).
The developed approach allowed to discriminate two Zn alloy substrates, one with intact and another with slightly damaged Cr(III) conversion layer, for which no strong differences in the electrochemical behavior or average surface composition was visible prior to the epoxy-polymer application. The results correlated with the observations obtained for the same substrates coated with thick strong epoxy primer after 1000 h immersion test. The proposed methodology offers the possibility of a rapid intelligent screening of various formulations of Cr(III)-based surface treatments for Zn based substrates designed for paint applications.

Highlights

- New approach for smart screening of conversion coatings is proposed
- Modified AC-DC-AC ageing procedure and model polymer are used
- Heterogeneous degradation of buried interfaces detected by coupling of TLM and LEIM
- Ranking obtained by the new procedure correlates with results of long immersion test

1. Introduction

Polymer coatings have been used for centuries for corrosion protection of metals and alloys due to their good barrier properties limiting water and oxygen access to the metallic substrates [1,2]. Barrier protection mechanisms of organic coatings have been extensively studied and the formulations of hydrophobic binders, as well as the addition of pigments, have been optimized to reduce the permeability of the coating to water and oxygen [3]. However, as water reaches the interface, underpaint reactivity can develop. Localized reactive spots under the polymer coating lead to the metal-oxide-polymer interface disbondment and delamination of the polymer coating from the metallic substrate. This delamination of the coating can accelerate the system degradation and must be considered with caution [4,5].

In order to ensure a good adherence of the polymer and improve corrosion resistance, the metallic interface is usually modified by conversion coatings [6]. These coatings are thin oxidized layers formed via chemical and/or electrochemical process at the metal surface [7,8],9]. Among conversion coatings, the most used in the last decades were chromate-based conversion coatings [10]. Their efficiency is supposed to be due to the combination of excellent anti-corrosion properties guaranteed by self-healing ability and good adhesion of chromates to polymer coating [11,12]. However, chromates were proved to be genotoxic and carcinogen [13] and since 2006, European legislation tries to tackle hexavalent chromium via Registration, Evaluation, Authorization and Restriction of Chemicals (REACh) and Restriction of the use of certain Hazardous Substances (RoHS) [14]. According to these legislations, the application of Cr(VI) compounds will be banned by 2022 in Europe. Therefore, the development and the optimization of new chromate-free conversion coating is strongly required [15,16,17], whereas Cr(III)-based conversion coatings have been considered as a possible replacement [18,19].

In order to optimize the new generation of conversion coatings in a reasonable time scale, and to better understand their performances, it is necessary to develop new analytical tools to access the metal-oxide-polymer interface stability. To detect and localize the interfacial disbondment or deterioration, Scanning Kelvin Probe (SKP) is the most well-known and precise tool, used for both, blisters or delamination front detection and the measurement of the kinetics of polymer delamination front propagation in atmospheric corrosion [20,21]. SKP showed that delamination of a polymer with weak adhesion to zinc is mainly cathodically driven [22]. In immersion conditions, electrochemical impedance spectroscopy (EIS) is the most used technique to detect interfacial disbondment from an artificially introduced defect as well as to monitor the polymer coating degradation [23,24,25].Different approaches have been developed to quantify the global degradation phenomena in painted systems: water uptake, diffusion of soluble ions, evolution of the total delaminated area etc. [26,27,28]. To localize the disbondment at polymer-metal interface, Local Electrochemical Impedance Mapping (LEIM) [29,30] and Scanning Vibrating Electrode (SVET) [31] can both detect the electrochemical reactivity in delaminated areas and distinguish the anodic and the cathodic reactive zones. However, contrary to LEIM, SVET cannot detect the underpaint reactivity in the absence of a defect in the paint. In addition, a quantitative LEIM was recently proposed to study the disbondment front propagation kinetics [32] during immersion. However, it should be mentioned that most of previously reported studies on local degradation of metal-oxide-polymer interfaces using local electrochemical techniques concerned the interface delamination

starting from an artificial defect, intentionally introduced at the metal-oxide-polymer interface or in the coating prior to the aging process.

For an undamaged coated surface, in addition to long term immersion, AC-DC-AC accelerated electrochemical degradation procedure via alternating cathodic polarization (DC) and EIS measurement at open circuit potential (AC) [33] is often used. Depending on the potential of the cathodic polarization during AC-DC-AC procedure, it can either be used to assess the polymer stability [34,35], or to study the underpaint reactivity and delamination [36]. The application of cathodic potential promotes the initiation and propagation of the metal-oxide-polymer interface degradation [37]. Under polarization lower than -1 V/SHE, both the oxygen reduction (**Eq. 1**) and the water reduction (**Eq. 2**) can occur [38] thus leading to a pH increase at the buried metal-oxide-polymer interface. Using pH sensitive indicator like phenolphthalein, these cathodic reactive areas can be evidenced by *in situ* Time Lapse Microscopy (TLM) of the sample surface [39,40].

$$\mathbf{O_2 + 2\,H_2O + 2\,e^- \rightarrow H_2O_2 + 2\,OH^-} \qquad \textbf{(3.1.a)}$$

$$\mathbf{H_2O_2 + 2\,e^- \rightarrow 2\,OH^-} \qquad \textbf{(3.1.b)}$$

$$\mathbf{2\,H_2O + 2\,e^- \rightarrow H_2 + 2\,OH^-} \qquad \textbf{(3.2)}$$

In the case of large cathodic over-potentials, high local pH, peroxides and free radicals can also damage the polymer matrix; the polarization conditions should then be chosen carefully for each system and should take into account the chemistry of the organic coating.

Epoxy resins are among the most used primers for Zn alloys because of their hydrophobicity and their ability to incorporate fillers and pigments for corrosion inhibition, anti-fouling, self-healing, etc. [41]. Due to the high impedance of thick commercial epoxy coatings and the presence of numerous additives, *in situ* study of the underpaint reactivity in such a system by means of electrochemical tests, vibrational spectroscopy and/or optical microscopy is often difficult and the results interpretation can be controversial. In order to understand the underpaint reactivity, the use of a model polymer seems to be a promising approach [42]. In the literature, several weakly adherent coatings, like polyvinyl butyral (PVB) or polyvinyl alcohol (PVA), were used in SKP studies of underpaint reactivity [43,44]. However, they do not sustain long term immersion because of their high solubility in water and weak adhesion to metallic substrates [45]. For stability evaluations in long immersion and aggressive aging tests, some groups performed experiment using thick epoxy polymers [29,46]. Nonetheless, the measurements were either made in atmospheric conditions or required to introduce a well localized artificial defect in the coating or at the interface prior to the degradation procedures. The latter can influence the degradation mechanisms and is not appropriate if the initial degradation is of interest.

Electrochemical impedance studies demonstrated that polymer also degrades in electrochemical tests (see for instance [47,48]); however, to our knowledge, a combined approach, taking into account the possible evolution of all the components of metal-oxide-polymer interfaces is still missing. It seems hence to be timely to develop an experimental approach able to consider the initiation and propagation of the underpaint reactivity and dissociate the intrinsic interface response from the possible polymer evolution under electrochemical testing of buried metal-oxide-polymer interface. The later requires the development of a model thin epoxy coating with a good adhesion to metal interfaces and characterized stability [49],[50]. The model polymer should be homogeneous in terms of chemical composition and

thickness, thin enough for *in situ* electrochemical impedance measurements, transparent in the visible light for an optical survey of the substrate/polymer interface and be stable to sustain AC-DC-AC procedure.

In this work, a new methodological approach is proposed for *in situ* accelerated mechanistic study of the underpaint stability of zinc alloy/epoxy interfaces in immersion condition without introducing an initial defect in the coated system. The methodology includes a specific aging procedure to accelerate the interface degradation and the use of an optimized model epoxy polymer, meeting the requirements listed above. The validation is made for a zinc alloy with Cr(III) conversion coatings designed for epoxy painting.

2. Materials and methods

2.1. Materials

2.1.1. Substrates preparation

Two substrate materials were used: hot dip galvanized zinc and zinc alloy coated steel.

Zn coated (hot dip galvanized, 0.2 wt. % of Al in the coating) plates of low carbon steel were used to test the developed epoxy coatings, because the behavior of this material is well known and the response of the epoxy can be easily distinguished from the response of Zn substrate. Prior to the application of organic coating, the Zn samples were rinsed with Milli-Q water and degreased in 1 M NaOH solution for 30 s to remove the oxide layer and then rinsed with Milli-Q water and absolute ethanol before being dried with compressed air.

Zinc-nickel alloy coating was used as the substrate for the conversion coating study. The alloy was prepared by a following procedure. Steel plates of 10×15 cm² were degreased and grit-blasted . Electrodeposition of Zn alloy was performed in alkaline 12-16 % ZnNi bath for 45 minutes at applied current of 3 A/dm². After electrodeposition, the samples were rinsed with deionized water for 10 min and dipped in trivalent chromium passivation bath, then rinsed for 3 min in deionized water and dried with compressed air. Relief-baking of the samples was performed at around 200 °C for 23 h to alleviate hydrogen embrittlement. X-ray fluorescence (XRF) measurement was performed by Fisherscope X-Ray XDAL and showed 18 ± 2 µm in thickness and 14 ± 2 % in nickel composition. X-ray diffraction (XRD) measurement was performed by Empyrean Panalytical and showed only the presence of the gamma phase ($Zn_{11}Ni_2$). The Cr(III) content at the top surface was found to be between 5 and 9 at. % from the XPS measurement.

In order to reduce adhesion of polymer coating to the substrate, conversion coating was modified for some samples. For this, the samples of Zn alloy with conversion coating were immersed in 0.1 M NaOH for 5 s then rinsed with milli-Q water and dried with compressed air before application of polymer coating. Zn alloy samples with modified conversion coating are referred as “samples of type 1” while the Zn samples with non-modified conversion coating are referred as “sample of type 2” below. XPS characterization of the surface could not evidence a chemical composition difference between the two types of coating within a 2% accuracy, which is consistent with the accuracy of the XPS measurement on rough surfaces.

For the model epoxy coating and degradation tests, 5×5 cm² samples were cut from the central part of each 15×10 cm² plate to prevent the edge effects that can be observed in electrodeposition process. Prior to the polymer coating, the samples were stored in a desiccator.

2.1.2. Epoxy coating

The model epoxy formulation was a DiGlycidyl Ether of Bisphenol-A prepolymer and TriEthylene TetrAmine hardener (DGEBA-TETA) used in (1:1) ratio. For viscosity requirements, the preparation was diluted in 3 mL of ethanol (analytical grade) for 4 g of mixture. Prior to spin-coating procedure, the

preparation was placed in a hermetic beaker and mixed at 300 rpm for 20 minutes then left to stand for 15 minutes in order to remove air bubbles.

Just before the coating application, the surface of the substrate was rinsed with absolute ethanol to improve the surface's wettability. The polymer coating was deposited by spin coating process using a POLOS SP15 spin-coater. Once the sample was placed and held in the spin-coater, the resin was poured in large excess and spread on the whole surface, the spin coating was performed twice with a 15 s relaxation time in between with following parameters: 3000 RPM rotary speed and 500 RPM/s linear acceleration for 35 s. After spin-coating, the samples were cured at 50 ± 5 °C for 14-16 h for curing and desolvatation [51].

With this procedure, the obtained coating's thickness controlled by optical microscopy (see section 2.2.2. for details of optical measurement) was *ca.* 10 ± 1 µm.

The samples were stored in a desiccator between the coating application and the degradation test. Degradation tests were made in the following week.

The chemical bonds formed after curing for stoichiometric formulation were reported in literature [52] and are schematically presented in **Fig. 3.1** [*53*]**.**

For the tests eight 5×5 cm² samples of each type (type 1 and type 2 described in section 2.1) were coated with model epoxy polymer and tested with the adapted AC-DC-AC procedure as detailed hereafter (see section 2.3.2). For comparison, additional four samples (size 10×15 cm² , two of each type) were also coated with a 60 µm thick layer of a commercial epoxy primer paint. The last four samples were used in 1000 h immersion test and AC-DC-AC degradation tests. These panels are named hereafter as "industrial epoxy coating".

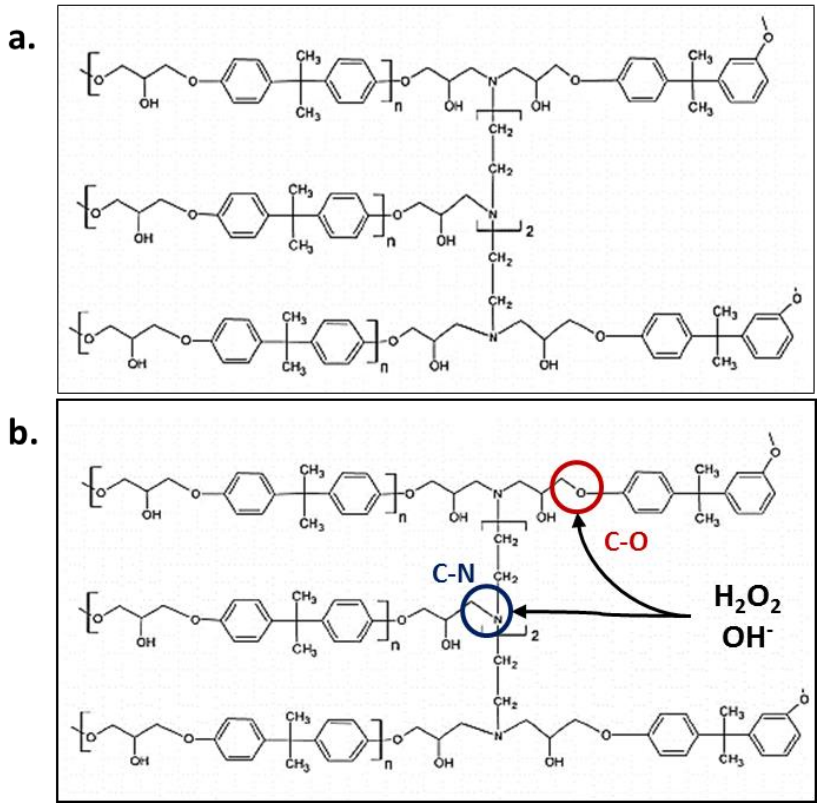

*Figure 3.1: Schematic representation of (**a**) chemical bonding in cured DGEBA-TETA epoxy resin (adapted from Bernassau et al. [53]) and (**b**) epoxy degradation induced by interfacial pH increase*

2.2. Polymer characterization

The evolution of the hydrophobic properties of the polymer were followed by static drop contact angle measurements using a Dataphysics OCA 15EC Package 2 contact angle automatic system with SCA 20 software module using a drop of 25 µL Quartex water deposited from 1 cm height. Each measurement was repeated 3 times with 3 drops and 3 different locations on each sample.

The chemical evolution of the polymer matrix was studied by Attenuated Total Reflectance Infrared Spectroscopy (ATR-IR) with Bruker Tensor 27 equipped with a Pyke MIRacle™ single reflection ATR. Each IR spectrum was recorded from 4000 to 400 cm^{-1} with a resolution of 2 cm^{-1} and integrated over 512 cycles, at least two spectra were measured for each sample at two different locations. Before every ATR measurement, the crystal was cleaned with absolute ethanol and a background measurement was performed for the cleaned crystal. Before the measurement, a spectrum of a reference coated sample stored in a desiccator was recorded. Thus, the reproducibility of the measurement could be verified so that normalization of the IR spectra of degraded samples was unnecessary. This protocol was proposed since during degradation of the polymer coating no constant peak could be defined in the ATR-IR spectra. The peaks positions of the characteristic functional groups in DGEBA-TETA epoxy resin followed in this study [54,55] are presented in ***Table* 3.*1***.

Optical characterization of the samples was performed using a Keyence VHX-5000 3D microscope. Due to its short depth of focus (< 1 µm), it was possible to measure the thickness of the model epoxy by focusing alternatively on the non-coated substrate and on the top of the transparent coating using the reflection of the confocal light source. It was also used to observe the presence of corrosion products under the coating, as well as the deformation of the top surface of the coating in 3D-composition mode.

Table 3.1: Attribution of ATR-IR peak positions to characteristic groups of DGEBA-TETA epoxy resin

Peaks attribution	Wavelength / nm	Legend
OH-stretching ($\nu_1 + \nu_3$) characteristic of "total" water with hydrogen bonds	3400 (large)	1
ν C(sp^3)-H - alkanes	2924 - 2853.5	5
OH-bending (ν_2) characteristic of "free" OH in water	1644	6
δ-NH	1608.5	2
δ-NH (secondary amine)	1509	2
δ-C(sp^3)-H (alkanes in plain)	1460.5	5
CO in epoxides	1247	3
Trimethydol propane triglycidether cyclic ether	1182.5	
CO in aliphatic ethers	1108.5	4

2.3. Degradation procedures

Three different degradation procedures were used. One sample was also kept in a desiccator after curing to obtain the evolution of a reference coating.

1. A humid chamber was used to first verify the stability of the model epoxy. Two samples were kept above 90 % relative humidity at room temperature. For contact angle and ATR-IR measurements, every hour they were taken out, rinsed with Milli-Q water and dried with compressed air before placed back in the humid chamber.

2. An immersion was used to verify immersion stability of the model epoxy. Four samples were immersed in 25 mL solution of 0.01 M NaCl with 1 wt. % of phenolphthalein in a sealed glass cell of 4.4 cm in diameter at room temperature. According to the literature, the influence of the phenolphthalein on the cathodic reactivity of polymer/zinc alloy interface can be neglected [32]. To perform *ex situ* measurements during immersion, samples were rinsed with milli-Q water and dried with compressed air before measurements and placed back to the immersion solution in less than 5 min. Immersion electrolyte was kept in a beaker during *ex situ* characterization and poured into the electrochemical cell to continue immersion test.

3. An AC-DC-AC test was applied to study the metal-oxide-polymer interface stability. For this test an electrochemical cathodic polarization cycling was performed on 5 coated samples. The samples were immersed for 1 hour in 25 mL of 0.01 M NaCl with 1 wt. % of phenolphthalein at room temperature to reach a stable value of open circuit potential (OCP). After the first EIS measurement, AC-DC-AC cycling was performed as presented in **Fig. 3.2**. It consists of 15 minutes of cathodic polarization at -1.5 V/Ag/AgCl followed by 15 min immersion at OCP and a remaining period of 30 min for different measurements at the OCP. The procedure lasted 7 cycles for a total duration of 8.5 hours. After the cycling and before *ex situ* characterizations the sample was rinsed with milli-Q water and dried with compressed air.

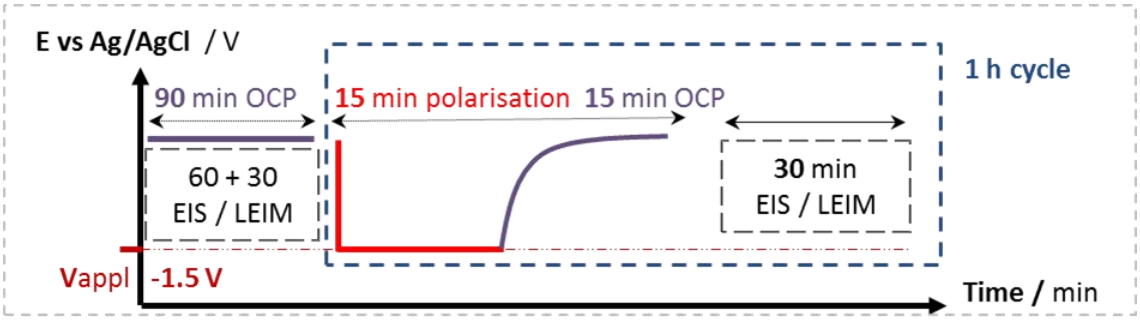

Figure 3.2: Schematic description of the AC-DC-AC procedure cycle used in the study

2.4. Electrochemical characterization and Time Lapse Microscopy

Electrochemical impedance spectroscopy (EIS) was performed using a Solartron Modulab potentiostat with ECS software interface. The three-electrode electrochemical cell consisted of a silver/silver-chloride (Ag/AgCl) reference electrode (RE), a 6.6 mm in diameter graphite rod as counter electrode (CE) and the coated sample as working electrode (WE). The cell was placed in a Faraday cage to avoid external

interferences. EIS spectra were carried out at the OCP from 100 kHz to 0.1 Hz with 6 points per frequency decade and 10 mV_{RMS} sinewave signal. Evolution of the low frequency (0.1 Hz) impedance modulus was used for tracking the stability of the metal-oxide-polymer interface.

Separately, local electrochemical impedance mapping (LEIM) was performed on three additional samples under AC-DC-AC tests. The electrochemical setup is described in detail in [30]. The local probe consisted of two Ag wires of 150 µm in diameter sealed in twin-capillaries using 3M glue. The distance between the two wires was 400 µm. The capillaries were bended so that the Ag electrodes were perpendicular to the surface of the sample, and thus, only the normal contribution of the current density was monitored. AgCl was deposited on both Ag electrodes of the probe prior to LEIS experiment by 5 min potentiostatic oxidation at 0.4 V/Ag/AgCl in 0.5 M NaCl solution. OCP and EIS measurements of the Ag/AgCl surfaces of the probe were performed during its immersion in 0.01 M NaCl solution at different times between 5 min and 10 h after the preparation of the probe to verify its stability. A home-made setup using Solartron Modulab software with auxiliary input and a 3-axis stepper motor-controlled by Sensolytics was used for LEIM measurement. The working electrode was a 2 cm diameter sample's surface. The counter electrode was a 3 cm diameter toroid of platinum wire placed above the surface of working electrode to guarantee symmetrical distribution of the current lines. During the measurement, the probe to sample distance was fixed at 100 ± 25 µm. For electrochemical impedance mapping, the potential oscillation was set to 15 mV_{RMS} and 100 Hz; the X-Y maps consisted of a square grid of 31×31 points distant of 100 µm to cover a 3×3 mm^2 area, the mapping was performed in 18 min.

In situ time lapse microscopy (TLM) using an HD USB microscope with 2 MP CMOS detector and a 4000 K white LED enlightenment was set up in the electrochemical cells for both AC-DC-AC and local electrochemistry tests. The objective to surface distance was set to 4 cm for a magnification of ×80, leading to a 100 μm^2 pixel size. A picture was taken every minute during immersion. Local underpaint cathodic reactivity was detected from the color change of phenolphthalein, turning from colorless to pink color in the pH range of 8.2 - 10. The increase of pH due to cathodic OH^- release (reactions 1-2) is relevant for both, immersion and cathodic polarization. Percolation of the polymer and opening of pores could also be observed by TLM during immersion test. During cathodic polarization in the AC-DC-AC test, the localized hydrogen evolution can be monitored.

3. Results

3.1. Stability of the epoxy coating on Zn substrate during immersion

Fig. 3.3.a shows typical ATR-IR spectra of the epoxy coated samples at different times of immersion. The peaks attribution is shown in **Table 3.1**. The peaks referred as 6 and 1 correspond to characteristic peaks of OH^- groups for scissors and stretching vibrations. The scissors vibration at 1644 cm^{-1} is related to the water molecule and is referred as "free OH" while the stretching vibration at 3400 cm^{-1} is related to all the OH groups and is referred as "total OH" [56,57]. The evolution of the peak's intensities averaged for the four immersed samples and the standard deviation are presented in **Fig. 3.3.c**. Both intensities increase and follow the same exponential trend (**Eq. (3.3)**) for the first 65 h. This trend is consistent with the water uptake of the coating, which seems to reach the saturation level from 20 to 25 hours of immersion: both peaks intensities associated with OH become stable. After 65 to 77 h of immersion, the intensities of these peaks change suddenly: the peak 1 corresponding to the "total OH" increases, whereas the peak 6 associated with the "free OH" decreases. This change in intensity is attributed to chemical evolution within the epoxy polymer coating occurring at around 70 h of immersion in a 0.01 M NaCl solution. The change in peak intensity can be described by equation:

$$A = A_1 \times e^{-b \times t} \quad \textbf{(3.3)}$$

where A is the peak intensity, A_1 is the pre-exponential factor, t is the immersion time and b is the exponential time constant obtained from the fitting. The value b = 0.16 ± 0.01 s^{-1} was the same for both "free OH" and "total OH" peaks evolution.

Fig. 3.3.d shows the average evolution of the intensities of the peaks attributed to the typical organic bonds in DGEBA-TETA epoxy coating 2, 3, 4 and 5 in **Table 3.1** for the four samples during immersion. For clarity, standard deviation of the measurement is not shown in the figure; however, the tendency was similar for all four samples. Their intensities are stable for the first 60 hours of immersion; therefore, it can be considered that only water uptake occurred during this period. After 60 hours, all the peaks' intensities attributed to the typical organic bonds in epoxy matrix (see **Table 3.1**) decrease strongly. This intensity drop coincides with the change in behavior of the two peaks corresponding to OH positions. These trends confirm that the model DGEBA-TETA epoxy coating starts to degrade after around 70 hours of immersion in a 0.01 M NaCl solution at room temperature.

In addition to ATR-IR spectra, the evolution of the contact angle is shown in **Fig. 3.4.a**. The contact angle of the reference sample stored in humid air was also measured for comparison. Under both conditions, immersion and humid air, the contact angle drops from 75° to around 70° during the first hour that evidences a first decrease in hydrophobicity. This can be attributed to the hydration of the top surface of the epoxy coating. Until the 70th hour, the contact angle remains stable (70° for all samples). After 70 hours of immersion, the contact angle decreases down to 60° and the values become more scattered depending on the analyzed areas. The increase in hydrophilicity of the coating corroborates with ATR-IR results: a first phase of water accumulation within the firsts hours, a saturation of water and stability domain of the system up to 50 hours and after 60-70 hours, the beginning of model epoxy matrix degradation.

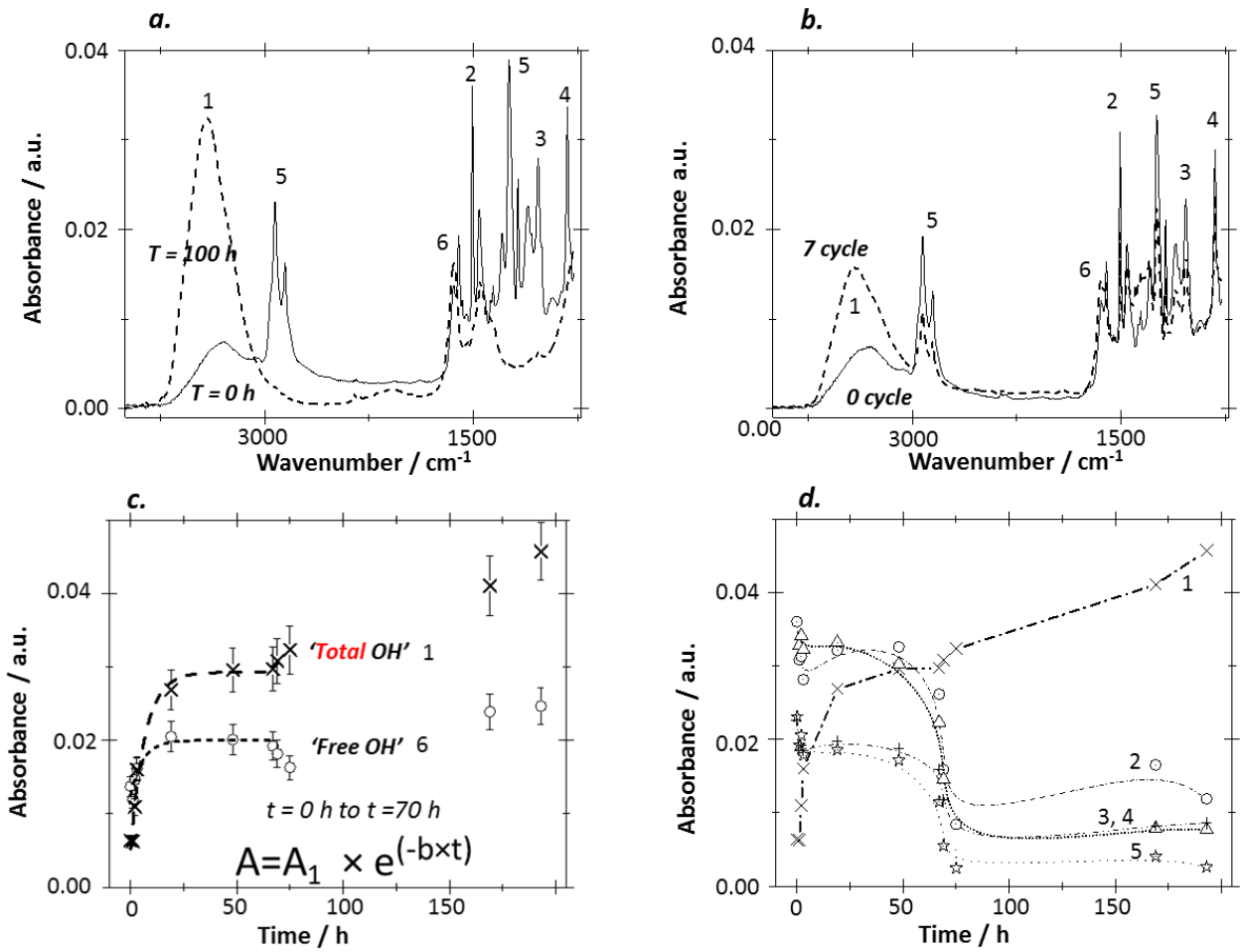

*Figure 3.3: ATR-IR spectra (**a, b**) and evolution of peaks intensities with time (**c, d**) of the epoxy polymer over Zn HDG in the low wavelength region. (**a**) after 100 h of immersion and (b) after 7 AC-DC-AC cycles compared with the initial spectra of as coated epoxy polymer as indicated; (**c**) average evolution of the OH peaks intensities corresponding to "free -OH" and "total -OH" as a function of immersion time (see text for definition) and (**d**) average evolution of epoxy characteristic peaks (Table 1) intensities as a function of immersion time. Dashed line in (**c**) corresponds to the exponential fitting with Eq. 3 of the peaks intensities (A) vs immersion time (t)*

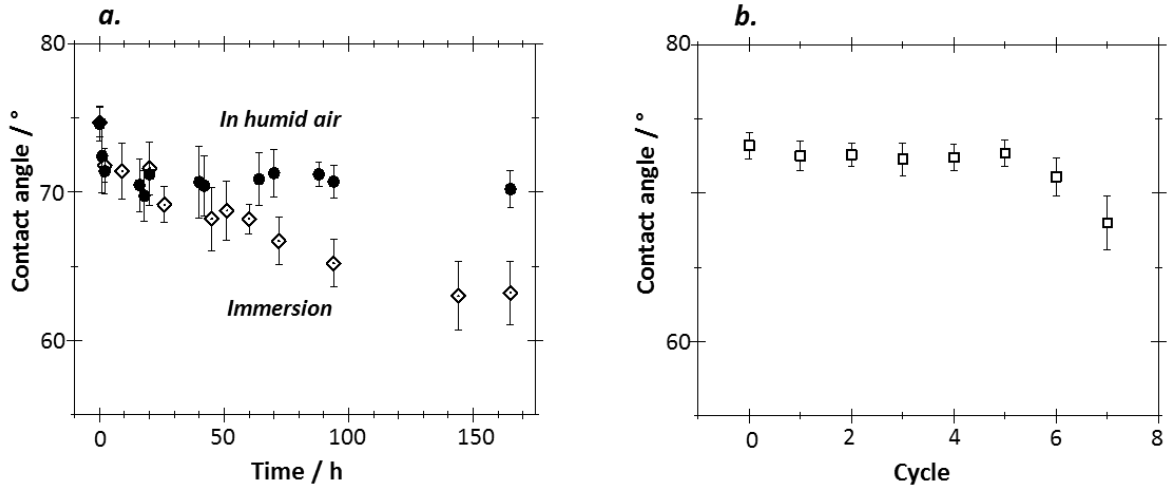

Figure 3.4: Evolution of average contact angle values on the model epoxy surface (a) in humid atmosphere (over 95%) and immersion in 10 mM NaCl water as indicated, (b) in modified AC-DC-AC ageing test

In situ optical TLM images (**Fig. 3.5.a**) show no change of the surface up to 50 hours of immersion. After around 75 hours of immersion (**Fig. 3.5.b**) localized porosity is visible in the coating, formation of corrosion products can also be detected around some open pores. A sudden formation of corrosion products with the opening pores could indicate the onset of Zn dissolution under the coating prior to the coating degradation and the decrease in the cross linking. This initial underpaint reactivity can be possible due to porosity of the polymer coating. **Fig. 3.5.c** shows the coating analysis in 3D microscope. The image was reconstructed using a high-resolution 3D-composition over 20 optical images taken over 9 µm depth range. The coating deformation is measured to be *ca.* 8 µm protruding above the coating surface. The colors are attributed to light reflection, thus corresponding to the deformation of the coating due to the growth of corrosion products underneath the coating. It can be seen that the coating surface is significantly deformed after the immersion test, which can be attributed to the swelling of the polymer and also is coherent with the ATR IR observed water content increase.

Typical electrochemical impedance spectra of the Zn coated samples after 1 and 72 hours of immersion are presented in **Fig. 3.6.a.** The EIS spectrum after 1 h of immersion shows two separate depressed semi-circles attributed to the polymer coating in the high frequency domain (1000 - 5 Hz) and the double layer at the metallic interface in the lower frequency domain (5 - 0.1 Hz) as reported in literature[24]. After 1 h of immersion the presence of second semi-arc at low frequencies clearly shows the existence of a double layer capacitance with a value of *ca.* 1 µF cm^{-2}. It clearly indicates that the polymer coating is highly porous so that water can reach the metallic substrate during this period of immersion. Moreover, it evidences also that the metallic surface is not entirely covered by the model epoxy coating, i.e. there are some zones with pre-existing disbondment at the metal-oxide-polymer coating interface. The Nyquist plot after 72 hours of immersion shows a single depressed semi-circle attributed to the response of the delaminated metallic surface. However, the contribution from the polymer coating and the corrosion product layer cannot be completely excluded at this time. A thorough data analysis with the fitting was attempted but no simple equivalent circuit was found to fit correctly this single time constant. Various parameter combinations could give valid fitting without proper physical meaning.

The evolution of the electrochemical impedance modulus at 0.1 Hz during the immersion is presented in **Fig. 3.6.b**. The impedance value of *ca.* 30 kΩ cm^2 remains stable with an abrupt drop at 50 hours to a steady value of *ca.* 5 kΩ cm^2. The decrease of electrochemical impedance modulus can be explained as a loss of adherence and the degradation at the paint/metal interface due to the formation of pores in the coating. It should be noted that the polymer composition remains stable for 50 hours as confirmed from ATR-IR and TLM observations (*vide supra*).

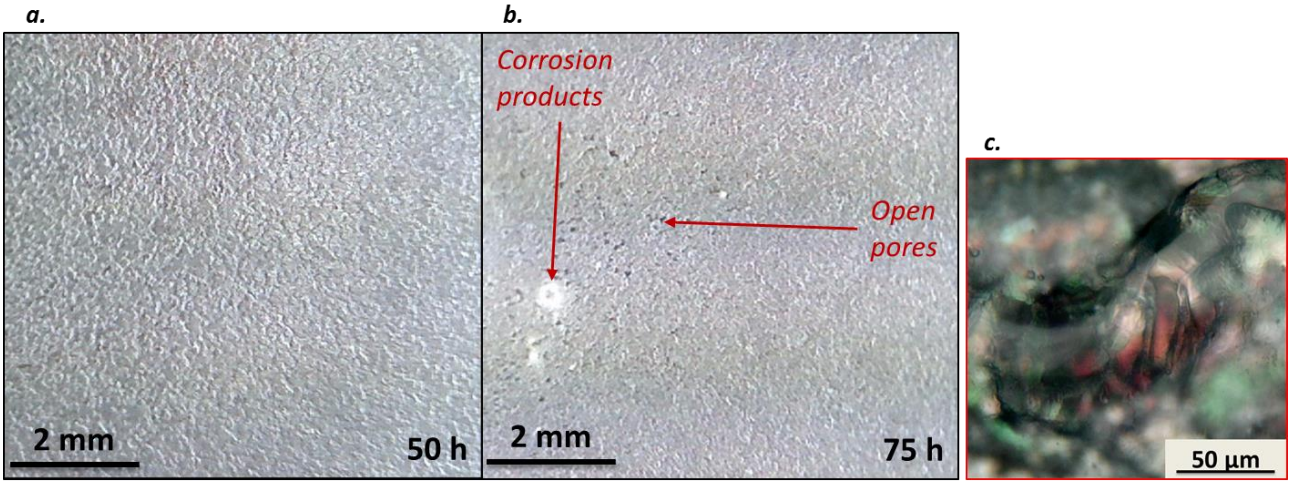

*Figure 3.5: Examples of optical images of the epoxy coating on Zn after (**a**) 50 h and (**b**) 75 h of immersion in a 10 mM NaCl electrolyte by in situ Time Lapse Microscopy. Image (**c**) represents a 3D image composition (see text for details)*

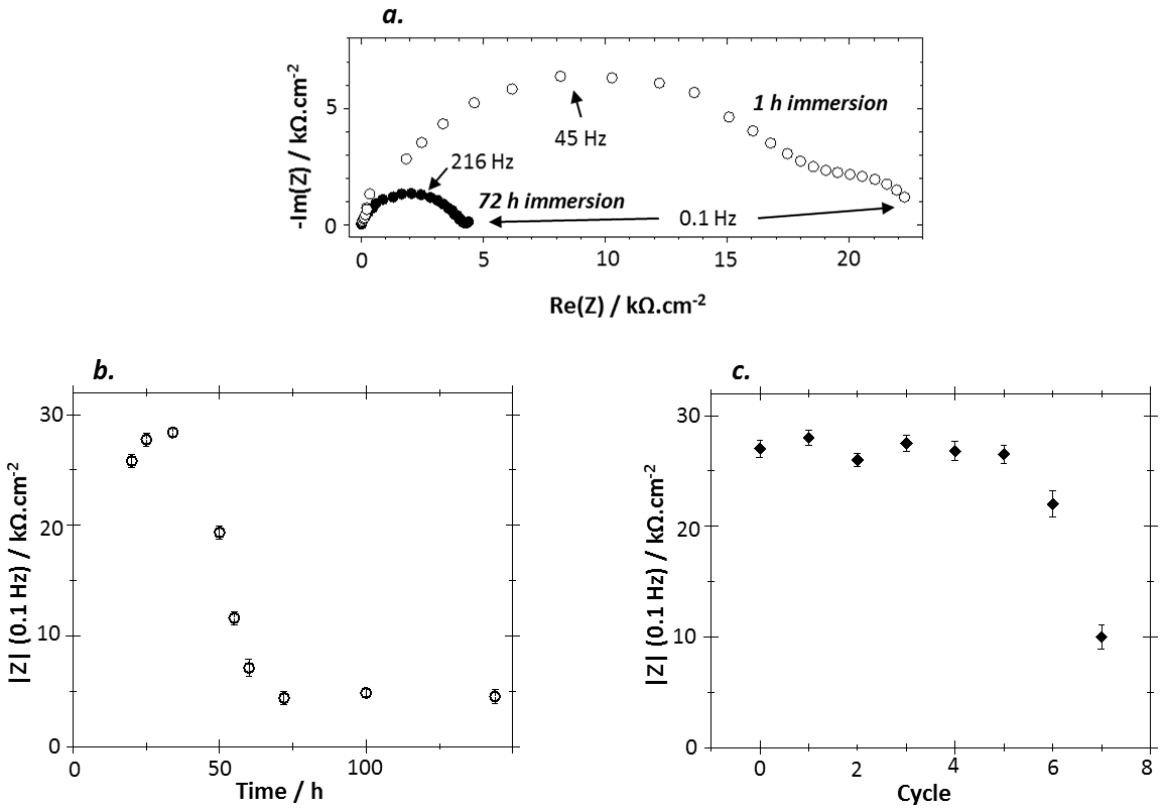

*Figure 3.6: Typical EIS spectra (**a**) and evolution of average low frequency electrochemical impedance modulus (**b, c**) of model epoxy coated Zn at different immersion times (example after 1 and 72 h of immersion time) in a 10 mM NaCl aqueous solution. (**a, b**) during immersion and (**c**) under modified AC-DC-AC degradation procedure*

3.2. Stability of the epoxy coating on Zn substrate under AC-DC-AC cycling

In order to prove the applicability of the proposed model epoxy coating for a fast-electrochemical assessment of epoxy paint/metal interface, the evolution of the model epoxy coating was surveyed during the AC-DC-AC test.

The ATR-IR spectra on **Fig. 3.3.b** show no variation in the peak intensities related to the characteristic groups of the epoxy matrix except the peak 5 corresponding to the C-H bond, while both peaks corresponding to "free OH" and "total OH", see **Table 3.1,** increase in intensity which is relevant to water uptake. In addition, the hydrophobicity measured by contact angle remains stable throughout the 6 polarization cycles, as presented in **Fig. 3.4.b**. The results are coherent with water uptake in the polymer pores without polymer degradation. As for the immersion test, electrochemical impedance at low frequency, shown in **Fig. 3.6.c**, is also stable for 4 cycles and decreases after the 5th cycle.

It can be then concluded that the proposed model epoxy coating can sustain up to 50 hours of immersion or 7 cathodic polarization cycles without degradation. In addition, with both degradation procedures, the polymer did not show any sign of degradation until the disbondment occurred at the metal-oxide-polymer interface [58].

3.3. Zn alloy/oxide/model epoxy interface evolution under modified AC-DC-AC test

The developed epoxy coating was applied on the Zn alloy with two types of conversion coating defined as described in the experimental part (section **2.1.1**: damaged and undamaged samples corresponding to sample 1 and sample 2, respectively). The modified AC-DC-AC procedure was used to compare the electrochemical stability of zinc alloy/conversion coating/polymer interfaces in these two systems.

In the first step, the behavior of two types of samples without application of the polymer was compared. After one hour of immersion in a 0.01 M NaCl solution, the OCP of both types of samples was around -0.56 V vs. Ag/AgCl. Furthermore, the samples with both types of conversion coating show a similar EIS response (**Fig. 3.7.a**). A slight difference in the roughness of the Zn alloy substrate can change the angle in the CPE used for the fitting [59], and can explain the slight differences in the shape of the Nyquist plot.

In contrast, once the samples are coated with the model epoxy coating, the electrochemical behavior of the two systems is quite different (**Fig. 3.7.b**). The steep decrease in the low frequency electrochemical impedance modulus (|Z| 0.1 Hz) from the 3rd cycle (**Fig. 3.7.c**) shows an important increase of the system reactivity in the case of the samples of type 1, while the impedance modulus value remains almost the same for the samples of type 2 during all the 7 cycles. For comparison, in the Zn samples without conversion coating (Fig. 6), the degradation of the metal-oxide-polymer interface was visible from the sharp decrease of electrochemical impedance modulus. Thus, the difference in the evolution of the EIS of Zn alloy with conversion coatings of type 1 and 2 with cycling reveals a lower adherence of the model paint to the substrate in the case of type 1 samples than in the case of type 2 samples.

The *in situ* microscopy images of both samples after 5 degradation cycles are presented in **Fig. 3.8**. The sample of type 1 (**Fig. 3.8.a**) shows a more significant cathodic hydrogen evolution (**Eq. 3.2**) than the sample of type 2 as it can be evidenced by the number of bubbles present on the surface. In addition, the spreading of pink-colored areas on the surface of type 1 sample indicates the presence of OH^- ions (**Eq. 3.1**

and **Eq. 3.2**) inside and over the coating because of the phenolphthalein indicator in the electrolyte. Although the oxygen reduction reaction can occur during the modified AC-DC-AC degradation cycling for both types of samples, no OH^- were detected by the indicator on the sample of type 2 **Fig. 3.8.b**.

Thus, *in situ* TLM confirms EIS results under modified AC-DC-AC procedure: samples of type 1 show a much weaker bonding at the metal-oxide-polymer interface than the samples of type 2. The difference in the surface properties of the sample type 1 and type 2 was not observed by EIS before epoxy coating application, however the proposed AC-DC-AC procedure applied on the epoxy coated samples in combination with EIS and TLM observations allowed easily to evidence a difference between these two types of samples.

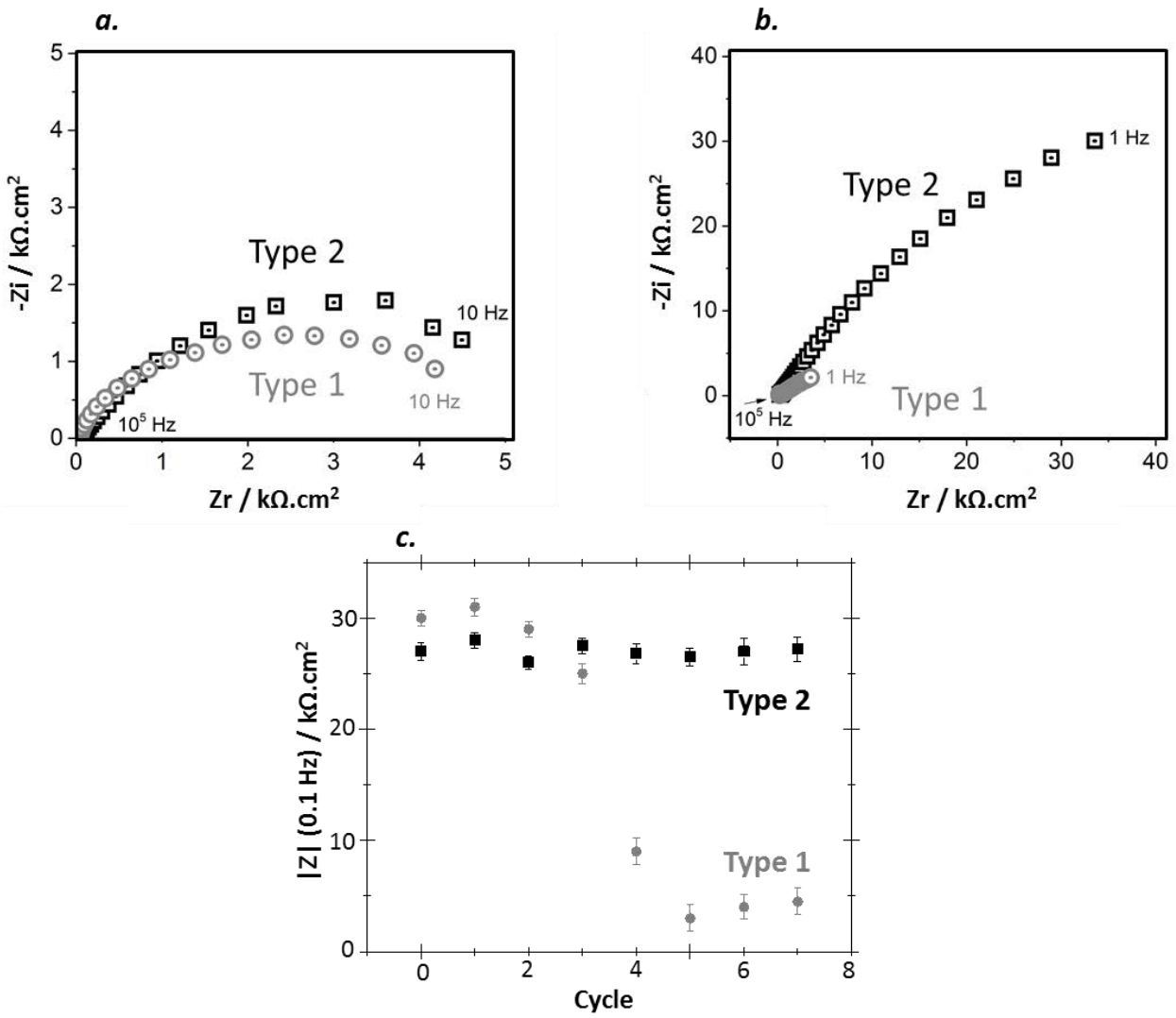

*Figure 3.7: Typical EIS responses of (**a**) uncoated and (**b**) model epoxy coated Zn alloy samples of type 1 and 2 in a 10 mM NaCl solution and (**c**) average evolution of the low frequency electrochemical impedance modulus over modified AC-DC-AC aging procedure for samples of type 1 and 2*

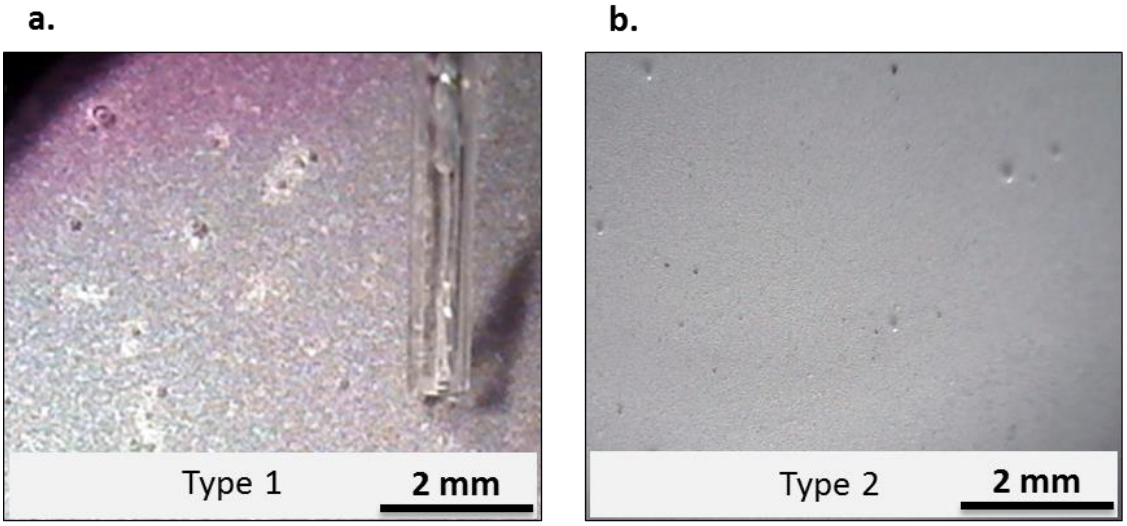

*Figure 3.8: In situ Time Lapse Microscopy observation after 5 AC-DC-AC test cycles for epoxy coated Zn alloy samples of type 1 (**a**) and type 2 (**b**)*

3.4. Spatial distribution of underpaint reactivity

Fig. 3.9.a presents an *in situ* image of a sample of type 1, coated with the developed epoxy coating. The picture was taken after the relaxation step of the 4th AC-DC-AC cycle, just before the LEIM measurement. Localized hydrogen evolution as well as slightly pink areas corresponding to oxygen reduction reaction sites are clearly visible in the figure. The black square on the TLM image represents the 3×3 mm² area scanned by LEIM at 100 Hz. TLM does not indicate a degradation of the metal-oxide-polymer interface in the scanned area until at least 3 cycles. The LEIM map of the modulus of the local electrochemical admittance, i.e. the inverse of impedance is shown in **Fig. 3.9.b**. The map shows inhomogeneous distribution of the local admittance, with an area (red) with an admittance about one order of magnitude higher compared with the other parts of the scanned surface, indicating strongly localized damage at the metal-oxide-polymer interface. The measured admittance values up to 0.52 μS cm^{-2}, meaning the current is in the mA range, ensure that the developed epoxy coating allows a proper measurement of the underpaint reactivity. For comparison, in the same testing procedure, the samples of Type 2 did not show degradation neither by TLM (**Fig. 3.8 b**) nor by LEIM (not shown).

In order to verify that the interface evolution under the model thin epoxy polymer is coherent with the degradation expected under a thick strong industrial epoxy polymer, and in order to verify if the difference between the conversion coatings of type 1 and type 2 can be detected by LEIM under such a thick layer, additional tests were made with the samples, coated by industrial paint.

The samples of type 2 with thick coatings did not evolve neither in TLM nor in LEIM during 10 AC-DE-AC cycles and are not shown in the figures. The samples of type 1 coated with the same industrial paint formed blisters during cycling. **Fig. 3.9 c** shows a typical *in situ* TLM image of a sample of type 1, coated with industrial epoxy coating after 10 AC-DC-AC cycles. Blisters are clearly visible on the surface, indicating localized degradation of the metal-oxide-polymer interface in their vicinity. The black square on the TLM image represents the 4×4 mm² area scanned by LEIM. The LEIM measured at 100 Hz is presented in **Fig.**

3.9.d. At the same time, the LEIM map shows a homogenous distribution of admittance values around 0.2 µS cm^{-2}. Although the presence of degraded area on the sample detected by TLM, the high impedance of the applied epoxy primer masks the electrochemical response from the metal-oxide-polymer interface in the case of our small local impedance probe.

Finally, several samples of type 1 and 2 with industrial coating were immersed for 1000 hours in the demineralized water. After the test the samples of type 1 were blistered while the samples of type two did not. To conclude, the LEIM experiments with model epoxy clearly distinguished two types of conversion coatings, evidenced the localized character of degradation and gave the ranking similar to the ranking obtained in immersion tests and AC-DC-AC tests of the same substrates coated by industrial coating.

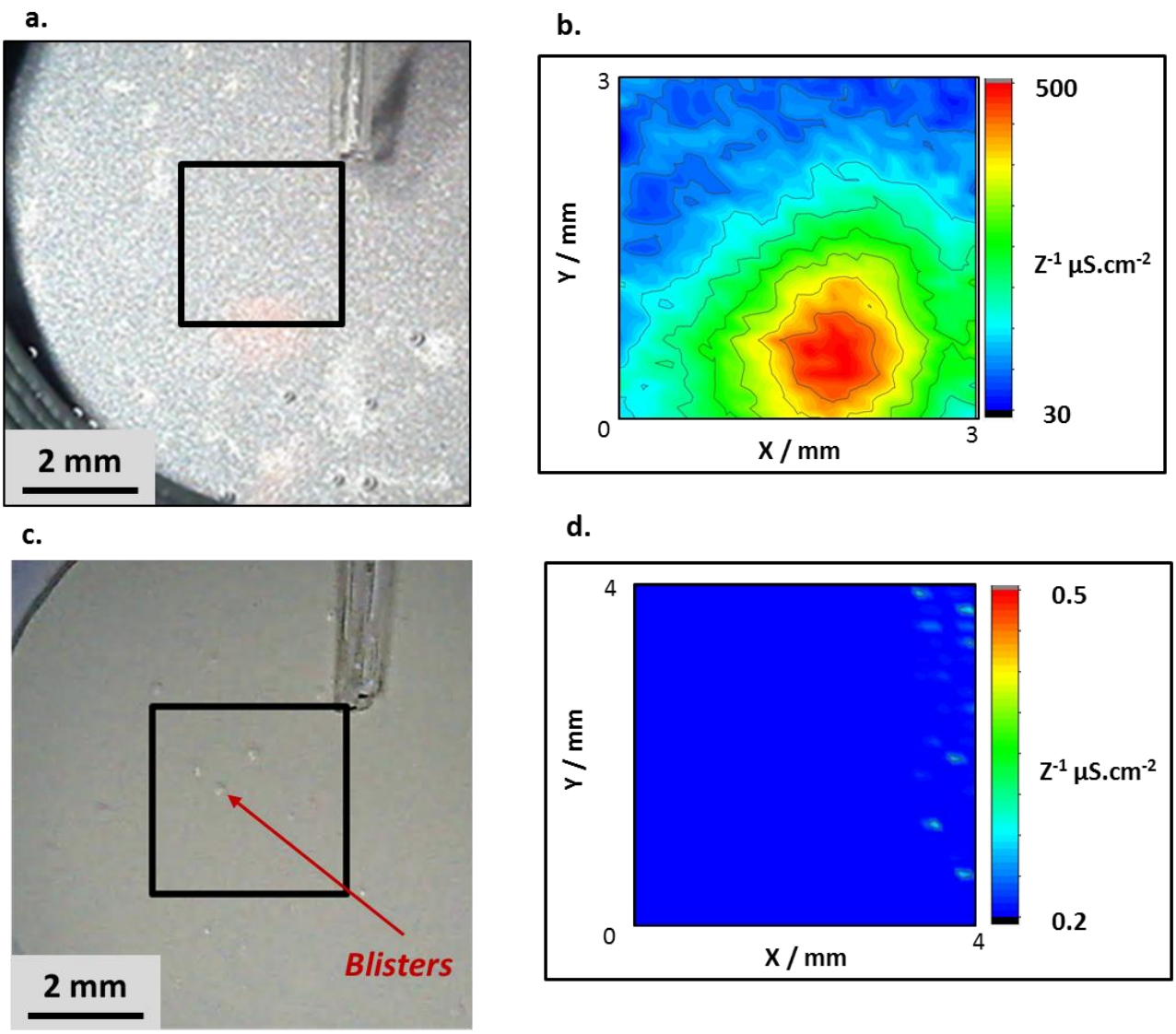

*Figure 3.9: in situ TLM (**a, c**) and LEIM maps (**b, d**) of the Zn alloy sample of type 1 covered with model epoxy after 4 AC-DC cycles (**a, b**) and with strong epoxy primer after 10 AC-DC cycle (**c, d**). The areas mapped by LEIM are delimited in TLM images by squares*

4. Discussion

4.1. Speculative degradation mechanism of model epoxy

Three steps of evolution were observed for the model zinc/epoxy interface with developed DGEBA-TETA epoxy polymer exposed 0.01M NaCl electrolyte, as demonstrated by combined EIS, ATR-IR and contact angle measurements:

- A saturation of the model epoxy coating by water reaching the metal-oxide-polymer interface during the first hours.
- A stable behavior of the polymer coating until the polymer disbondment at the metal-oxide-polymer interface at around 50 hours of immersion.
- A polymer coating degradation after 70 h of immersion.

In situ TLM demonstrated the emergence and the opening of pores, the percolation of the epoxy coating, which can be attributed to a decrease of the cross-linking of the polymer. The evolution of the ATR-IR peaks corresponding to characteristics bonds of epoxy polymer also evidences that the organic bonds were most likely broken during the polymer's degradation (**Fig. 3.1.b**). Our results also demonstrated that the degradation of both the metal-oxide-polymer interface and the epoxy coating was enhanced by the cathodic polarization cycling of the coated samples. During AC-DC-AC aging procedure, the main produced species should be OH^- and peroxides (**Eq. 3.1** and **Eq. 3.2**); indeed, hydroxides ions were detected by TLM.

The degradation mechanism of the polymer coating seems hence to be driven by the local pH increase and the production of peroxides and free radicals formed by the cathodic reactions reported in ref. [60,61]. Consequently, with a stronger metal-oxide-polymer interfacial bonding the cathodic current under polarization cycling would be reduced leading to a less significant increase of pH under the paint. Hence, the developed model epoxy coating could sustain more severe AC-DC-AC degradation test, such as lower potential or increased number of cycles.

4.2. Applicability of the modified AC-DC-AC protocol to discriminate conversion coatings

The combination of local electrochemical impedance and *in situ* Time Lapse Microscopy evidenced that the methodology using DGEBA-TETA polymer coating and modified AC-DC-AC procedure permitted to detect localized metal-oxide-polymer interface degradation. A schema of the metal-oxide-polymer interface degradation process induced by the test is presented in **Fig. 3.10**. Once water and aggressive species diffuse through the polymer and reach the metal-polymer interface, deadhesion is stronger for conversion coating of type 1 samples than for type 2 samples. More intensive cathodic reaction leads to a quicker evolution of the impedance modulus with time for type 1 samples than for type 2 samples. Finally, hydroxides and peroxides generated at the interface and diffused through the coating degrade the polymer, which arrives quicker for the type 1 sample than for type 2 sample.

The approach allowed to discriminate two conversion coatings on Zn alloys as a function of their ability to form a stable metal/epoxy polymer interface. The proposed methodology is of great interest, because the results can be obtained in approximately 24 hours (1 hour for the coating preparation, 14 hours for curing, 9 hours for the measurements), in comparison to the commonly used 1000 hours of immersion.

Thus, this methodology can be used as a fast and smart screening test of conversion coatings on Zn alloys for epoxy primers compatibility. In addition, it could give more comprehensive insights into the degradation mechanism of the metal-oxide-polymer interface such as its sensitivity to cathodic delamination. The combination of TLM and LEIM can indicate the heterogeneous or homogeneous nature of the metal-oxide-polymer disbondment with a spatial resolution of approximately 100 µm.

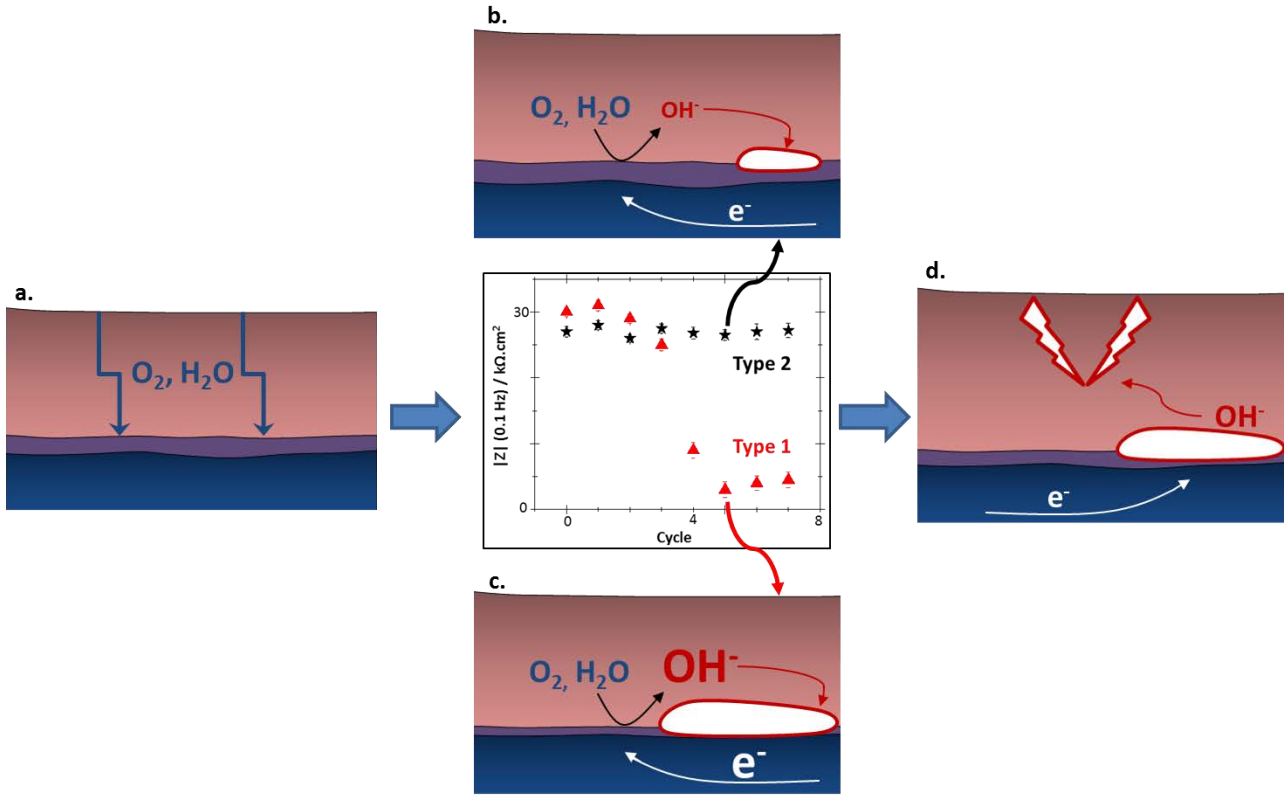

*Figure 3.10: Schematic description of the metal-polymer interface degradation in the proposed accelerated test. During immersion, water and aggressive species diffuse through the polymer and reach the metal-polymer interface (**a**). In function of weak (**b**) or strong (**c**) stability of the metal-oxide-polymer interface, the underpaint reactivity under polarization leads to different intensity of cathodic reaction and to different EIS response (Type 1 or Type 2) respectively. Finally, hydroxides and peroxides generated at the interface diffuse through the coating and degrade the polymer (**d**)*

4.3. Physical interpretation of LEIM on undamaged coated samples

Although LEIM is a common technique in the investigation of metal-oxide-polymer interface, most published studies demonstrate that pre-degraded polymer coating with either scarification and/or drilling of the coating was used to initiate the delamination process [29]. Other groups have studied blistering mechanism, i.e. a destabilization of buried metal/paint interface via LEIM without the generation of a localized defect in the coating. In most cases, the reactivity was enhanced at metal-oxide-polymer interface by using either NaCl salt powder or a drop of NaCl solution at the defined area of the metal substrate prior to the polymer coating deposition [62,63]. Thus, in these experiments a detection of the defect was foreseen. In our work, in order to initiate the metal-oxide-polymer interface reactivity, the conversion coating was slightly degraded then the samples were cleaned prior to paint application so that the loss of stability of the buried metal-oxide-polymer interface was only originating from the conversion coating quality. According to our knowledge, this approach with the unknown random distribution of surface defects before measurements, corresponding to the potentially weak interfacial bonding, was used for the first time.

On the other hand, one could contest the accurate contribution of the underpaint reactivity detected by LEIM in this work. Indeed, this technique is often used to detect defects within the organic coating itself more than at the hidden metal-oxide-polymer interface [64]. One could then wonder whether the active sites detected by LEIM were related to interfacial reactivity or to intrinsic defects in the polymer like a localized higher porosity of the model coating [65] or locally thinner polymer [66] as described in the literature. Indeed, the existence of local high porosity in the polymer coating could induce a higher diffusion of oxygen under cathodic polarization and therefore, a pH increase leading to the locally accelerated disbondment. A corollary hypothesis would be that these intrinsic defects in the polymer coating could result from the presence of a locally damaged conversion coating underneath: during the paint application and curing, the constraint relaxation within the polymer coating could lead to a segregation of intrinsic defects in the vicinity of a locally weaker metal-oxide-polymer interface. However, as described by Taylor *et al.* [65] the presence of underpaint reactivity and, therefore, the corrosion products in the pores leads to an enhancement of the barrier effect, thus, the increase of impedance modulus of the system. It was pointed out, that the deposition of zinc corrosion products occurs very shortly after the pore opening in the coating, indicating that the underpaint metal already reacts.

The question of the initiation of the local reactivity remains uncertain, both metal-oxide-polymer disbondment and intrinsic defect in the polymer could be the origin of the local reactivity, and might also be linked one to another. Still, this behavior was only evidenced on the samples of type 1, i.e. with supposedly weaker metal-oxide-polymer interface.

5. Conclusions

A new methodology using a model epoxy polymer and adapted to an AC-DC-AC accelerated degradation procedure was proposed to study and to understand stability of buried metal-oxide-polymer interface. It allowed to rank conversion coatings on zinc alloys in terms of ability to generate a stable metal-oxide-polymer interface in epoxy coated systems. The ranking result was coherent with the ranking obtained in conventional 1000 hours of immersion tests of the same substrate (metal-oxide combination) coated with a thick layer of strong industrial polymer. The proposed testing procedure lasts less than 24 h compared with a classical immersion test, making it interesting for the fast and smart ranking of the quality of conversion coatings.

In addition, the combination of *in situ* Time Lapse Microscopy and local electrochemical impedance in the accelerated test allowed to identify the heterogeneous character of interfacial disbondment on a large surface for which the possible locations from which the degradation can initiate are initially unknown and randomly distributed. This allows to obtain reliable results without preliminary introducing of an artificial defect as usually reported in the literature. The latter allows to have the true response of the sample protected by the coating without having to ask the question of the driving role that the artificial defect could have on the degradation of the coating.

1 References

[1] T. Prosek, *Mechanisms of degradation of organic coatings*, The Journal of Association of Corrosion Engineers 61 (2017), 155-161
[2] G. W. Walter, A critical review of the protection of metals by paints, Corrosion Science 26 (1986), 27-38
[3] M. F. Montermor, Functional and smart coatings for corrosion protection: A review of recent advances, Surface and Coatings Technology 258 (2014), 17-37
[4] W. Funke, Towards environmentally acceptable corrosion protection by organic coating, Anti Corrosion (1984), 4-7
[5] W. Funke, Problems and progress in organic coatings science and technology, Progress in Organic Coatings 31 (1997), 5-9
[6] W. Funke, The role of adhesion in corrosion protection by organic coatings, Journal of the oil and colour chemists' association 68 (1985), 229-232
[7] G. L. Song, Surface Engineering of light alloys (2010), 3-39
[8] A.S.H. Makhlouf, Current and advanced coating technologies for industrial applications, Nanocoatings and Ultra-Thin Films (2011), 3-23
[9] T. Biestek, J. Weber, Electrolytic and chemical conversion coatings: a concise survey of their production, properties and testing, J. Electrolytic and Chemical Conversion Coatings (1976), 200
[10] J. Zhao, R.L. McCreery, G.S. Frankel, *Effects of chromate and chromate conversion coatings on corrosion of aluminum alloy 2024-T3*, Surface and coating technologies 140 (2001), 51-57
[11] D. Gilroy, P.J. Eddowes, , F.L. Bentes, *Techniques for assessing the protective properties of chromated conversion coatings—Part II*: Galvanized steel, Metal Finishing 94 (1996), 14-22
[12] C.S. Jeffcoate, H.S. Isaacs, A.J. Aldykiewicz, M.P. Ryan, Chromate in conversion coatings: a XANES study of its concentration and mobility, JOCS 147 (2000), 540-547
[13] U.S. EPA (1998) Principles of Environmental Impact Assessment Review: Appendix A: Environmental Impact Assessment Checklist
[14] European Commission regulation report n°2017/999 - REACH, Official Journal of European Union (2017)
[15] G.D. Wilcox, J.A. Wharton, *A review of chromate-free passivation treatments for zinc and zinc alloys*, Transactions of the Institute of Metal Finishing 75 (1997), B140-B142
[16] G. Wilcox, *Replacing chromates for the passivation of zinc surfaces*, Transactions of the Institute of Metal Finishing 81 (2003)
[17] J.W. Bibber, Non-chrome-containing conversion coatings for zinc and zinc alloys: Environmentally friendly alternatives provide equal or better adhesion and corrosion resistance as conventional methods, Metal Finishing (106 (2008), 41-46
[18] R. Berger, U. Bexell, T.M. Grehk, S.E. Hörnstörm, A comparative study of the corrosion protective properties of chromium and chromium free passivation methods, Surface and Coating technologies 202 (2007), 391-397
[19] X. Zhang, C. van den Bos, W.G. Sloof, A. Hovestad, H. Terryn, J.H.W. de Wit, *Comparison of the morphology and corrosion performance of Cr(VI)- and Cr(III)-based conversion coatings on zinc*, Surface and Coating Technologies 1999 (2005), 92-104
[20] A. Nazarov, D. Thierry, Application of Scanning Kelvin Probe in the Study of Protective Paints, Frontiers in Materials 6 (2019), art. 192
[21] M. Stratman, H. Streckel, R. Feser, A new technique able to measure directly the delamination of organic polymer films, Corrosion Science 32 (1991), 467-470
[22] W. Fürbeth, M. Stratman, The delamination of polymeric coatings from electrogalvanized steel – a mechanistic approach. Part 3: delamination kinetics and influence of CO2, Corrosion Science 43 (2001), 207-227
[23] A. Amirudin, D. Thierry, Application of electrochemical impedance spectroscopy to study the degradation of polymer-coated metals, Progress in Organic Coatings 26 (1995), 1-28
[24] J.N. Murray, Electrochemical test methods for evaluating organic coatings on metals: an update. Part III: Multiple test parameter measurements, Progress in Organic Coatings 31 (1997), 375-391
[25] P.L. Bonora, F. Deflorian, L.Fedrizzi, Electrochemical impedance spectroscopy as a tool for investigating underpaint corrosion, Electrochimica Acta 41 (1996), 1073-1082

[26] K. Ogle, S. Morel, N. Meddahi, An electrochemical study of the delamination of polymer coatings on galvanized steel, Corrosion Science 47 (2005) 2034-2052
[27] F. Deflorian, S. Rossi, *An EIS study of ion diffusion through organic coatings*, Electrochimica Acta 51 (2006), 1736-1744
[28] E. Akbarinezhad, M. Bahremandi, H.R. Faridi, F. Rezaei, Another approach for ranking and evaluating organic paint coatings via electrochemical impedance spectroscopy, Corrosion Science 51 (2009), 356-363
[29] J-B. Jorcin, E. Aragon, N. Pébère, Delaminated areas beneath organic coating: A local electrochemical impedance approach, Corrosion Science 48 (2006) 1779-1790
[30] V. Shkirskiy, A. Krasnova, T. Sanchez, A. Amar, V. Vivier, P. Volovitch, *Development of anodic and cathodic blisters at a model Zn/epoxy interface studied using local electrochemical impedance*, Electrochemistry Communications 111 (2020), 106633
[31] J.J. Santana, J. González-Guzmán, J. Izquierdo, S. González, R.M. Souto, Sensing electrochemical activity in polymer-coated metals during the early stages of coating degradation by means of the scanning vibrating electrode technique, Corrosion Science 52 (2010), 3924-3931
[32] V. Shkirskiy, P. Volovitch, V. Vivier, Development of quantitative Local Electrochemical Impedance Mapping: an efficient tool for the evaluation of delamination kinetics, Electrochimica Acta 235 (2017) 442-452
[33] K.N. Allahar, G.P. Bierwagen, V.J. Gelling, *Understanding ac–dc–ac accelerated test results*, Corrosion Science 52 (2010), 1106-1114
[34] J.J. Suay, M.T. Rodríguez, R. Izquierdo, A.H. Kudama, J.J. Saura, *Rapid assessment of automotive epoxy primers by electrochemical techniques*, Journal of Coatings Technology 75 (2003), 103-111
[35] M. Bethencourt, F.J. Botana, M.J. Cano, R.M. Osuna, M.Marcos, *Lifetime prediction of waterborne acrylic paints with the AC–DC–AC method*, Progress in Organic Coatings 49 (2004), 275-281
[36] J. Hollaender, Rapid assessment of food/package interactions by electrochemical impedance spectroscopy (EIS), Food Additives and Contaminants 14 (1997), 617-626
[37] R. Montoya, F.R. García-Galván, A. Jiménez-Morales, J.C.Galván, *A cathodic delamination study of coatings with and without mechanical defects*, Corrosion Science 82 (2014), 432-436
[38] H. Leidheiser, *Cathodic delamination of polybutadiene from steel: a review*, Journal of Adhesion Science Technology 1 (1987) 79-98
[39] J. Zhang, G. S. Frankel, Corrosion-Sensing Behavior of an Acrylic-Based Coating System, CORROSION 55 (1999), 957-967
[40] F. Maia, J. Tedim, A.C. Bastos, M.G.S. Ferreira and M.L. Zheludkevich, *Active sensing coating for early detection of corrosion processes*, RSC Advances 34 (2014), 17780-17786
[41] G. Howarth, The use of water-based epoxies for anti-corrosive primers, Anti-Corrosion Methods and Materials 43 (1996), 23-28
[42] T.H.Y. Qhach, Etude de la durabilité d'un primaire epoxy anticorrosion: rôle de l'interphase polymère/métal et conséquence sur l'adhérence, PhD Manuscript (2010), Polymères. Université du Sud Toulon Var, fftel-00647580
[43] W. Fürbeth, M. Stratman, The delamination of polymeric coatings from electrogalvanized steel – a mechanistic approach. Part 1: delamination from a defect with intact zinc layer
[44] D. Iqbal, R. Singh Moirangthemy, A. Bashir, A. Erbe, Study of polymer coating delamination kinetics on zinc modified with zinc oxide of different morphologies, Materials and Corrosion 65 (2014), 370-375
[45] S.K. Mallapragada, N.A. Peppas, Dissolution mechanism of semicrystalline poly(vinyl alcohol) in water, Polymer Physics 34 (1996), 1339-1346
[46] A. Nazarov, N. Le Bozek, D. Thierry, Assessment of steel corrosion and deadhesion of epoxy barrier paint by scanning Kelvin probe, Progress in Organic Coatings 114 (2018), 123-134
[47] J.T. Zhang, J.M. Hu, J.Q. Zhang, C.N. Cao, Studies of water transport behavior and impedance models of epoxy-coated metals in NaCl solution by EIS, Progress in Organic Coatings 51 (2004), 141-151
[48] M.G. Olivier, M. Poelman, Use of Electrochemical Impedance Spectroscopy (EIS) for the evaluation of Electrocoatings performances, Recent researches in corrosion evaluation and protection Chapter 1, Intech (2012)
[49] X. Gu et al., Linking Accelerated Laboratory Test with Outdoor Performance Results for a Model Epoxy Coating System, Service Life Prediction of Polymeric Materials (2009) Springer, 3-28
[50] A.C. Rouw, Model epoxy powder coatings and their adhesion to steel, Progress in Organic Coating 34 (1988), 181-192

[51] D. Nguyen Dang, S. Cohendoz,S. Mallarino, S. Touzain, *Effects of curing program on mechanical behavior and water absorption of DGEBA/TETA epoxy network*, Journal of applied polymer science 129 (2013), 2451-2463
[52] J. R. Moraes d'Almeida, G. Wagner de Menezes, S. Neves Monteiro, *Ageing of the DGEBA/TETA Epoxy System with off-Stoichiometric Compositions*, Vol. 6, No. 3, (2003)
[53] A.L. Bernassau, D. Hutson, C.E.M. Demore, S. Cochran, *Characterization of an Epoxy Filler for Piezocomposites Compatible with Microfabrication Processes*, IEEE Transactions on Ultrasonic, Ferroelectrics, And Frequency Control 58 (2011), 2743-2748
[54] A. Charlesby, Crosslinking and degradation of polymers. Radiation Physics and Chemistry (1977) 18, 59
[55] S. Morsch, S. Lyon, S.R. Gibbon, *The degradation mechanism of an epoxy-phenolic can coating*, Progress in Organic Coatings, 6th International Conference: Advances in Corrosion Protection by Organic Coatings 102, Part A, 37–43
[56] S. Morsch, S. Lyon, P. Greensmith, S.D. Smith, S.R. Gibbon, *Water transport in an epoxy–phenolic coating*. Progress in Organic Coatings 78 (2015), 293–299
[57] P. Musto, L. Mascia, G. Ragosta, G. Scarinzi, P. Villano, The transport of water in a tetrafunctional epoxy resin by near-infrared Fourier transform spectroscopy, Polymer 41 (2000), 565–574
[58] J. Hollaender, R. Brandsch, *Application of impedance methods for corrosion protecting properties of coated substrates in metal packaging*, International Meeting on Corrosion Science and Control Technologies, IMCORR, Rio de Janeiro, Brazil (1995).
[59] D.S. Viera, P.R.G. Fernandes, H. Mukai, R.S. Zola, G.G. Lenzi, E.K. Lenzi, Surface roughness influence on CPE parameters in electrolytic cells, International Journal of Electrochemical Science 11 (2016), 7775-7784
[60] D. Gervasio, I. Song, J.H. Payer, *Determination of the oxygen reduction products on ASTM A516 steel during cathodic protection*, Journal of Applied Electrochemistry, 28 (1998), 972-989
[61] H. Leidheiser, W. Wang, Some Substrate and Environmental Influences on the Cathodic Delamination of Organic Coatings, Journal of Coatings Technologies 53 (1981), 77
[62] F. Zhou, D. Thierry, *Localized electrochemical impedance spectroscopy for studying the degradation of organic coatings*, Electrochimica Acta 42 (1997), 3293-3301
[63] G. Williams, and H.N. McMurray, *The mechanism of group (I) chloride initiated filiform corrosion on iron*, Electrochemical Communications 5 (2003), 871–877
[64] V. Upadhyay, D. Battocchi, *Localized electrochemical characterization of organic coatings: A brief review*, Progress in Organic Coatings 99 (2016), 365-377
[65] S.R. Taylor, *Incentives for using local electrochemical impedance methods in the investigation of organic coatings*, Progress in Organic Coatings 43 (2001), 141-148
[66] K. Darowicki, M.Szociński, A. Zieliński, Assessment of organic coating degradation via local impedance imaging, Electrochimica Acta 55 (2010), 3741-3748

1

Chapter 4

Conversion coating distribution on rough surface analyzed by combining surface analytical techniques

Thomas Sanchez, Sandrine Zanna, Antoine Seyeux, Melanie Vaudescal, Philippe Marcus, Polina Volovitch, Jolanta Światowska

The content of this chapter was published in Applied Surface Science

https://doi.org/10.1016/j.apsusc.2021.149734

The content of the chapter corresponds tothe publication before peer review and corrections

1

Chapter 4: Conversion coating distribution on rough surface analyzed by combining surface analytical techniques

As highlighted in Chapter 1, conversion coatings are a key parameter in metal-polymer interface stability. However, their chemical description and distribution on rough substrates is not an evident task. This chapter demonstrates the interest of the combination of Glow Discharge Optical Emission Spectroscopy and X-ray Photoelectron Spectroscopy in order to access the interfacial chemistry of nanometric oxides on rough substrates (Ra up to 5 µm; Rz up to 10 µm).

Abstract

In order to describe the chemical composition and the distribution of a thin trivalent chromium conversion coating on rough electrodeposited Zn-based alloy substrate, a new methodology was proposed, combining surface analytical techniques. A sputtering by argon in Glow Discharge Optical Emission Spectrometry (GD-OES) and by oxygen ion gun using Time-of-Flight Secondary Ion Mass Spectrometry (ToF-SIMS) were used to monitor the in depth chemical composition evolution of the conversion coating and define the metal-conversion coating interface. The surface topography was checked by high resolution 3D optical microscope. The chemical characterization of the conversion coating on the top surface and near the rough metal-oxide interface inside the craters was performed by X-Ray Photoelectron Spectroscopy (XPS).

The local depth of the sputtered craters and the local composition of the conversion layer inside and outside the craters were characterized by Auger Electron Spectroscopy (AES) nanoprobe equipped with coaxial detector to prevent from shadowing effect during measurement. The results demonstrated inhomogeneous sputtering inside the ToF-SIMS craters, which was attributed to the shadowing effect, caused by the roughness of the substrate and the 45 ° incidence angle ion gun. GD-OES sputtering appeared homogeneous in different locations inside the crater despite the roughness of the substrate, which is attributed to the perpendicular incidence angle of the sputtering.

Highlights:

- Chemical speciation of buried interface on rough substrate can be achieved
- GD-OES and ToF-SIMS sputtering were used to access interfaces for XPS analysis
- GD-OES can sputter homogenously conversion coating on rough substrate
- Auger nanoprobe is an efficient tool to verify the sputtering homogeneity
- Homogenous in-depth distribution of Cr in conversion coating

1. Introduction

Zinc alloys are known to provide good corrosion protection to ferrous-based alloys, forming a barrier layer and serving as sacrificial anodes [1]. Among different zinc alloys, Zn-Ni alloy is used for specific applications due to its good mechanical properties [2]. The Zn-Ni alloys show the highest corrosion resistance for a monophasic alloy with Ni content of 12-14 wt.% [3]. In order to enhance the corrosion resistance of the Zn-Ni alloys, thin conversion coatings (usually an oxide layer of 25-45 nm thickness) are often used to passivate the surface and/or to improve the paint adhesion [4,5]. Among them, chromate conversion coatings offer excellent corrosion protection properties related to a "self-healing" effect of Cr(VI) [6]. However, chromates were proved to be genotoxic and carcinogen [7] and, since 2006, European legislation tries to tackle hexavalent chromium via Registration, Evaluation, Authorization and Restriction of Chemicals (REACh) and Restriction of the use of certain Hazardous Substances (RoHS) [8]. According to these legislations, the application of Cr(VI) compounds will be banned in Europe. Therefore, the development and the optimization of new chromate-free conversion coating is strongly required [9,10,11]. One of the most promising candidates to replace Cr(VI) conversion coatings are Cr(III)-based conversion coatings [12].

In order to better understand the formation and the corrosion protection properties of trivalent chromium conversion coatings on zinc-nickel alloys, they were studied by electrochemical methods and atmospheric corrosion tests [13,14]. However, only few studies have been focused on a more detailed chemical characterization of trivalent chromium conversion coatings on electrodeposited rough zinc-alloy substrates [15], especially in the case of thin conversion coatings [16,17]. The challenges for the study of such a system is related not only to their complex chemistry but also to the important roughness of the substrate and the difficulties to reveal buried interfaces for chemical analysis. Such systems require the development of specific methodological approach in characterization in order to overcome the gap between the micrometric roughness of the electrodeposited Zn-based alloy and the nanometric thickness of the chromium conversion coating.

X-ray Photoelectron Spectroscopy (XPS) is widely used for nanometric oxides characterization because of its outmost ability to examine and quantify the surface's chemical composition [18]. It is often used in parallel with elemental profiling techniques for in-depth analysis of the surface chemistry such as Time-of-Flight Secondary Ion Mass Spectrometry (ToF-SIMS) [19]. More recently, Glow Discharge Optical Emission Spectrometry (GD-OES) techniques have been successfully applied in that matter [20]. Although no common strategy was defined to perform this type of characterization, it appears that the coupling between ion beam sputtering and XPS offers a better understanding of the in-depth composition of the thin oxide layers [21].

The combination of XPS and ToF-SIMS measurements was previously applied for studies of buried interfaces in the case of conversion coatings on aluminium alloy [22] and passive films on duplex stainless steel [23]. In the case of polished smooth metallic substrates with presence of thin oxide layers, the ion-depth profiles for which a gradual increase and decrease of the signals of the species characteristic of the coating/passive layer and the substrate, respectively, can be observed [24].

The ToF-SIMS can however sputter only at very limited depth and the use of low angle incidence ion beam in ToF-SIMS (45°) can show some limitations in studies of rough substrates due to topographical effects.

Recently, the combination of GD-OES and XPS analysis to obtain a detailed chemical description of the surface chemistry at different depths of a multi-layer system was proposed [25,26]. One of the advantages of the GD-OES is the high depth resolution with high etching rate [27]. The other advantage is a normal direction of the argon beam to the sample surface, which could prevent from the shadowing effect in the crater generation [28]. Nonetheless, it was previously demonstrated that near zenithal ion etching can induce a roughness increase and therefore limit the depth resolution [29,30]. This effect was indeed reported during argon plasma sputtering by GD-OES profiling [31,32]. In addition, extreme surface perturbation in the GD-OES crater were reported, especially redeposition of species on the border of the crater and high temperature leading to burns or melting processes at the surface. The plasma parameters should be carefully adjusted for each system. The principle of GD-OES sputtering relying on a Grimm-type gas flow for the injection of argon in the plasma chamber, the gas nature (argon, argon-oxygen mixture, argon-nitrogen mixture, etc. [33]), pressure and power control are the key parameters to consider in order to obtain a homogeneous sputtering in the crater [34]. GD-OES is however unable to perform accurate localized sputtering, the minimum diameter of the crater in the existing systems being 2 mm.

To verify the local chemical composition in the crater and the local residual thickness of the studied layer, Auger Electron Spectroscopy nanoprobe (Nano-AES) combined with argon beam in the analytical chamber [35] seems of interest. The great interest of AES relies on its sensitivity to the extreme surface and the possibility of the localized analysis with resolution up to several nanometers [36]. The combination of nano-AES with an argon ion beam allows to perform local in-depth chemical profiling of the surface in the model craters [37]. Nonetheless, sputtering rate by the argon ion beam might still be affected by local surface chemistry and the detection can be limited by surface topography [38,39]. The use of normal ion etching and the geometry of coaxial Cylindrical Mirror Analyzer (CMA) seems to be the best solution to improve sensitivity [36] and reduce the shadowing effects for surfaces with complex topography [40].

In this paper, in order to characterize the chemistry of the top surface of the coating and near the coating-substrate interface of a thin trivalent chromium conversion coating on rough electrodeposited Zn-based alloy; we combine GD-OES and ToF-SIMS sputtering with XPS and nano Auger characterization. The crater morphology is also verified by high resolution 3D optical microscopy. The main purpose of this study is to provide a reliable methodology, allowing to describe the chemical composition and its 3D distribution for thin oxide layers on rough substrates. The stake of our approach dwells in the comparison of different combination of profiling techniques. In addition, the novelty resides in the combination of an ion etching (using GD-OES or ToF-SIMS) and XPS analysis with a third local profiling technique (nano Auger), which enables to verify the influence of the sputtering mode (low incidence ion-etching by ToF-SIMS and on orthogonal low energy argon plasma GD-OES sputtering) on rough electrodeposited surfaces on the homogeneity of sputtering.

2. Experimental

2.1. Materials

2.1.1. Zn-Ni alloy with chromium conversion coating

The samples consisted of electrodeposited Zn-Ni alloy treated with thin trivalent chromium conversion coating. First, steel plates of 10 × 15 cm² used as substrates were degreased, grit-blasted and electrodeposition was performed in alkaline 12-16 % Zn-Ni bath for 45 minutes at 3 A/dm². After electrodeposition, samples were rinsed with deionized water for 10 minutes and dipped in trivalent chromium passivation bath then rinsed for 3 minutes in deionized water and dried with pressurized air. Relief-baking of the samples was performed at around 200 °C for 20 h to alleviate hydrogen embrittlement. X-ray fluorescence (XRF) showed that the deposited ZnNi was of 18 ± 2 µm in thickness and the composition of 14 ± 2 %at. in nickel. X-ray diffraction (XRD) showed only the presence of the gamma phase ($Zn_{21}Ni_5$).

For all the following tests, 2 × 2 cm² samples were cut from the central part of each 15 × 10 cm² plate to avoid the edge effects observed in electrodeposition process.

2.1.2. Model $Zn(OH)_2$ ALD layer

A zinc oxide thin film (with a thickness of few micrometers) reference sample for XPS analysis was prepared by atomic layer deposition (ALD) on silicon wafer with (0001) orientation. It was produced at low temperature (80 °C) following the production procedure of doped ZnO films for semi-conductors [41]. Following the ZnO deposition, the ZnO layer was hydrated during one week in a humid chamber (relative humidity 85%, temperature 20 °C) to produce the $Zn(OH)_2$.

2.2. Morphological and chemical characterizations

2.2.1. Morphological characterization

Optical characterization of the samples was performed using a Keyence VHX-5000 microscope equipped with the VH-Z500T objective allowing for magnification from 500x to 5000x. With 500x magnification, the area of view was of 610 × 457 µm² for a 2000 × 1600 px image. Stitching was performed for wider area image acquisition [42]. Thanks to its short depth of field (< 0.5 µm), multiple images with different objective-to-sample distance were taken in order to obtain a three-dimensional image of the surface [43]. It was performed by a stitching of twenty-five 3D-composition images at 500x magnification over 2.8 × 2.3 mm². Each 3D-composition was computed from 100 images over 50 microns in depth. High resolution images were obtained by 3D-composition with 2000x magnification.

In addition to the in-depth composition of images, the Keyence VHX-5000 microscope records the height of each focused pixel and therefore allow a topographic measurement of the surface. The height

cartography was converted to an 8-bit grey nuance image and the roughness parameters were calculated with the use of Gwyddion software version 2.50 [44].

2.2.2. Chemical characterization of the thin oxide layer

The methodological approach for in-depth chemical description on the conversion coating is presented in the **Fig. 4.1**. Briefly, first the initial top surface was characterized by XPS (**Fig. 4.1a**, see details in section **2.2.3**). Then, thanks to the full depth profiles preliminary made by GD-OES and ToF-SIMS, the time necessary to sputter 80 % of the initial thickness of the conversion coating was defined (see section **2.2.4**) and the craters were prepared by GD-OES and ToF-SIMS sputtering to obtain the expected conversion coating removal: 80 % of the initial thickness (**Fig. 4.1b**, see details in section **2.2.4**). Then, the general chemical surface characterization inside the crater was performed by XPS (**Fig. 4.1c**, details in section **2.2.3**) and the distribution of the remaining conversion coating inside the crater was verified by Nano-Auger (**Fig. 4.1d**, see section **2.2.5** for details).

2.2.3. XPS

XPS analysis was performed (**Fig. 4.1.a**) with a Thermo Electron Escalab 250 spectrometer, using a mono-chromated Al Kα X-ray source (*hv* = 1486.6 eV). The base pressure in the analytical chamber was maintained at 10^{-9} mbar. The spectrometer was calibrated using Au $4f_{7/2}$ at 84.1 eV. The take-off angle was 90°. A 500 µm X-ray spot size was used. Survey spectra were recorded with a pass energy of 100 eV with a step size of 1 eV and high-resolution spectra of the C 1s, O 1s, Zn 2p, Cr 2p, Ni 2p, Zn LM2 and N 1s regions were recorded with a pass energy of 20 eV and a step size of 0.1 eV. To compensate the charge effect, a 1 eV flood-gun was used on the sample and the analyzed spot was centered as close as possible to the mount contact. The data analysis was performed with the CasaXPS software version 2.3.17PR1.1 using an iterative spline-Shirley-type background subtraction. Symmetrical peaks (Gaussian 70 % – Lorentzian 30 %) were used for fitting except for the Cr 2p where a corrected fit describing Cr 2p multiplet was used as described in [45]. Charge correction of the spectra was performed with reference to C-C peak at 285 eV.

The presence of Zn Auger peaks in the Cr 2p region ($L_3M_{23}M_{45}$ (^1P) and $L_3M_{23}M_{45}$ (^3P) [46]) was considered for spectra decomposition on chromium passivated ZnNi. The analysis of model reference zinc hydroxide sample was performed to allow a quantitative decomposition of the Cr 2p region. This reference sample was the zinc oxide thin film deposited on Si substrate by ALD and aged in humid chamber to form the zinc hydroxide as described above.

2.2.4. ToF-SIMS and GD-OES

Time-of-Flight Secondary Ion Mass Spectrometry (ToF-SIMS) analysis was performed using an IonTof ToF-SIMS 5 spectrometer operating at a pressure of 10^{-9} mbar. A pulsed 25keV Bi^+ primary ion source delivering 1.2 pA of target current over a 100 × 100 µm² area was used for analysis, the considered

secondary ions were ZnO^-, Ni_2^- and CrO_2^- that are characteristic species of zinc oxides, metallic nickel and chromium oxides respectively. Depth profiles were obtained by interlacing the primary gun with a 2 keV Cs^+ sputter beam delivering 130 nA of target current over a 300 × 300 µm² area (45° incidence angle to the specimen surface). For the depth profiles, the intensity of the ionized fragments, all measured quasi-simultaneously, was plotted vs the Cs^+ ion sputtering time. The intensity in the depth profiles was reported using a logarithmic scale. Data acquisition and post processing analysis were performed using the SurfaceLab software version 6.5.

Glow-Discharge Optical Emission Spectroscopy (GD-OES) was performed with a Horiba GD-Profiler 2™ fueled by Arcal 1 argon from Air Liquide. The plasma conditions, power-chamber pressure, were optimized to obtain homogeneous sputtering with 800 Pa and 30 W argon plasma with a 4 mm in diameter anode. The intensities of the 46 wavelengths calibrated in the polychromator were recorded simultaneously during the argon plasma sputtering at a rate of one hundred points per second. Among them, the emission wavelength corresponding to carbon, oxygen, chromium, iron, nickel and zinc were considered. The intensities were normalized to the total emitted light in the plasma so that it reflected the variation of the in-depth concentrations of the considered elements and reported as a function of sputtering time. As for the analysis of ToF-SIMS ion profiles, nickel signal was used as a marker of the conversion coating to ZnNi alloy substrate interface.

In order to reveal the metal-oxide interface, sputtering of the conversion coating was performed using either GD-OES or ToF-SIMS technique (**Fig. 4.1.b** and **4.1.c**). For both techniques, prior to the generation of the crater in the conversion coating, elemental in-depth profiles were acquired in 4 different areas of the 10 x 15 cm² plate. The thickness of the conversion coating (in sputtering time) was determined as the sputtering time corresponding to the increase of Ni related signal in the profile which is a marker of the ZnNi alloy. Subsequently, the defect generation was performed on a 2 x 2 mm² sample cut from the same plate. Sputtering was stopped at 80% of the measured sputtering time corresponding to conversion coating thickness to let the ZnNi alloy underneath preserved.

For the crater generation by ToF-SIMS (**Fig. 4.1.c**), in order to avoid the effect of cesium implantation on the chemistry of the conversion coating, the oxygen (O_2^-) ion source was used at 2 keV acceleration voltage delivering 100 nA of target current over a 30 × 30 µm² area. The crater generation itself was performed without using the Bi^+ primary ion gun to limit the ion implantation in the crater. For the crater generation by GD-OES, low sputtering rate was chosen to have a better control on the crater depth. The plasma conditions were set to 650 Pa and 8 W argon plasma with a 2 mm in diameter anode.

XPS analysis was performed in the generated craters subsequently to its formation to obtain near metal-oxide chemical description (**Fig. 4.1.d**).

2.2.5. Nano Auger

Auger electron spectroscopy was performed using a PHI 700Xi Auger nanoprobe equipped with a cylindrical mirror analyzer (CMA) mounted coaxially with respect to the electron column. The pressure in the analysis chamber was maintained between 10^{-10} and 10^{-9} mbar. The electron beam was set normal to

the surface, at 10 keV accelerating energy and 10 nA current to obtain approximately 20 nm spot size. Specific zones of a few micron-square were selected for scanning and spectra acquisition in order to optimize the signal intensity to noise ratio and limit the charge effect of the surface. Spectra were acquired in direct mode with a step size of 3 eV. The C KLL, O KLL, Cr LMM, Ni LMM and Zn LMM peaks were considered. Curve fitting of the spectra was performed with the in-built PHI-Ulvac MultiPak software using a Shirley-type background subtraction. In our case, in-depth composition profiles were performed by combining Auger electron spectroscopy and normal argon ion gun sputtering thanks to eucentric rotation. The ion gun was set at 2 kV acceleration voltage and 1 µA current on a 2 x 2 mm² surface; its sputtered depth was calibrated on SiO_2 substrate prior to the measurement. The ion gun sequence was set to obtain approximately one spectrum per sputtered equivalent nanometer (eq-nm) for the first 10 nm then one spectrum per 4 eq-nm. The variation of the peak's intensities was reported in function of the equivalent sputtered depth in SiO_2 eq-nm.

AES microscopy was used as a complementary technique to GD-OES and ToF-SIMS respectively, to determine the distribution of the remaining trivalent chromium conversion coating on the ZnNi alloy in the two types of crater and compare it to the unsputtered conversion coating. To do so, local in-depth chemical profiles were performed in the conversion coating at various location of the craters. In order to observe the effect of the surface roughness on sputtering, two types of zones were distinguished, the hills, i.e. the high zones of the surface, and the valleys of the surface (**Fig. 4.1.e**).

Prior to Auger analysis, secondary electron microscopy (SEM) was used to obtain topographic contrast of the surface and localize the areas of interest. It should be noted that since the ion sputtering of the surface for local composition profiles was in the nanometer range, it had a limited impact on the surface topography. SEM image was therefore used to correct the sample shift during chemical profile acquisitions, ensuring the analysis was performed in the areas of interest.

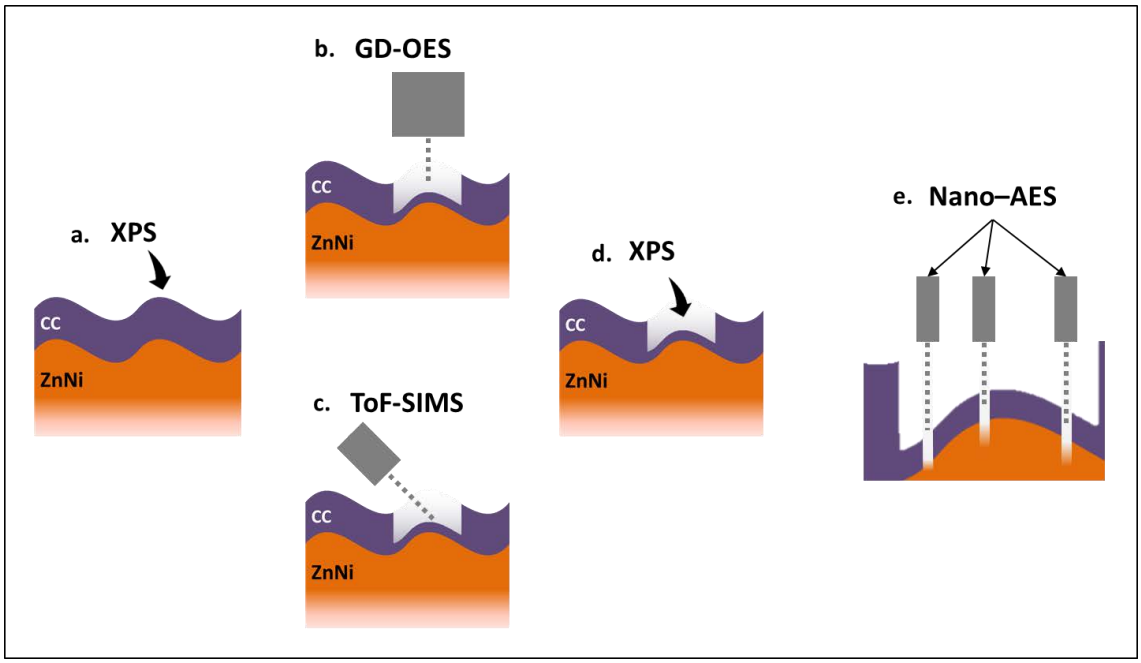

Figure 4.1: Scheme illustrating the methodological approach used to describe in-depth chemical characterization of thin coatings on rough substrates.

3. Results and discussion

3.1. Surface composition of ZnNi alloy with conversion layer

The XPS results obtained on the model $Zn(OH)_2$ thin film sample and ZnNi alloy after the conversion treatment in trivalent chromium passivation bath are presented in **Fig. 4.2**. Because of the superposition of Zn Auger (Zn $L_3M_{23}M_{45}$) peaks in the Cr 2p core level region (**Fig. 4.2.f**), the preliminary XPS characterization of the model $Zn(OH)_2$ was required. The analysis of model $Zn(OH)_2$ sample allowed the detection and the quantitative analysis of Zn Auger peaks overlaid with Cr 2p peaks. As a result, the contribution of the Zn Auger peaks were subtracted in the Cr 2p region and a quantitative analysis of Cr and Zn was obtained.

3.1.1. $Zn(OH)_2$ reference sample

The survey spectrum recorded on the reference $Zn(OH)_2$ after cleaning (not presented here) indicated only the presence of zinc and oxygen and small carbon contamination.

Fig. 4.2.a. Fig. 4.2.b and **4.2.c** show Zn 2p, Zn $L_3M_{45}M_{45}$ (LMM) and Zn $L_3M_{23}M_{45}$ Auger signals, respectively. Due to the significant spin–orbit splitting of Zn $2p_{3/2}$ and Zn $2p_{1/2}$ (ΔBE of around 23 eV), only one Zn $2p_{3/2}$ was decomposed. The fitting of the Zn $2p_{3/2}$ was done with a single symmetrical peak at 1023.1 eV (**Fig. 4.2.a**). The details of the peak decomposition are shown in **Table 4.1**. However, due to the overlapping of the zinc oxide and zinc metal contributions in the Zn $2p_{3/2}$ peak, the calculation of modified Auger parameter was necessary for the identification of Zn chemical state [47]. The modified Auger parameter (using the position of the Zn $2p_{3/2}$ and LMM peaks) was 2009.2 eV, which confirmed the presence of zinc hydroxide on the surface [47,48].

The second $ZnL_3M_{23}M_{45}$ Auger signal (**Fig. 4.2.c**) was acquired in order to get information about the peak's shapes and intensity in order to be able to subtract their contribution from the Cr 2p core level peaks occurring in the same range of binding energies (for the conversion coated samples showing the presence of Cr oxides as described hereafter). In this region, the signal shows two peaks: $L_3M_{23}M_{45}(^1P)$ and $L_3M_{23}M_{45}(^3P)$, which are labeled as Zn(II) A_1 and Zn(II) A_2, respectively (**Fig. 4.2.b**). Then, the area ratio of these peaks (A_1 and A_2) and Zn LMM peak was calculated. The obtained area ratio versus Zn LMM are 0.168 and 0.270 for Zn A_1 and Zn A_2, respectively. The relative position of the two Zn Auger peaks (Zn $L_3M_{23}M_{45}$) was measured: ΔBE(Zn A_2 – Zn A_1) = 8.6 eV as well as their position relative to the Zn LMM peak: ΔBE(Zn A_1 – Zn LMM) = 78 ±1 eV. These values will be used for quantitative chemical analysis (chromium and zinc species) for the conversion coated ZnNi alloys.

3.1.2. Surface atomic composition of the conversion coating

The survey spectrum recorded for chromium passivated ZnNi (not presented here) indicated the presence of carbon, oxygen, zinc and chromium as main components and traces of sodium, chlorine, calcium and aluminum on the surface. Nickel was not detected neither on the survey nor on the high-resolution spectrum (Ni 2p region), indicating either a very small amount or even the absence of nickel in the conversion coating.

Fig. 4.2.d, **4.2.e** and **4.2.f** show XPS high resolution spectra of Zn 2p, Zn LMM and Cr 2p together with Zn $L_3M_{23}M_{45}(^1P)$ and $L_3M_{23}M_{45}(^3P)$ peaks of chromium passivated ZnNi. Peak assignment and fitting parameters are reported in **Table 4.2**.

The Zn $2p_{3/2}$ peak was fitted with a single peak at around 1023.7 eV. The value of the modified Auger parameter of 2009.4 eV confirmed the presence of $Zn(OH)_2$ on the top surface layer [48]. Thus, it was possible to use the fitting parameters extracted from the reference $Zn(OH)_2$ sample showing also the presence of $Zn(OH)_2$ on the extreme surface as described above: the measured binding energies and the calculated Zn LMM to Zn A_1 and Zn A_2 peaks area ratio were used to identify the Zn Auger peaks in the Cr 2p region (**Fig. 4.2.f**). The position of the Cr $2p_{3/2}$ peak at 577.2 eV indicates that the chromium of the conversion coating is present as Cr(III) species [49,50]. According to quantitative analysis on the Cr 2p and Zn $2p_{3/2}$ peaks, the passivated ZnNi alloy top surface is composed of zinc hydroxides and trivalent chromium species with an atomic ratio of 1.6 zinc to 1 chromium.

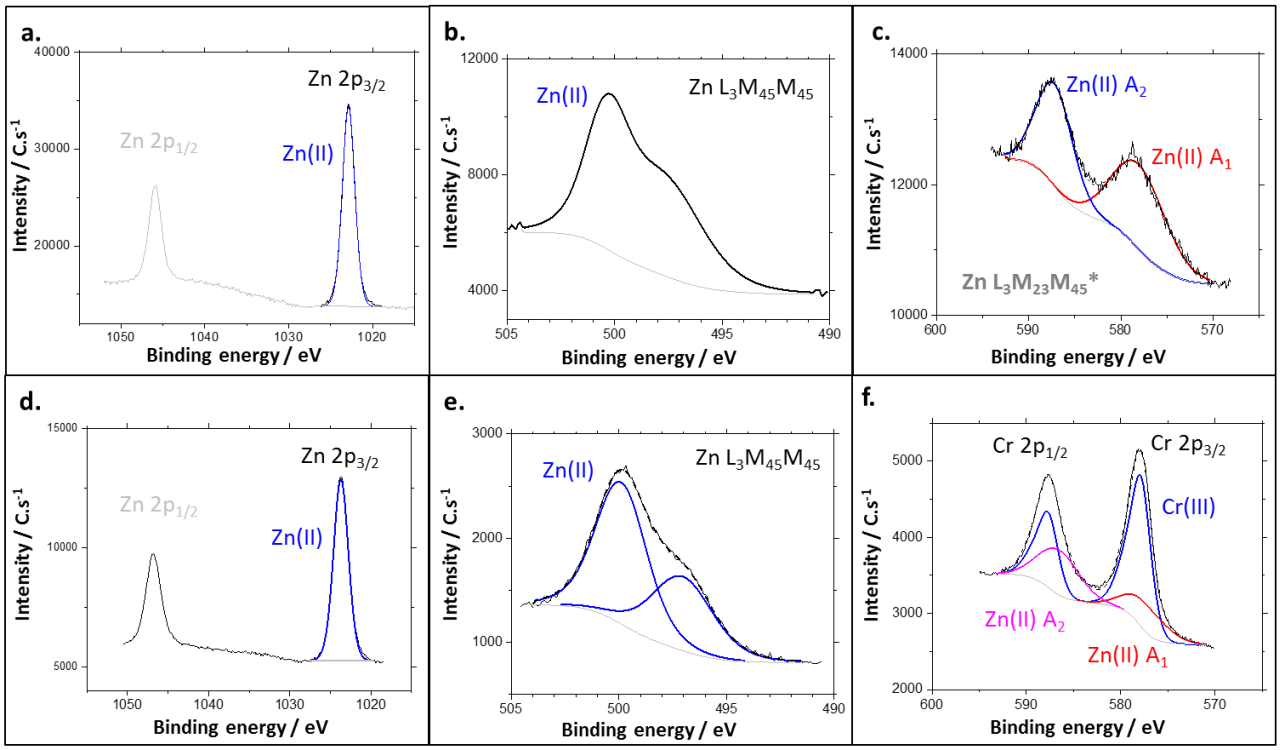

*Figure 4.2: Example of high resolution XPS spectra for: the reference Zn(OH)2 sample: (**a**) Zn 2p, (**b**) Zn LMM Auger, (**c**) Cr 2p region with Zn Auger peaks ; and for Cr(III) passivated ZnNi sample: (**d**) Zn 2p, (**e**) Zn LMM Auger, (**f**) Cr 2p region with Zn Auger peaks.*

Table 4.1: Peak assignment and fitting parameters used for the decomposition of XPS core level spectra of model $Zn(OH)_2$ reference sample presented in Fig. 4.1. a, b and c.

Peak	Peak BE (eV)	Area ($C.s^{-1}.eV$)	FWHM (eV)
A : Zn LMM	500.5	74751	ø
B : Zn(II) A2	586.9	20252	3.37
C : Zn(II) A1	578.3	12531	3.37
D : Zn $2p_{3/2}$	1023.1	19143	1.95

Table 4.2: Peak assignment and fitting parameters used for the decomposition of XPS core level spectra of trivalent conversion coating on ZnNi substrate sample presented in Fig. 4.1. d, e and f.

Peak	Peak BE (eV)	Area ($C.s^{-1}.eV$)	FWHM (eV)
A : Zn LMM	500.9	2833	ø
B : Cr $2p_{3/2}$	577.2	6358	3.00 Fixed
C : Cr $2p_{1/2}$	587.1 B + 9.8 (±0.2)	718 B * 0.5	3.00 B * 1
D : Zn(II) A_1	584.3 A + 77.8 (±0.2)	476 A * 0.168	3.4 Fixed
E : Zn(II) A_2	592.9 D + 8.6 (±0.2)	768 A * 0.270	3.4 Fixed
F : Zn $2p_{3/2}$	1023.7	17907	1.95

3.1.3. Chemical composition of the conversion coating by ToF-SIMS and GD-OES depth profiles

To detect the composition in bulk of the conversion coating and at the conversion coating / ZnNi alloy interface, depth profiling was performed by means of ToF-SIMS and GD-OES techniques. In these profiles, the variation of the ion or element intensity with sputtering time reflects the variation of the in-depth concentration of the species as shown in **Fig. 4.3**. As in XPS, in GD-OES and ToF-SIMS profiles nickel doesn't appear in the beginning of sputtering in the conversion coating. Therefore, the metal-oxide interface zone was defined from the increase of the intensity of the Ni signal. ToF-SIMS ion depth profiles performed on

the sample with trivalent chromium conversion coating are presented in **Fig. 4.3.a**. The ions characteristic of the coated sample CrO_2^- (83.9285 u), ZnO^- (79.9252 u) and Ni_2^- (57.2516 u) correspond to the oxidized chromium typical for chromium-based conversion coatings [51], zinc oxide and nickel as the ZnNi substrate species, respectively. The intensity of the ions varies as a function of sputtering time. The intensity is presented in the logarithmic scale to enhance the low intensity signals. Three regions can be distinguished here as a function of sputtering depth:

- the conversion coating region (up to about 50s s of sputtering) with the high and stable intensity of CrO_2^-, ZnO^- signals, and no Ni signal,
- the metal-oxide interface region (from 50 s to about 130 s) with CrO_2^- decrease and ZnO^- and Ni_2^- intensity increase,
- the substrate region (from about ~130 ± 15 s) with a stable intensity of ZnO^- and Ni_2^- signals.

The presence of chromium and zinc oxidized species in the conversion coating layer is coherent with the XPS result presented above. The gradual decrease or increase of ion signals at the metal-oxide interface is attributed to the significant surface roughness of the electrodeposited ZnNi [24]. The surface roughness will be also discussed hereafter.

The in-depth homogeneity of the conversion coating can be estimated from the ratio of the ZnO^- to CrO_2^- shown in **Fig. 4.3.b**. The ZnO^- to CrO_2^- ratio of about 0.6 is stable within the sputtering time corresponding to the conversion coating (from 10 to 40 s), whereas on the top surface (up to 10 s of sputtering), it reaches 1.5. This indicates that the conversion coating has a homogeneous in-depth chemical composition with a segregation of zinc species on the extreme surface. The lower intensity of CrO_2^- on the top surface can be also related to surface enrichment in the hydroxides and contaminants.

The same conversion coated sample was also characterized by GD-OES. The GD-OES elemental depth profiles of carbon, oxygen, chromium, zinc, nickel and iron were performed at high sputtering rate as presented in **Fig. 4.3.c**. Similarly, to ToF-SIMS ion depth profiles, few regions can be distinguished in GD-OES elemental depth profiles. The first three regions are the same as the regions observed by ToF-SIMS ion depth profiles, and the last (the steel substrate) region was not attained by ToF-SIMS much lower sputtering yield. The GD-OES four regions, which can be distinguished in **Fig. 4.3.c** are:

- the conversion coating region (from 0.3 to 1.3 s) with high and stable intensity of chromium, zinc and oxygen signals, where no nickel is detected,
- the metal-oxide interface region (from 1.3 s to about 5 s) with Cr and O intensity decrease and Zn and Ni intensity increase,
- the ZnNi region (from 5 s to about 100 s) with a stable intensity of Zn and Ni signals,
- the steel substrate region (from about 100 s) where the Fe and Cr signal intensities increase.

As for the ion depth profiles obtained by ToF-SIMS, the gradual decrease and increase of the chromium and nickel intensities, respectively, at the metal-oxide interface region are the result of the rough ZnNi surface. The roughness in the interfacial region can be also enhanced during the sample immersion in the conversion bath. In the first tenth of second of sputtering, in the top surface region, the intensity of the zinc signal is higher than deeper in the conversion coating, indicating a segregation of Zn-containing species on the extreme surface of the conversion coating. The conversion coating enrichment in Zn species was also demonstrated by the higher ToF-SIMS ZnO^-/CrO_2^- ratio in the beginning of sputtering time (Fig.

3.b). According to the intensity of the carbon signal in the first tenth seconds of sputtering, the presence of a surface contamination is also confirmed.

To easier observe the chemical distribution of the thin conversion coating on ZnNi substrate, the low energy Ar plasma sputtering (as described in the experimental part) was also applied and the elemental profiles are shown in **Fig. 4.3.d**. the application of low energy Ar plasma sputtering was also necessary in order to obtain well resolved elemental profiles and better define the time of sputtering to reach the conversion coating/ZnNi interface. The analysis was necessary for further preparation of a crater defect, which will be discussed below.

To sum-up, ToF-SIMS and GD-OES analysis confirmed that the surface of passivated ZnNi alloy is mainly composed of zinc hydroxides segregated on the top surface and Cr(III) oxide species. Nickel was not detected in the conversion coating. It was also demonstrated that some C-like contaminants are essentially present at the extreme surface of the conversion coating. GD-OES showed also that these C-like contaminations can penetrate inside the conversion coating, which can be explained by the coating porosity and presence of some cracks leading to the contamination during exposure to the ambient air [16].

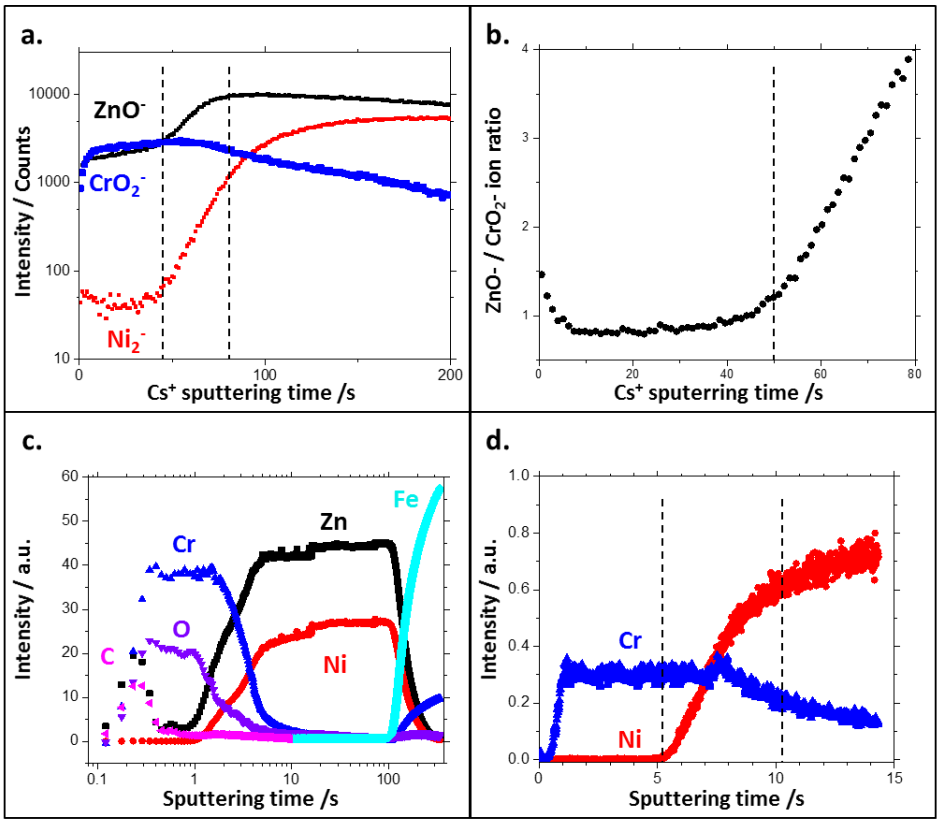

*Figure 4.3: **(a)** ToF-SIMS secondary ion depth profiles (ZnO^- CrO^- and Ni_2^-) on passivated ZnNi surface, **(b)** Average ToF-SIMS ZnO^- to $CrO2^-$ ion ratio profile. And GD-OES elemental depth profiles (Cr, Zn, O, Ni, C, Fe) on passivated ZnNi alloy: **(c)** high energy argon plasma, **(d)** low power argon plasma*

3.2. Chemical characterization of the interface conversion coating / substrate alloy

3.2.1. Crater generation

As aforementioned, the chromium and nickel elemental in-depth profiles performed with low sputtering rate (using specific plasma conditions of GD-OES 650 Pa, 8 W) presented in **Fig. 4.3.d** were used to precisely define the sputtered depth. In these sputtering conditions, the conversion coating is sputtered in about 5 s (**Fig. 4.3.d**). Thus, considering the time of sputtering necessary to reach a near-interface region, the crater in the conversion coating was performed at 80% of the depth of the interface: 4 s of sputtering. A schematic representation of this model defect and the observation by optical microscope of the surface in the vicinity of the defect are presented in **Fig. 4.4.a.** and **Fig. 4.4.c**. The sputtered zone of about 2 mm in diameter, consistent with the use of 2 mm-diameter anode, is easily distinguished in the optical microscopy image where the sputtered region shows a grey color while the undamaged conversion coating shows a brown gold color. The slightly darker area on the border of circle-shape sputtered area is attributed to a redeposition of eroded species in the argon plasma.

Similar approach was used in the case of the ToF-SIMS craters generation. The time necessary to reach the near-interface region was evaluated based on the ion depths profiles (Ni_2^- and CrO_2^-). The conversion coating layer was sputtered up to 80% of the interfacial depth. 49 defects (a square grid of 7 × 7 defects with size and space between each as presented in Fig. 4.b) constituting a grid-pattern defect of about 800×800 µm², were performed in the conversion coating. The image of this grid-pattern defect is shown in **Fig. 4.4.d**. As for the 2 mm in diameter defect generated by GD-OES, the sputtered areas are easy to distinguish from the undamaged areas because of the different color. No darker area attributed to the re-deposition of species could be found. Although each of the 49 defects can be detected on the optical microscopy image, their size and shape are not consistent with a grid of 30 µm size squares spaced by 100 µm distance between the centers of the squares. The difference is attributed to the sprawl of the focused oxygen beam of the ToF-SIMS and/or the rough surface on which the sputtering was performed. According to the observation, the obtained dispersion of defects is more consistent with a grid of defects with ~70 µm in diameter spaced by ~60 µm.

3.2.2. Surface morphology and distribution of the conversion coating in the sputtered areas

A topographic analysis in the defects prepared by GD-OES and ToF-SIMS sputtering was performed. The roughness of the electrodeposited ZnNi alloy in both types of defect as well as far away from the defects were evaluated from these topographic mappings. No significant differences were observed between the values of the arithmetical mean deviation roughness R_a (~5 µm) between the three types of surfaces. These results were predictable since the roughness of the ZnNi is in the range of the tenth of micrometers while the thickness of the sputtered conversion coating is of three orders of magnitude below, *i.e*. in the tenth of nanometer range.

In addition to topographic images, high magnification optical images were obtained by 3D-composition of multiple images obtained with different depths as described in section 2. The **Fig. 4.4.e.** and **4.4.f.** present a comparison of sputtered (left) and non-sputtered (right) areas for both samples. Apart from the difference in the surface color of these two types of areas, the surface topography appears unchanged after the sputtering. The micro-roughness and the cauliflower-shape remain typical of electrodeposited ZnNi (which is caused by a competition between nucleation and grain growth) [52].

In the defect generated by GD-OES (**Fig. 4.4.e.** on the left), the color of the surface is homogeneous and grey, while the color of the unsputtered surface is goldish (**Fig. 4.4.e.** on the right). On the contrary, in the defect generated by ToF-SIMS (**Fig. 4.4.f.** on the top left), the surface's color is more heterogeneous. The hills (i.e. the highest zones of the surface) show the same grey color than in the GD-OES crater; however, around the valleys (*i.e.* the deepest areas), the surface exhibits a goldish color. The presence of this "conversion coating color-like" in the defect could indicate that some undamaged or lowly sputtered conversion coating remained in the valleys of the surface after ToF-SIMS sputtering. This could be explained by the surface micrometric roughness influence on the low incidence angle ion gun in the case of ToF-SIMS (shadowing effect). The GD-OES generated defects does not seem to be influenced as much by sputtering, probably because the acceleration of the argon plasma is normal to the surface.

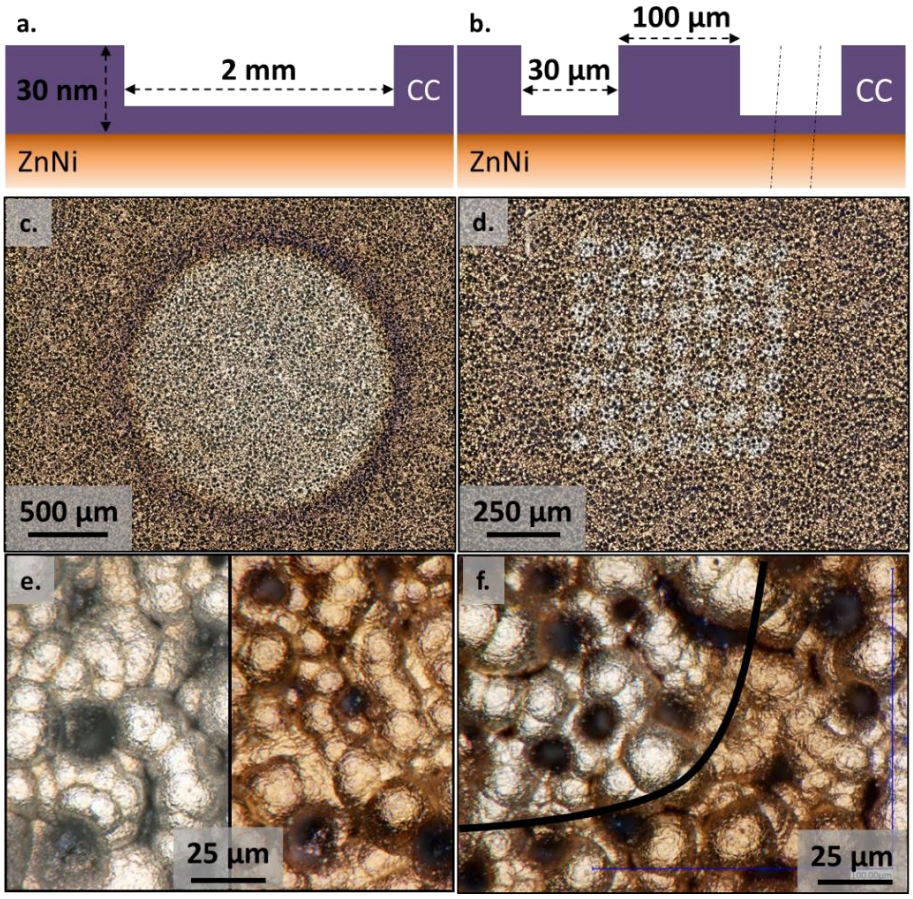

*Figure 4.4: Schematic representation of the generated model defect: **(a)** 2mm anode with GD-OES, **(b)** 30 µm oxygen ion source with ToF-SIMS; and optical micrographs of the defects by Keyence high resolution 3D microscope: **(c)** 2 mm crater produced by GD-OES, **(d)** Grid of 49 defects produced by ToF-SIMS. High magnification optical microscopy comparison of sputtered and unsputtered regions **(e)** of GD-OES 2 mm defect, **(f)** of ToF-SIMS defect*

3.2.3. Chemical composition near the conversion coating/substrate interface

In addition to the morphological study and the analysis of the distribution of the conversion coating in the sputtered area, the chemical composition of the remaining conversion coating after ToF-SIMS and GD-OES sputtering was analyzed by XPS.

GD-OES crater

Fig. 4.5.a, **4.5.b**, **4.5.c** show XPS high resolution spectra of Zn 2p, Zn LMM and Cr 2p together with Zn $L_3M_{23}M_{45}(^1P)$ and $L_3M_{23}M_{45}(^3P)$ peaks in the 2 mm in diameter model defect generated by GD-OES.

The Zn $2p_{3/2}$ peak (**Fig. 4.5.a**) was fitted with two symmetrical peaks at 1023.4 eV and 1021.6 eV, which can be attributed to the Zn(II) in the conversion coating and the metallic Zn, respectively. The Zn LMM peak (**Fig. 4.5.b**) was fitted according to the fitting performed on the undamaged conversion coating presented above (**Fig. 4.2.e**). It shows a third peak at lower binding energy of 494.9 eV, which can be attributed to Zn metal. The presence of metallic Zn corresponding to the ZnNi alloy substrate indicates that the thickness of the remaining conversion coating after sputtering is less than ten nanometers [53].

The modified Auger parameters for the two zinc species were calculated for the high and low energy Zn 2p (BE=1023.4 eV and BE=1021.6 eV) peaks to Zn LMM (BE=500.6 eV and BE=495.9 eV). The two Auger parameters equal 2009.5 eV and 2013.4 eV, respectively. According to the literature, the value of 2009.5 indicates the presence of zinc hydroxides, although this value is slightly higher compared to the $Zn(OH)_2$ reference (2009.2 eV) and might show the presence of hydrozincite [48]. The formation of hydrozincite on the top surface of the sample could be explained by the formation of carbonate contamination of the zinc hydroxide on the surface. The value of 2013.4 eV confirms the presence of metallic zinc [48].

Assuming that the possible presence of hydrozincite does not influence significantly the position of the zinc Auger peaks, the parameters extracted from the reference $Zn(OH)_2$ sample showing also the presence of $Zn(OH)_2$ on the extreme surface were used to subtract the zinc Auger contribution in the Cr 2p region as described above (**Fig. 4.2.f**). Here (**Fig. 4.5.c**), two contributions attributed to the zinc hydroxide (Zn (II) A1 and Zn(II) A2 peaks) and two contributions attributed to the metallic zinc (Zn(m) A1 and Zn(m) A2) were considered. As for the contribution of zinc hydroxide, the same methodology was used for the calculation of BE position and the areas of the two zinc metallic contributions, using the Zn LMM peak related to the metallic contribution (BE = 494.9 eV). The decomposition of the spectra is presented in **Fig. 4.5.c**.

The other peaks in the area of Cr $2p_{3/2}$ region are the asymmetrical peak at 577.3 eV, attributed to Cr(III) species as described above (**Fig. 2.c**) and a higher binding energy peak at 580.5 eV (+3.2 eV), attributed to the traces of Cr(VI) species which could be formed occasionally at the interface in Cr(III) based conversion coating [46]. The quantitative analysis of the Cr 2p (considering all Cr species) and Zn $2p_{3/2}$ peak corresponding to the oxidized zinc species shows that the composition of the remaining conversion layer is similar to the top surface where zinc hydroxides to Cr-species atomic ratio is about of 1.8. These results are in agreement with the ToF-SIMS ion profiles showing a stable intensity of Zn and Cr-corresponding signals all over the conversion layer thickness as discussed above (**Fig. 4.3.a.** and **4.3.b.**).

ToF-SIMS crater

Similar XPS analysis was performed on the sample with the ToF-SIMS defect**. Fig. 4.5.d***,* **4.5.e***,* **4.5.f.** show high resolution XPS spectra of Zn 2p, Zn LMM and Cr 2p together with Zn $L_3M_{23}M_{45}(^1P)$ and $L_3M_{23}M_{45}(^3P)$ peaks in the area of craters generated by ToF-SIMS.

Since the XPS spectra were performed in identical conditions in both GD-OES and ToF-SIMS sputtered area, the signal to noise ratio in the case of the ToF-SIMS defect is expected to be lower because of the heterogeneity of the surface chemistry. Indeed, the analyzed area consists of both sputtered and non-sputtered areas. The presented results confirm this hypothesis. However, the fitting parameters used for the XPS obtained in the GD-OES-made defect were applied for the decomposition of XPS spectra obtained in the ToF-SIMS defects.

The Zn $2p_{3/2}$ peak (**Fig. 4.5.d.**) is similar to Zn $2p_{3/2}$ peak obtained for the GD-OES-made defect (**Fig. 4.5.a.**) and two peaks at 1023.7 eV and 1021.8 eV attributed to the Zn(II) in the conversion coating and the metallic Zn(0) respectively, can be observed. The presence of metallic Zn can be confirmed by the Zn LMM Auger signal (**Fig. 4.5.e.**) where a lower binding energy peak (at 495.0 eV) corresponding to the metallic Zn is observed. The Zn LMM shows the same characteristic peaks as described here above for GD-OES-made defect. The values of the modified Auger parameters: 2009.4 eV for the high Zn 2p binding energy peak and 2013.4 eV for the low energy Zn 2p are consistent with the presence of zinc hydroxides or hydrozincite in the conversion coating and metallic zinc underneath.

In the case of the decomposition of the XPS in the Cr 2p core level (**Fig. 4.5.f**), the methodology described previously was used. The peak at 577.5 eV was attributed to the presence of Cr(III) species and here the presence of Cr(VI) species was not evidenced. Similar to GD-OES generated crater, the ratio between zinc hydroxides and Cr-species is about of 1.8 in the remaining layer, very close to the composition of the top surface.

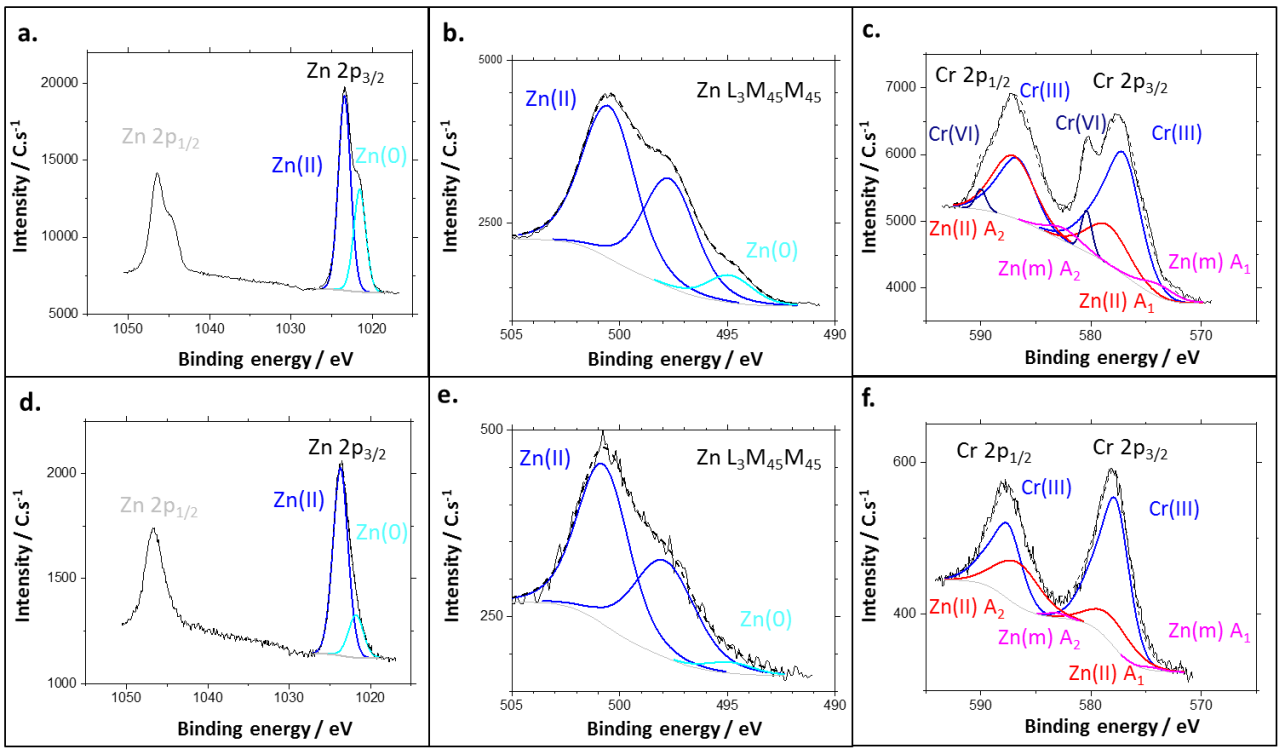

*Figure 4.5: Examples of high resolution XPS spectra in the middle of the GD-OES crater: **(a)** Zn 2p, **(b)** Zn LMM Auger, **(c)** Cr 2p region with Zn Auger peaks ; and in the middle of the grid of 49 defects produced by ToF-SIMS: **(d)** Zn 2p, **(e)** Zn LMM Auger, **(f)** Cr 2p region with Zn Auger peaks.*

3.2.4. Local chemistry distribution in sputtered area from Nano Auger

Scanning electron microscopy (SEM) images of the samples prepared by both, GD-OES (**Fig. 4.6.a**) and ToF-SIMS (**Fig. 4.7.b**) sputtering, clearly show the sputtered zones. Lighter sputtered and darker non-sputtered areas related to the different chemical contrast between the heavier (metallic ZnNi substrate) and lighter elements (carbon and oxygen present in the conversion coating), respectively.

Fig. 4.6.a. shows the SEM images of the crater obtained by GD-OES. The observation is in accordance with the optical microscopy of the sample (**Fig. 4.4.c**), the crater measures approximatively 1.8 mm in diameter. Three different areas are detailed: one near the center of the crater, one close to the border of the crater, and one outside the crater to serve as a reference. The high-resolution SEM image of the area in the center of the crater is presented in **Fig. 4.6.b.** As already observed by the optical microscopy image (**Fig. 4.4.e**) the SEM reveals also the same roughness and the cauliflower-type topography. On this figure, three “valley”-type, and three hill-type features of the surface are highlighted by black and white circles, respectively. The same types of zones (hills and valleys) were identified on the three different areas (in the center, on the border and outside the crater). Local Auger depth profiles were performed on these twelve (6 valleys and 6 hills) specific areas.

Fig. 4.6.c. shows the Auger depth nickel and chromium profiles performed outside the sputtered crater. Only the first 16 eq. nm are presented to show the depth of the conversion coating in details. The results agree with the GD-OES and ToF-SIMS profiles, showing a layer containing chromium and depleted in nickel deposited on a nickel containing substrate. The metal-oxide interface, *i.e.* the beginning of the Ni signal increase, is placed at 7 eq. nm in depth.

Fig. 4.6.d. and **4.6.e.** show the local Auger depth profiles on the valley type and the hill type areas respectively. On both profiles, it can be noticed that the thickness of the remaining conversion coating is much thinner than outside the crater (**Fig. 4.6.c**). However, the composition in nickel is around 0 at. % on the extreme surface (at 0 eq. nm in depth). In agreement with the depth profiles presented above (**Fig. 4.3**), it can be concluded that the ZnNi alloy was not reached by the sputtering of the crater. These results confirm the hypothesis used for XPS analysis performed in the crater and fits the schematic description of the surface (**Fig. 4.4.a**).

Moreover, on both profiles corresponding to the valleys (**Fig. 4.6.d**) and the hills (**Fig. 4.6.e**) of the surface, the thickness of the remaining conversion coating is the same, about 1 eq. nm. This indicates that the sputtering by low energy argon plasma with the GD-OES technique is homogeneous on the surface and does not suffers from the roughness of the sample. This result is in accordance with the optical microscopy observation showing a homogeneous color of the sputtered crater by GD-OES (**Fig. 4.4.e** on the left).

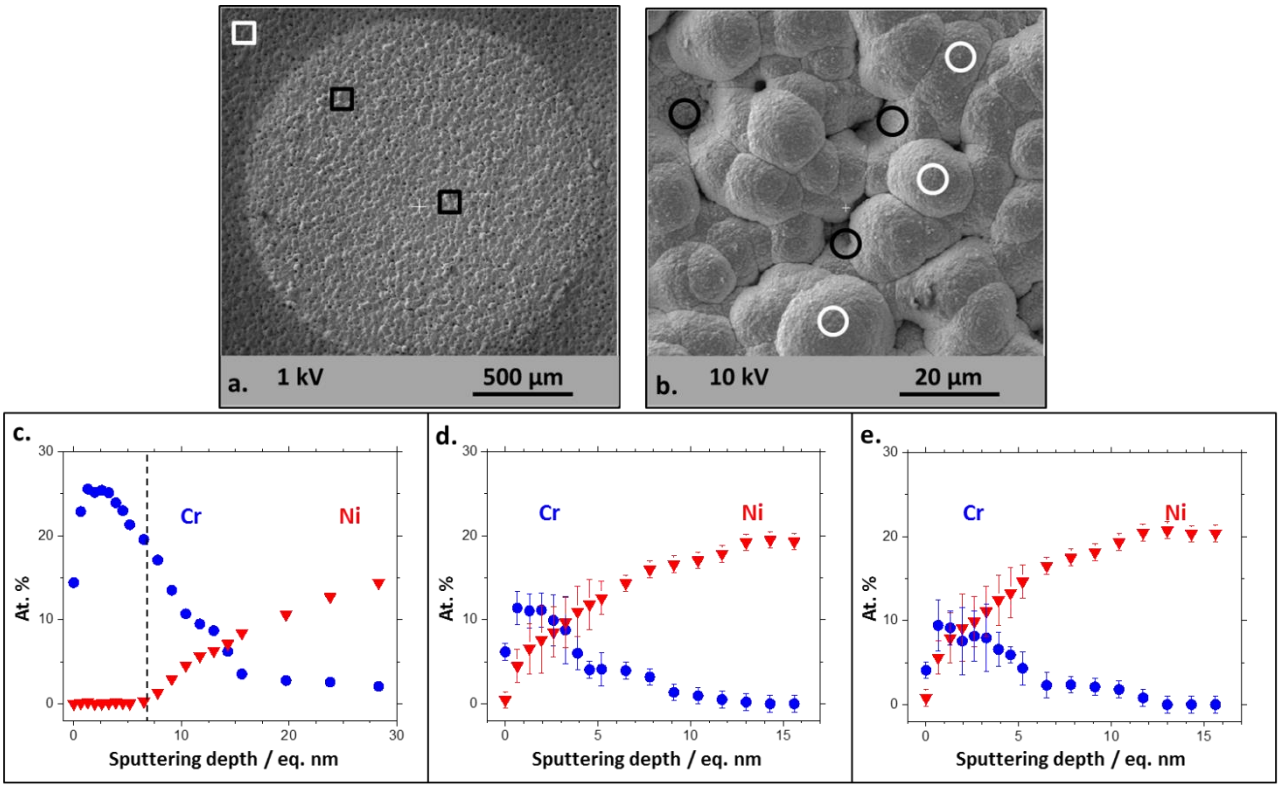

Figure 4.6: SEM images and Nano Auger elemental profiles in the vicinity of the 2 mm diameter sputtered area generated by GD-OES. ***(a)*** *General view showing sputtered and not-sputtered zones,* ***(b)*** *magnification showing an example of the zone selected for AES profiling inside the defect (valley-type zones are shown with black circles while hill-type are shown by white circles).* ***(c)*** *Example of in-depth chemical profiling of chromium and nickel on intact unsputtered surface,* ***(d)*** *Example of in-depth chemical profiling of chromium and nickel in the valley-type zones inside the crater,* ***(e)*** *Example of in-depth chemical profiling of chromium and nickel on the hill-type zones of the crater*

In order to compare the sputtering between the two techniques, a similar analysis was performed in the area of the crater obtained by ToF-SIMS. **Fig. 4.7.a.** shows the SEM image with two different areas one near the center and one near the border of the grid-pattern defect crater. The magnification of the area near the center is presented in **Fig. 4.7.b.** Here also three valley type and three hill-type zones were defined and marked with black and white circles, respectively. The same types of zones were considered in the second area (near the border of the crater) of the sample.

Fig. 4.7.c. and **Fig. 4.7.d.** show the local Auger depth profiles on the valley type and the hill type areas respectively. As for the GD-OES made crater, the absence of nickel on the top surface (at 0 eq. nm depth) indicates that the ZnNi substrate was not exposed by the ToF-SIMS sputtering. However, the comparison between the depth profile in the valley type (**Fig. 4.7.c**) and the one in the hill type (**Fig. 4.7.d**) areas, the remaining thickness of conversion coating in the valley type areas is much more important: about 3 eq. nm versus less than 1 eq. nm. These results clearly indicate that the ToF-SIMS sputtering is more efficient on the hill type than on the valley types areas of the surfaces, thus that the influence of the micrometric roughness is important (shadowing effect). This result also confirms our findings by 3D optical microscopy (**Fig. 4.4.d**) showing a heterogeneous distribution of conversion coating in the craters obtained by ToF-SIMS.

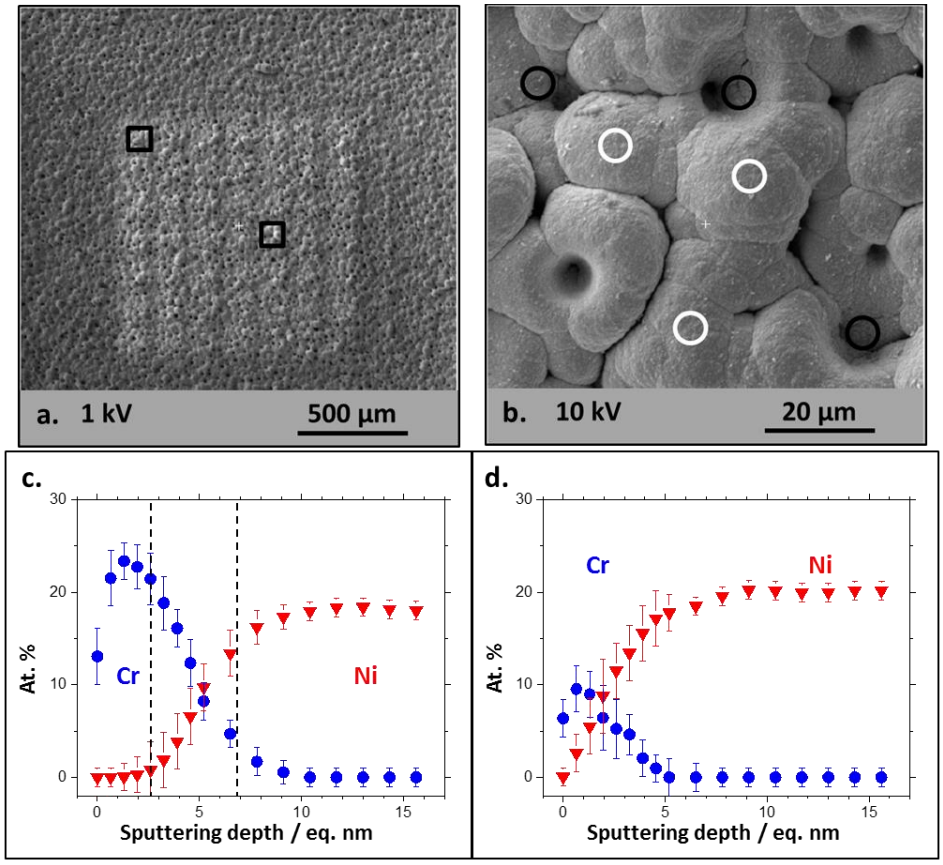

Figure 4.7: SEM images and Nano Auger elemental profiles in the vicinity of the sputtered area generated by ToF-SIMS. ***(a)*** *General view showing sputtered and non-sputtered zones,* ***(b)*** *magnification showing an example of the zone selected for AES profiling inside the defect (valley-type zones are shown with black circles while hill-type are shown by white circles).* ***(c)*** *Example of in-depth chemical profiling of chromium and nickel in the valley-type zones inside the crater,* ***(d)*** *Example of in-depth chemical profiling of chromium and nickel on the hill-type zones of the crater.*

3.3. Discussion: feasibility of thin layers characterization on rough substrates

The novelty of the present work is the attempt to apply a combination of different sputtering and surface characterization technics to explore the in-depth evolution of chemical composition of thin conversion coatings on rough substrates. GD-OES and ToF-SIMS were tempted to reveal the inner part on the thin oxide layer so that high resolution XPS acquisition could be performed in the depth of the conversion coating. Auger electron microscopy, which seems to be the less sensitive to the samples' surface topography, especially when equipped with co-axial cylindrical mirror analyzer [36], and extensively used for local surface characterization and in-depth chemical profiles of oxide layers [54] was proposed to verify the lateral distribution of the remaining conversion coating after surface sputtering by GD-OES and ToF-SIMS.

Our work demonstrated that the crater generation by ToF-SIMS on rough surfaces can result in a more heterogeneous sputtering than the crater generation by GD-OES due to shadowing effect.

As the GD-OES permitted to perform homogeneous sputtering on rough surfaces in the proposed conditions, the combination of GD-OES and XPS techniques seems to be an easy and rapid way to obtain the in-depth quantitative chemical surface composition of the thin oxide layers on rough substrates, which has never been demonstrated to our knowledge.

The so-called shadowing effect of the surface roughness on the ion beam can be described by simple geometry [55]. The significant roughness of the analyzed sample can result in the zones less accessible for sputtering with the ion beam oriented 45 ° to the surface and influence the shape of the crater. The application of ToF-SIMS sputtering on the rough surfaces for the purpose of generating a crater to perform XPS analysis inside the crater, can be hence questionable due to the homogeneity of the sputtering. This lateral homogeneity issue of the sputtering was previously observed in the case of ToF-SIMS imaging [56]. If the sputtering inhomogeneity is well described and considered, ToF-SIMS still offers interesting perspectives for localized sputtering and following localized analysis.

However, the induced roughness in the nanometer range was less significant after low angle ion beam from ToF-SIMS sputtering than after argon plasma sputtering by GD-OES, which is consistent with the literature [57]. An alternative solution to perform the in-depth quantitative chemical description on rough substrate would be to couple XPS with an in situ argon ion gun normal to the surface as it is set up in the Nanosonde Auger Phi 710.

In addition, the development of the so called "ultra-fast sputtering" using argon-oxygen gas mixture in the plasma for GD-OES analysis has permitted to obtain fast sputtering of painted systems [58]. To some extent, the proposed methodology in this work could be coupled to the use of such technique and allow a quantitative chemical description of buried metal-polymer interfaces at every steps of the degradation of painted systems.

4. Conclusions

A methodological approach was proposed to obtain a chemical characterization in the depth of conversion coating on rough substrates by combining XPS, low energy argon plasma sputtering by GD-OES or ion gun oxygen sputtering in ToF-SIMS and nanoprobe Auger electron microscopy. Homogeneously sputtered craters with nanometric depth were obtained. The chemical composition evolution during sputtering was very similar for both GD-OES and ToF-SIMS elemental in-depth profiles.

Auger electron microscopy was used to measure the local thickness of the remaining conversion coating after sputtering in different areas of the model craters. It was shown that due to the low incidence angle of the ToF-SIMS ion etching, the sputtering can be uneven for the rough samples because of shadowing effect as in the case of the electrodeposited substrate. The sputtering performed by GD-OES argon plasma was much less affected by the substrate roughness, showing a more homogeneous topography and chemistry along the crater. This allows to propose GD-OES as an interesting tool for sample preparation prior to XPS analysis at buried interfaces, permitting a representative chemical characterization inside the crater.

For the studied Cr(III) conversion coatings deposited on Zn alloy substrate, a methodological approach was proposed and performed in XPS analysis of the Cr 2p core level peaks. It resides in the subtraction of the contribution of zinc Auger peaks in the Cr 2p region, allowing for a quantitative analysis of the surface chemistry of conversion coating composed of zinc and chromium.

High resolution XPS spectra were measured on the top surface of Cr(III) based conversion coating on rough Zn alloy substrate and in the sputtered craters near the coating/substrate interface. The XPS demonstrated that the coating is mainly composed of zinc hydroxides and Cr(III) species with an atomic ratio of 1.6 Zn to 1 Cr. Interestingly, Cr to Zn ratio in the whole conversion coating depth (outer and inner part) was similar, demonstrating homogenous depth distribution of Cr species.

Finally, the coupling of XPS with GD-OES was shown to be an efficient methodology for the in-depth chemical description of oxide layers on electrodeposited rough substrates.

1 References:

1 T.J. Natorski, Zinc and zinc alloy plating in the 90s, Metal Finishing 90 (1992), 15-17

2 D.E. Hall, Electrodeposited zinc-nickel alloy coating: A review, Plating and Surface Finishing 70 (1983), 59-65

3 M.S. Chandrasekar, S. Srinivasan, M. Pushpavanam, Properties of Zinc alloy electrodeposits produced from acid and alkaline electrolytes, Journal of Solid State Electrochemistry 13 (2009), 781-789

4 T. Biestek, J. Weber, Electrolytic and chemical conversion coatings: a concise survey of their production, properties and testing, J. Electrolytic and Chemical Conversion Coatings (1976), 200

5 A.S.H. Makhlouf, Current and advanced coating technologies for industrial applications, Nanocoatings and Ultra-Thin Films (2011), 3-23

6 C.S. Jeffcoate, H.S. Isaacs, A.J. Aldykiewicz, M.P. Ryan, Chromate in conversion coatings: a XANES study of its concentration and mobility, JOCS 147 (2000), 540-547

7 U.S. EPA (1998) Principles of Environmental Impact Assessment Review: Appendix A: Environmental Impact Assessment Checklist

8 European Commission regulation report n°2017/999 - REACH, Official Journal of European Union (2017)

9 G.D. Wilcox, J.A. Wharton, *A review of chromate-free passivation treatments for zinc and zinc alloys*, Transactions of the Institute of Metal Finishing 75 (1997), B140-B142

10 G. Wilcox, *Replacing chromates for the passivation of zinc surfaces*, Transactions of the Institute of Metal Finishing 81 (2003)

11 J.W. Bibber, Non-chrome-containing conversion coatings for zinc and zinc alloys: Environmentally friendly alternatives provide equal or better adhesion and corrosion resistance as conventional methods, Metal Finishing (106 (2008), 41-46

12 R. Berger, U. Bexell, T.M. Grehk, S.E. Hörnstörm, A comparative study of the corrosion protective properties of chromium and chromium free passivation methods, Surface and Coating technologies 202 (2007), 391-397

13 J.A. Wharton, G.D. Wilcox, K.R. Baldwin, Non-Chromate Conversion Coating Treatments For Electrodeposited Zinc-Nickel Alloys, The International Journal of Surface Engineering and Coatings 74 (1996), 210-213

14 J.A. Wharton, G.D. Wilcox, K.R. Baldwin, An Electrochemical Evaluation of Possible Non-Chromate Conversion Coating Treatments for Electrodeposited Zinc-Nickel Alloys, The International Journal of Surface Engineering and Coatings 77 (1999), 152-158

15 K. Cho, V.S. Rao, H. Kwon, Microstrcture and electrochemical characterization of trivalent chromium based conversion coating on zinc, Electrochimica Acta 52 (2007), 4449-4456

16 H.H Sheu, H.B. Lee, S.Y. Jian, C.Y. Hsu, C.Y. Lee, Investigation on the corrosion resistance of trivalent chromium conversion passivate on electroplated Zn-Ni alloy, Surface and Coating Technology 305 (2016), 241-248

17 X. Zhang, C. van den Bos, W.G. Sloof, A. Hovestad, H. Terryn, J.H.W. de Wit, *Comparison of the morphology and corrosion performance of Cr(VI)- and Cr(III)-based conversion coatings on zinc*, Surface and Coating Technologies 1999 (2005), 92-104

18 G. Greczynski, L. Hultman, X-ray photoelectron spectroscopy: Towards reliable binding energy refenrencing, Progress in Materials Science 107 (2020), 100591

19 J.E. Devries, Surface Characterization methods – XPS, ToF-SIMS, and SAM a complementary ensemble of tools, Journal of Materials Engineering and Performances 7 (1998), 303-311

20 A.I. Stoica, J. Światowska, A. Romaine, F. Di Franco, J. Qi, D. Mercier, A. Seyeux, S. Zanna, P. Marcus, Influence of post-treatment time of trivalent chromium protection coating on aluminium alloy 2024-T3 on improved corrosion resistance, Surface and Coatings Technology 369 (2019), 186-197

21 R.E. Galindo, R. Gago, D. Dudy, C. Palacio, Towards nanometric resolution in multilayer depth profiling: a comparative study of RBS, SIMS, XPS and GDOES, Analytical and Bioanalytical Chemistry 386 (2010,) 2725-2740

22 M. Ely, J. Światowska, A. Seyeux, S. Zanna, P. Marcus, Effect of Post-treatment on Improved Corrosion Behavior of Trivalent Chromium Protection (TCP) Coating Deposited on Aluminium Alloy 2024-T3, Journal of the Electrochemical Society 164 (2017), C276-C284

23 E. Gardin, S. Zanna, A. Seyeux, A. Allion-Maurer, P. Marcus, XPS and ToF-SIMS characterization of the surface oxides on lean duplex stainless steel – Global and Local approaches, Corrosion Science 155 (2019), 121-133

24 S.V. Baryshev, J.A. Klug, A.V. Zinovev, C.E. Tripa, Q. Peng, J.W. Elam, I.V. Veryovkin, *Measuring the roughness of buried interfaces by sputter depth profiling*, Nanotechnology 24 (2013), 015708

25 D. Mercier, M. Bouttemy, J. Vigneron, P. Chapon, GD-OES and XPS coupling : A new way for the chemical profiling of photovoltaic absorbers, Applied Surface Science 347 (2015), 799-807

26 A. Loubat, S. Béchu, M. Bouttemy, C. Eypert, S. Gaiaschi, Mathieu Frégnaux, D. Aureau, J. Vigneron, N. Simon, P. Chapon, A.M. Gonçalves, A. Etcheberry, Coupling GD-OES and XPS profiling to perform advanced physico-chemical characterizations of III-V layers for photovoltaic applications, Conference WCPEC-7 (2018), 10.1109/PVSC.2018.8547731

27 T. Nelis, R. Payling, Glow Discharge Optical Emission Spectroscopy, Royal Society of Chemistry Cambridge (2004)

28 N. Trigoulet, T. Hashimoto, I.S. Molchan, P. Skeldon, G.E. Thompson, A. Tempez, P. Chapon, Surface topography effect on glow discharge depth profiling analysis, Surface and Interface Analysis 42 (2010), 328-333

29 S. Hoffman, A. Zalar, Depth Profiling with Sample Rotation: Capabilities and Limitations, Surface and Interface Analysis 21 (1994), 304-309

30 E.H Cirlin, Auger electron spectroscopy and secondary ion mass spectroscopy depth profiling with sample rotation, Thin Solid Films 220 (1992), 197-203

31 J. Karlsson, S.E. Hörnström, H. Klang, J.O. Nilsson, Sputter-induced effect on quantitative GD-OES depth profiles from hot-dip zinc-coated steel, Surface and Interface Analysis 21 (1994), 365-369

32 R.E. Galindo, L. Vasquez, Dynamics of GDOES-induces surface roughening in metal interfaces, Analytical and Biologycal Chemistry 406 (2014), 7483-7495

33 A.F. Heude, S. Gaiashi, P. Chapon, Optimizing GDOES sputtering of metal-polymer multilayer systems by plasma gas switching during the test, 8th International GD Day [Conference] (2016), P28

34 V. Hoffman, R. Dorka, L. Willken, V.D.Hodoroaba, K. Watzig, Present possibilities of thin-layer analysis by GDOES, Surface and Interface Analysis 35 (2003), 575-582

35 C.C. Chang, Analytical Auger Electron Spectroscopy, Characterization of Solid Surfaces (1974), 509-575

36 E. Martinez, P. Yadav, M. Bouttemy, O. Renault, L. Borowik, F. Bertin, A. Etcheberry, A. Chabli, Scanning Auger microscopy for high lateral and depth elemental sensitivity, Journal of electron spectroscopy and related phenomena 191 (2013), 86-91

37 T.S. Sun, D.K. McNamara, J.S. Ahearn, J.M. Chen, B. Ditchek, J.D. Venables, Interpretation of AES depth profilies of porous Al anodic oxides, Application of Surface Science 5 (1980), 406,425

38 A. Berna, P.B. Barna, A. Zalar, Ion Beam Induced Roughness and its Effects in AES Depth Profiling of Multilayer Ni/Cr Thin Films, Surface and Interface Analysis 12 (1988), 144-150

39 A.W. Czanderna, T.E. Madey, C.J. Powell, Beam effects, surface topography, and depth profiling in surface analysis, Methods of Surface Characterization, Springer Books, (2002)

40 S.N. Raman, D.F. Paul, J.S. Hammond, K.D. Bomben, Auger electron spectroscopy and its application to nanotechnology, Microscopy Today 19 (2011), 12-15

41 Z. Gao, P. Banerjee, Review article: Atomic layer deposition of doped ZnO films, Journal of Vacuum Science & Technology 37 (2019), 050802

42 Keyence Corporation, Keyence VHX Digital Microscope, Quality 53 (2014), S47

43 Keyence Corporation (Osaka, JP), Three-dimensional image processing apparatus, three-dimensional image processing method, three-dimensional image processing program, computer-readable recording medium, and recording device, US Patent 9,756,314, issued September 5, 2017

44 D. Necas, P. Klapetek, Gwyddion: an open-source software for SPM data analysis, Central European Journal of Physics 10 (2012), 181-188

45 V. Maurice, H. Peng, L. Klein, A. Seyeux, S. Zanna, P. Marcus, Effects of molybdenum on the composition and nanoscale morphology of passivated austenitic stainless-steel surfaces, Farraday Discussions 180 (2015), 151-170

46 J. F. Moulder, Handbook of X-ray Photoelectron Spectroscopy: A Reference Book of Standard Spectra for Identification and Interpretation of XPS Data, Physical Electronics Division, Perkin-Elmer Corporation (1992)

47 L.S. Drake, D.R. Baer, J.M. Zachara, Auger Parameter Measurements of Zinc Compounds Relevant to Zinc Transport in the Environment, Surface and Interface Analysis 14 (1989), 71-75

48 M. C. Biesinger, L. W.M. Lau, A. R. Gerson, R. St.C. Smart, Resolving surface chemical states in XPS analysis of first row transition metals, oxides and hydroxides: Sc, Ti, V, Cu and Zn, Applied Surface Science 257 (2010), 887–898

49 A. E. Hughes, R. J. Taylor, B.R.W. Hinton, Chromate Conversion Coatings on 2024 Al Alloy, Surface and Interface Analysis 25 (1997), 223-234

50 W. P. Yang, D. Costa, P. Marcus, Resistance to Pitting and Chemical Composition of Passive Films of Fe-17%Cr Alloy in Chloride-Containing Acid Solution, Journal of the Electrochemical Society 141 (1994), 2669

51 E. Cuynen, P.V. Espen, G. Goeminne, H. Terryn, *On the structure and chemical composition of chromium-based conversion coatings on aluminium: A ToF-SIMS Study*, Journal of Analytical Atomic Spectroscopy 14 (1999), 483-486

52 R. Ramanauskas, R. Juskenas, A. Kalinicenko, L.F. Garfias-Mesias, Microstructure and corrosion resistance of electrodeposited zinc coatings, Journal of Solid State Electrochemistry 8 (2004), 416-421

53 P.J. Cumpson, Angle-resolved XPS and AES: depth-resolution limits and a general comparison of properties of depth-profile reconstruction methods, Journal of Electron Spectroscopy and Related Phenomena 73 (1995), 25-52

54 X. Zhang, C. van den Bos, W.G. Sloof, H. Terryn, A. Hovestad, J. H.W. de Wit, Investigation of Cr(III) based conversion coatings on electrogalvanized steel, Surface Engineering 20 (2004), 244-250

55 J.L.S. Lee, I.S. Gilmore, I.W. Fletcher, M.P. Seah, Topography and field effects in the quantitative analysis of conductive surfaces using ToF-SIMS, Applied Surface Science 255 (2008), 1560-1563

56 S. Rangarajan, B.J. Tyler, Topography in secondary ion mass spectroscopy images, Journal of Vacuum Science and Technology A: Vacuum, Surfaces and Films 24 (2006), 1730-1736

57 M W Thompson, Defects and Radiation Damage in Metals, Cambridge University Press, London,
1968, p. 113

58 P. Chapon, A. Tempez, C. Olivero, T. Nakamura, H. Nakamura, A. Fujimoto, Procédé de mesure par spectrométrie de décharge luminescente d'un échantillon solide organique ou polymère, Europeen Patent EP2434275A1 (2012)

1

Chapter 5

Detection and quantification of defect evolution at buried metal-oxide-polymer interface on rough substrate by local impedance mapping

Thomas Sanchez, Ekaterina Kurchavova, Viacheslav Shkirskiy, Jolanta Swiatowska, Vincent Vivier, Polina Volovitch

The content of this chapter was submitted in Electrochimica Acta in 2021

https://doi.org/10.1016/j.electacta.2021.138467

The content of the chapter corresponds tothe publication before peer review and corrections

1

Chapter 5: Detection and quantification of defect evolution at buried metal-oxide-polymer interface on rough substrate by local impedance mapping

In chapter 3, the new in situ methodology able to distinguish the conversion coatings according to their ability to generate a stable metal-polymer interface was proposed. However, the analytical limits of the method to describe the effect of conversion coating distribution on the interface stability was not explored.

In the present chapter, the ability of the method to: (1) detect local thinning of buried conversion oxides, (2) localize the initiation of the degradation, and (3) measure the local degradation rate are presented.

Abstract

The role of the local nanometric thinning in trivalent chromium conversion coating on the electrochemical stability of buried metal-oxide-model epoxy interface formed on rough electrodeposited substrate (Ra = 5 µm) was studied. Quantitative local electrochemical impedance mapping (LEIM) was able to detect the grid of 7x7 defects with 70 µm size (total area of 0.5 mm²) at the buried interface and to survey the growth of the defect size for the defects with the initial lateral size in order of mm. Degradation of the system during AC-DC-AC ageing procedure was studied for the defects with different morphologies and size. Based on the evolution of transferred cathodic charge, LEIM and ex situ optical microscopy, it was demonstrated that the local thinning of conversion coating on the rough substrates needs to have some critical size to affect significantly the underpaint reactivity. For smaller defects, the surface inhomogeneity related to the initial roughness hinders the effect of the artificial thinning. LEIM was able to measure in situ the degradation kinetics and distinguish the defects for which the interface suffered severe degradation from the defects, which reached a certain stability in both terms of the defect size and underpaint reactivity. The evolution of LEIM maps was in good agreement with the optical observations on 3D images reconstruction performed ex situ; thus, validating quantitative LEIM as a tool for the local degradation quantification for buried interfaces.

Highlights

- Controlled nanometric local oxide thinning on rough substrate prior to painting
- Oxide thinning on area < mm² did not affect the overall underpaint stability
- Reactivity front advancement from underpaint defect was quantified in situ by LEIM
- LEIM discriminated degradation modes confirmed by ex situ microscopy

1. Introduction

Polymer coated metals are among the most used combinations in hybrid materials and materials composites designed for multiple applications, from structural materials in building, automotive, aerospace industries [1,2,3] to electronic devices [4] and medical disposals [5]. In many cases, these assemblies arise from the necessity to combine mechanical strength of metallic substrates with improved lifetime, offered by protective polymer coatings. The reliability and the lifetime of these assemblies strongly depend on the stability of the interface between the metal and the polymer. To improve the corrosion resistance of the substrate metal and the polymer adhesion in such assemblies, the metallic surface is often passivated with formation of a thin layer conversion coating (oxides [6], phosphates [7], titanates [8]). The metal-oxide-polymer interfaces degrade under an interplay of multiple constrains resulting from their fabrication and service conditions (residual or applied mechanical stresses, presence of pollutants at the interface or in the atmosphere, humidity, temperature, UV radiation etc.) and are particularly sensitive to the formation of liquid phase which can lead to polymer permeability, swelling or blistering, water adsorption at the interface with degradation of the oxide layer or even corrosion of the underneath metal [9,10,11].

Although multiple accelerated tests have being used in different applications for stability verification of metal-oxide-polymer systems (continuous salt spray test, cyclic climatic tests (VDA [12], pressure cooker test (PC test [13]) common in electronic devices, immersion test to reveal blistering [14,15], etc.), these tests only permit the observation of the initial and final state but do not allow to survey the system evolution with time. As a result, despite their necessity, accelerated tests remain long, expensive and insufficient to access degradation mechanisms, moreover, they could irreversibly modify these mechanisms. For this reason, the development of in situ methods able to understand the evolution of metal-oxide-polymer interfaces during degradation attracts more and more attention [11,16,17,18,19,20].

In situ chemical analysis of the evolution of buried metal-oxide-polymer interfaces is usually approached using model systems formed by thin layer deposition [21].

To access the overall (average over the whole sample) stability of painted systems, electrochemical technics (open circuit potential (OCP), linear polarization resistance, electrochemical noise and electrochemical impedance spectroscopy (EIS) can be applied in situ to complex systems including industrial coatings made of thick layers [22,20,23] and offer rapid quantitative or semi-quantitative evaluation of the system using simple instruments. In particular, EIS was used to describe the inhomogeneities of painted systems, the distribution of polymer coating properties [24], to survey degraded areas at metal-oxide-polymer interface [25] and water uptake in the polymer coating [26,27].

Although the EIS technique allows to describe some heterogeneous processes occurring during ageing of painted systems, being an integral method, it can detect the existence of such defects but cannot assign them to certain points on the examined surface. The development of local electrochemical technics is therefore necessary for such studies. Several technics were previously used for polymer coated systems: Scanning Kelvin probe (SKP) detects the differences in corrosion potential at different locations of the buried interface [28,29,30]. Scanning vibrating electrode technique (SVET) measures the local DC currents, which can be helpful to characterize defects in coating but cannot overcome the inherent difficulty in measuring currents underneath high resistance coatings [31,32]. Local electrochemical impedance

spectroscopy and mapping (LEIS and LEIM) [33,34,35,36,37,38] measure local AC currents at a selected frequency and become widespread techniques to study buried interfaces for the systems in which the polymer does not have initial defects [39,40,41].

Despite the increasing number of works applying LEIS and LEIM for the description of degradation at metal-oxide-polymer interfaces, very small number of them treat the evolution of the system in a quantitative way [35,36] and to our knowledge no studies were devoted to the verification of the analytical limits of LEIS and LEIM for the detection of the active areas under intact polymer. Moreover, the theoretical limits of LEIS and LEIM technics are elaborated for flat substrates, while many industrial substrates are electrodeposited alloys, therefore rough. For instance, these substrates can have important roughness parameters: Ra from 2 to 5 µm and Rz from 5 to 15 µm. Such morphological parameters can affect both local polymer coating thickness and local current distribution; leading to an alteration of the local electrochemical techniques' abilities.

The understanding of the analytical limits of the LEIS and LEIM technics to detect and to quantify the defects at buried metal-oxide-polymer interfaces on rough substrates can be of high importance for the development of new conversion coatings, which is an emerging technology because of the European directives prohibiting the use of hexavalent chromium based conversion coatings [42,43].

The main objective of the present work is to propose a methodology for analytical limits evaluation in the case of Zn-based electrodeposited substrate with Cr(III) conversion coating and epoxy paint. The proposed approach is based on the interplay of the concepts developed in our previous works, namely:

1) a quantitative description of the deadhesion (delamination) advancement from a defect in the polymer coating at metal-polymer interface using LEIM [36]
2) an application of a model epoxy – based coating which allows LEIM measurements underneath without a preliminary defect formation and helps to mimic the behavior of buried interface and distinguish conversion coating with and without defects [41]
3) a methodology able to produce a controlled local nanometer thinning of conversion coating without affecting the roughness of the substrate [44].

This methodology is able to localize *in situ* defects in conversion coating and quantify their evolution at buried metal-oxide-polymer interface formed by rough metallic substrate, thin (nanometric) conversion coating and thick (tens of µm) intact polymer coating.

The choice of the studied system was made on the basis of the large application Zn-based metallic coatings used for sacrificial protection of steel [45] and Cr(III) based conversion coatings as an alternative for the replacement of hexavalent Cr based coatings [46,47]; also, epoxy based polymers are among the most used in packaging applications.

By combining LEIM, EIS and high-resolution 3D optical microscopy, the question about the minimal size/distribution of the defect in conversion coating which evolution can be detected and quantified by LEIS/LEIM with the used experimental set up is addressed.

2. Experimental

2.1. Materials

2.1.1. Substrate

Mild steel with electrodeposited Zn-based metallic coating and Cr(III)-based conversion coating, produced as described in [41], was used as the substrate. The coating consisted of approximately 18 ± 2 µm thick layer of electrodeposited Zn-14 at. % Ni intermetallic ($Zn_{21}Ni_5$) and trivalent chromium conversion coating layer with ~30±5 nm thickness. Six coupons of 3 x 3 cm² were cut from the central part of each sample to avoid the edge effects possible in electrodeposition process. The coupons coming from the same plate are considered further as the same batch. Prior to the generation of the model defects and polymer coating, the samples were stored in a desiccator.

2.1.2. Model defects generation and initial characterization

In order to produce model craters on the surface, sputtering of the conversion coating was performed using either GD-OES or ToF-SIMS technique (See **Chapter 4, Section 3.2.1**). The sputtering parameters were chosen in a way that for both types of generated craters the conversion layer was thinned but still present all over the crater area and was not chemically modified.

To determine the erosion duration, four elemental in-depth profiles were acquired in different locations for each batch prior to the generation of the crater in the conversion coating. Because Ni is not incorporated in the conversion coating but present in the metallic coating (**Chapter 4**, **Section 3.1.2** and **3.1.3** ; [44]), Ni signal evolution was used as a marker in order to define the interface between the metallic substrate and the conversion coatings. The interface was assigned to a point with 50 % of the maximum Ni signal in the profile. The sputtering time necessary to reach the interface, t_{sp}, was thus detected for each batch and the craters were generated using the sputtering time of $0.8\times t_s$. It was assumed that 80 % of the initial thickness is eroded in such a procedure (see **Chapter 4**, **Section 3.2.4** ; [44] for details).

For the crater generation by GD-OES, the Ar plasma pressure was set at 650 Pa and the power at 8 W power. For the crater generation by ToF-SIMS, an oxygen ion source (O_2^-) was used at 2 keV acceleration voltage delivering 100 nA of target current over a 30 × 30 µm² area; thus, avoiding Cs^- implantation in the conversion coating. For the same reason, the crater generation was performed without using the Bi^+ primary ion gun.

In both cases, the surface roughness and the chemical composition in the crater were very close to the ones of the initial composition of the conversion layer on the intact samples. As previously reported, topographic analysis of the surfaces inside and outside the sputtered areas showed no significant differences between the arithmetical mean deviation roughness R_a ~5 µm (See **Chapter 4 Section 3.2.2.**). Also, the O fraction in the conversion layer (measured by AES, see **Chapter 4, Section 3.2.4.** for the measurement details) varied less than 5 % between different craters and between craters and intact samples.

2.1.3. Types of defects

Six coupons were cut from each batch. Two of them were used as reference samples (without defect) and on four others four different types of model defects were produced. Two types of the model defects and their characteristics are illustrated in **Fig. 5.1.b.** and **5.1.c.** The samples produced by GD-OES presented a single circle limited crater in conversion coating. The crater diameter, d, was 2 or 4 mm (see **Fig. 5.1.b**). The defect zone produced by ToF-SIMS is more complex; it consists of a *NxN* square grid of craters with a controlled geometry, leading to an inhomogeneous defect zone with a total defect diameter D<1 mm, schematically illustrated in the **Figure 5.1.c**.

The defects were characterized with a 3D microscope. Despite the initial roughness of the substrate and the fact that only conversion coating is damaged [44], the crater is clearly distinguishable in reflection mode (**Fig. 5.2,** photos). The profilometry scan confirm that the surface roughness is unchanged inside the crater and corresponds to the roughness of the electrodeposited Zn alloy (**Fig. 5.2**, profiles). The targeted as well as the measured dimensions of the five types of the samples studied in this work are summarized in **Table 5.1**.

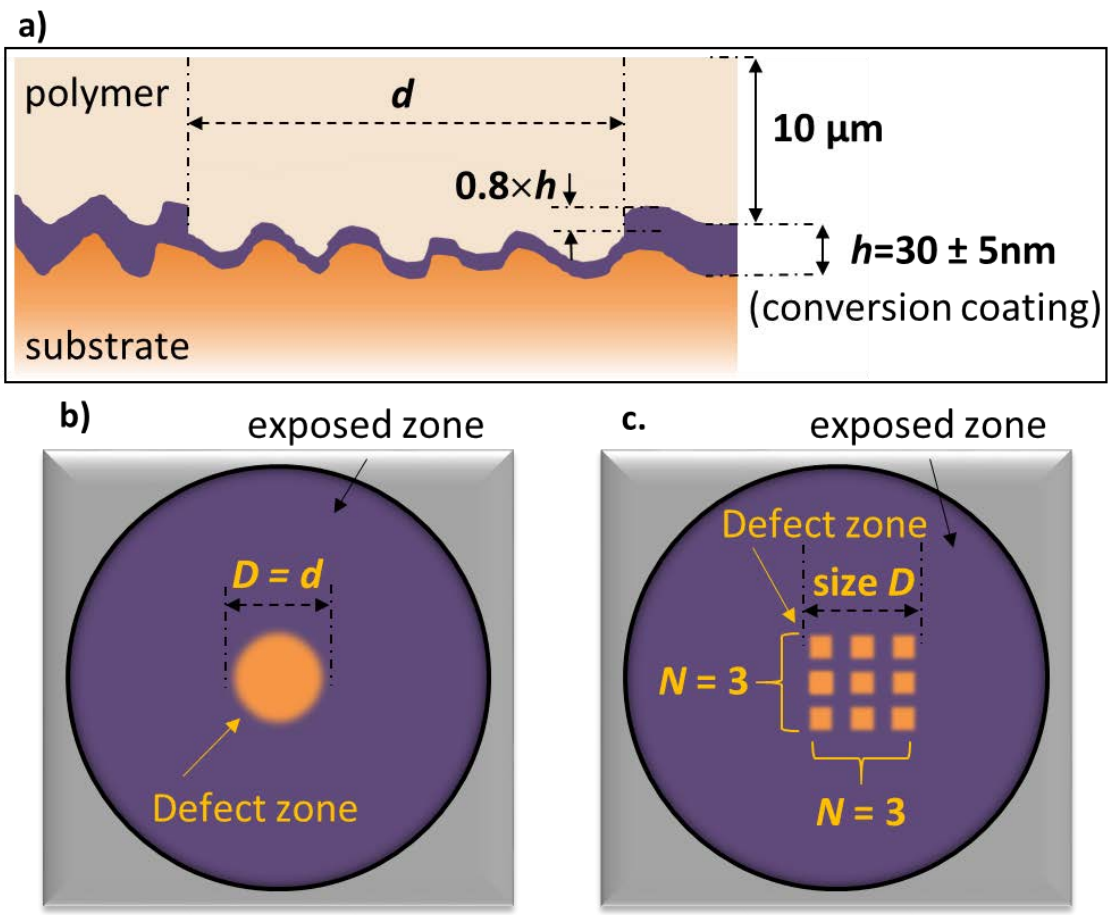

*Figure 5.1: (**a**) Cross sectional and (**b-c**) top view schematics of model systems for the parameters definition. Linear dimension d and depth 0.8 h, where h is the initial conversion coating thickness) of an individual defect as well as the grid size NxN and the considered linear defect size (D) are shown*

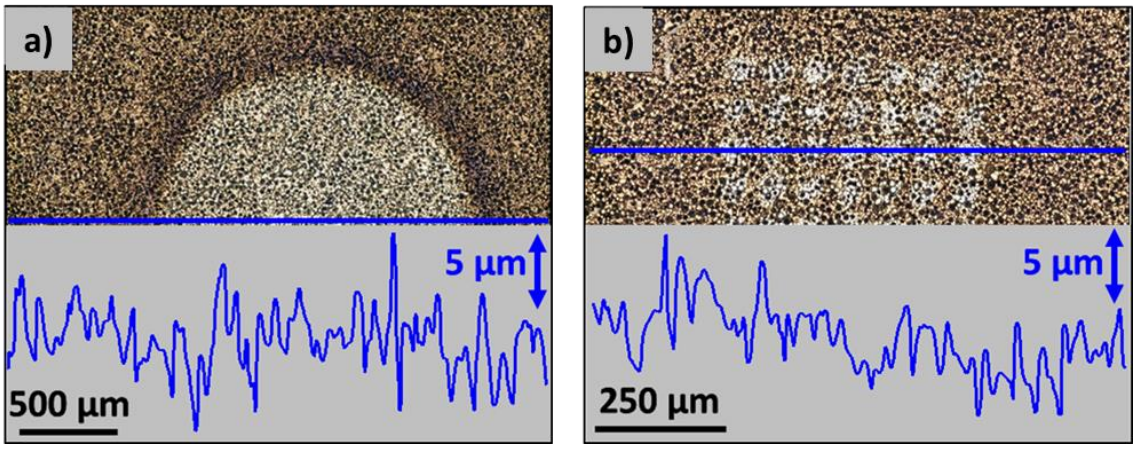

*Figure 5.2: Examples of 3D-microscopy images and corresponding topographic profiles of surfaces with defect in conversion coating produced by (**a**) GD-OES (2 mm crater, sample B) and (**b**) ToF-SIMS (grid of 49 craters, sample C). The imaging is made before polymer coating. The blue curves represent the z-axis evolution of the surface extracted from the topographic information of 3D-microscopy.*

*Table 5.1: Description of defects in conversion coatings of studied samples. Parameters defined in the text and in **Fig. 5.1***

Sample	Erosion technique	Individual crater diameter d /µm		Craters arrangement in defect zone		Considered defect dimension D_0 / mm
		Targeted	Measured	Grid size N x N	Inter-crater distance /µm	
I	No craters	-	-	-	-	-
A	GD-OES	4000	3800±20	-	-	3.8
B	GD-OES	2000	1800±20	-	-	1.8
C	ToF-SIMS	30	70±5	7x7 = 49	0.04	0.8
D	ToF-SIMS	30	70±5	3x3 = 9	0.04	0.3

2.1.4. Polymer coating

Prior to electrochemical testing, the samples with and without model defect were coated by the model epoxy polymer (see **Chapter 3**, **Section 2.1.2.** for details). It consisted of DiGlycidyl Ether of Bisphenol-A prepolymer and TriEthylene TetrAmine hardener (DGEBA-TETA) used in (1:1) ratio. For viscosity requirements, the preparation was diluted in 3 mL of ethanol (analytical grade) for 4 g of mixture. Prior to spin-coating procedure, the preparation was placed in a hermetic beaker and mixed at 300 rpm for 20 minutes then left to stand for 15 minutes in order to remove air bubbles. Just before the coating application, the surface of the substrate was rinsed with absolute ethanol to improve wettability.

The polymer was deposited by spin coating using a POLOS SP15 spin-coater. Once the sample was placed and held in the spin-coater, the resin was poured in large excess and spread on the whole surface, the spin coating was performed twice with a 15 s relaxation time in between with following parameters:

3000 RPM rotary speed and 500 RPM/s linear acceleration for 35 s. After spin-coating, the samples were cured at 50 ± 5 °C for 14-16 h.

This procedure allows controlled coating thickness at *ca.* 10 ± 1 µm (See **Chapter 3**, **Section 2.2.2.** for details).

The samples were stored in a desiccator between the coating application and the degradation test. Degradation tests were performed in the following week.

2.2. Electrochemical set up and degradation procedure

Electrochemical experiments were performed using a Solartron Modulab potentiostat with the ECS software interface in a home-made electrochemical cell, with a silver/silver-chloride (Ag/AgCl) reference electrode (RE), the coated sample (2 cm in diameter delimited by an O-ring) as a working electrode (WE) and a 3 cm IN diameter platinum toroid wire as the counter electrode (CE); This setup configuration was used to guarantee symmetrical distribution of current lines, thus minimizing artefact in EIS measurements (see **Chapter 2**, **Section 3.2.**). All the experiments were performed at placed in a Faraday cage room temperature (25±2°C) in 25 mL of 0.01 M NaCl containing 1 wt. % of phenolphthalein as a pH indicator to detect cathodic pH increase.

The degradation procedure was based on our previous work (**Chapter 3**, **Section 2.3.** [41]). Prior to degradation, all the coated samples were immersed for 1 hour to reach a stable value of open circuit potential (OCP). After the first EIS measurement, AC-DC-AC cycles were performed. Each cycle, schematically presented in **Fig. 5.3**, consisted of 15 minutes of cathodic polarization at -1.5 V/Ag/AgCl followed by a 15 min immersion at OCP and a remaining period of 30 min for EIS and LEIM measurements at the OCP. The procedure was repeated 7 time for a total duration of 8.5 hours. After the cycling and before ex situ characterizations the sample was rinsed with milli-Q water and dried with compressed air.

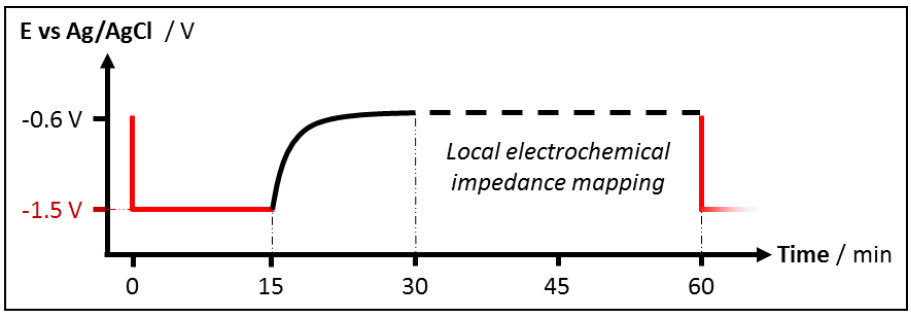

Figure 5.3: Schematic representation of an ageing electrochemical cycle

2.3. Electrochemical impedance

EIS spectra were carried out at the OCP from 100 kHz to 0.1 Hz with 6 points per frequency decade and 20 mV_{RMS} sinewave signal.

For local electrochemical impedance mapping (LEIM), the set up used in [40,41] was adopted. The local probe consisted of two Ag wires (each of 150 µm in diameter) sealed in twin-capillaries and separated by 400 µm. AgCl deposit was obtained by five minutes potentiostatic polarization at 0.4 V/Ag/AgCl in 0.5 M NaCl solution. The quality and the stability of the deposit were verified by EIS measurements of the Ag/AgCl electrodes in 0.01 M NaCl solution after different times between 5 min and 10 h. A home-made setup using Solartron Modulab software with auxiliary input and a 3-axis stepper motor-controlled by Sensolytics was used for LEIM. The electrodes were placed perpendicular to the surface of the sample at a probe to sample distance of 100 ± 25 µm.

The mapping was made with the potential oscillation of 50 mV_{RMS} at a 100 Hz frequency. 6×6 mm² area maps were acquired by measuring the local impedance on series of 31×31 points spaced by 200 µm. Each mapping was performed in approximately 20 min.

The size evolution of the active zone was estimated from the evolution of the distance between the extrema of the local impedance gradient mapping [48]. The gradient maps of the local impedance were calculated and represented with an in-lab developed Python script [36], the value on each pixel of the gradient map corresponding to the modulus of the 2D gradient in the cartesian coordinate system.

2.4. Optical characterization

In situ time lapse microscopy (TLM) using an HD USB microscope with 2 MP CMOS detector and a 4000 K white LED enlightenment was set up in the electrochemical cell. This allowed to complete the electrochemical measurement with a monitoring of a possible surface evolution, the local solution coloration (pink color in phenolphthalein due to the cathodic pH increase) and the hydrogen evolution could be monitored.

The objective to surface distance was set to 4 cm for a magnification of ×80, leading to a 50 µm² pixel size. A picture was taken every minute during immersion and during cathodic polarization in the AC-DC-AC test.

Ex situ optical characterization of the samples was performed using a Keyence VHX-5000 microscope equipped with the VH-Z500T objective allowing for magnification from 500x to 5000x. With 500x magnification, the area of view was of 610 x 457 µm² for a 2000 x 1600 px² image. For wider area image acquisition, an image stitching was performed [49]. Thanks to its short depth of field (< 0.5 µm), multiple images with different objective-to-sample distances were taken, allowing the reconstruction of a 3D image of the surface [50].

The wide area observation of the sample's surfaces consisted of the stitching of 100 (10 x 10) 3D-composition at 500x magnification over 5.0 x 4.1 mm². Each 3D-composition was computed from 50 images over 50 microns in height. High resolution images were obtained by 3D-composition with 2000x magnification. The height range of the composition was selected either to observe the surface of the polymer coating using grazing light or the substrate below the polymer coating.

In addition to the in-depth composition of images, the Keyence VHX-5000 microscope records the height of each focused pixel and therefore allow a topographic measurement of the surface. The height cartography was converted to an 8-bit grey nuance image. Topography and roughness parameters were extracted and calculated with the use of Gwyddion software version 2.50 [51].

3. Results

3.1. Optical surface evolution during cycling

The **Fig. 5.4** shows the in situ images taken during the cathodic polarization step of the first and the fourth cycle of the samples with the defects A, B and C with the initial D_0=3.8, D_0=1.8 and D_0=0.8 mm, respectively.

The localization of the defect is highlighted by the black circle on the images taken during the first cycle (**Fig. 5.4**, left column). Defect A (D_0 = 3.8 mm) can be easily identified from the first cycle: a 4 mm dark circular shape in the center of the black circle is visible. Defect B (D_0 = 1.8 mm) can also be detected by its 2 mm circular shape of lighter contrast than the residual surface. On the contrary, defect C (D_0 = 0.8 mm) and smaller defect D (not shown) are not visible through the coating at this magnification.

After four cathodic polarizations (**Fig. 5.4**, right column) all samples show some hydrogen evolution, proof of the cathodic reactivity, according to the little bubbles dispersed on the surface of the three samples. However, only for the sample A, the hydrogen evolution is clearly more pronounced in the vicinity of the defect while it seems to be homogeneously distributed over all the surface of the samples B and C.

3.2. Electrochemical characterizations

After one hour of immersion, all the samples showed a stable open circuit potential (OCP). In the presence of the defect, the OCP was 30 to 60 mV more cathodic that the OCP of the undamaged sample (I) (around -0.66±0.02 V vs. Ag/AgCl).

In **Fig. 5.5.a** the examples of the OCP evolution during the relaxation step after cathodic polarization for the first, fourth and seventh AC-DC-AC cycles are presented in the extreme cases of samples with millimeter size defects A (D_0 = 3.8 mm) and B (D_0 = 1.8 mm) and the sample I with intact conversion coating. In all cases, after polarization the OCP tends to recover to its original values but the relaxation time increases with cycling. One should note that we were obliged to mix the electrolyte prior to LEIM measurement due to the formation of hydrogen bubbles on the surface during cathodic cycle in the case of the big defect. These bubbles detachment can be responsible for the OCP instability for the sample A, as can be seen in **Fig. 5.5 a**.

Fig. 5.5 b shows the examples of cathodic current evolution during cathodic polarization for the first, the fourth and the seventh cycles on the sample I (intact conversion coating). The surfaced seems to be initially more active than during the polarization because cathodic current slightly decreases in the first seconds of polarization and reaches a stable value in approximately 100 seconds; the current increases gradually with cycling indicating gradual activation of the interface. The behavior was similar for the small defect grids C and D of all different batches.

The evolution of the cathodic current at the first, third, fifth and seventh cycles on samples A (D_0 = 3.8 mm) and B (D_0 = 1.8 mm) show a different behavior. During the three first cycles, the current decreases with polarization time as well but without reaching a stable value. From the 5th cycle the shape of the current curve of the sample B changes, reflecting no initial current peak but in contrast less current in the first seconds of polarization and the following current increase and rapid stabilization. For the sample A

there is no modification of the shape of the curves even if after several cycles the initial current peak decreases. From the 5th cycle, the cathodic current achieved at the end of polarization decreases with cycling for the sample B while it still grows for the sample A.
To sum up, the cathodic reactivity of the surface with the "medium" defect (type B) passes through a maximum between the 3rd and the 5th cycles and then decreases, while for the bigger defect (type A) such a "passivation" is not observed, even if the current increase becomes slower.
One should note that even though the absolute values of the cathodic currents measured in different batches were slightly different, the tendencies illustrated in **Fig. 5.5** were observed for all batches.

The evolution of the total exchanged charge during cathodic polarization with cycling is presented in **Fig. 5.6.a** for samples A, B, C and D (D_0 = 3.8, 1.8, 0.8 and 0.3 respectively) from the same batch 1. For comparison, the exchanged charge measured for two intact samples I from two batches 1 and 2 (intact 1 and intact 2) and samples A and B from batch 2 are shown in **Fig. 5.6.b**. First, it is clear from the figures that the increase in the size of the defect results in higher exchanged charge, which is coherent with the observed in **Fig. 5.4** two order of magnitude increase of the cathodic current by the defect in conversion coating. The comparison of two different batches of samples for the two extreme cases (no defect and the biggest defect, **Fig. 5.6b**) show that the behavior of the samples with intact substrates can vary within a factor 3. However, the behavior of the sample with 3.8 mm defect is almost unchanged. For the two big defects generated by GD-OES (D_0 = 1.8, 3.8 mm), a similar behavior is noticed: the exchanged charge increases for the three first cycles then it stabilizes and starts to decrease (**Fig. 5.6.a**). It is interesting to note that: the exchanged cathodic charge on the sample C continuously decreases with cycling, reaching the values in order of $2x10^{-3}$ C; while for the reference sample I with the intact conversion coating, the charge transfer continuously increases reaching the same values. Considering the discussed above error in the charge transfer measurement between different samples (see intact 1 and intact 2 in **Fig. 5.6.b**), after 4-5 cycles the cathodic reactivity (exchanged charge) of the sample C can be considered as similar to the cathodic activity of an intact sample.

Fig. 5.6 c shows the evolution of the exchanged charge during cathodic polarization in function of the estimated surface of the underpaint defect (detailed in 3.4) for the first, fourth and seventh cycles. No linear correlation between the defect surface and the exchanged charge nor current could be established.

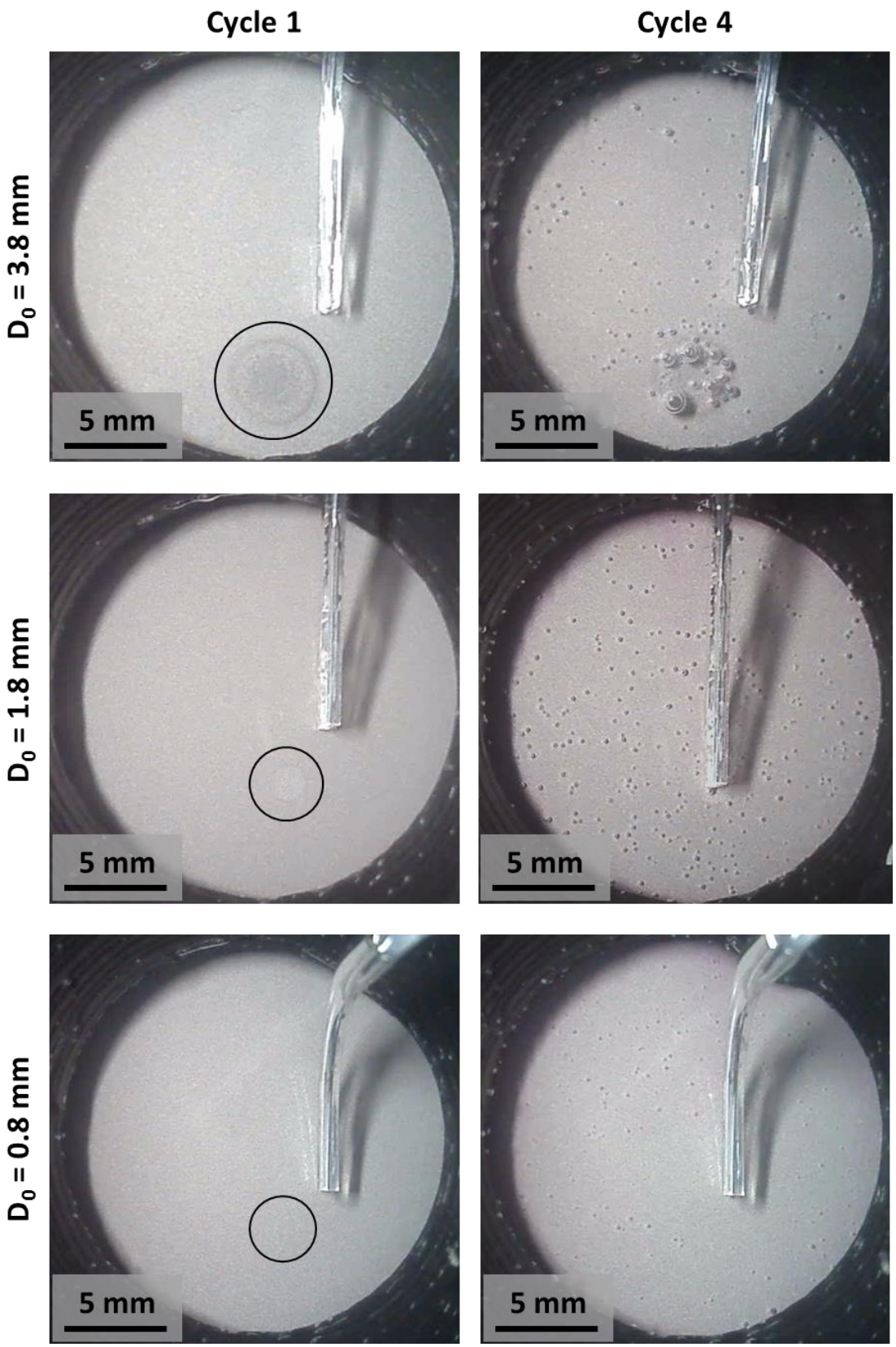

Figure 5.4: Time Lapse Microscopy images of samples A, B and C (D0 = 3.8, 1.8 and 0.8 mm, respectively) at the beginning of first and fourth degradation cycles

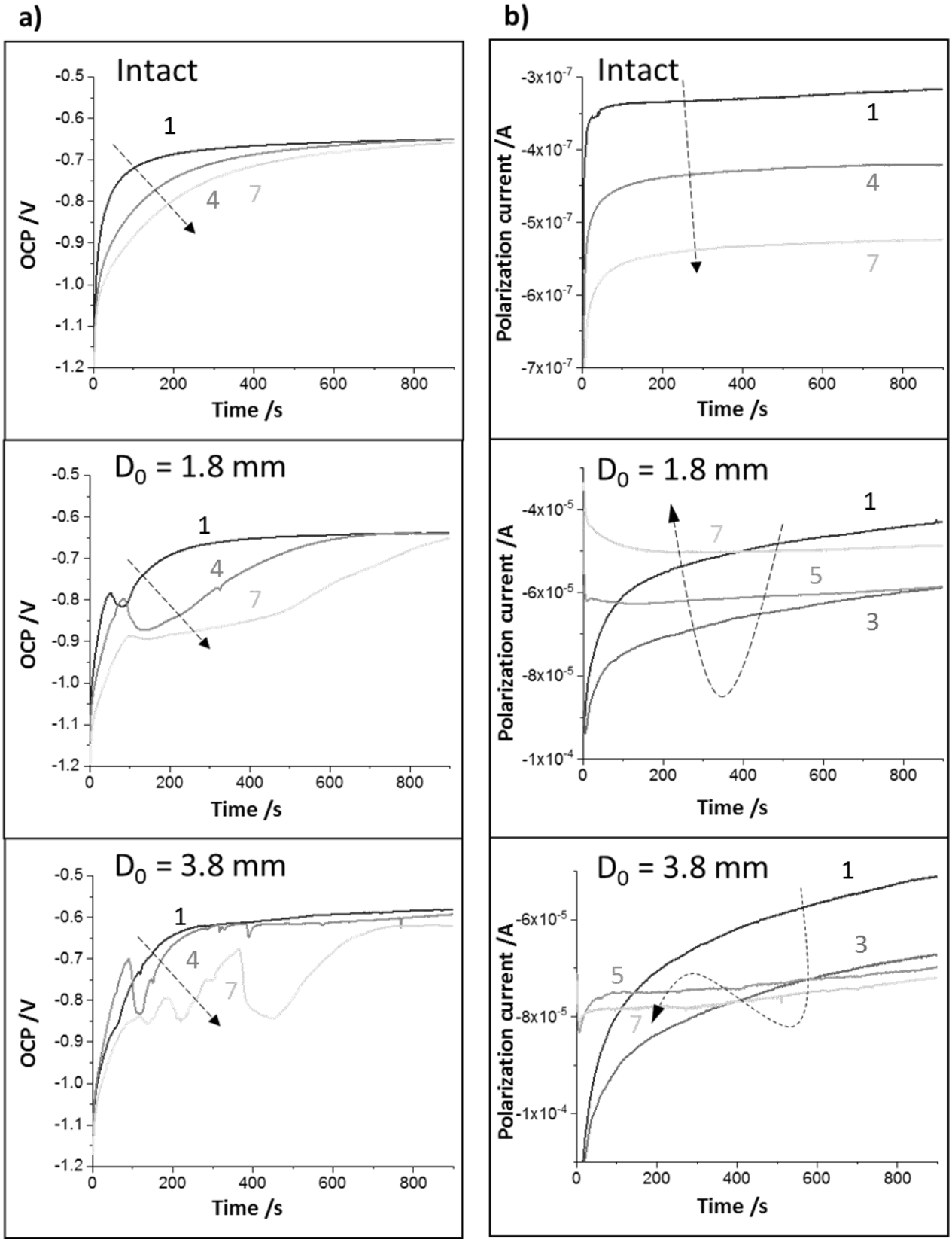

*Figure 5.5: Examples of (**a**) OCP evolution during the relaxation stage and (**b**) potentiostatic current evolution during cathodic polarization for different cycles as indicated*

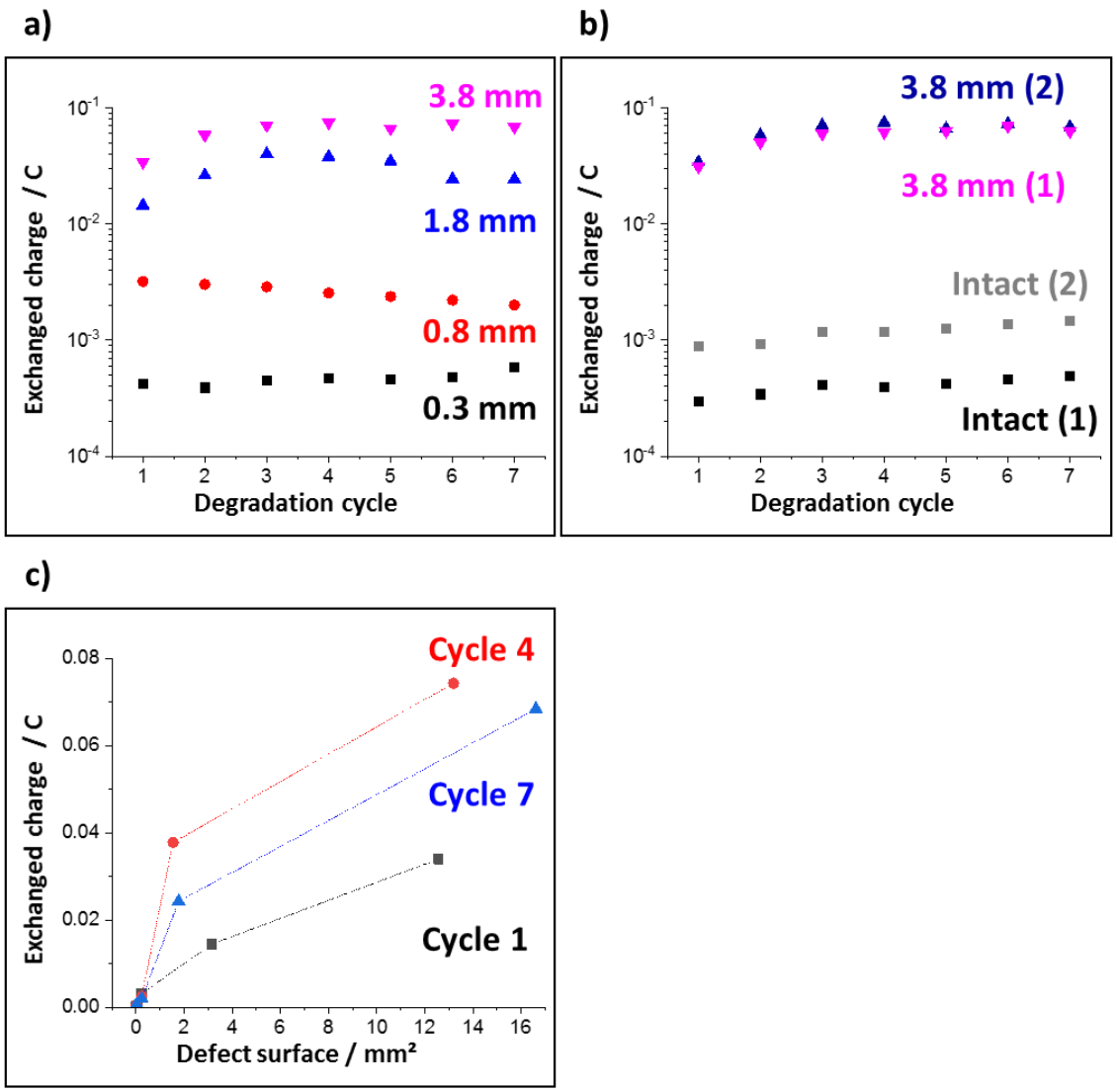

*Figure 5.6: Total charge, exchanged during cathodic polarization stage of the degradation cycle, as a function of the cycle number, for intact samples and samples with different initial dimension of the defect zone D0 (as indicated). (**a**) and (**b**) show samples from 2 different batches. (**c**) Exchange charge during cathodic polarization as a function of the surface of the underpaint defect*

3.3. Electrochemical impedance spectroscopy

The electrochemical impedance spectra at OCP of the samples A, B, C, D and I in the Bode representation at the first, fourth and seventh cycles were recorded. The results are presented in **Supplementary**.

All spectra demonstrated similar response involving two time constants reflecting two main contributions:

- The polymer coating in the HF domain (above 10^4 Hz)
- The metal-oxide-electrolyte interface in the LF domain (below 10^3 Hz)

The polarization cycling lead to a gradual decrease in the modulus of the impedance in the lower frequency domain which was consistent with the degradation of the painted system.

Once the system has passed the fourth cycle, the impedance spectra did not vary and showed a similar trend whatever the size of the defect. The absence of significant differences between the samples is not so surprising, considering the surface fraction of the defect area in the total analyzed surface: 3.3%, 0.8%, 0.06% and 0.01%, respectively for defect types A, B, C and D. As EIS is an integral method, it seems coherent that the contributions of the defects are not significant. Previously, the theoretical estimations of the effect of various percentages of defect area in the polymer coating on the impedance [52] showed that below approximately 0.01% area fraction of the defect on the studied surface an accurate description becomes difficult.

3.4. Detection and quantification of the underpaint defects in conversion coating by LEIM

The measurement of the global EIS being unable to describe the evolution of the defect, it was studied by LEIM. LEIM experiments were performed at 400 Hz. This value was chosen so as to evidence any change in the capacitance of the interface, but also in a sufficiently high frequency range in order to be able to carry out the mapping on a reasonable time scale, i.e. a duration which makes it possible to assume that the sample has remained in at steady-state throughout the duration of the electrochemical imaging.

Fig. 5.7 presents the examples of the local impedance modulus distribution mapped in the vicinity of the defects on the samples A, B and C produced from the same batch during the first (**Fig. 5.7.a**) and the fourth (**Fig. 5.7 b**) degradation cycles. The lower the impedance modulus is, the darker is the color of the area. During the first degradation cycle, all the samples A, B and C from different batches showed the presence of a lower impedance area where the nanometric defects in the conversion coatings were located. The defect of type D was not detectable, and the results are not present. Comparing the maps obtained after the 1st and the 4th cycle, one can see that with cycling the impedance modulus decreases on the whole scanned surface and the initially intact surface becomes more heterogeneous. This behavior is characteristic for all the batches and continues with cycling. Interestingly, after the 4th cycle only the millimeter size defects of the samples A and B could be detected by LEIM, while the defects grid C is dissimulated by the increased reactivity of the initially intact interface.

Fig. 5.8 presents the maps of the calculated from **Fig. 5.7** local gradient of impedance. The values of the gradient are normalized by the maximum gradient value of each map for a better readability of the figure. It is possible to observe a specific shape of the maximum of the gradient for samples A and B which is attributed to the borders between the zones with different electrochemical activity. As from impedance maps, the defect can be seen on the samples A, B and C after the first cycle, but only for the samples A and B after four cycles.

To extract the defect size, the defects shape was approximated by a circle and the average radius evolution with cycling was calculated. The black circle in Fig. 5.8 illustrates the chosen positions of the local extremum of the gradient, attributed in our work to the front position between the less active and more active (degraded) buried interface.

The evolution of the size of the underpaint defect with AC-DC-AC cycling, estimated from the gradient maps, is presented in **Fig. 5.9** for the samples A and B (D_0 = 3.8 and 1.8 mm). First, it is worth noting that the detected size of the initially active zone for both samples are different that the ones measured by optical microscopy before the degradation cycling. Sample A has an average 3.5 mm in diameter active zone instead of expected 3.8 mm and sample B a 2 mm in diameter active zone instead of expected 1.8 mm. As detailed in previous work [40], LEIM in mainly able to detect underpaint anodic reactivity, hence the possible difference between the size of detected reactivity and the size of the actual conversion coating thinning.

Concerning the size evolution of the active zone, it seems that the defect area evolves in several steps:

1) Initiation: the size of the defect varies
    - Increases on sample A with 4 mm defect up to cycle 1
    - Decreases on sample B with smaller defect up to cycle 3
2) Stabilization: the detected size of the defect is stable.
    - From cycle 2 to 4 on sample A with 4 mm defect
    - From cycle 3 to 7 on sample B with twice smaller defect
3) In the case of the biggest defect (sample A) after the stability phase, the size of the detected defect increases once more, which can be attributed to the degradation of the metal-polymer interface in the front positions of the initial defect and gradual delamination of the polymer coating from the active defect. This stage was not achieved in the case of the smaller defect (sample B), suggesting re-passivation of the defect front.

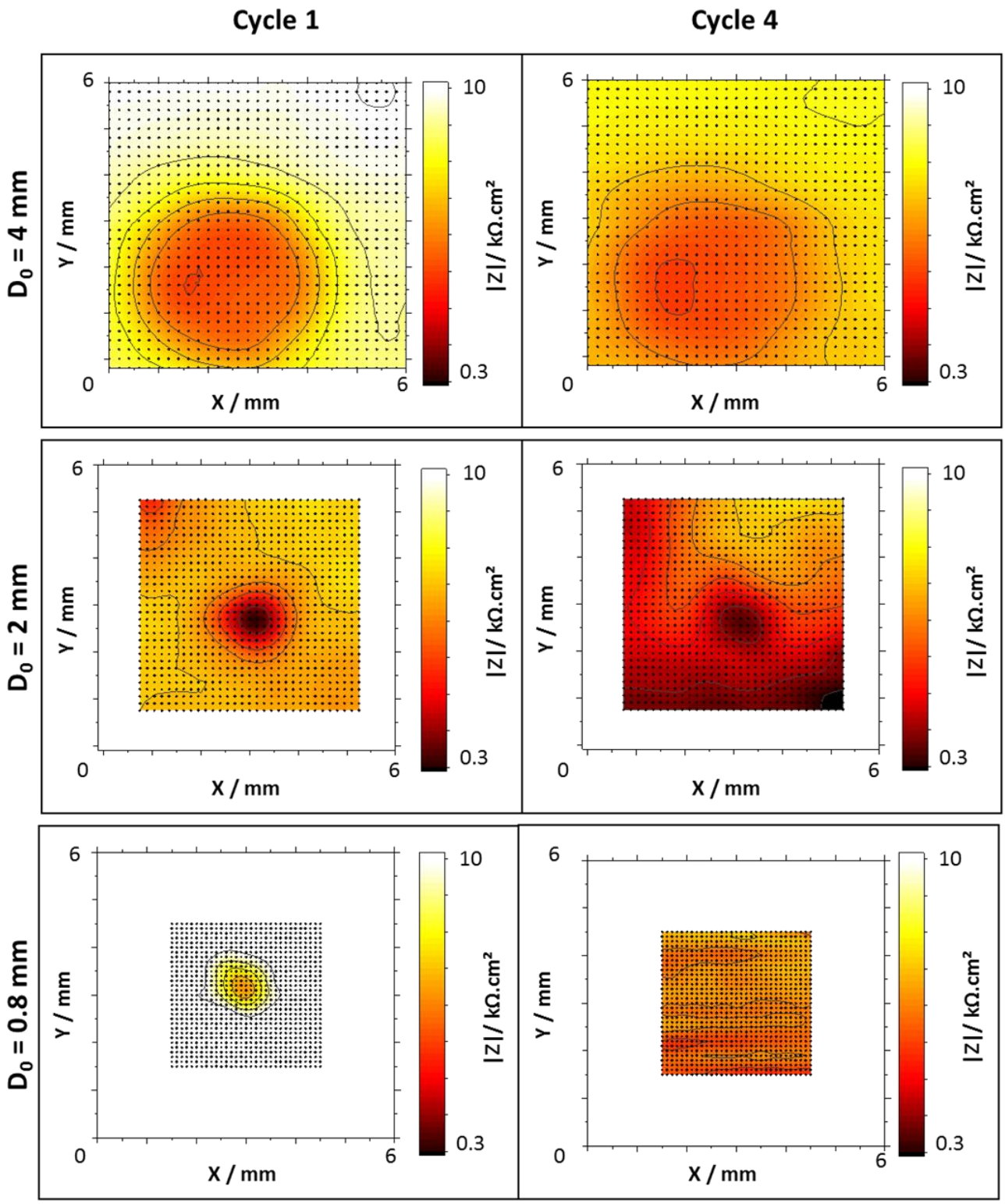

Figure 5.7: LEIM maps of the local impedance modulus, |Z| in the vicinity of the defects for samples A, B and C (D0 = 3.8, 1.8 and 0.8 mm, respectively) at first and fourth degradation cycles

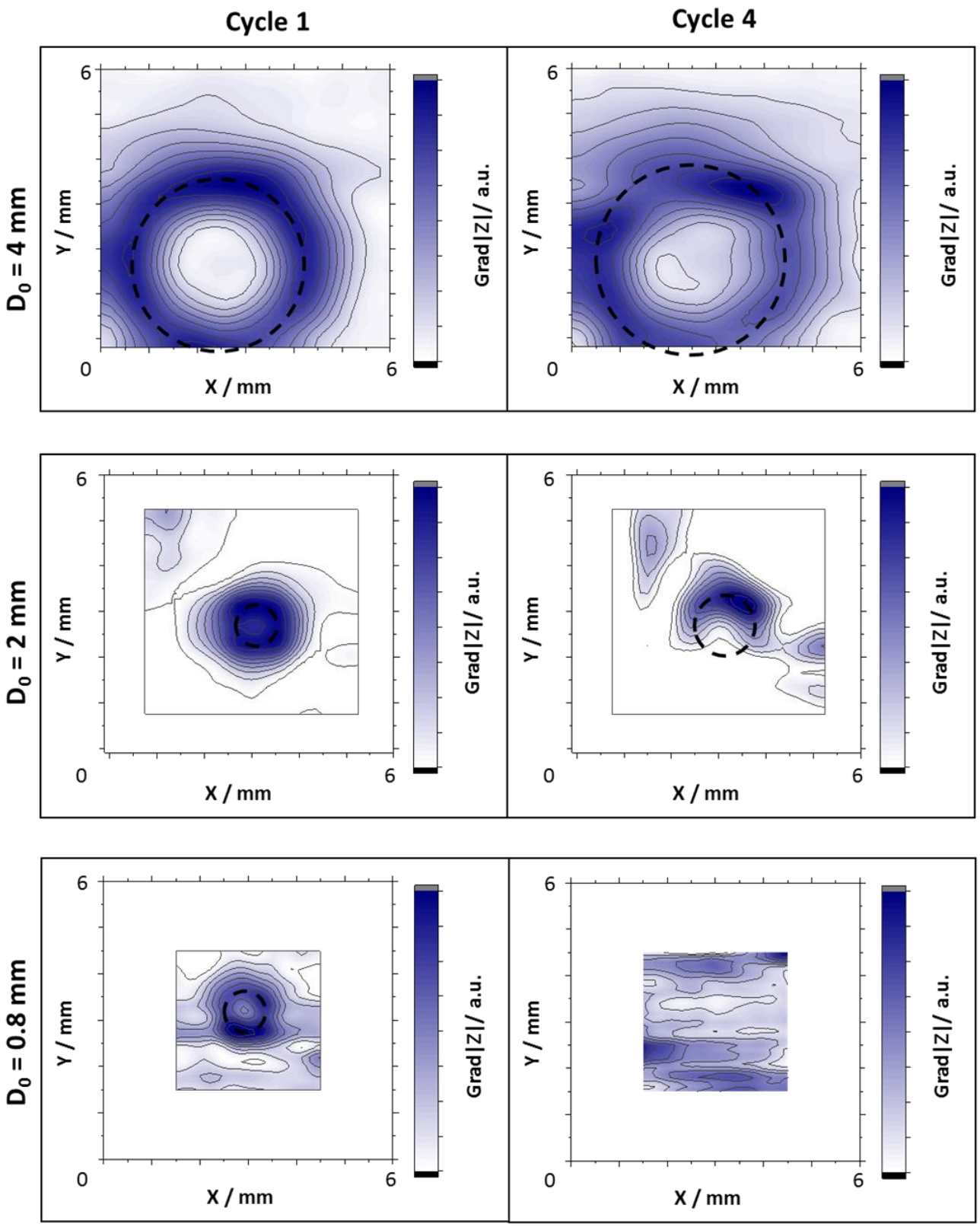

Figure 5.8: Maps of the gradient of the local impedance modulus, Grad |Z| in the vicinity of the defects for samples A, B and C (D0 = 3.8, 1.8 and 0.8 mm, respectively) at the first and fourth degradation cycles. All the values are normalized by the value of the maximum of gradient through the map

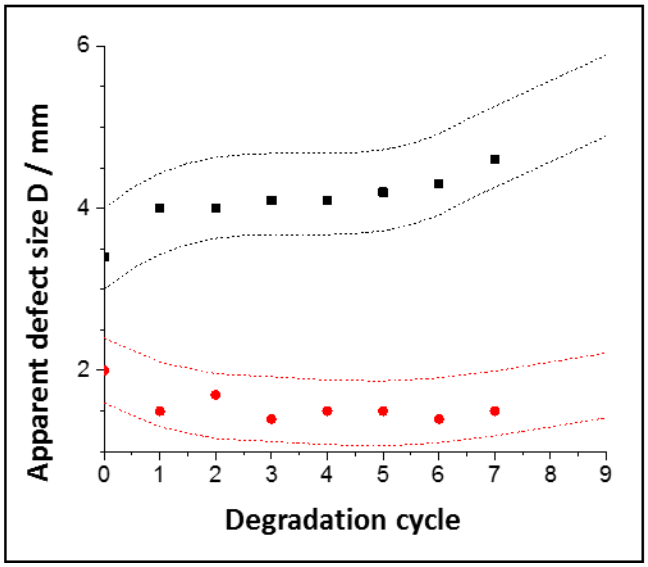

Figure 5.9: Evolution of the LEIM measured size of the defects with degradation cycling for sample A (D0 = 3.8, black squares) and B (D0=1.8 mm, red dots)

3.5. Ex situ optical observations in the vicinity of the defect after cycling

Fig. 5.10.a presents typical optical micrographs in grazing light, recorded around the defects after the complete degradation procedure for the samples of type A (D_0=3.8 mm, gradual reactivity increase and defect size increase detected by LEIM) and B (D_0=1.8 mm, reactivity stabilization and defect size stabilization detected by LEIM). The dashed red line represents an estimated position of the defect borders. The area inside the defect A looks different from the outside of the defect: the lighter spots are present which are attributed to blisters reflecting the grazing light. On the contrary, the defect is difficult to detect on the sample B since the surface of the defect appears lighter than the rest of the sample but no signs of evident degradation of the system can be noticed.

Fig. 5.10.b shows high magnification 3D composition images performed near the center of the defect on the samples A, B and I; thus, the top polymer surface (on the left) and the substrate under the paint (on the right) are shown. The analysis of the paint surface in the defect of sample A (**Fig. 5.10.b**, on top-left)) reveals that the polymer is distorted and rough: the grazing light comes from the right side of the image, thus the inhomogeneity of the paint surface is visible thanks to the light reflection. Topographical analysis of this area revealed a local thickness increase of approximately 15 µm (more than twice than the initial polymer thickness of 10 µm). Because of the shape and localization of this protrusion, it is attributed to blistering. For comparison, similar observations on the samples of type B and I (**Fig. 5.10.b**, on the left, middle and bottom pictures, respectively) did not revealed the formation of blisters. On these images, the focus on the paint surface was ensured by the micro scratch performed on the surface preliminary to the observation and visible by little dark dots. Only the underpaint substrate shows light reflection, but the paint surface looks flat and smooth.

The observations of the underpaint substrate reveals another difference between the degradation mode of the sample of type A (active increasing defect) and the two others (**Fig. 5.10.b**, right pictures). For the intact sample I and the sample with the defect of type B, which did not reach the growth stage, the substrate reflects the typical morphology and the color of the initial Zn alloy with conversion coating and shows no sign of degradation. For the sample A, specifically in the location of the blister detailed above, the substrate surface changes the color (white areas). Such a color is typical for the initial Zn-alloy substrate observed prior to conversion coating procedure and therefore reflects a lack of conversion coating. Interestingly, no traces of corrosion products are visible in the blisters at least at the scale of the observation.

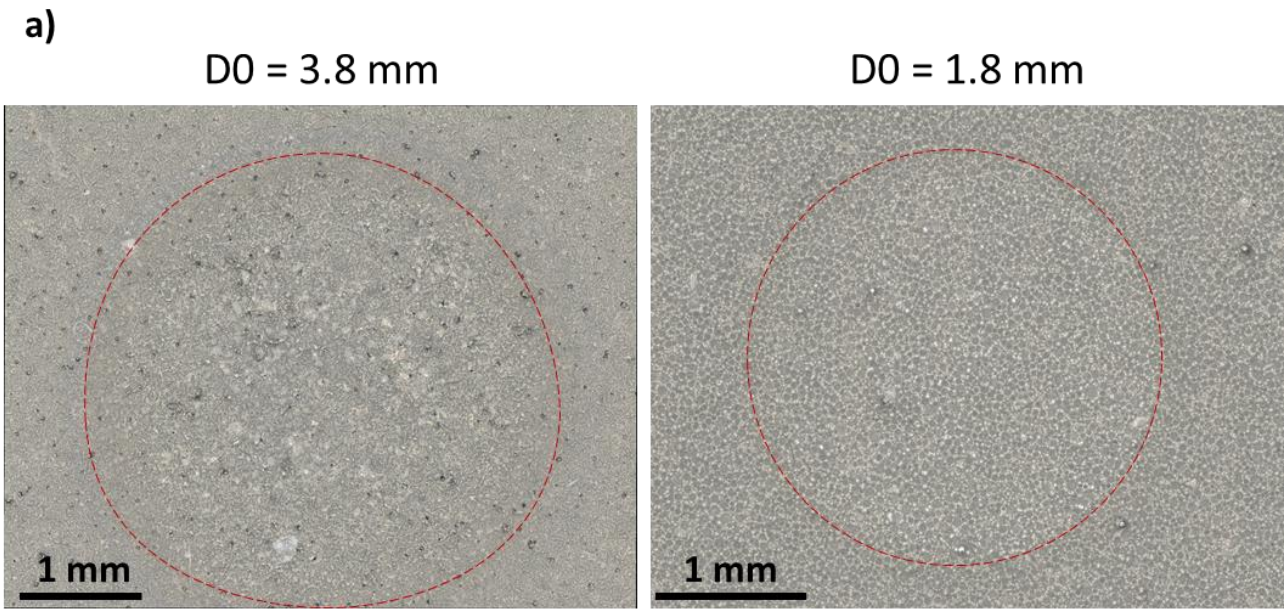

*Figure 5.10: (**a**) High resolution optical micrographs showing the general appearance of the defect for samples A (left) and B (right) after ageing procedure (7 cycles)*

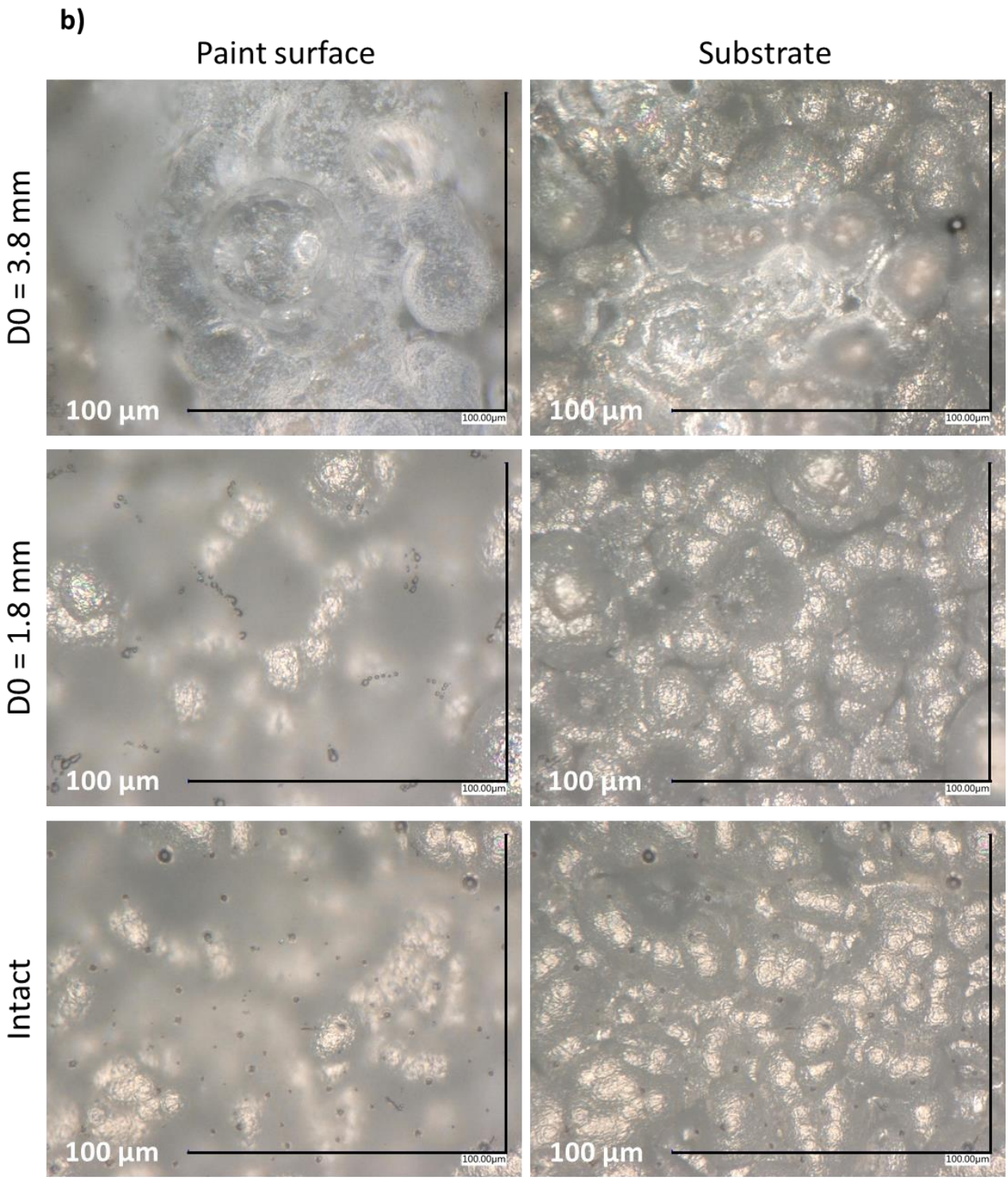

*Figure 5.10: (**b**) High magnification optical observation performed near the center of the defect of samples A, B and I. The focus was set on the top of the polymer coating (left) and at metal-polymer interface (right)*

4. Discussion: LEIM detection of nanometer depth defects in conversion coating on rough surface

Although metal-polymer systems have extensively been studied by multiple groups, to our knowledge, all the reported local observations of the system degradation were initiated by damaging the polymer coating or by adding reactivity enhancers agents at the metal-polymer interface, but no works were focused on the effects of the local thinning of the conversion oxide layer without its complete degradation [53].Defects in conversion coatings were previously studied [19,47,54]. These studies focus mainly on coating performance and average evolution of the system, without considering the local evolution of the defects. In this work, controlled local nanometric thinning of the conversion coating was performed prior to the model epoxy paint application. One of the main objectives of the work was to explore the analytical capacity of different methods (global impedance, LEIM, visual inspection, charge transfer) to detect and describe the evolution of these buried nanometer thick defects in conversion coatings on rough substrate.

First, we checked the minimum defect area which can be seen on the example of the four types of defects produced in a controlled way prior to painting (**Table 5.1**). For these defects, the area fraction occupied by the defect on the total reacting surface in the electrochemical cell represents between 3.30 and 0.01 %. Thus, two main reasons could lead to analytical limitations in the detection of these defects: the instrumental limitation of the used setup and the contribution of the defect to the electrochemical response. The results obtained for four studied types of the defect are sum up in **Table 5.2**.

The presence of the smallest defect, D_0 = 0.3 mm (sample D) was not detected by any of the tested methods. The electrochemical response and the degradation mode were similar to the observed for the intact sample (sample I). Considering macroscopic detection techniques (EIS, polarization current, OCP etc.), the impossibility to see the effect of such a defect could be explained by its small surface coverage, representing only around 0.01 % of the analyzed surface. However, the defect size D_0 is in the same order of magnitude than the scanned area by the local electrochemical impedance probe (0.3 x 0.3 mm); hence the technique should be available to detect the influence in the normal contribution of the current during impedance measurement. It is reasonable to suppose that the inhomogeneity introduced by this defect is comparable with the initial inhomogeneity of the system related to the substrate roughness.

The grid of 49 crater, showing a total defect surface of 0.5 mm², (sample C) was detected before ageing, however the local reactivity in the defect was not distinguishable once the initially intact surface started to degrade, so after 4 and more cathodic polarization cycles. This can be interpreted as either the influence of the defect becomes negligible compared to the average ageing of the metal-oxide-polymer interface of the system, or that the defect can heal with cathodic polarization cycling. It is likely that a thinning of the conversion coating to less than 10 nm in thickness on only 9 or 49 spots of 70 µm width does not significantly influence the stability of the painted system on the rough substrate.

All the defects with an average diameter in the millimeter range (A, B and C) were detected by all the techniques. Hence, local thinning of the conversion coating on areas bigger than a square millimeter seems to significantly affect the underpaint reactivity.

In addition, the treatment of LEIM data was able to measure in situ the evolution of the size of the active zone induced by the nanometric thinning of the conversion coating with accurate precision. This measurement validates the ability of quantitative LEIM for the evaluation of degradation kinetics for

initially undamaged coated systems. Although quantitative LEIM had already been used to track delamination kinetics on weakly adherent coatings and model systems with highly resistive coatings, all the reported quantitative works measured the delamination from an artificially produced defect in the paint [28,35]. The use of quantitative LEIM to track the front propagation kinetics at buried interfaces in the case of an undamaged coating was never demonstrated to our knowledge. It seems that the proposed analytical approach could be used for quantitative description of local reactivity in the systems with conversion coatings.

Table 5.2: Summary of the detection capacity of different technics for the model systems for various size of defects in the conversion coating

D_0 /mm	Defect type	Detection Charge transfer	Detection TLM	Detection LEIM	Size quantification LEIM	Size evolution LEIM
3.8	Single crater	✓	✓	✓	✓	✓
1.8	Single crater	✓	✓	✓	✓	✓
0.8	Grid of craters	~	✗	✓	✓	✗
0.3	Grid of craters	✗	✗	✗	✗	✗

5. Conclusion

For the first time the effect of the nanometer depth defect in conversion coating on the stability of buried metal-oxide-polymer interface on rough substrate was studied. It was demonstrated that electrochemistry is able to detect the initially present thinning in conversion coating, including the small defects with the diameter less than 1 mm which are not visually detectable after the paint application.

The local thinning of the trivalent chromium conversion coating on Zn alloy leads to a localized initial increase of the activity at buried metal-oxide-polymer interface in the vicinity of the defect.

The local thinning of conversion coating on the rough substrate can still not enhance the underpaint reactivity. In some cases, the surface inhomogeneity related to the initial roughness hinders the effect of the artificial thinning.

LEIM was able to measure in situ the degradation kinetics and distinguish the defects for which the interface suffered severe degradation from the defects, which reach a certain stability in both terms of the defect size and underpaint reactivity. The measured by LEIM ranking of degradation rates was confirmed by ex situ high resolution optical observations and 3D images reconstruction thus validating quantitative LEIM as a tool for the local degradation quantification for buried interfaces.

Supplementary

Examples of EIS in Bode representation of modulus (left) and phase angle (right) obtained after 0, 4 and 7 AC/DC cycles applied for samples without initial defect (intact) and with defects zone of different linear size D0 (as indicated)

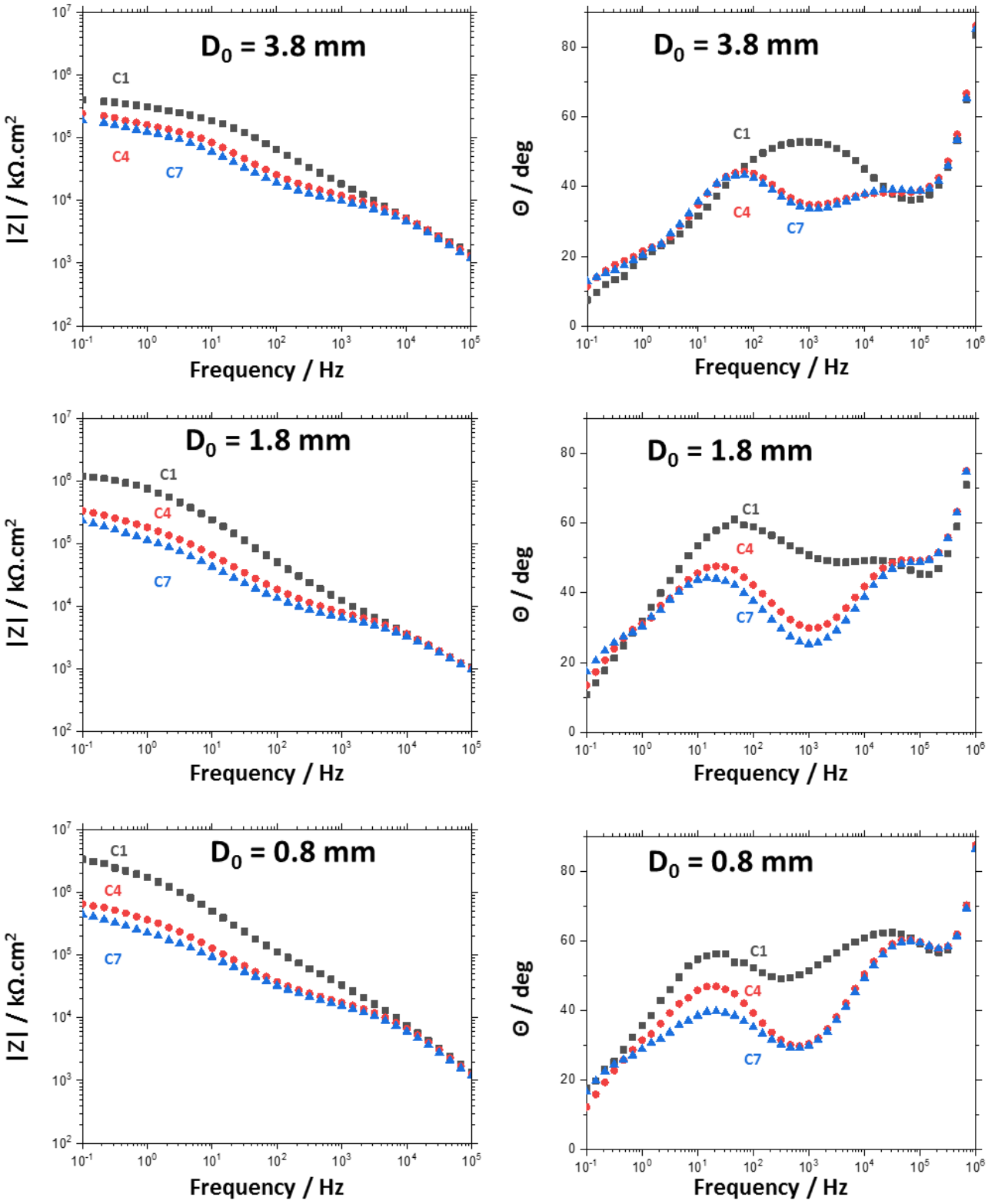

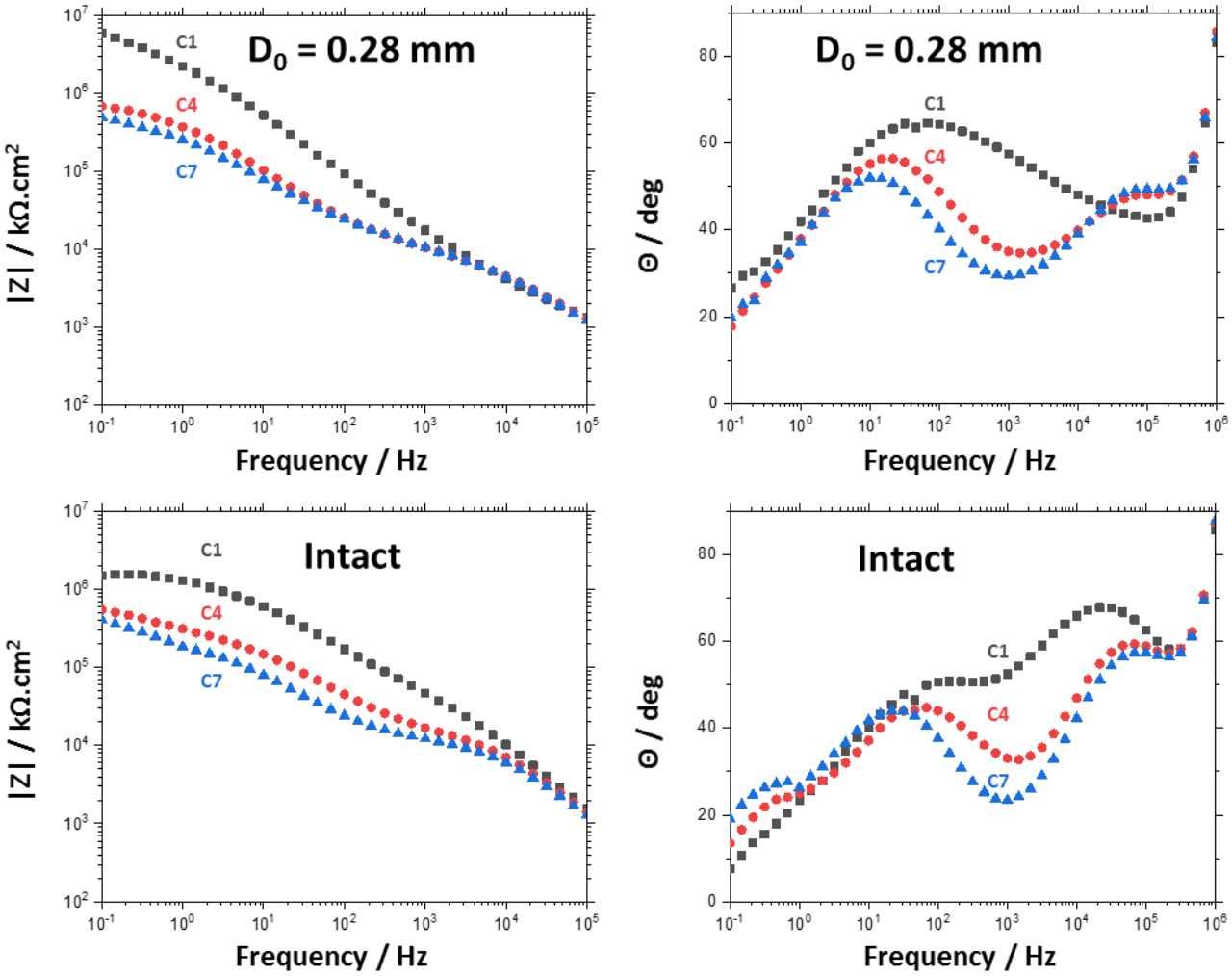
D0 = 0.28 mm
C1
C4
C7
|Z| / kΩ.cm2
Frequency / Hz
Θ / deg
Intact

1 References

1 Total Materia, Corrosion protection of Steel [Online], available on: https://www.totalmateria.com/page.aspx?ID=CheckArticle&site=kts&NM=300, [Accessed on 16/08/2020]

2 N. K. Akafuah, S. Poozesh, A. Salaimeh, G. Patrick, K. Lawler, K. Saito, Evolution of the Automotive Body Coating Process—A Review, Coatings, 24 (2016) 1‑22

3 W. Funke. Corrosion Control by Coatings, H. Leidheiser, Jr., Editor, Science Press, Princeton, N. J., p. 35 (1979)

4 M. Schneider, U. Gierth, L. Simunkova, P. Gierth, L. Rebenklau, Complementary EIS/FTIR study of the degradation of adhesives in electronic packaging, Materials and Corrosion (2020), DOI: 10.1002/maco.202011772

5 M.A. Sebaa, S. Dhillon, H. Liu, Electrochemical deposition and evaluation of electrically conductive polymer coating on biodegradable magnesium implants for neural applications, Journal of Material Science: Materials in Medecine 24 (2013), 307-316

6 D.M. Johnson, Zinc and cadmium passivation bath, US2559878A, (1951)

7 W. Zhou, D. Shan, E.-H. Han, W. Ke, Structure and formation mechanism of phosphate conversion coating on die-cast AZ91D magnesium alloy, Corros. Sci., 50 (2008) 329–337

8 O. Lunder, C. Simensen, Y. Yu, K. Nisancioglu, Formation and characterization of Ti–Zr based conversion layers on AA6060 aluminium, Surf. Coat. Technol., 184 (2004), 278‑290

9 W. Funke, Toward a unified view of the mechanism responsible for paint defects by metallic corrosion, Ind. Chem. Prod. Res. Dev. 24 (1985), 343-347

10 W. Funke, Problems and progress in organic coatings science and technology, Progress in Organic Coatings 31 (1997), 5-9

11 G. Grundmeier W. Schmidt M. Stratmann Corrosion protection by organic coatings: electrochemical mechanism and novel methods of investigation, Electrochimica Acta 45 (2000) 2515–2533

12 VDA 233-102 “Cyclic corrosion testing of materials and components in automotive construction” June 2013

13 J.W. Hwang, M.J. Yim, K.W. Paik, Effects of thermoplastic resin content of anisotropic conductive films on the pressure cooker test reliability of anisotropic conductive film flip-chip assembly, Journal of Electronic Materials 34 (2005), 1455-1461

14 ASTM International D 870 – 15 “Standard practices for testing water resistance of coatings using water immersion” (2020)

15 ASTM International D 714 – 02 “Standard test method for evaluating degree of blistering of paints” (2017)

16 B. Munirathinam, J.P.B. van Dam, A. Herrmann, W.D. Driel, F. De Buyl, S.J.F. Erich, L.G.J. van der Ven, O.C.G. Adan, J.M.C. Mol, Exploring water and ion transport process at silicone/copper interfaces using in situ electrochemical and Kelvin probe approaches, Journal of Materials Science & Technology (2019), https://doi.org/10.1016/j.jmst.2019.07.044

17 M. Stratmann, Whitney Award Lecture: Corrosion Stability of Polymer-Coated Metals—New Concepts Based on Fundamental Understanding, CORROSION 2005, Vol. 61, No. 12, pp. 1115-1126

18 M. Stratmann, G. Grundmeyer, ADHESION AND DE-ADHESION MECHANISMS AT POLYMER/METAL INTERFACES: Mechanistic Understanding Based on In situ Studies of Buried Interfaces, Annual Review of Materials Research 2005 Vol. 35:571-615

19 A. Gonzalez-Orive, I. Giner, T. de los Arcos, A. Keller, G. Grundmeyer, Analysis of polymer/oxide interfaces under ambient conditions – An experimental perspective, Applied Surface Science 442 (2018), 581-594

20 M. Poelman, M-G. Olivier, N. Gayarre, J-P. Petitjean, Electrochemical study of different ageing tests for the evaluation of a cataphoretic epoxy primer on aluminium, Progress in Organic Coatings 54 (2005), 55-62

21 P. Taheri, H. Terryn, J.M.C. de Mol, Studying interfacial bonding at buried polymer-zinc interfaces, Progress in Organic Coatings 89 (2015), 323-331

22 F. Meng, L. Liu, Electrochemical evaluation technologies of organic coatings, intechopen (2018) [Online] available on https://www.intechopen.com/books/coatings-and-thin-film-technologies/electrochemical-evaluation-technologies-of-organic-coatings, [Accessed on 10/02/2019]

23 A. Amirudin, D. Thierry, Application of electrochemical impedance spectroscopy to study the degradation of polymer-coated metals, Progress in Organic Coatings 26 (1995), 1-28

24 E.P.M. van Westing, G.M. Ferrari, J.H.W de Wit, The determination of coating performance with impedance measurement-I. Coating polymer properties, Corrosion Science 34 (1993), 1511-1530

25 E.P.M. van Westing, G.M. Ferrari, J.H.W de Wit, The determination of coating performance with impedance measurement-III. in situ determination of loss of adhesion, Corrosion Science 36 (1994), 979-994

26 E.P.M. van Westing, G.M. Ferrari, J.H.W de Wit, The determination of coating performance with impedance measurement-II. in situ determination of loss of adhesion, Corrosion Science 36 (1994), 957-977

27 S. Amand, M. Musiani, M.E. Orazem, N. Pebere, B. Tribollet, V. Vivier, Constant-phase-element behavior caused by inhomogeneous water uptake in anti-corrosion coatings, Electrochimica Acta 87 (2013), 693-700

28 G. Grundmeier, W. Schmidt, M. Stratmann, Corrosion protection by organic coatings: electrochemical mechanism and novel methods of investigation, Electrochimica Acta 45 (2000), 2515-2533

29 A. Nazarov, T. Prosek, D. Thierry, Application of EIS and SKP methods for the study of the zinc/polymer interface, Electrochimica Acta 53 (2008), 7531-7538

30 G. Williams, A. Gabriel, A. Cook, H.N. McMurray, Dopant effects in Polyaniline inhibition of corrosion-driven organic coating cathodic delamination on iron, Journal f the Electrochemical Society 153 (2006), 425-433

31 H.S. Isaacs, Initiation of stress corrosion cracking of sensitized type 304 stainless steel in dilute thiosulfate solution, Journal of the Electrochemical Society 135 (1988), 2180

32 A.C. Bastos, M.C. Quevedo, O.V. Karavai, M.G.S. Ferreira, Review – On the application of Scanning Vibrating Electrode Technique (SVET) to corrosion research, ournal of the Electrochemical Society 164 (2017), 14

33 F. Zou, D. Thierry, H.S. Isaacs, J. Electrochem. Soc. 144 (1997) 1957

34 V.M. Huang, S.L. Wu, M.E. Orazem, N. Pebere, B. Tribollet, V. Vivier, Local electrochemical impedance spectroscopy: a review and some recent developments, Electrochimica Acta 56 (2011), 8048-8057

35 J-B. Jorcin, E. Aragon, N. Pébère, Delaminated areas beneath organic coating: A local electrochemical impedance approach, Corrosion Science 48 (2006) 1779-1790

36 V. Shkirskiy, P. Volovitch, V. Vivier, Development of quantitative Local Electrochemical Impedance Mapping: an efficient tool for the evaluation of delamination kinetics, Electrochimica Acta 235 (2017) 442-452

37 L.V.S. Philippe, G.W. Walter, S.B. Lyon, Investigating localized degradation of organic coatings: comparison of electrochemical impedance spectroscopy with local electrochemical impedance spectroscopy, Journal f the Electrochemical Society 150 (2003), 111

38 Z. Kefallinou, S.B. Lyon, S. Gibbon, A bulk and localized electrochemical assessment of epoxy-phenolic coating degradation, Progress in Organic Coatings 102 (2016), 88-98

39 G. Williams, and H.N. McMurray, *The mechanism of group (I) chloride initiated filiform corrosion on iron*, Electrochemical Communications 5 (2003), 871–877

40 V. Shkirskiy, A. Krasnova, T. Sanchez, A. Amar, V. Vivier, P. Volovitch, Development of anodic and cathodic blisters at a model Zn/epoxy interface studied using local electrochemical impedance, Electrochemistry Communications 111 (2020), 106633

41 T. Sanchez, S. Gillet, V. Shkirskiy, V. Vivier, J. Echouard, J. Swiatowska, P. Volovitch, A new system for intelligent screening of buried interfaces: local electrochemistry characterization of undamaged model epoxy coated Zn alloys, Electrochimica Acta [Submitted on 06/2020]

42 U.S. EPA (1998) Principles of Environmental Impact Assessment Review: Appendix A: Environmental Impact Assessment Checklist

43 European Commission regulation report n°2017/999 - REACH, Official Journal of European Union (2017)

44 T. Sanchez, S. Zanna, A. Seyeux, M. La Haye, P. Volovitch, J. Swiatowska, Conversion coating distribution on rough surfaces analyzed by combining surface analytical techniques, [Under submission]

45 G.D. Wilcox, Electrodeposited zinc alloy coatings, Corrosion Science 35 (1993), 1251-1258

46 G. Wilcox, *Replacing chromates for the passivation of zinc surfaces*, Transactions of the Institute of Metal Finishing 81 (2003)

47 X. Zhang, C. van den Bos, W.G. Sloof, A. Hovestad, H. Terryn, J.H.W. de Wit, *Comparison of the morphology and corrosion performance of Cr(VI)- and Cr(III)-based conversion coatings on zinc*, Surface and Coating Technologies 1999 (2005), 92-104

48 V. Shkirskiy, P. Volovitch, V. Vivier, Development of quantitative Local Electrochemical Impedance Mapping: an efficient tool for the evaluation of delamination kinetics, Electrochimica Acta 235 (2017) 442-452

49 Keyence Corporation, Keyence VHX Digital Microscope, Quality 53 (2014), S47

50 Keyence Corporation (Osaka, JP), Three-dimensional image processing apparatus, three-dimensional image processing method, three-dimensional image processing program, computer-readable recording medium, and recording device, US Patent 9,756,314, issued September 5, 2017

51 D. Necas, P. Klapetek, Gwyddion: an open-source software for SPM data analysis, Central European Journal of Physics 10 (2012), 181-188

52 J.R. Scully, S.T. Hensley, Lifetime prediction for organic coatings on steel and a magnesium alloy using electrochemical impedance methods, Corrosion 50 (1994) 705

53 S. Pletincx, L. Lynn, I. Fockaert, J.M.C. Mol, T. Hauffman, H. Terryn, Probing the formation and degradation of chemical interactions from model molecule/metal oxide to buried polymer/metal oxide interfaces, NPJ Materials Degradation 3 (2019), 23

54 D.H. van der Weijde, E.P.M. van Westing, J.D.H. de Wit, Electrochemical techniques for delamination studies, Corrosion Science 36 (1994), 643-652

Chapter 6: Conclusions & Perspectives

Conclusions

The main objective of this work was to propose methodologies able to assess *in situ* buried metal-oxide-polymer interface stability. Specifically, the proposed methodologies should be applicable to the degradation of buried interfaces under intact polymer coating in immersion condition; including systems formed on rough metallic substrates with nanometric conversion coatings. In order to tackle the complex degradation mechanisms of such multi-layered systems, the analytical approach was divided in several steps:

- Develop a methodology for the in situ local quantification of the reactivity at buried metal-polymer interface.
- Explore the analytical limits of the proposed approach to detect reactivity initiation from nanometric defects in the conversion oxide layer.
- Combine several *ex situ* surface characterization technics permitting the chemical description of thin oxide conversion coatings distribution on rough electrodeposited substrates.

The main results are summarized below.

In situ probing buried metal-polymer interface reactivity

The big challenge in the description of metal-polymer interface was <u>to de-correlate interface stability from the polymer stability</u> and to describe <u>in situ the metal-oxide-polymer interface degradation under immersion</u> in reasonable times. These difficulties were overcome by the application of a model epoxy-based polymer coating and the use of adapted AC-DC-AC electrochemical ageing procedure. The stability of the model epoxy polymer coating in the proposed ageing procedure was preliminary studied making possible to decorrelate the degradation of the coating from the degradation of the interface. The local reactivity was assessed by in situ Time-lapse-microscopy combined with EIS measurement and local electrochemical impedance mapping.

The ability of the proposed methodology to distinguish between the systems able or not to form a stable metal-polymer interface was tested on the example of two batches of electrodeposited zinc-alloy on mild steel with trivalent chromium conversion coating. The conversion coating for the samples of one batch was slightly damaged by 5 s rinsing of 0.5 M sodium hydroxide solution and deionized water in a way that the total Cr content at the surface did not vary more than 1-2 at. %.

Prior to model polymer application, neither electrochemistry (OC measurement, EIS), nor microscopy were able to differentiate the two batches. The developed approach permitted to clearly discriminate the intact substrate from the damaged one via the evolution of the low frequency electrochemical impedance modulus during the proposed ageing cycling. Indeed, the damaged substrate, *i.e.* the one which leads to a less stable metal-oxide-polymer interface, showed a rapid decrease in the impedance modulus. In

addition, TLM demonstrated high hydrogen evolution and local pH increase at metal-polymer interface on this 'damaged' batch. The conclusions about the relative stability of these interfaces, issued from this accelerated testing, were coherent with the observations made for the same substrates painted by an industrial 60 µm thick paint and immersed for 1000 hours in water. The local assessment of the underpaint stability provided by TLM and LEIM permitted to define that in the case of unstable metal-oxide-polymer interface the degradation resulted from the formation of randomly distributed localized anodic sites under the undamaged polymer coating.

In order to understand the possible effect of the local thinning of the conversion coating and to determine the analytical limits of the proposed methodology, model systems with controlled localized thinning in the conversion oxide were also studied.

Using GD-OES and ToF-SIMS prior to polymer coating, model craters of approximately 20 nm in depth and defined diameter (from 30 µm to a few millimeters) were performed in trivalent chromium conversion coating on electrodeposited zinc alloy substrate. The proposed approach permitted to detect and rank the samples in function of the initial size of the model crater. It was demonstrated that the methodology is able to detect the reactivity resulting from a 20 nm in-depth thinning on less than 0.05% of the analyzed surface.

The understanding of the role of the conversion oxide on the localized degradation kinetics using LEIM also justifies the methodological novelty of the work. Since it was developed, quantitative-LEIM had always been used for the characterization of defects in polymer coatings. In this work, LEIM was proved to be able to quantify the size of the anodic area resulting from nanometric thinning in the conversion coatings under intact model epoxy coating. The smallest crater in the conversion coating that was detected and whose evolution was quantified by LEIM was about 0.7 mm in diameter.

To summarize:

- ***The proposed procedure provides reliable results on the ability of conversion coatings to generate a stable metal-polymer interface in epoxy coated systems. In particular, it does not require the formation of initial artificial defects, modifying either the integrity of the polymer or the chemistry of the interface.***

- ***Intelligent screening of conversion coatings using the new procedure can be achieved in approximately 72 hours with comparable results to the ones obtained in 1000 h immersion used in standard procedures.***

- ***It was demonstrated that quantitative local electrochemical impedance mapping is able to describe local underpaint reactivity at metal-oxide-polymer interface on rough substrate under undamaged polymer coating.***

Characterization of thin conversion coatings on rough substrates

The second objective of this PhD was to permit the correlation between the chemistry of a conversion coating on rough substrate and the stability of painted systems. Among numerous surface techniques, the combination between X-ray Photoelectrons Spectroscopy and Time of Flight Secondary Ion Spectrometry is known to provide an accurate description of thin oxide layers by allowing quantitative chemical speciation at different depth. Although this combination gives unparalleled results on model and smooth surfaces, its application on rough surfaces is more complicated and can lead to misinterpretation because of uneven sputtering of the conversion coating by ToF-SIMS on rough surfaces (shadowing effect).

The approach proposed in this work combines low energy sputtering by argon plasma in Glow Discharge Optical Emission Spectrometry (GD-OES) and XPS characterization inside the sputtered crater. This allowed in-depth identification of species and chemical quantification of nanometric conversion coatings on rough electrodeposited zinc alloy. The distribution of the remaining conversion coating in the crater was verified by Auger nano-probe. In the case of electrodeposited Zn-based alloy with trivalent chromium conversion coating, Auger nano-probe characterization demonstrated the lateral homogeneity of the GD-OES sputtering in the nanometer range although the substrate roughness was in the micrometer range.

As proof of concept, this methodology was compared with the couple ToF-SIMS/XPS for the characterization of the same system. The results demonstrated that, on rough surfaces, ToF-SIMS ion etching causes more inhomogeneous sputtering than GD-OES. As a result, on rough substrate, in-depth XPS analysis performed in GD-OES crater can be more accurate than in ToF-SIMS crater.

To summarize:

- ***GD-OES argon plasma sputtering allows to generate homogeneous craters in thin conversion coatings on rough substrates.***

- ***The combination between GD-OES and XPS techniques permits accurate in-depth chemical quantification of conversion coatings on rough surfaces.***

Perspectives

In this work, two novel approaches were proposed for both in situ probing the reactivity of buried interfaces and the characterization of thin conversion coatings on rough substrates. The applicability of these approaches was demonstrated on electrodeposited zinc-based alloy treated with trivalent chromium conversion coating in very specific conditions; however, the methodologies are not limited to these specific types of samples, nor conditions.

The efficiency of the "new system for intelligent screening of buried interfaces" presented in the Chapter 3 was demonstrated for damaged and undamaged conversion coatings; such a tool can be used for smart ranking of various conversion coatings in function of their ability to form stable metal-oxide-polymer interfaces.
Furthermore, the proposed approach must not be limited to trivalent chromium conversion coatings on zinc alloys: for instance, the methodology proposed in this PhD could be used in other systems such as stability of phosphates and titanates conversion coatings. Moreover, the capacity of LEIM to localize the electrochemical reactivity can be an interesting tool for the understanding of the microstructure effects on the underpaint stability of the multiphase substrates, such as ZnAlMg alloys.

The homogeneity of nanometric GD-OES sputtering combined with XPS and Auger nano-probe (Chapter 4) offers the possibility of 3D chemical characterization of thin coatings on rough substrates. The couple GD-OES/XPS seems to be a very promising combination for characterization of thin layers and buried interfaces on rough surfaces. It could bridge the gap between surface characterizations at the nanometer scale on the perfectly flat substrates (usually limited to model samples) and coarse surface treatments which are needed for industrial applications. This approach could be useful for the description of newly developed conversion coatings which fit the requirements of REACh and RoHS regulations.

In addition, thanks to the recent advances in GD-OES technique, in particular, ultra-fast-sputtering (UFS) of thick polymer coatings using Ar-O_2 gas mixture, the application of the combination GD-OES /XPS can be extended to other areas. It could for instance help to reach more important depths for XPS analysis and reveal buried interfaces by sputtering polymer coatings.

APPENDIX 1. Protocol for manufacturing of LEIS micro-probe

1. Equipment required for 1 probe

- ✓ 2 Ag wire (L = 3-4 cm ; ø = 150 µm)
- ✓ 2 Ni or Cu wire (L = 15-18 cm ; ø = 100-150 µm) from electrical wire
- ✓ 2 borosilicate made capillaries (L = 15 cm ; $ø_{external}$ = 1 mm ; $ø_{internal}$ = 0,5 mm)
- ✓ 1 Lighter
- ✓ 1 tube of 3M Superglue

2. Protocol

- Bend two capillaries with a lighter so that they're exactly stackable
  - 3-4 cm from an edge ; 35-45°
  - Blue part of the flame for 7 seconds works well
- Take an Ag and Ni wire and wind them with each other on 1 cm crossing length
  - At least 2 cm of only Ag wire must remain free
  - The bonding must be very thin
- Thread both wires into the capillary
  - Ag wire is in the bended part of capillary and does not exceed
  - Ni wire must outreach of a few cm
- Fill the tip of the capillary with 3M superglue up to the bond between the two wires
  - Glue should flow by capillary action, Act fast so that glue doesn't take
  - There must be no air bubble in the glued part of the probe (~2 cm after bending)
- Put glue on the top of the capillary to secure Ni wire and seal the hermetic half-probe
- Let both glue point dry for a few minutes

- Take two stackable dried half-probes
- Bond them with each other with 3M superglue starting with the tip
- Paste the two capillaries on the whole length (15 minutes)
- Polish the tip with P800 parallel to the body of the probe

The Local probe is now finished

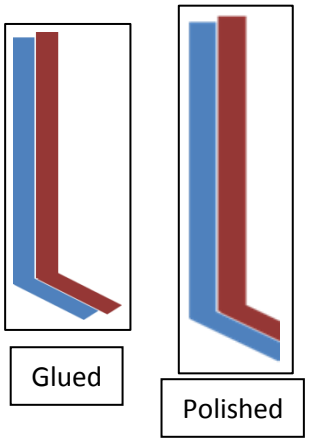

APPENDIX 2. Protocol for a homogeneous epoxy coating preparation and deposition

- Cut the samples at the size you wish. Pay attention to the size parameters, it has to suit 2 conditions
    - Small enough to be spin-coatable
    - Large enough to fit into the cell without any leak
- The Epoxy/hardener mix used is formulated by the brand "SADER".
- When the samples are cut, start preparing the epoxy resin/hardener mixture, the mass are the followings
    - For each gram of resin put a gram of hardener. $1g_{epoxyresin}=1g_{hardener}$
    - To have a homogeneous mixture, add ethanol
    - Thanks to previous calibration, we saw that, in order to spin coat two to four 5cmx5cm samples, we put in a beaker and agitate:
        - 2g of epoxy resin
        - 2g of hardener
        - 3mL of ethanol
- Cover the beaker with parafilm to prevent evaporation and drying
- Put the mix to mechanical stirring for 20 minutes at high rotation speed
- Stop stirring and wait for 10 minutes to help evacuate air bubbles from the mix
- Perform last minute stirring at low speed to homogenise the mix without trapping air bubbles
- Place the sample on the spin-coater. Put the vacuum on and place it until it doesn't move anymore and is fixed thanks to the pressure exercised by the vacuum. The parameters are the followings
    - 3000 RPM with a 500RPM/seconds acceleration
    - 35seconds long
- Spread the mix all over your sample's surface in large amount
- Close the lid and launch the spin-coating procedure
- Wait 15'' after the 1st run and launch a 2nd time
- Place the sample in an oven at 50°C for 14 hours. The thickness of the coating is approximately 10µm ±2µm.

APPENDIX 3. Protocol fof grey scale topographical data extraction

Transfert Image 3D VHX-5000 vers nuance de gris

Par Gwiddion

1) Ouvrir le logiciel d'extraction 3D dans le répertoire d'installation VHX-Communication software :

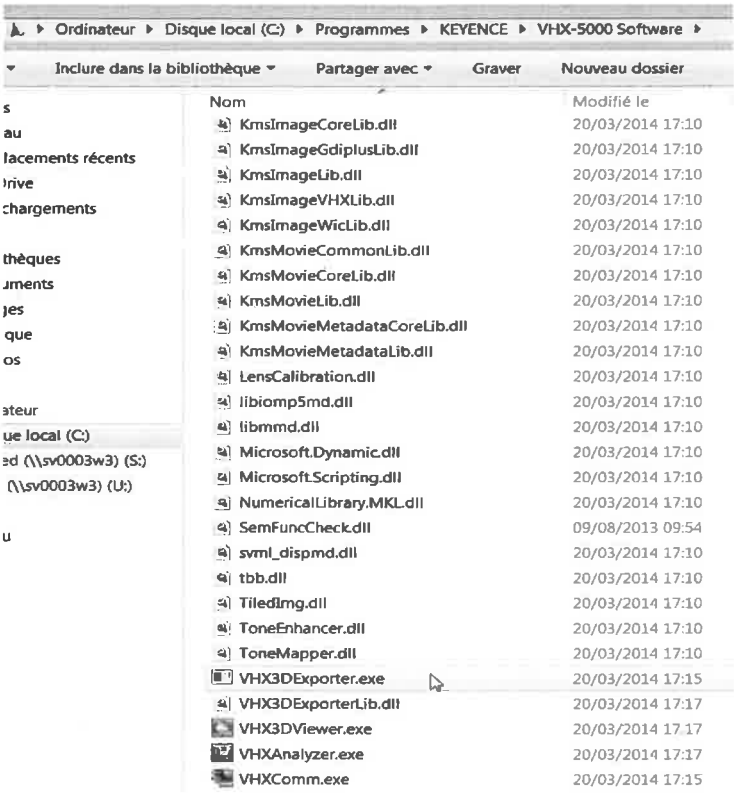

2) Ouvrir le fichier 3D, vous avez la confirmation que les datas 3D sont dans le fichier grâce au logo 3D bleu

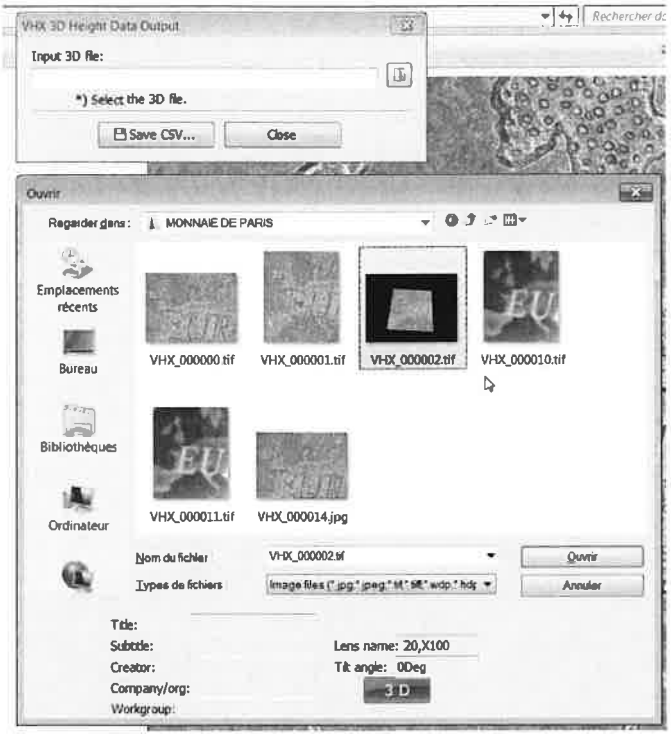

3) Puis vous sauvegardez

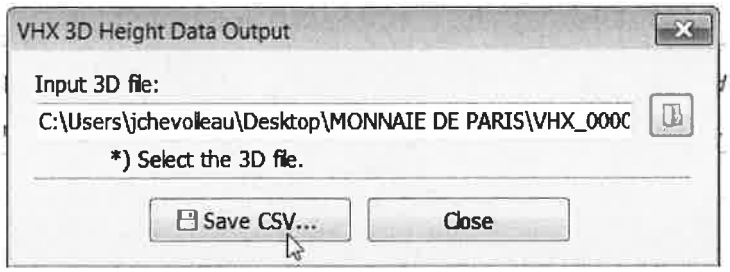

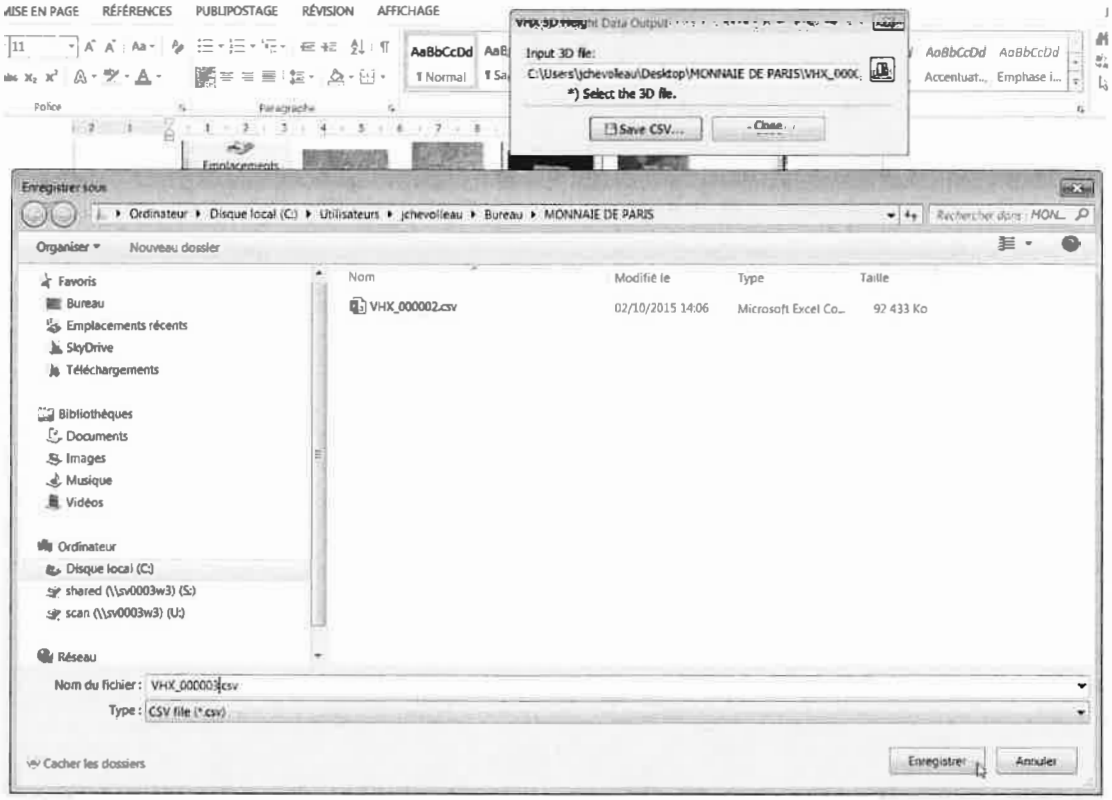

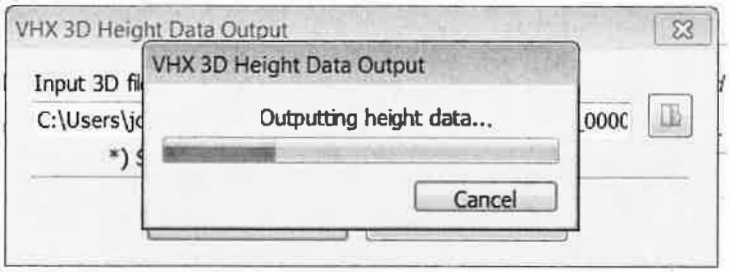

4) Vous ouvrez Gwyddion, ouvrir... Fichier Tiff en données ASCII ou binaires

hier à afficher.

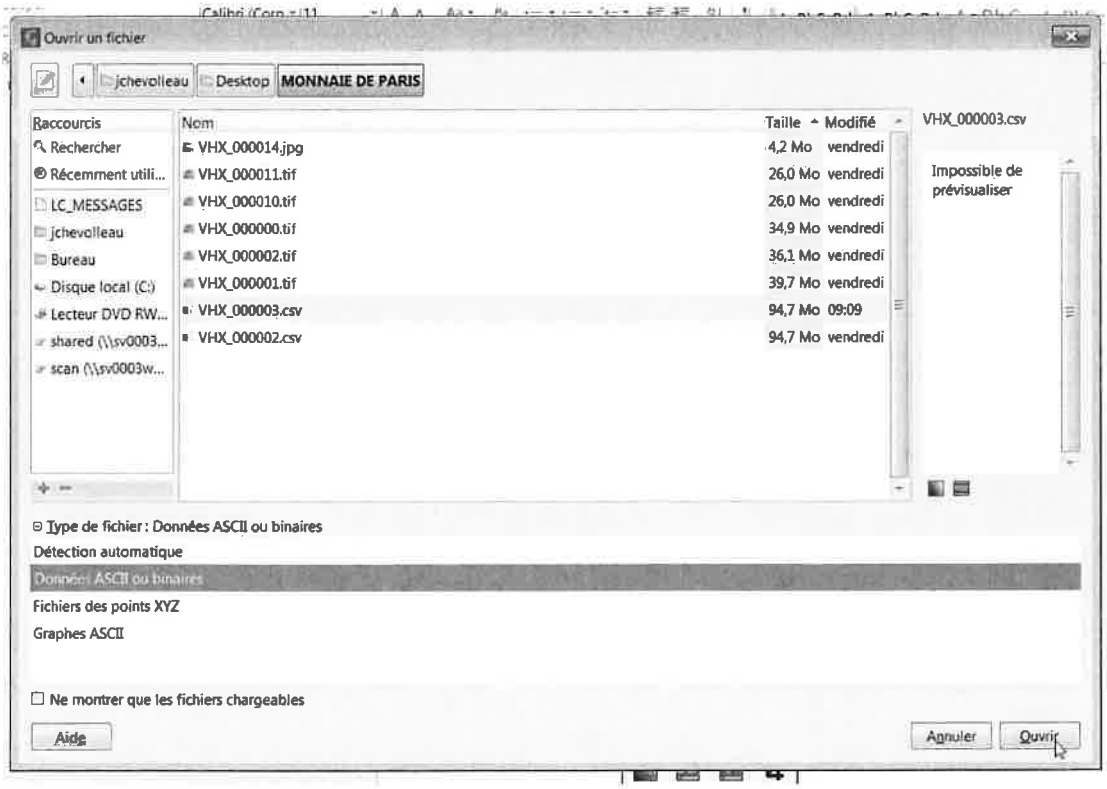

5) Voici les paramètres de réglage, vous devez connaitre à l'avance les dimensions du fichier en pixels mais aussi en mm

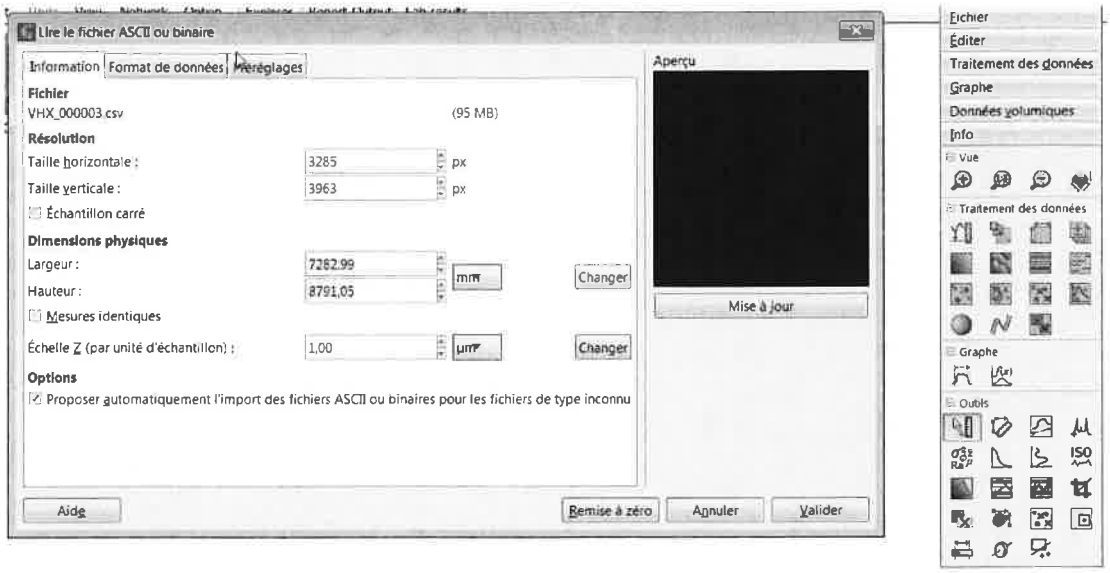

6) Pensez à régler le format de données, comme ci-dessous

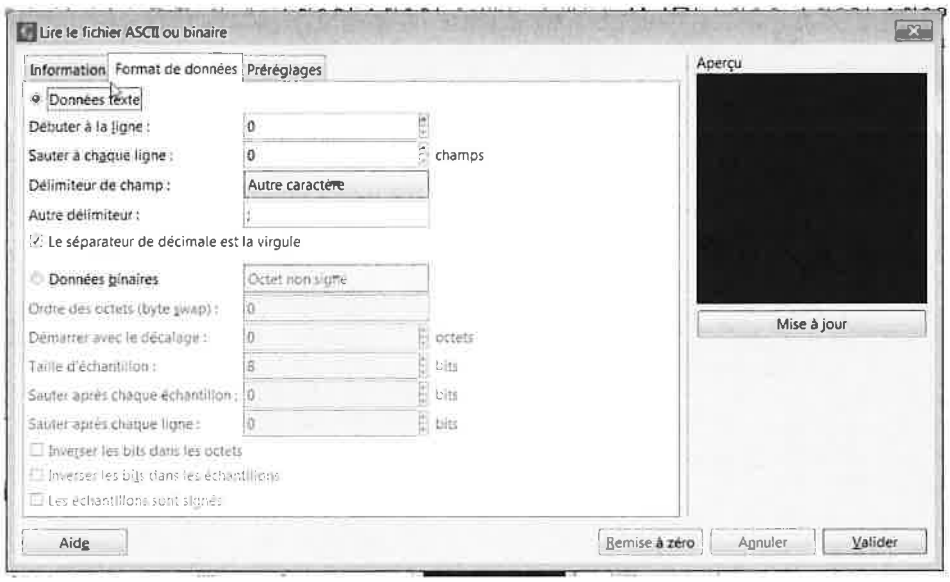

7) Puis vous validez et voilà le résultat

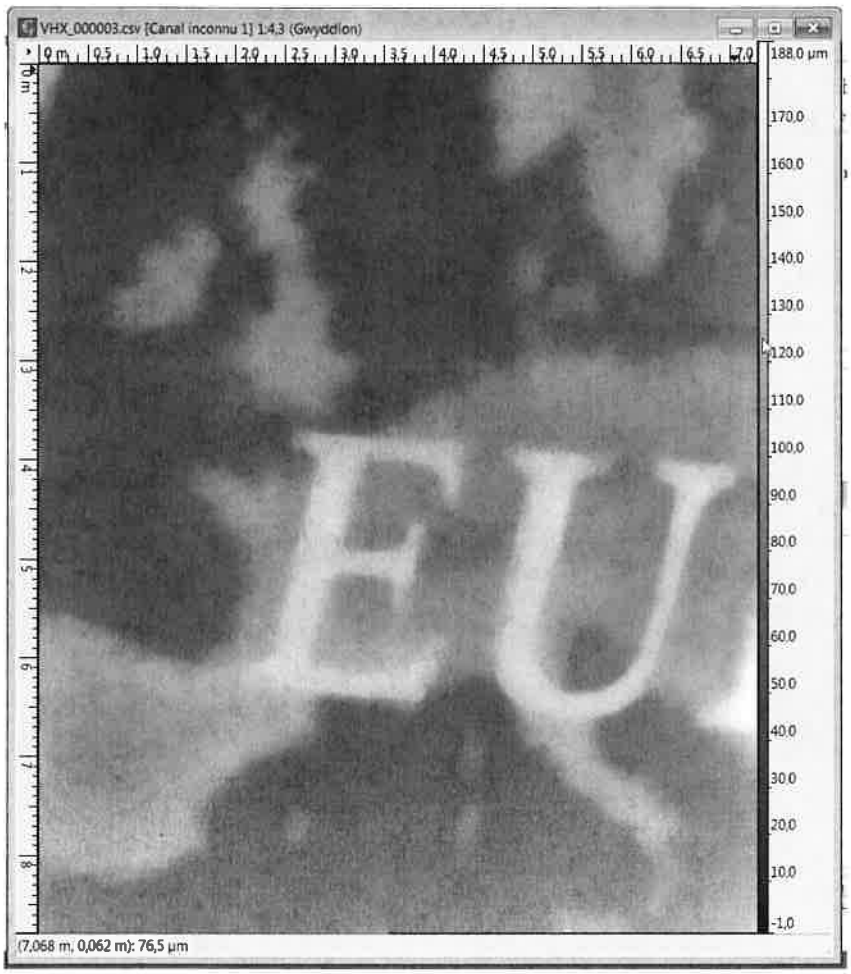

8) Pour voir en 3D c'est là

9) Et sauvegarder en 16 bits : Bien mettre le nom de fichier « .tif », type de fichiers tif et cocher l'option 16bits

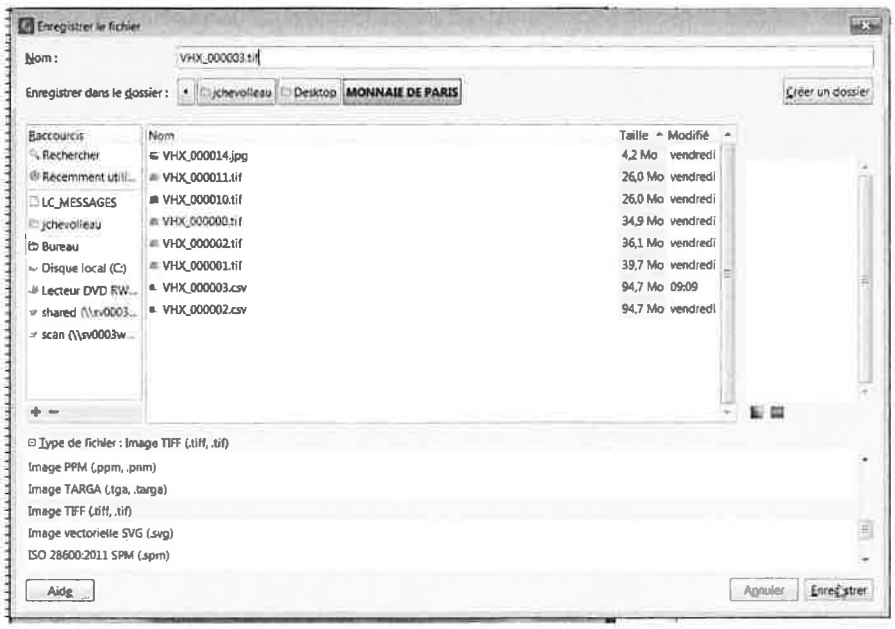

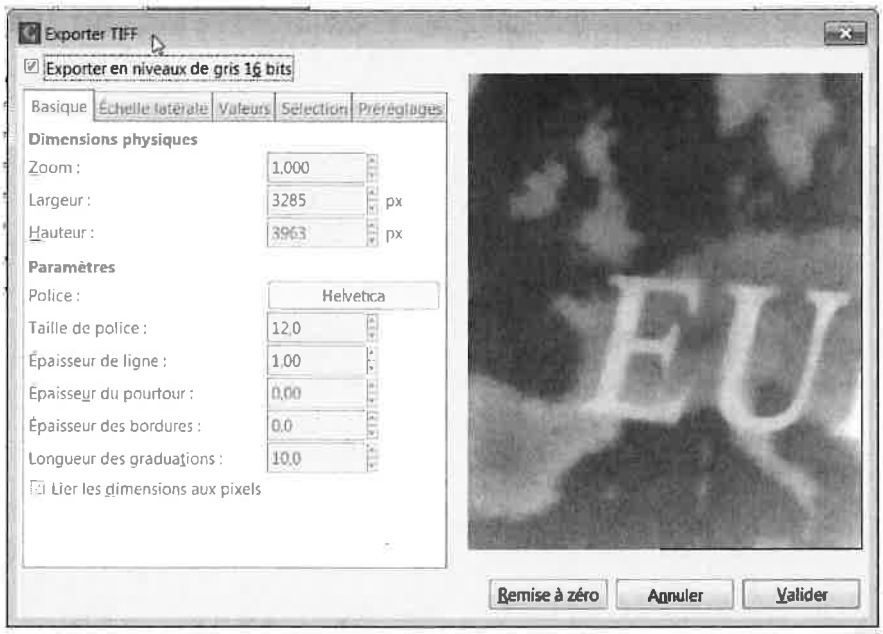

10) Gwiddion offre toutes les possibilités de manipulation de données 3D, ainsi que les outils de mesures de rugosités linéaires.

APPENDIX 4. Conference presentation

Organic coatings delamination from Zn-Ni coated steel

Presented by Thomas SANCHEZ,

thomas.sanchez@chimie-paristech.fr

Co-authors: D. BURLIAEV, V. SHKIRSKIY, J. SWIATOWSKA, J. ECHOUARD, P. VOLOVITCH

Outline

1. **Experimental**
   - Approach
   - Technics

2. Degradation kinetics in model system

3. Conclusions and perspectives

Approach to disbondment and measurement principles

Possible interface degradation phenomena*

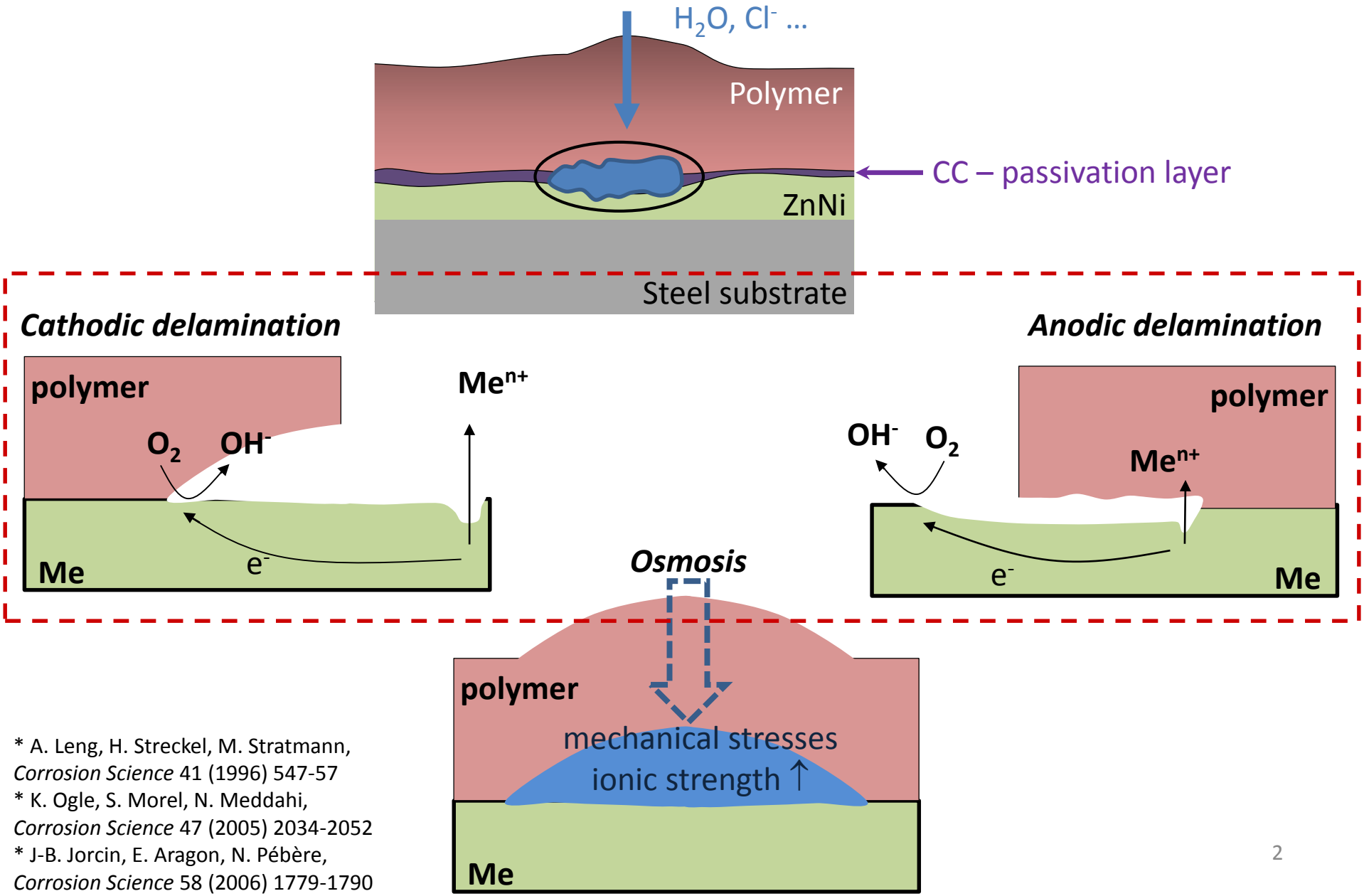

* A. Leng, H. Streckel, M. Stratmann, *Corrosion Science* 41 (1996) 547-57
* K. Ogle, S. Morel, N. Meddahi, *Corrosion Science* 47 (2005) 2034-2052
* J-B. Jorcin, E. Aragon, N. Pébère, *Corrosion Science* 58 (2006) 1779-1790

Approach to disbondment and measurement principles

Model system preparation

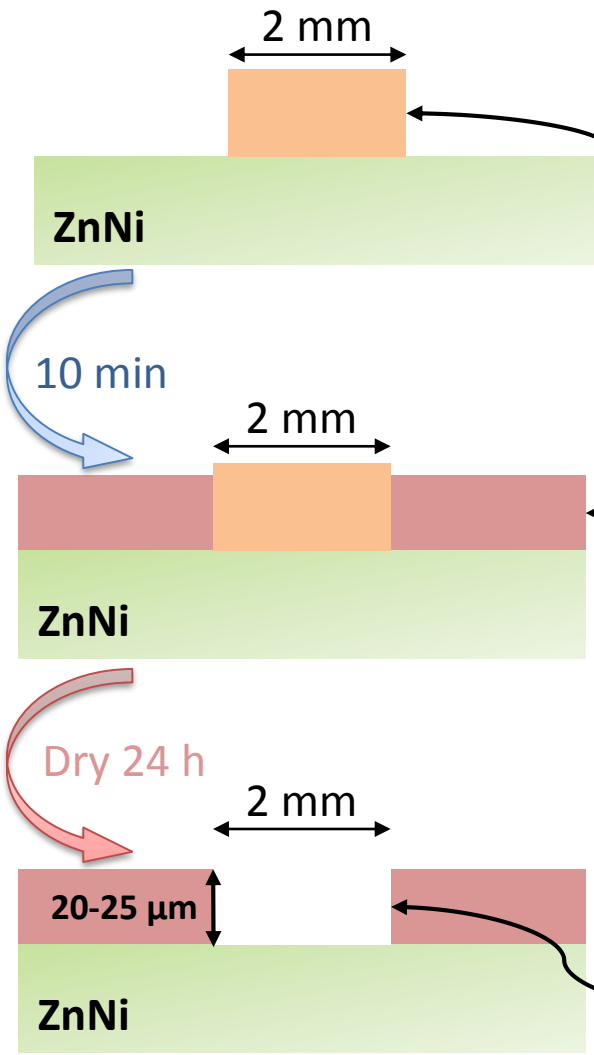

1. Paste Ø2 mm 3M Scotch

2. Polymer:
- 10 wt. % polyvinil butyral in ethanol, 25 ± 1 µm
- Model epoxy resin, 10 ± 1 µm

3. Remove Scotch carefully

Approach to disbondment and measurement principles

Model system preparation

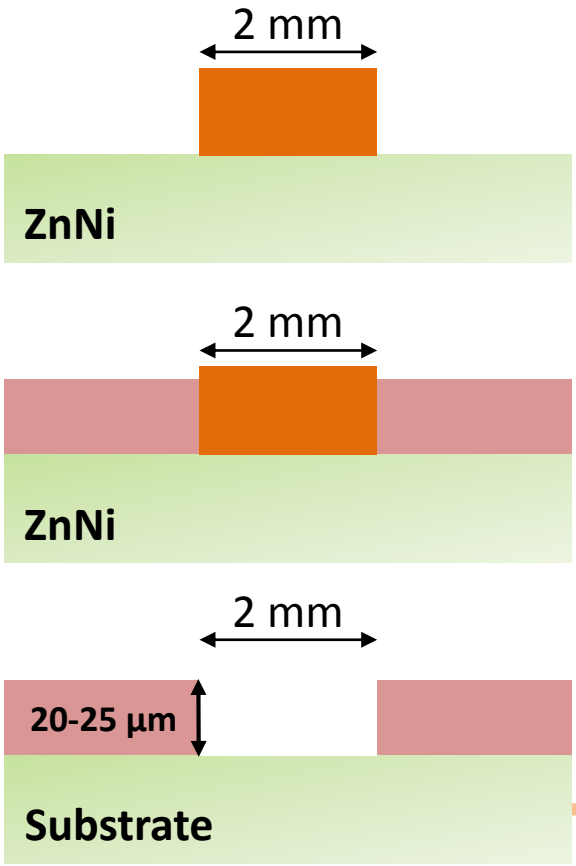

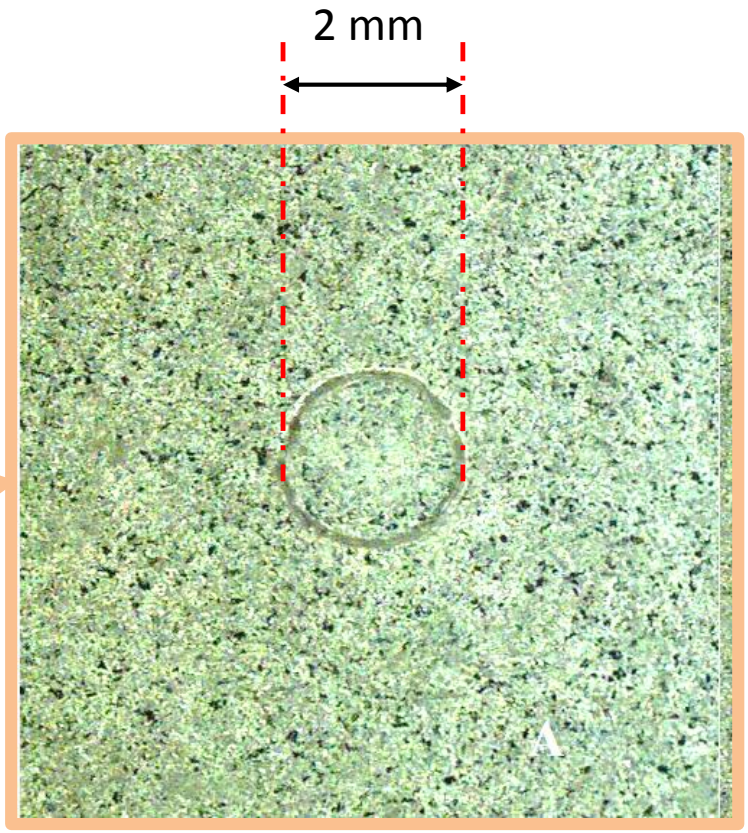

PVB, 25 µm

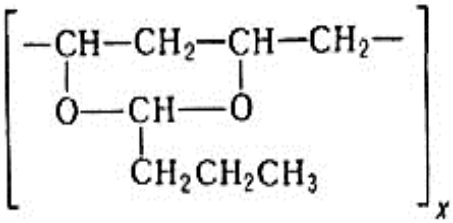

Approach to disbondment and measurement principles

Anodic reactivity measurement by Local Electrochemical Impedance Mapping (LEIM*)

AC perturbation → *Local difference in the potentials* (**E_2** *and* **E_1**)

Local current: $i_{local} = {(E_2 - E_1)}/{R}$

Maps of local admittance:

$$Z^{-1}(w) = {i_{local}}/{E_{global}}$$

Local admittance (reactivity)

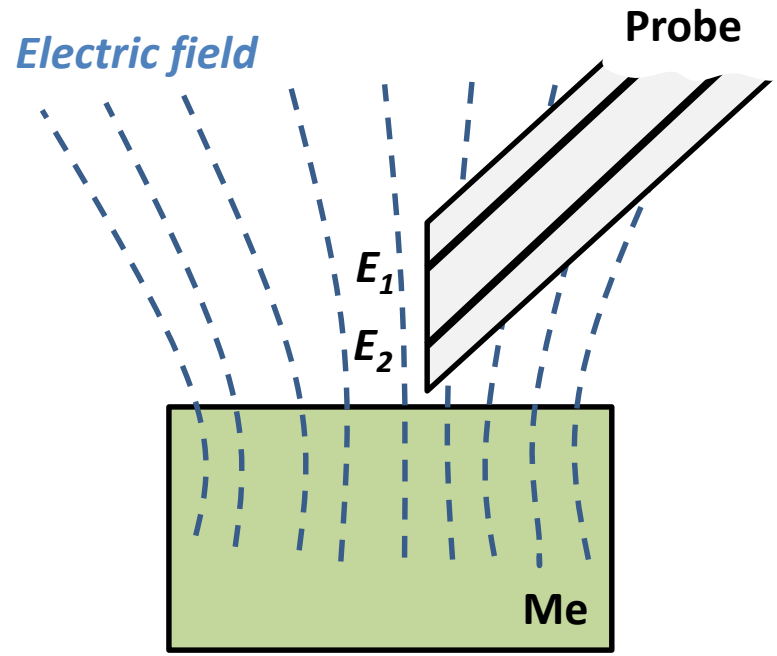

Spatial resolution under polymer: ~100 µm

* R. S. Lillard, P. J. Moran, H. S. Isaacs, *J. Electrochem. Soc.* 139 (1992) 1007-1012
* V. Shkirskiy, P. Volovitch, V. Vivier, *Electrochimica Acta* 235 (2017), 442-452

Details in presentation of V. Shkirskiy
Organic Coatings session, Wednesday 11 h 30

Approach to disbondment and measurement principles

Kinetics of delamination

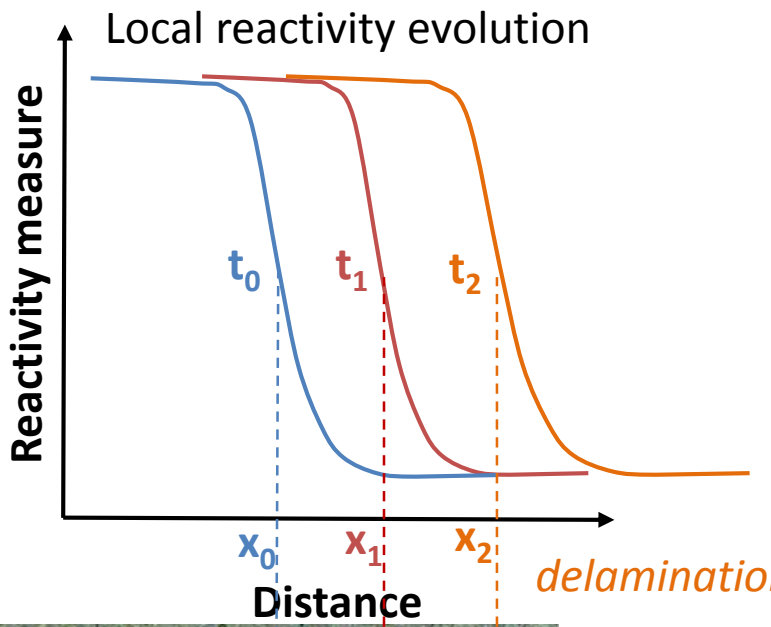

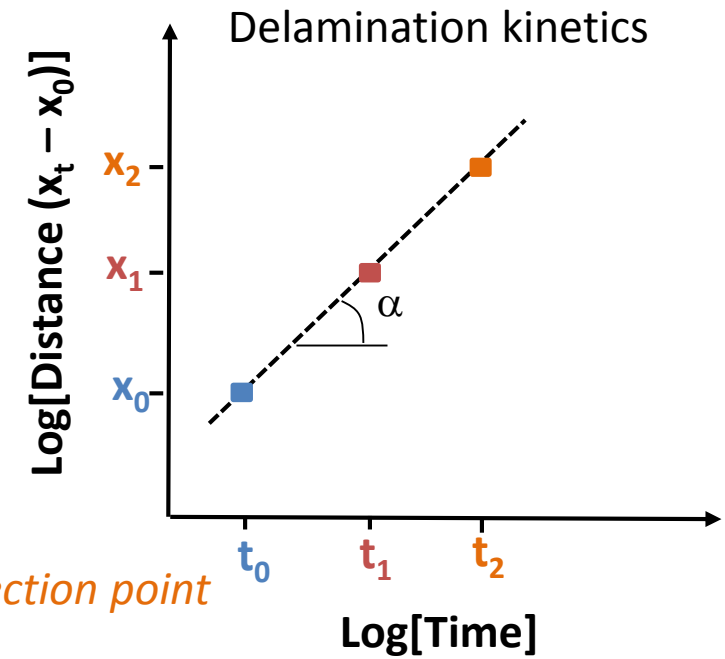

delamination front <==> inflection point

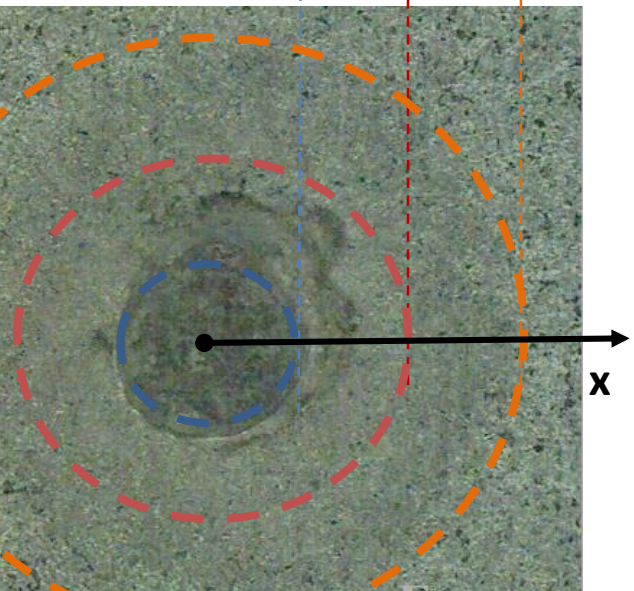

Local Reactivity Measurement

cathodic front – pH indicator

anodic front – local EIS

$$O_2 + 2\,H_2O + 4\,e^- = 4\,OH^-$$

Outline

1. Experimental approach

2. **Degradation kinetics in model system**
   cathodic delamination by TLM
   anodic delamination by LEIM

3. Conclusions and perspectives

Cathodic delamination by pH indicator

Visual evolution around a defect

non-passivated

t=0 h

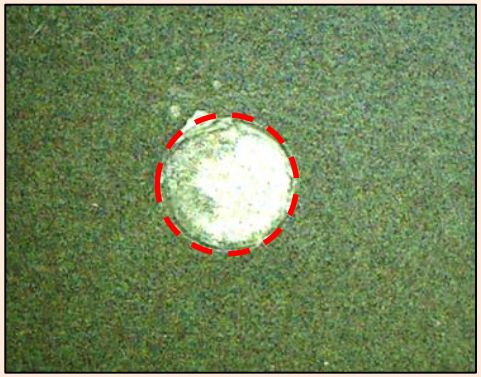

t=24 h / 0.5 M NaCl

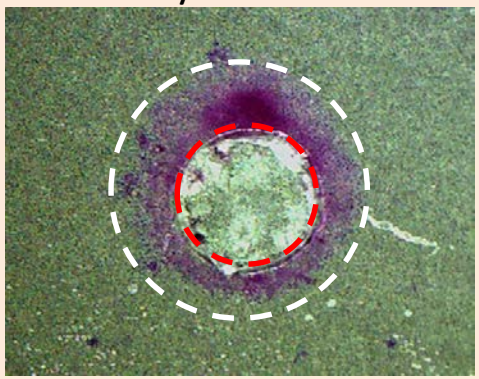

t=24 h / 0.5 M $NaHCO_3$

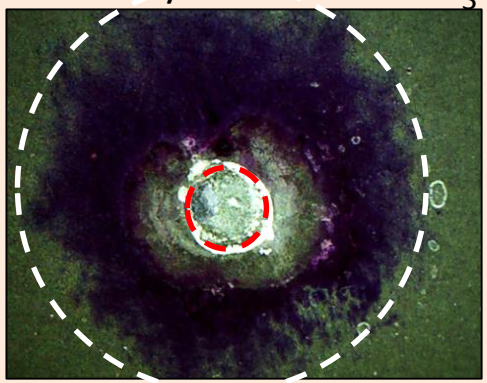

passivated

t=0 h

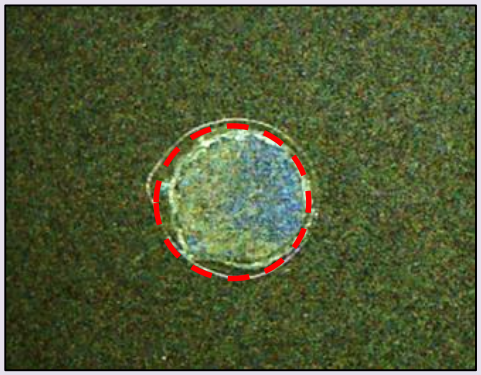

t=24 h / 0.5 M NaCl

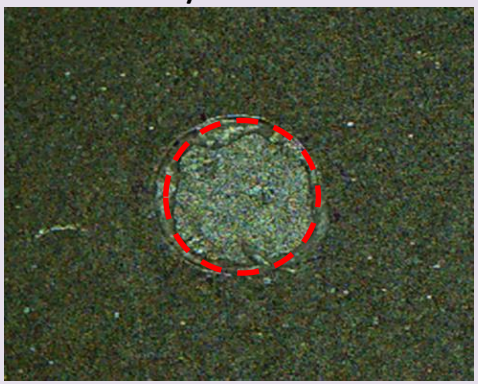

t=24 h / 0.5 M $NaHCO_3$

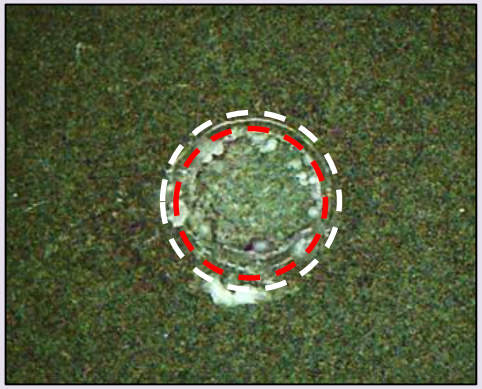

- ✓ *Slower cathodic delamination from passivated ZnNi*
- ✓ *Faster cathodic delamination in carbonates*
  effect reduced by conversion coating

pH buffering?
modification of cathodic reaction?

Cathodic delamination by pH indicator

Delamination kinetics

$$[D_t - D_0] = kt^{\alpha}$$

$$\alpha_{exp} = 0.8 - 0.9$$

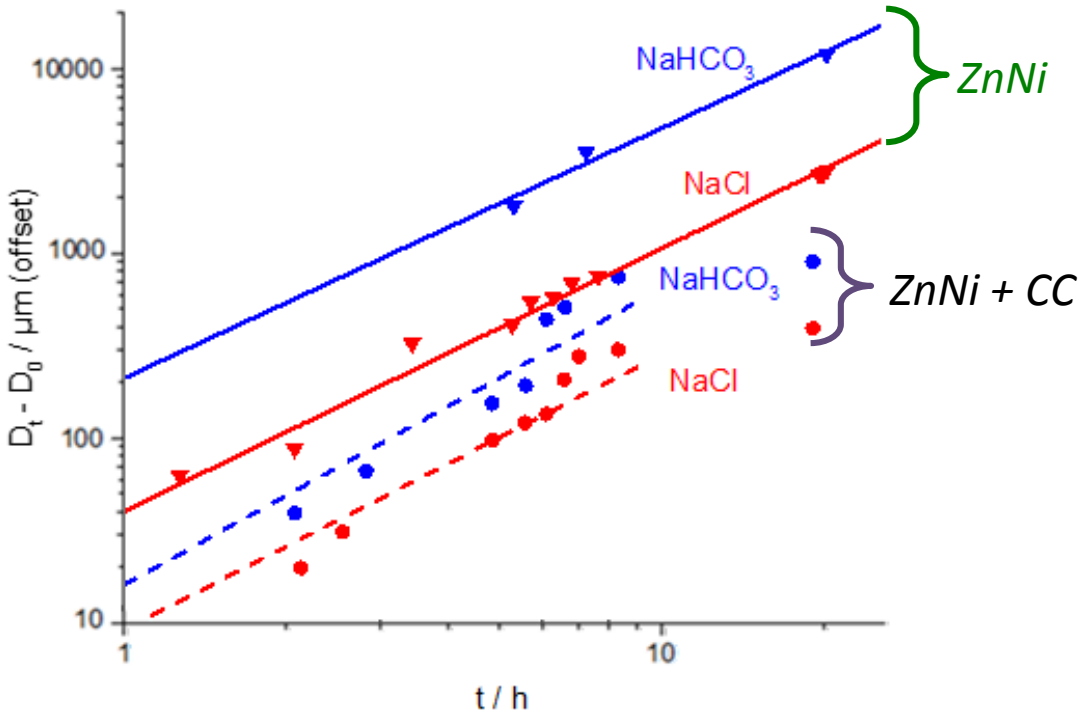

*Expected rate limiting step**

- ***Rate limited by surface reaction***
  - ✓ ***α = 1 – surface reaction***
  - ✓ ***α = 0.5 – mass transport (Zn)***

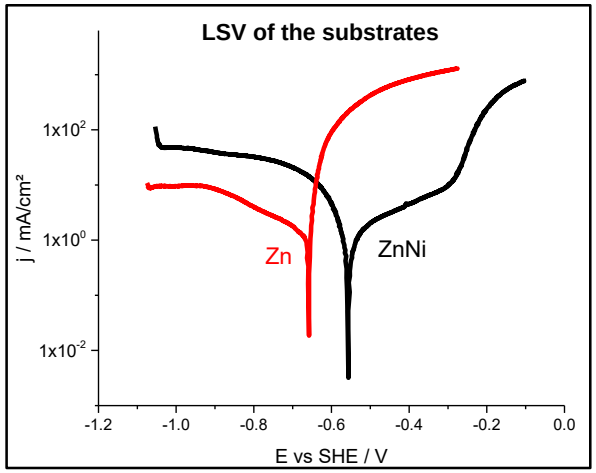

*Preferential dissolution of Zn***

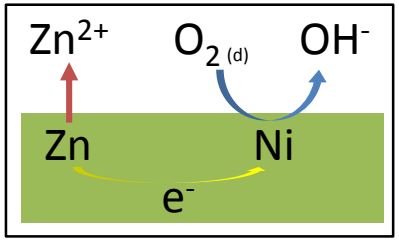

- *Confirmed*
  - ✓ *Slower cathodic delamination from passivated ZnNi*
  - ✓ *Faster cathodic delamination in carbonates effect reduced by conversion coating*

*W. Furbeth, M. Stratmann, *Corrosion Science* 43 (2001) 243-254

***See poster 96207 (O. Kozaderov)*

Anodic front propagation in 0.5 M NaCl by LEIM

Admittance (Z^{-1}) maps as a function of exposure time

Bare ZnNi

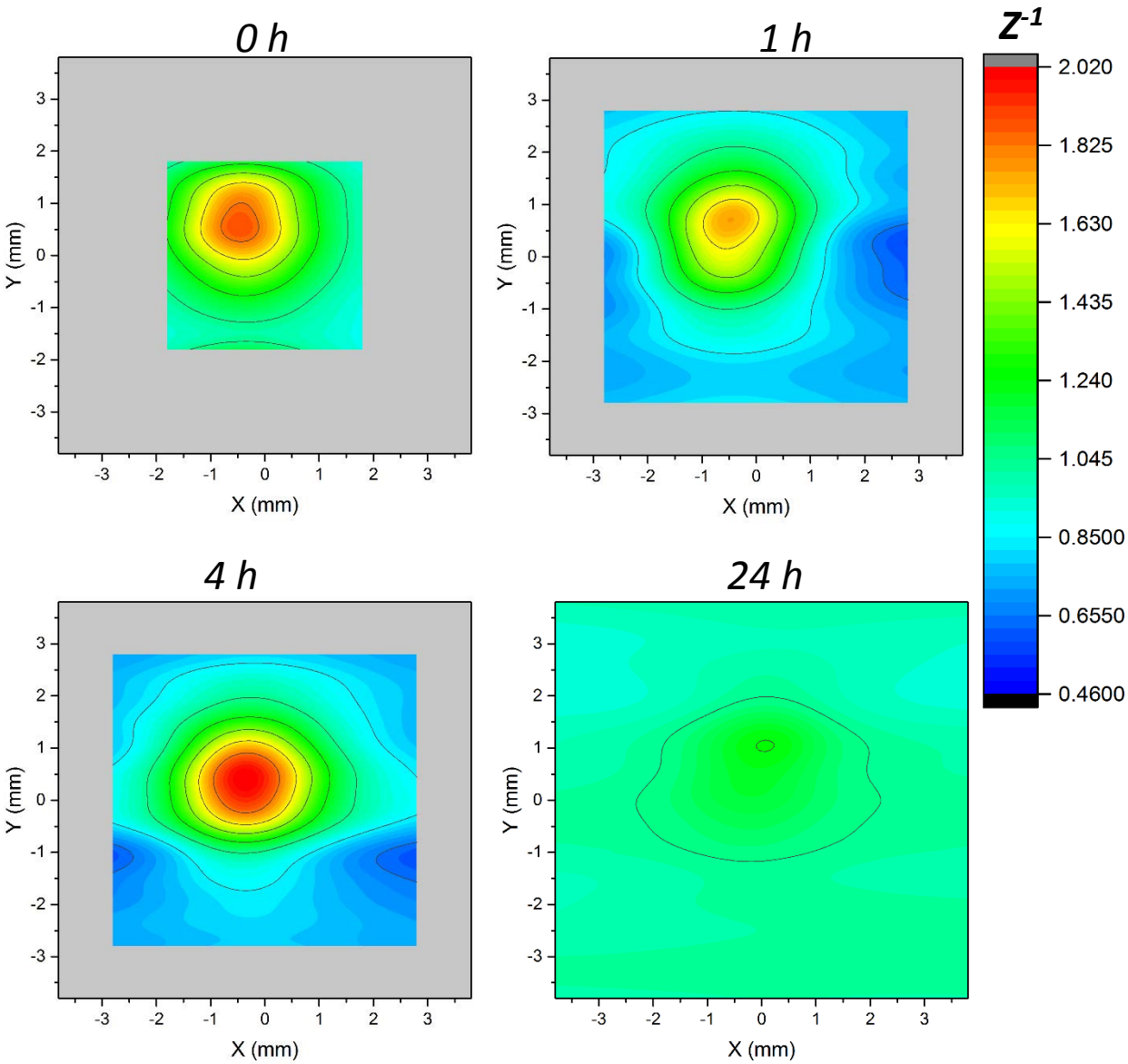

✓ Z^{-1} ↑ then ↓ in the defect

Ennoblement → *corrosion products*

Ennoblement → *Ni enrichment**

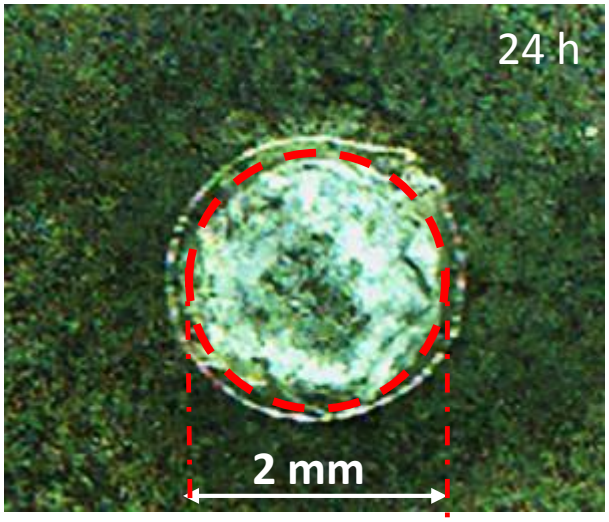

✓ Z^{-1} ↑ under the polymer

Reactivity under the polymer

***See poster 96207 (O. Kozaderov)*

Anodic front propagation in 0.5 M NaCl by LEIM

Gradient of admittance (Z^{-1}) maps at different exposure times

ZnNi CC

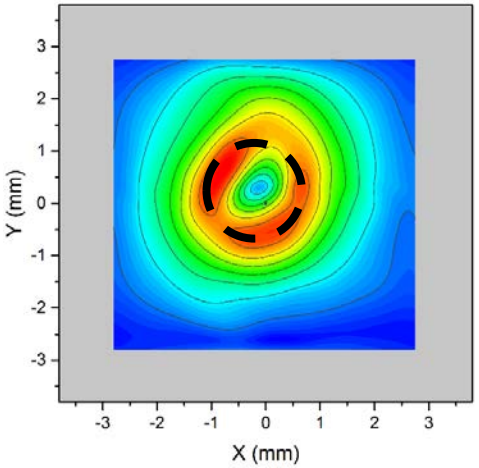

0 h

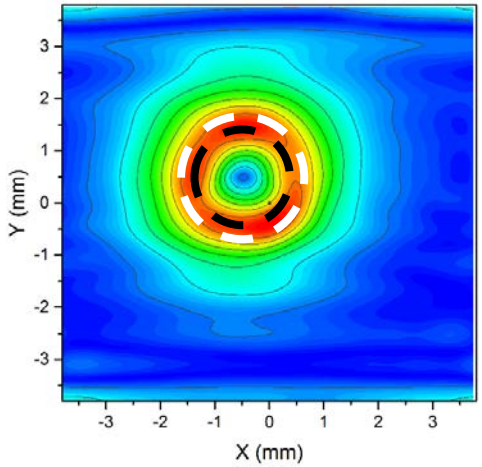

24 h

Lower reactivity of ZnNi + CC

Delamination kinetics

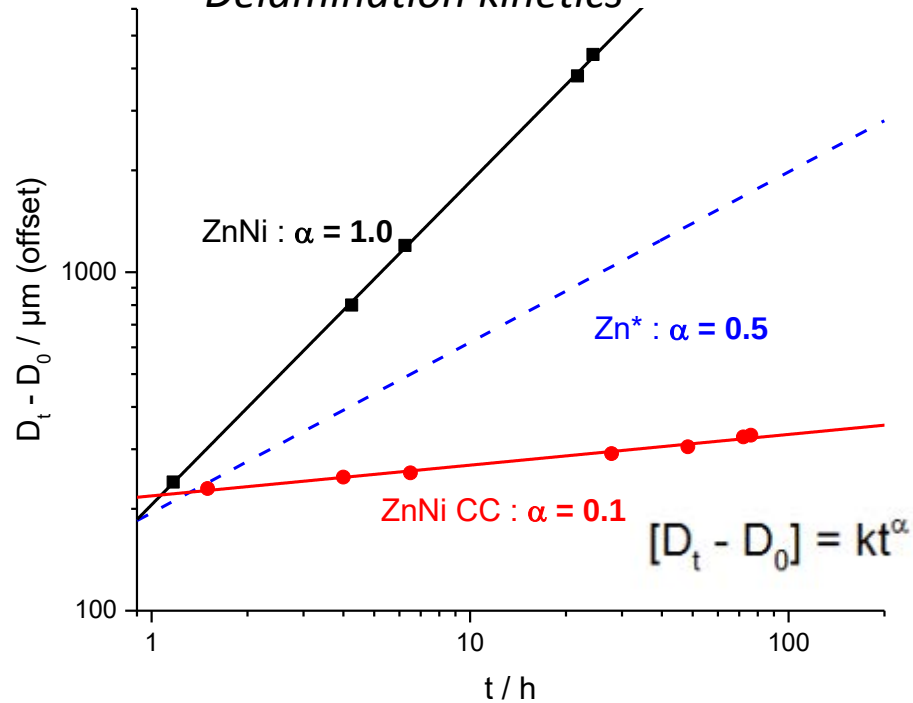

*Expected rate limiting step**

- ✓ ***α = 0.5 – mass transport (Zn)***
- ✓ ***α = 1 – surface reaction (ZnNi)***

- ✓ ***Mechanism on passivated ZnNi - to explore***

*W. Furbeth, M. Stratmann, *Corrosion Science* 43 (2001) 243-254
* V. Shkirskiy, P. Volovitch, V. Vivier, *Electrochimica Acta* 235 (2017), 442-452

Mechanistic conclusions for model ZnNi/paint interface

1. Mechanistic results from kinetic data

Surface reaction governs cathodic front propagation

No mass transfer limitation in any case

Soluble carbonates change delamination rate

Soluble carbonates don't change rate limiting step of cathodic reaction

2. Clear difference between ZnNi and passivated ZnNi:

Passivation
- changes rate limiting step
- slows cathodic front propagation
- slows anodic front propagation
- reduces the effect of carbonates

Résumé

Détection et quantification de la réactivité à l'interface metal-polymère in-situ: exemple de revêtements d'alliages en base zinc peints

Par

Thomas Sanchez

Thèse de doctorat en Chimie Physique Analytique

Introduction

Les alliages électrodéposés en base zinc sont majoritairement utilisés pour la protection sacrificielle des aciers, souvent de structure, dans le bâtiment, l'automobile, électronique et l'aéronautique. Pour augmenter lé durée de vie de ces assemblages anticorrosion, la protection sacrificielle de ces alliages est souvent combinée à une protection barrière via l'application de revêtements organiques (peintures)isolant les surfaces métalliques des environnement corrosifs.

Pour assurer une bonne adhérence des peintures sur les surfaces métalliques, et de ce fait améliorer la résistance à la corrosion de ces systèmes, des couches de conversions (CC) sont appliquées sur les métaux avant peinture. Ces conversions chimiques sont des fines couches organiques (sol-gel) ou inorganiques (oxydes, phosphates …). Il en résulte une stratégie de protection contre la corrosion multicouche : Substrat/alliage de protection sacrificielle/couche de conversion/couche(s) de peinture.

Bien que ces systèmes multicouches soient résistants à la corrosion, la complexité de leur structure les rend sensibles à de nombreuses causes de dégradation. La certaine perméabilité des peintures face à l'eau et des pertes d'adhérence localisées de la peinture sur la surface métallique peuvent entrainer une accumulation d'eau à l'interface. La présence d'eau à cette interface métal-polymère engendre souvent de la corrosion sous peinture ou un cloquage du revêtement. L'initiation et le développement de ces phénomènes de dégradation localisée est très complexe à détecter et mesurer.
Tenter d'appréhender les mécanismes de dégradation et mesurer la cinétique de corrosion de ces systèmes est encore aujourd'hui un défi. De plus, du fait de process industriels, ce défi est d'autant plus ardu à surmonter dans le cas de substrats rugueux, comme les alliages de zinc électrodéposés peints.

Dans ce doctorat, nous avons proposé une nouvelle méthodologie capable de corréler l'influence d'une fine couche de conversion avec la stabilité de l'interface métal-polymère dans des conditions d'immersion. Cette méthodologie consiste à combiner la détection de réactivité sous peinture par mesure de cartographie de spectroscopie d'impédance électrochimique locale et de l'imagerie in-situ avec des

caractérisations chimiques et morphologiques de surface ex-situ. L'objectif de ce doctorat est de répondre à la question suivante :

« Comment quantifier, in-situ et de manière localisée, l'évolution de la stabilité d'un assemblage métal-conversion-polymère intact en conditions d'immersion ? »

Pour répondre à cette problématique, nous avons proposé trois étapes analytiques :

- Proposer un système modèle permettant la mesure localisée de réactivité sous peinture et la combinaison de techniques analytiques in-situ
- Définir les limites analytiques des techniques choisies sur le système modèle
- Valider la méthodologie proposée pour la sélection intelligente de couches de conversion chimiques appliquées à des alliages en base zinc avec des mesures étalon.

Un objectif annexe de ces travaux de thèse fut de corréler la structure et la chimie d'une couche de conversion sur un substrat rugueux avec sa capacité à générer une interface métal-oxyde-polymère stable. Pour ce faire, il fut nécessaire de proposer une approche novatrice pour la caractérisation de couches de conversion à l'échelle nanométrique.

Ce manuscrit de thèse est organisé en quatre partie et six chapitres :

La première partie comporte une introduction ainsi qu'un état de l'art.

La deuxième partie comprend le développement de la méthodologie expérimentale ainsi que la description des techniques utilisées dans le cadre de la thèse.

La troisième partie comprend trois chapitres de résultats, sous forme de publication, et qui se focalisent sur les thématiques suivantes :

Le Chapitre 3 : « Un nouveau système pour l'examen intelligent des interfaces cachées : caractérisations électrochimiques locales d'alliages de zinc revêtus de peinture époxy modèle » présente l'approche méthodologique pour l'étude accélérée de perte de stabilité de l'interface métal-oxyde-polymère. La méthodologie inclus un protocole spécifique de vieillissement accéléré par voie électrochimique ainsi que l'application d'une peinture époxy modèle spécifiquement développée pour rester stable durant ce protocole. Il y est associé une mesure par électrochimie locale ainsi qu'une analyse d'image in-situ. Sur l'exemple d'alliage de zinc avec une couche de conversion au chrome trivalent, nous avons démontré que la méthode permet de discriminer les couches de conversion offrant une meilleure stabilité sous peinture que d'autres, pour des composition chimiques analogues.

Le Chapitre 4 : « Analyse de différentes distributions de couches de conversion appliquées sur de substrats rugueux par combinaison de techniques de surface localisées » couvre une approche méthodologique développée dans ce projet, permettant une description de la chimie et de la structure des fines couches d'oxyde sur des substrats électrodéposés rugueux. Cette méthodologie permet également un décapage homogène des couches d'oxydes à l'échelle nanométrique en dépit de la rugosité micrométrique du substrat. Différentes techniques de décapage de surface sont comparées en fonction de leur capacité à caractériser des surfaces rugueuses.

Le Chapitre 5 : « Limites analytiques de la cartographie d'impédance électrochimique localisée pour détecter des défauts nanométriques sous peinture » détaille les limites de la méthodologie proposée au chapitre trois sur des échantillons modèles générés avec la méthodologie développée dans le chapitre 4. L'influence du diamètre d'amincissements dans la couche d'oxydes sur la stabilité des systèmes peints est décrite. L'existence d'une taille critique de défaut pour induire une dégradation à l'interface métal-oxyde-peinture est soulignée.

La quatrième partie de ce manuscrit couvre la conclusion et les perspectives de ces travaux.

Ce résumé en français reprend la même structure que la version en anglais en proposant pour chaque partie, une synthèse des conclusions majeures des chapitres.

1. Etat de l'art

Ce chapitre introduit les bases à propos des interfaces métal-oxyde-polymère dans le cadre de surfaces métalliques peintes et présente un aperçu des techniques de caractérisation de ces interfaces cachées. Dans ce but, l'état de l'art reprend en trois sections les stratégies de protection contre la corrosion, les différents types de couches de conversion, promoteur d'adhérence de la peinture et les modes et mécanismes de dégradation de ces interfaces dans le cadre de systèmes multicouches. Les sections 4 et 5 décrivent ensuite les méthodes d'analyse in-situ de dégradation sous peinture et les possibles analyses de surfaces. Cette introduction se clos sur une série de question auxquelles le manuscrit de thèse tâchera de répondre.

1.1. Les bases de la protection contre la corrosion

La corrosion est un processus naturel décrivant la destruction graduelle des matériaux, souvent des métaux, par voie chimique ou électrochimique. Elle consiste en une oxydation des métaux (M^0) en espèces plus stables dans les conditions normales de pression, température et hygrométrie : des oxydes et hydroxydes trouvés dans la nature (M^{n+}). Le diagramme de Pourbaix présenté en figure 1.1 illustre l'impossibilité de stopper la corrosion du fer métallique en présence d'eau. On pourrait ainsi dire que « Tenter de stopper la corrosion des métaux, c'est comme jouer contre dieux, ou dans ce cas spécifique, la thermodynamique : vous courrez à votre perte, mais come vous le faites avec des technologies chères et raffinées, alors tout va bien ».

Dans ce cadre, la protection de la corrosion ne consiste pas à la stopper, mais à la ralentir du mieux possible.

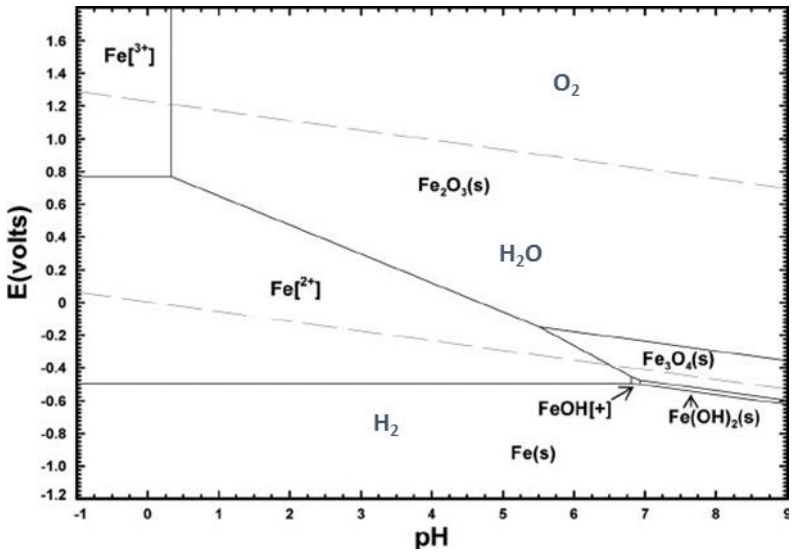

Figure 1.1: Superposition des diagrammes de pourbaix du fer et de l'eau à 298K.

Pour déterminer au mieux la stratégie de protection contre la corrosion, il faut comprendre le mécanisme de corrosion et agir sur les étapes élémentaires de ce processus. On dénombre deux moyens de ralentir la corrosion : la protection active et la protection passive.

La protection active contre la corrosion

La protection active contre la corrosion consiste à déposer une espèce chimiquement ou électrochimiquement active au contact du métal à protéger pour modifier le mécanisme de corrosion. Ce peut être effectué par usage d'un alliage sacrificiel ou par l'utilisation d'inhibiteurs de corrosion.

La protection sacrificielle consiste à connecter la surface métallique à protéger à un autre métal plus actif (ou moins noble) qui s'oxydera à sa place. Ceci permet de supprimer l'étape anodique sur le métal à protéger et ainsi de limiter sa corrosion. Cette méthode est aujourd'hui une des plus utilisée pour protéger l'acier contre la corrosion. Les alliages les plus utilisés sont ceux en base zinc et cadmium.

La protection active par utilisation d'inhibiteurs de corrosion consiste à modifier la réactivité, soit en formant un film organique protecteur localisé sur la surface métallique dans les sites anodiques ou cathodiques, soit en formant une couche d'oxyde imperméable sur la surface métallique lorsqu'elle est agressée, soit en agissant comme tampon (pH, chlorures …) pour réduire l'agressivité du milieu auquel le métal est exposé. Le chrome hexavalent est un des inhibiteurs de corrosion les plus utilisés.

La protection passive contre la corrosion

2galement appelée « protection barrière », elle est assurée par une couche protectrice formée sur la surface métallique, souvent de la peinture, qui assure une isolation du métal par rapport à

l'environnement. La composition des peintures est souvent complexe. Une manière simple de voir la protection passive contre la corrosion est qu'elle permet de retarder la dégradation du matériau.

Structure typique d'un système de protection contre la corrosion

Les systèmes anticorrosion sont souvent complexes pour combiner à la fois protection actives et passives tel qu'illustré dans la figure 1.2.

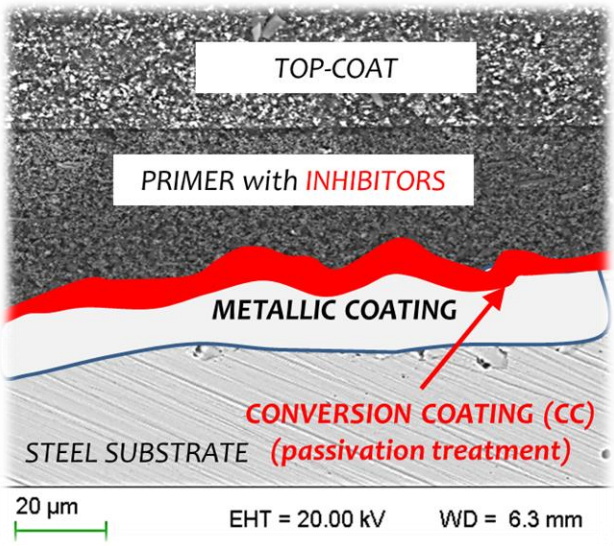

Figure 1.2: Schéma typique d'un système de protection contre la corrosion (echelle non respectée)

Ces systèmes consistent en un alliage métallique sacrificiel protégeant le métal, une couche de conversion permettant une meilleure adhérence de la peinture, une première peinture (primaire) anticorrosion et une couche de peinture de finition (top-coat) assurant une résistance face aux agression de l'environnement (UV, rayures etc.)

D'après la bibliographie, la bonne adhérence de la peinture sur le substrat métallique est un paramètre clef dans la protection contre la corrosion.

1.2. Couches de conversions

Comme énoncé précédemment, la conversion chimique de la surface permet d'améliorer l'adhérence de la peinture sur le substrat métallique. Dans le cadre des alliages en base zinc, les couches de conversions au chromes hexavalents étaient les plus utilisées, mais du fait de leur toxicité, elles doivent aujourd'hui être remplacées. On note l'existence de couches de conversion organiques (sol gel) ou inorganiques (oxydes). Dans le cadre de ces travaux, le choix sera porté sur une fine couche de conversion au chrome trivalent (TCC) tel qu'illustré en figure 1.3.

Ces couches de conversion sont très fines, et de fait, sensibles aux environnements.

Leur capacité à protéger les métaux contre la corrosion n'est plus à prouver, mais leur capacité à induire une interface métal-oxyde-polymère stable reste à élucider.

1.3. Modes de dégradation des interfaces métal-oxyde-peinture

Les modes de dégradation des métaux peints ne sont pas tous élucidés et restent complexes à mesurer. Il existe 6 modes fondamentaux de décohésion d'une peinture telle que décrite par Leidheiser : le cloquage, la rouille avancée, la rouille flash, la dissolution sous peinture, la délamination cathodique et la corrosion filiforme.

Avant d'initier de la corrosion sous peinture, l'origine de l'instabilité des systèmes peints provient du fait que la peinture n'est pas imperméable à l'eau, et que des oxydes ou traces de minéraux sont souvent présents à l'interface métal-peinture. Ainsi, l'eau traverse la peinture et solubilise ces espèces, générant un gradient de concentration qui force l'eau à diffuser vers l'interface tel qu'illustré dans la figure 1.4.

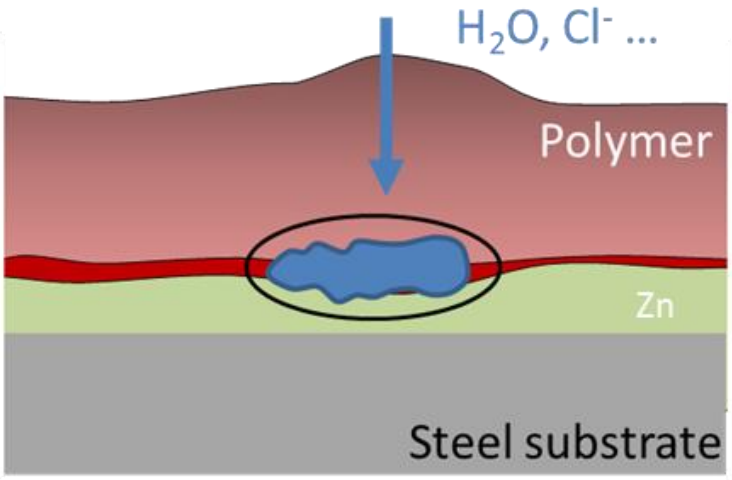

Figure 1.3: Illustration de la diffusion de l'eau à travers une peinture par force osmotique

Pour résumer la théorie de Leidheiser, la perte d'adhérence d'une peinture provient de zones de plus faibles adhérence préexistantes à l'interface.

Conclusion de l'état de l'art

De nombreux processus expliquent la dégradation des systèmes peints et peuvent se produire à l'interface métal-oxyde-peinture. La plupart d'entre eux sont des processus électrochimiques. De ce fait, un vieillissement électrochimique et une mesure par spectroscopie d'impédance électrochimique dans sa variante localisée semblent être un choix optimal pour ces travaux de thèse.

Cet état de l'art nous a mené à se poser trois interrogations auxquelles nous tenterons de répondre dans la thèse :

1. Comment mesurer la réactivité locale in-situ à l'interface métal-oxyde-polymère sur es substrats rugueux, et sous une couche de peinture intacte ?
2. Comment décorréler les effets des couches de conversion sur la stabilité du système peint des effets des épaisses couches de peinture ou des défauts introduits dans les systèmes peints ?
3. Comment décrire de manière précise la structure et la chimie des couches de conversion déposées sur des substrats électrodéposés rugueux ?

Les deux premières questions trouveront leurs réponses dans les chapitres 3 et 5 alors que la dernière question sera adressée dans le chapitre 4.

2. Expérimental

A partir de la bibliographie, plusieurs techniques ont été sélectionnées pour permettre de de comprendre les mécanismes de dégradation des couches de conversion dans les interfaces cachées en condition d'immersion.

Matériaux

Les substrats utilisés seront de l'acier galvanisé fourni par Chemetall ainsi que de l'acier THR revêtu d'un alliage de ZnNi électrodéposé. Les couches de conversion étudiées seront des couches au chrome trivalent.

Afin de modéliser les peintures industrielles, un polymère époxy modèle de composition DGEBA-TETA sera proposé dans la thèse.

Méthodologies

Pour permettre un vieillissement accéléré des échantillons peints, le test ACET de vieillissement électrochimique sera utilisé (Figure 2.4).

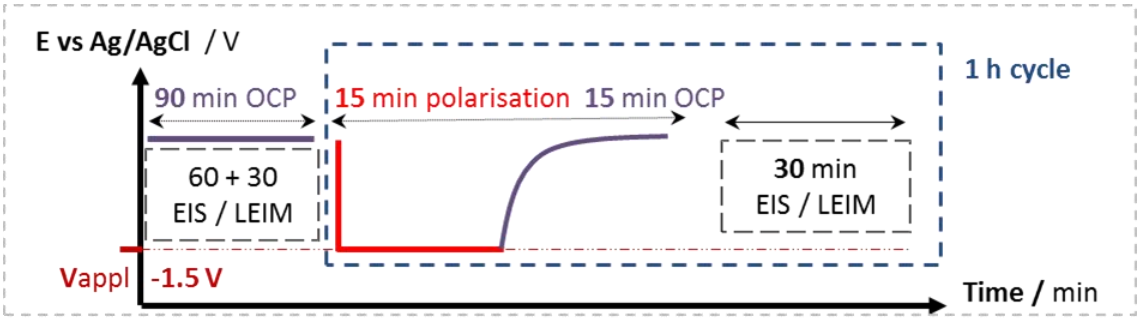

Figure 2.4: Schematic description of the AC-DC-AC procedure cycle used in the study

L'enjeu de ces travaux consistera à proposer une combinaison entre la cartographie d'impédance électrochimique et l'imagerie in-situ pour déterminer les cinétiques de dégradation aux interfaces cachées, tel qu'illustré en figure 2.5.

Afin d'améliorer la résolution de la technique électrochimique, une cellule spécifique à l'étude a été développée et imprimée en 3D, permettant une uniformisation radiale de la distribution en courant dans l'électrolyte durant les mesures.

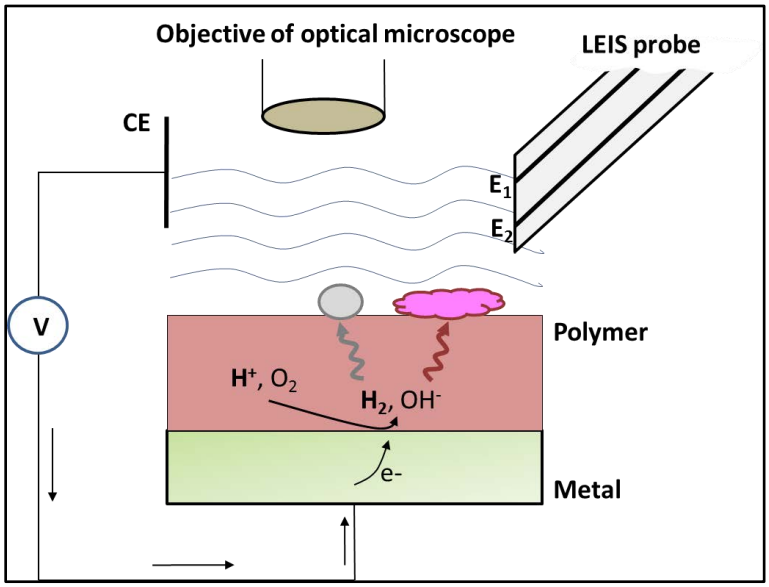

Figure 2.5: Schéma du setup expérimental

Une première vérification de la méthodologie proposée et décrite en Chapitre 3 a été proposée et publiée : elle consiste à mesurer la cinétique de croissance de délamination dans la peinture à partir d'un défaut modèle par cartographie EIS et par imagerie in-situ. Les cinétiques mesurées sont corrélées aux mesures empiriques déterminées par d'autres techniques sur les mêmes systèmes (Figure 2.5).

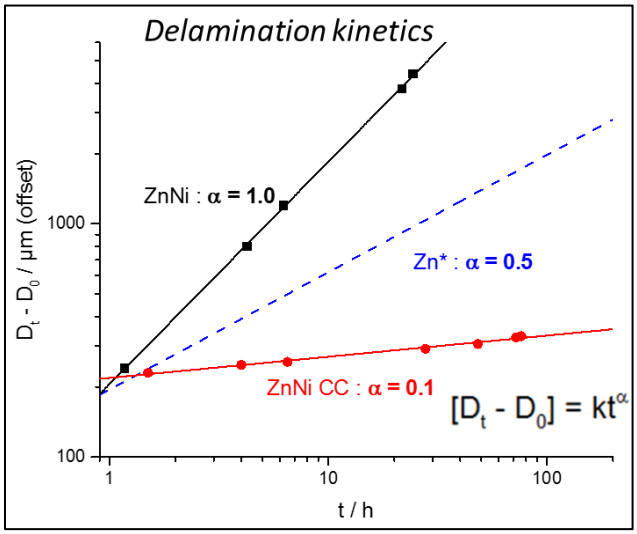

Figure 2.6: Exemples de cinétiques de delamination anodiques par LEIMà partir d'un défaut de 2 mm de diameter dans une peinture PVB

3. Un nouveau système pour l'examen intelligent des interfaces cachées : caractérisations électrochimiques locales d'alliages de zinc revêtus de peinture époxy modèle

La méthodologie proposée consiste en un vieillissement ACET tel que décrit en Figure 2.4. Elle permet une classification rapide en termes de performances de couches de conversion pour induire une interface métal-oxyde-peinture stable.

Lors de la mise en place de cette méthodologie, la stabilité de la peinture a été vérifiée afin de décorréler son vieillissement de celui de l'interface cachée. Des mesures en EIS et en infra-rouge ont été effectuées (Figure 3.7).

Elles permettent de conclure que l'accumulation de l'eau se fait en environ 5h dans la peinture. En revanche, l'évolution des pics OH et H_2O démontrent une formation de liaisons OH dans le polymère au détriment de la présence de pics caractéristiques dans les cycles époxy phénoliques. On observe ainsi une dégradation de la peinture au-delà de 70h d'immersion.

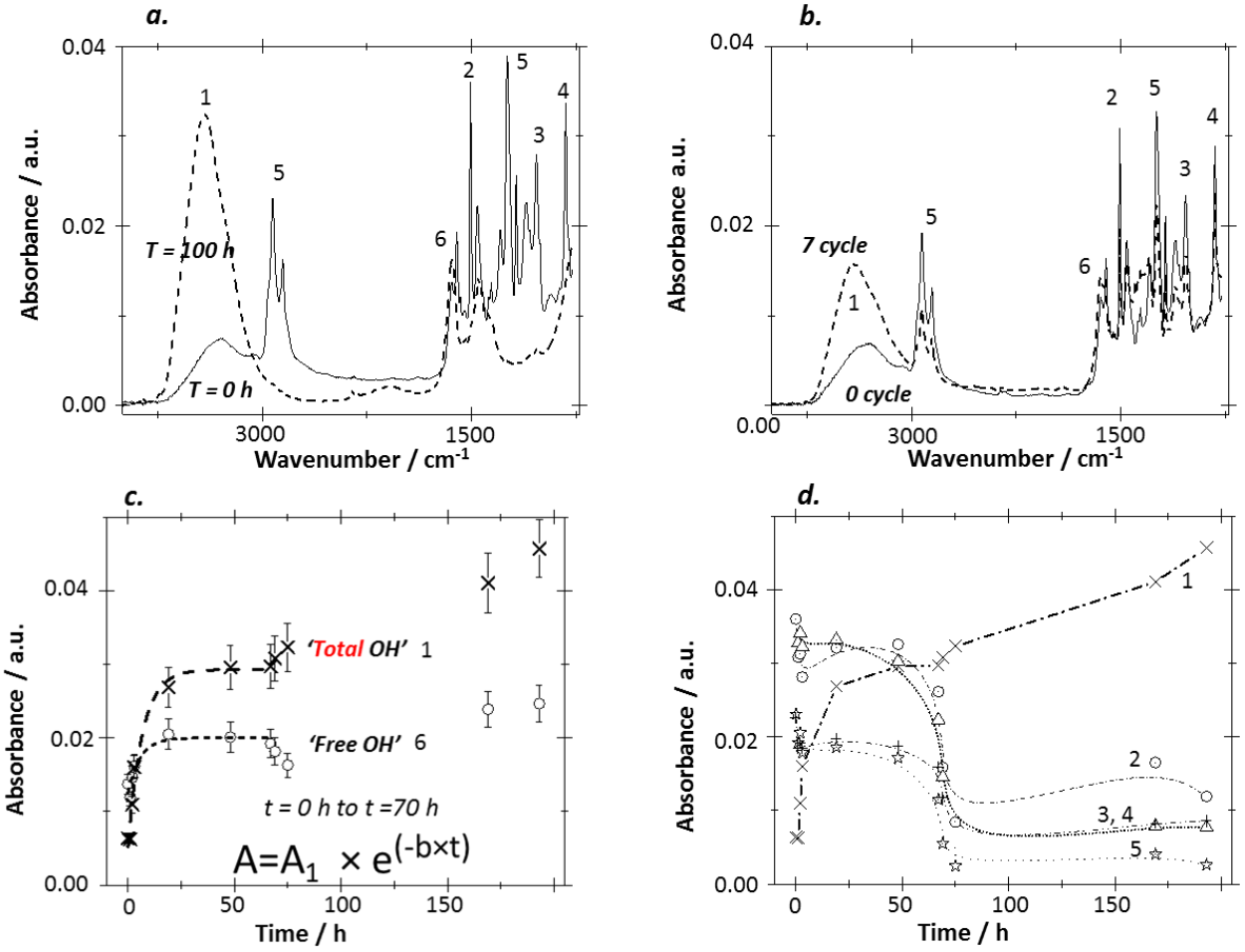

*Figure 3.7: ATR-IR spectroscopie (**a, b**) et évolution des pics caractéristiques de la peinture en function du temps d'immersoin (**c, d**). (**a**) après 100h d'immersion, (b) après 7 cycles ACET compares à la reference telle qu'appliquée; (**c**) évolution des pics caractéristiques de l'eau libre (H_20) et des liaisons OH totals dans la peinture (**d**)*

La dégradation du système a été caractérisée par de nombreuses techniques in-situ, notamment la cartographie d'impédance électrochimique et la microscopie in-situ. L'interface semble se dégrader de manière localisée à partir d'environ 50h d'immersion d'après l'évolution du module d'impédance mesuré. On peut ainsi conclure que la peinture ne se dégrade pas tant que l'interface métal-oxyde-polymère (i.e. la couche de conversion) reste stable.

De plus, les mesures de cartographie LEIM permettent de détecter des sites réactifs sous peinture lors de la dégradation du système avant que ceux-ci ne soient visible par microscopie in-situ àl'aide de la peinture modèle. Les sites réactifs ne sont pas visualisables en EIS sous des peintures industrielles (figure 3.8).

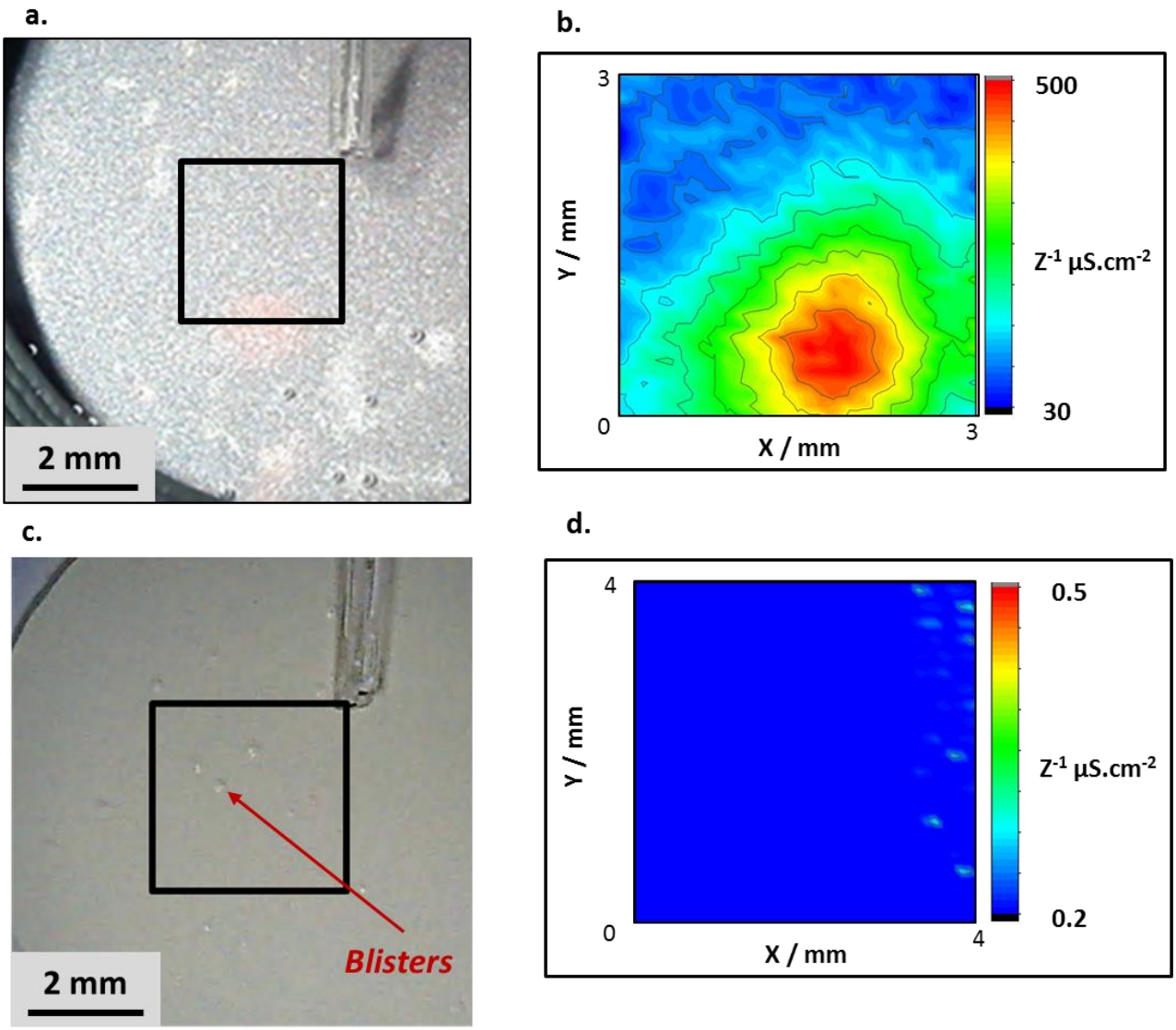

*Figure 3.8: Microscopie in-situ (**a, c**) et cartographies LEIM (**b, d**) de l'échantillon avec la peinture modèle (**a, b**) d'un échantillon peint avec une peinture industrielle (**c, d**).*

En plus de permettre une mesure de la réactivité sous peinture, cette méthodologie permet de discriminer les couches de conversion générant une interface stable des couches de conversions instables tel qu'illustré dans la figure 3.9.

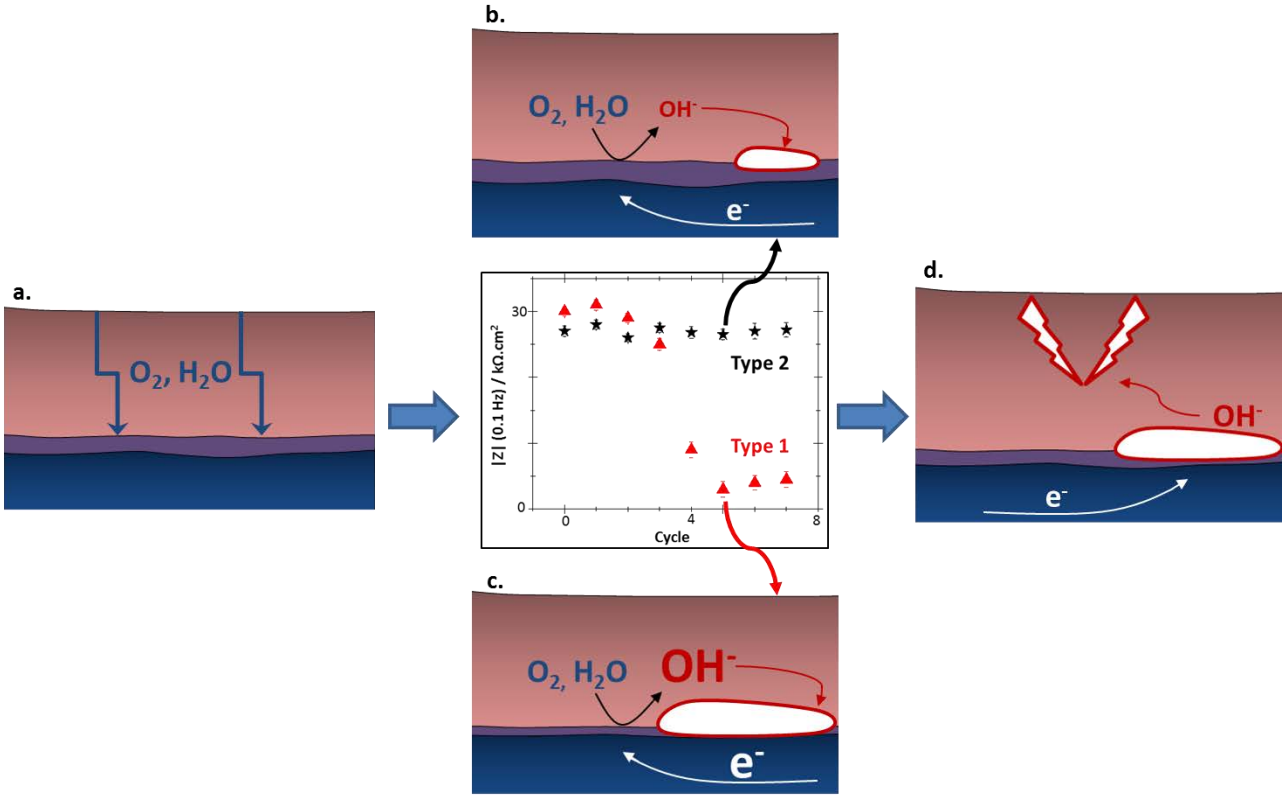

*Figure 3.9: Description schématique de la degradation de l'interface metal-peinture dans la méthodologie proposée (**a**). Pour une faible (**b**) ou forte (**c**) stabilité de l'interface metal-peinture. La mesure de stabilité est associée au module d'impédance électrochimique. Une fois l'interface dégradée, la peinture se degrade à son tour (**d**)*

En plus de permettre une mesure de la réactivité sous peinture, cette méthodologie permet de discriminer les couches de conversion générant une interface stable des couches de conversions instables tel qu'illustré dans la figure 3.9.

Cette méthodologie est proposée pour la classification rapide des systèmes de conversion chimiques pour peinture en fonction de leur capacité à permettre une bonne adhérence de la peinture en immersion.

4. Analyse de différentes distributions de couches de conversion appliquées sur de substrats rugueux par combinaison de techniques de surface localisées

Une méthodologie combinant plusieurs techniques d'analyse de surface a été proposée dans ces travaux de thèse pour caractériser la chimie et la distribution des oxydes dans une couche de conversion au chrome trivalent sur un substrat électrodéposé en base zinc (Figure 4.10). De manière classique, l'XPS et le ToF-SIMS sont des techniques hautement recommandées pour caractériser ce type de substrats. L'XPS permet une description quantitative de la chimie de la couche d'oxydes alors que le ToF-SIMS permet une mesure de la distribution des oxydes sur la surface. Or, certains travaux revus dans la bibliographie décrivent une incapacité du ToF-SIMS à caractériser les surfaces rugueuses du fait de la géométrie des canons à ion dans la chambre d'analyse. Pour évaluer son influence, ces travaux ont été également effectués par couplage entre l'XPS et le GD-OES.

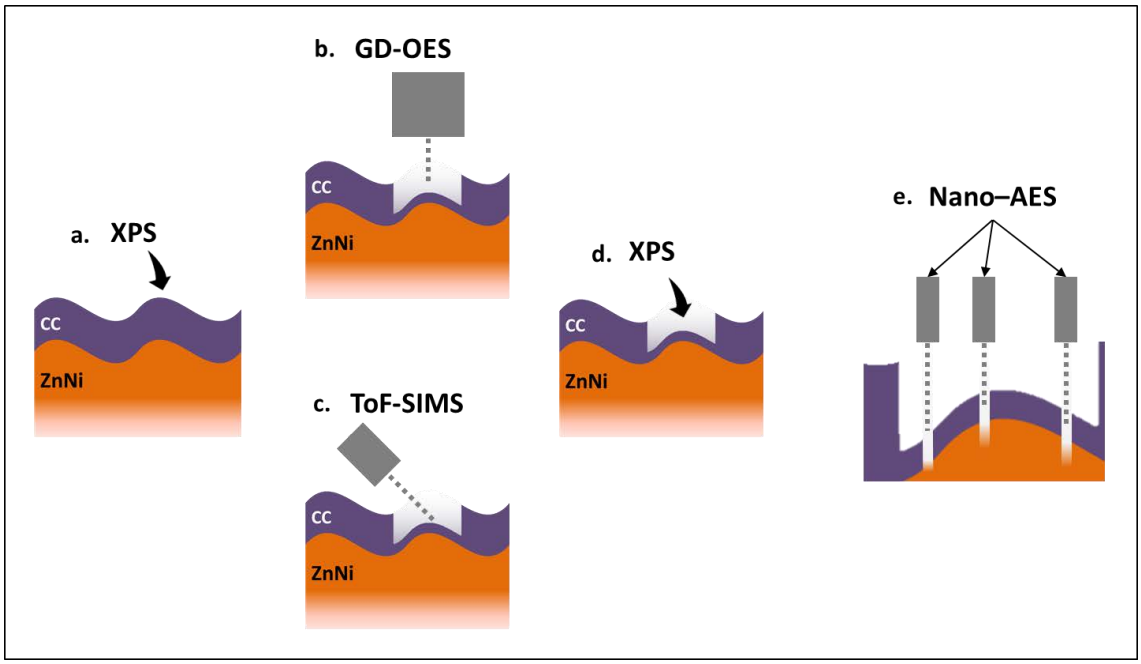

Figure 4.10: Schéma illustrant la méthodologie de caractérisation de surface par combinaison d'XPS (a) et de techniques de dacapage (b. GD-OES, c. ToF-SIMS) pour donner lieu à une caractérisation globale du coeur de la couche d'oxyde (d) et localisée à l'aide du microscope Auger (e)

Cette méthodologie permet de décrire quantitativement la chimie de la couche de conversion proche de l'interface métal-oxyde, environ à 20 nm de profondeur. Ces résultats montrent la présence de chrome hexavalent dans la couche de conversion au chrome trivalent. De plus, ils démontrent que le décapage par GD-OES et ToF-SIMS ne modifient que très peu la chimie de la couche d'oxyde qui est uniforme en profondeur (figure 4.11).

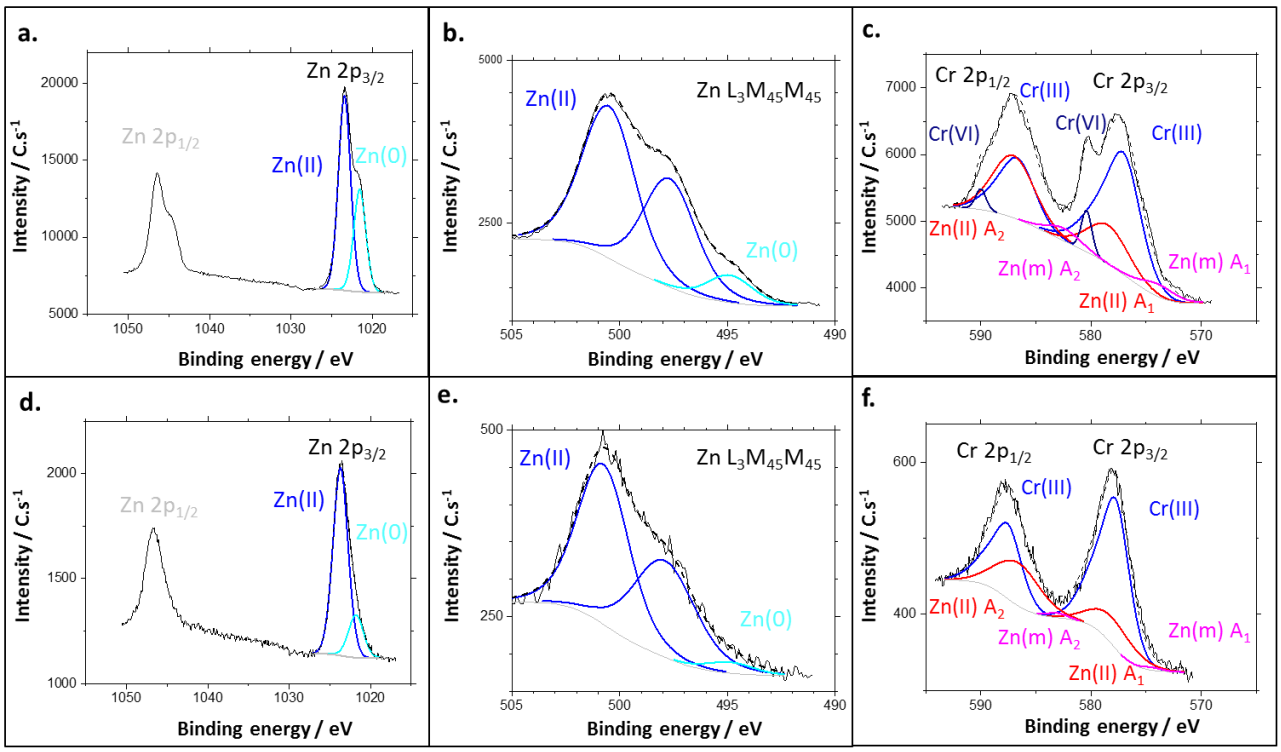

*Figure 4.11: Exemples de spectres XPS à haute resolution dans le cratère GD-OES: **(a)** Zn 2p, **(b)** Zn LMM Auger, **(c)** Cr 2p avec pics Zn Auger ; et dans le cratère ToF-SIMS: **(d)** Zn 2p, **(e)** Zn LMM Auger, **(f)** Cr 2p avec pics Zn Auger.*

Les résultats de ce chapitre sont la caractérisation à l'aide d'un microscope Auger à canon confocal de surfaces décapées par ToF-SIMS et par GD-OES. Ces résultats illustrent l'hétérogénéité du décapage et l'effet d'ombrage lors de la mesure par ToF-SIMS. En effet, sur la figure 4.12, on observe que dans les zones de creux de la surface, l'oxyde résiduel est plus épais que dans les zones en hauteur sur la surface, plus exposées au décapage du Tof-SIMS.

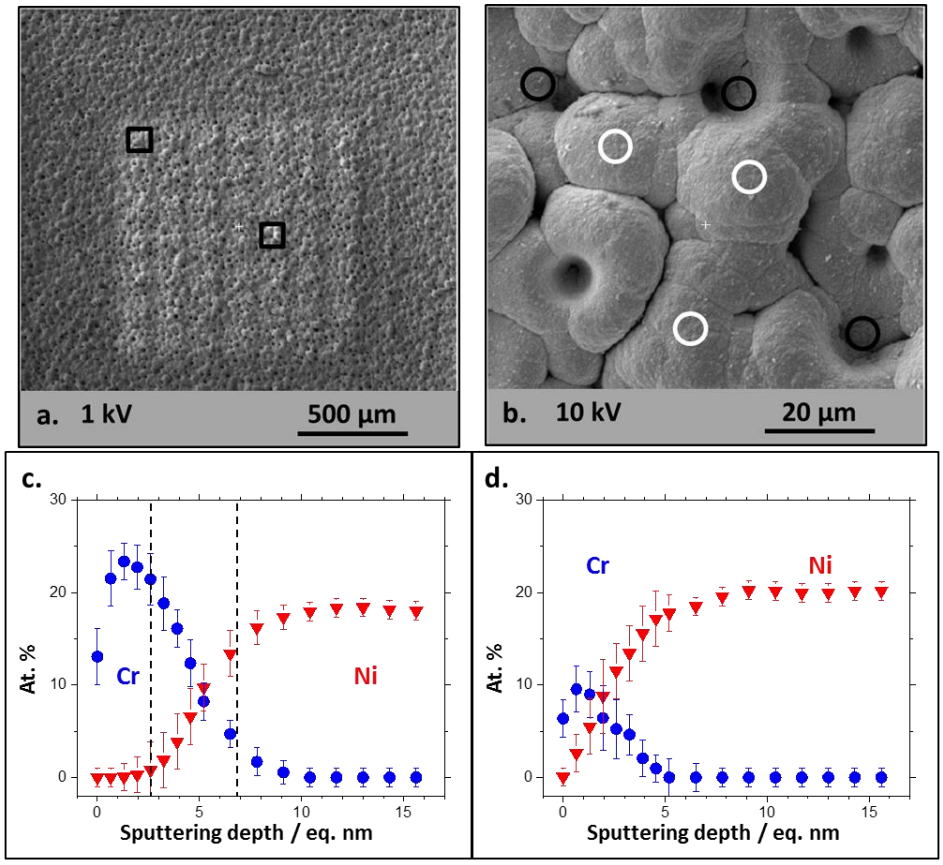

*Figure 4.12: Images MEB et profils locaux par Nano-Auger dans un cratère réalisé par ToF-SIMS. **(a)** Vue globale montrant la présence de cratères par électrons secondaires, **(b)** Zone réduite illustrant un exemple de fzones sélectionnées pour les profils Auger (les vallées sont identifiées par des cercles noirs alors que les collines sont identifiées par des cercles blancs). **(c)** Exemple de profil en profondeur dans les zones de « vallées », **(d)** Exemple de profils chimique en profondeur dans des zones de « bosses »*

Ces travaux démontrent la faisabilité du couplage GD-OES / XPS pour la caractérisation de fines couches d'oxydes sur des surfaces électrodéposées rugueuses. De plus, les mesures ont démontré la capabilité du GD-OES pour effectuer des amincissements localisés de profondeur maitrisée dans des couches d'oxydes d'épaisseur nanométriques.

5. Limites analytiques de la cartographie d'impédance électrochimique localisée pour détecter des défauts nanométriques sous peinture

Les travaux présentés dans ce chapitre combinent les méthodologies présentées dans les chapitres 3 et 4. En effet, des échantillons modèles comportant des amincissements locaux de dimensions différentes dans leur couche de conversion générés par GD-OES et ToF-SIMS (méthodologie chapitre 4) ont été utilisés afin de servir de modèles pour évaluer les limites analytiques de la méthodologie de vieillissement électrochimique accéléré présentée en chapitre 3. Un schéma des défauts modèles est présenté en figure 5.13. Nous nous intéresserons ici à la fois aux limites de détection localisées et via les techniques d'électrochimie globales.

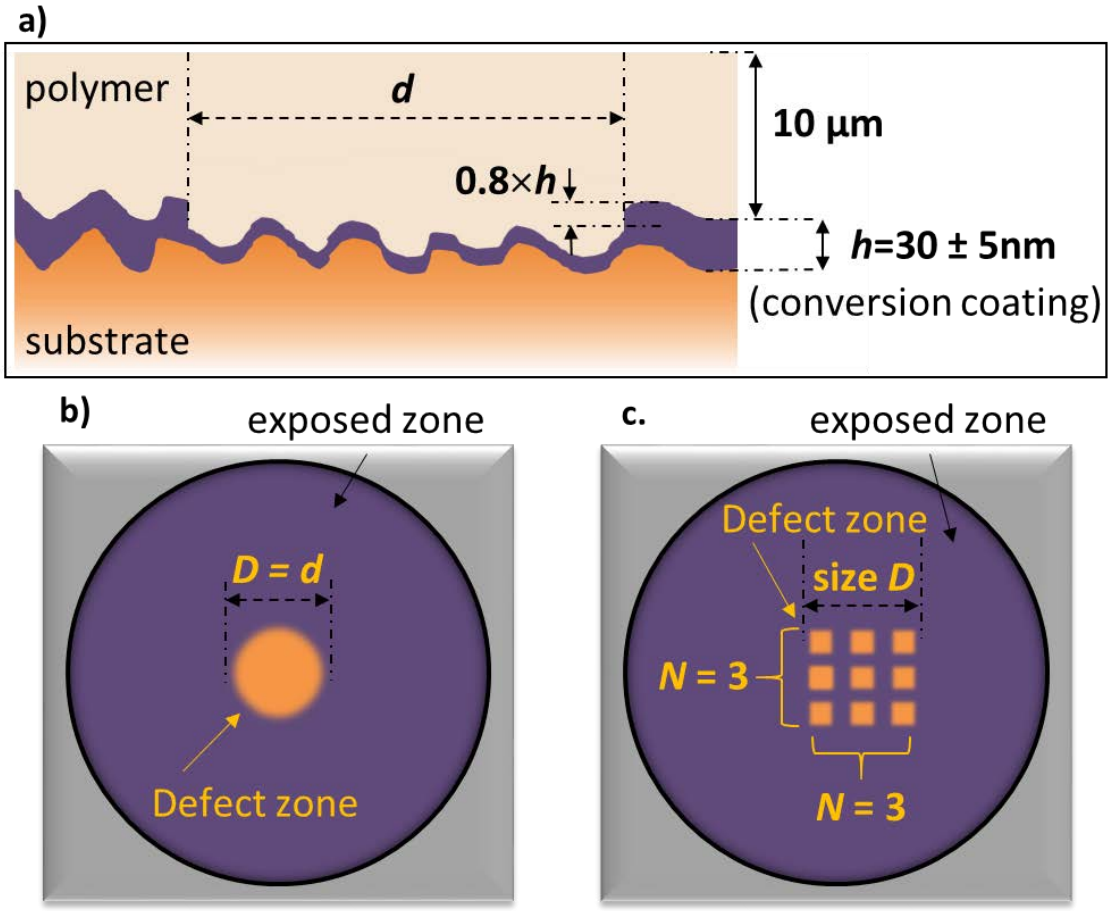

*Figure 5.13: (**a**) Schémas en coupe et (**b-c**) vue du dessus des systems de défauts modèles.*

Les premiers résultats démontrent que la méthodologie proposée permet de détecter des amincissements nanométriques dans la couche d'oxyde comportant un diamètre supérieur à 500 µm, soit environ 1% de la surface totale analysée. Les cartographies LEIM associées sont présentées en figure 5.14.

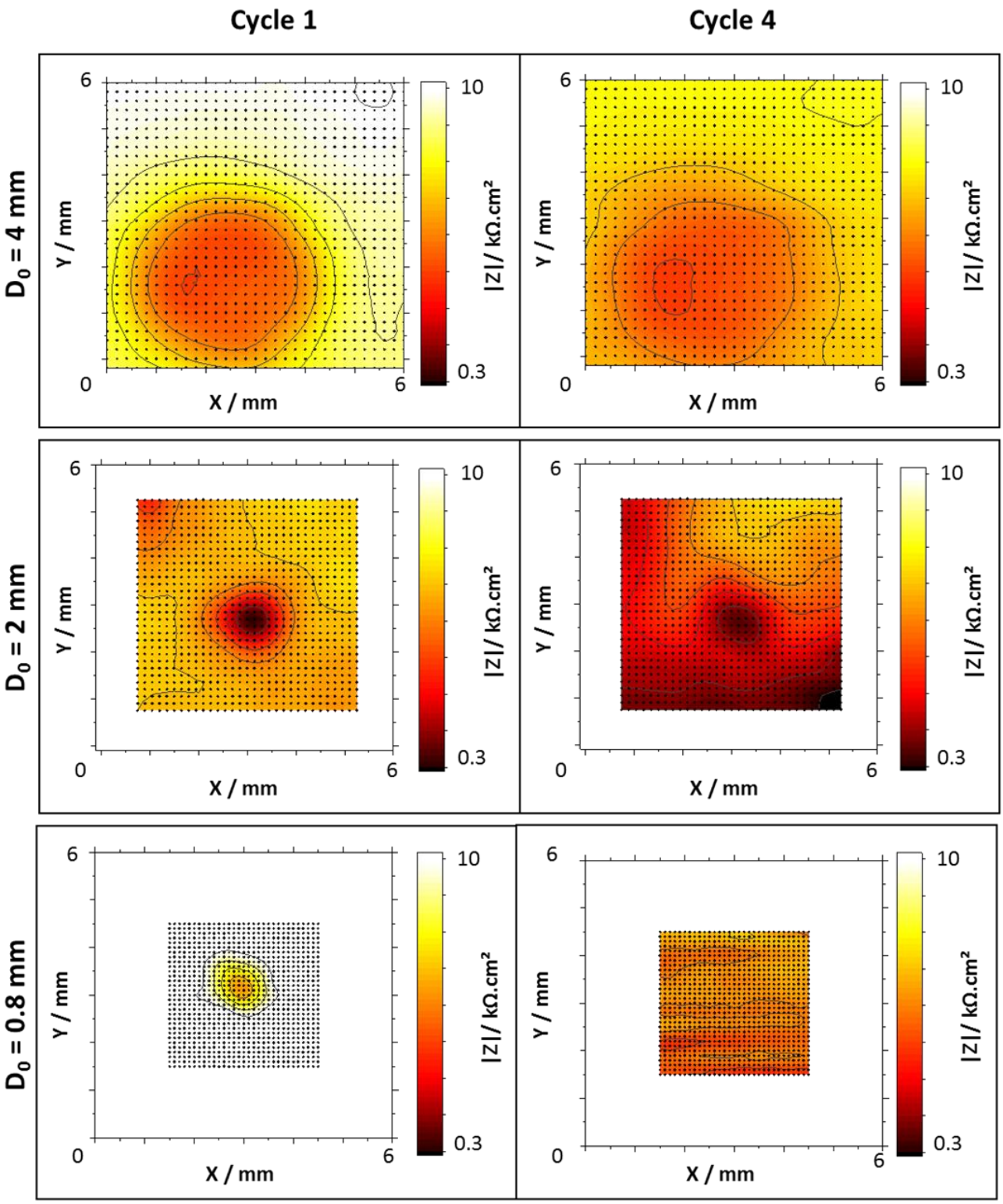

Figure 5.14: Cartographies LEIM du module d'impédance |Z| dans la region des défauts modèles A, B et C (D0 = 3.8, 1.8 et 0.8 mm, respectivement) après les premiers et quatrièmes cycles de degradation ACET

Ces travaux sont les premiers démontrant la capacité du LEIM à détecter des amincissements nanométriques dans une couche d'oxyde sous peinture.

Les résultats montrent également des comportements différents lors de la dégradation des systèmes peints en fonction de la taille du défaut modèle introduit dans la couche d'oxyde. En effet, pour les défauts de plus de 2mm de diamètre, la dégradation s'accélère avec le nombre de cycles ACET. En revanche, les défauts de taille inférieure à 1 mm de diamètre tendent à disparaitre et se repassiver. Les défauts intermédiaires restent présents sous la peinture mais restent stables avec le vieillissement accéléré. La figure 5.15 illustre l'évolution quantitative des tailles de zones de réactivité sous peinture avec le cyclage ACET.

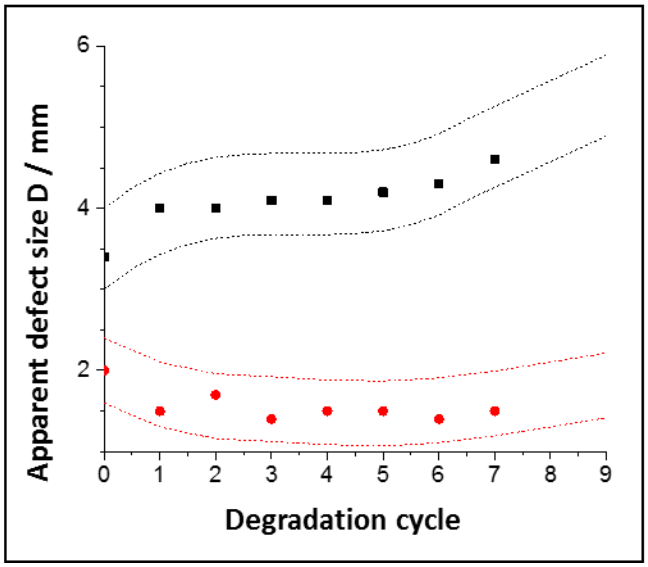

Figure 5.15: évolution du diamètre apparent de la zone de réactivité anodique sous peinture pour les défauts A et B, de taille initiale respectives 3.8 et 1.8 mm de diamètre.

Ces résultats sont concordants avec les observations de la dégradation des systèmes ex-situ après le test de dégradation.

Le tableau présenté ci-dessous résume les capacités analytiques de la méthodologie proposée.

Table 5.1: Résumé des capacités analytiques de la méthodologie proposée

D_0 /mm	Defect type	Detection Charge transfer	Detection TLM	Detection LEIM	Size quantification LEIM	Size evolution LEIM
3.8	Single crater	✓	✓	✓	✓	✓
1.8	Single crater	✓	✓	✓	✓	✓
0.8	Grid of craters	~	✗	✓	✓	✗
0.3	Grid of craters	✗	✗	✗	✗	✗

Conclusions et perspectives

L'objectif de ces travaux de thèse était de proposer des méthodologies permettant d'évaluer in-situ la réactivité des interfaces métal-oxyde-polymère.

Un des défis de cette thèse était de proposer une approche permettant de décorréler l'influence de la couche d'oxydes de celle de la couche de peinture sur la cinétique de dégradation des systèmes anticorrosion. Cette difficulté a pu être surmontée par le développement et l'application d'une peinture modèle dont le mécanisme de dégradation a été étudié. De plus, la combinaison de méthodes de vieillissement accéléré par électrochimie (ACET) avec des mesure de spectroscopie d'impédance électrochimique locales et de microscopie in-situ offre une quantification de la cinétique de dégradation à l'interface métal-polymère.

Les limites analytiques de cette méthodologie ont pu être étudiées, il a de plus été démontré que la spectroscopie d'impédance électrochimique locale était capable de détecter et quantifier la taille d'amincissements nanométriques dans les couches de conversion lors de la dégradation des systèmes peints, bien que la peinture reste intacte. Cette étude a permis d'améliorer la compréhension existante de l'influence de la distribution et de la chimie des couches de conversion sur l'adhérence de la peinture, notamment en conditions d'immersion.

Le second défi de ces travaux de thèse était de rendre possible la description quantitative de la distribution et de la chimie des oxydes dans les couches de conversion appliquées sur des substrats électrodéposés rugueux.

L'approche combinant XPS, GD-OES et microscopie Auger a permis de démontrer la faisabilité du couple GD-OES / XPS pour réaliser ces caractérisations et surmonter les difficultés apportées par la rugosité des surfaces. Un corolaire de cette conclusion est la mise en lumière de l'incapacité de la technique ToF-SIMS à caractériser les fines couches d'oxydes sur des substrats rugueux.

Les travaux présentés dans cette thèse se focalisent à des substrats en base zinc ainsi que des couches de conversion au chrome trivalent. Cependant, l'étendue des méthodologies développées ne sont pas limités à ces matériaux ; elles sont extensibles à une grande partie des morphologies de surface et de types de matériaux ainsi que d'autres conditions de vieillissement.

La combinaison entre ces deux méthodologies, telle que présentée en chapitre 5 peut également être étendue à d'autres système afin de quantifier la cinétique de dégradation des surfaces peintes, potentiellement en la présence de mécanismes auto-cicatrisant tels que décrits dans les travaux de thèse.

RÉSUMÉ

Les couches de conversion sont très largement utilisées dans l'industrie, de la construction à l'aéronautique, pour protéger les métaux contre la corrosion et améliorer la tenue de la peinture. Cependant, les mécanismes de dégradation à l'interface métal-oxyde-polymère sont complexes à élucider ; à fortiori lorsque le substrat est rugueux. In-fine, trois enjeux demeurent : (1) différencier la dégradation de l'interface de celle de la peinture, (2) localiser la réactivité sous peinture et (3) quantifier la cinétique de dégradation.
L'objectif principal de ces travaux de thèse était de proposer une approche méthodologique permettant l'étude in situ de l'effet des couches de conversion sur la stabilité de l'interface métal-polymère, sous des couches de peintures intactes en immersion. Celle-ci combine l'utilisation d'un revêtement polymère modèle et d'un test de vieillissement électrochimique. La dégradation de la peinture a été suivie par spectroscopies infra-rouge et d'impédance électrochimiques ; la réactivité à l'interface a été étudiée par électrochimie locale et microscopie in situ. L'approche proposée permet d'effectuer un contrôle rapide des couches de conversion en fonction de leur capacité à générer une interface métal-oxyde-peinture stable. Elle offre également la possibilité de localiser les zones les moins stables et de quantifier leur propagation.
Un second objectif de ces travaux était d'identifier et de quantifier en profondeur les espèces chimiques composant les fines couches de conversion (quelques nm d'épaisseur) sur des substrats rugueux (quelques µm). L'utilisation d'un plasma argon dans une machine de spectroscopie à décharge luminescente pulsée (RF-SDL) a permis d'obtenir des cratères modèles (amincissements de quelques nm) sur des surfaces de taille millimétriques ; l'analyse de la couche de conversion à l'interface métal-oxyde a été effectuée par XPS et nanosonde Auger dans les cratères.
En combinant les deux approches proposées ci-avant, les travaux de thèse ont montré l'effet néfaste d'amincissement nanométriques localisés dans les couches de conversion sur la stabilité de l'interface métal-oxyde-polymère.
L'influence de la taille et de la distribution de ces défauts a été observée et discutée.
L'ensemble de ces résultats ont été démontrés sur l'exemple de substrats en alliage de zinc électrodéposé après un traitement de conversion au chrome trivalent.

MOTS CLÉS

Electrochimie, Interface, Couche de conversion, Analyse de surface

ABSTRACT

Conversion coatings are used to enhance paint adherence and protect metals in numerous industrial applications from construction to aeronautics. The degradation mechanism of buried metal-oxide-polymer interface is difficult to elucidate, especially on rough metallic substrates. All the more so, the challenges reside in: (1) the distinction between the interface and the polymer degradation, (2) the localization of the underpaint reactivity initiation and (3) the survey of local degradation kinetics.
The main objective of this work was to propose a methodological approach able to describe in situ the effect of thin conversion coatings on the stability of buried metal-oxide-polymer interface, under stable intact polymer, in immersion condition. The approach is based on the combination of model epoxy coating and adapted electrochemical ageing procedure. The stability of the polymer coating was verified by infrared spectroscopy and electrochemical methods. The degradation mode of the interface was studied by combined local electrochemical impedance mapping and time lapse microscopy. This approach allowed an intelligent screening and fast-ranking of conversion coatings in function of their ability to form stable metal-oxide-polymer interfaces. It also permitted to localize the degradation initiation and to quantify its lateral propagation.
A secondary objective of the PhD was to allow in-depth chemical characterization of nanometric conversion coatings on rough substrates. Low energy argon plasma sputtering in GD-OES was used to perform homogeneous nanometric thinning (model craters) of the conversion coating on millimetric areas; near metal-oxide interface chemical description was achieved by XPS and Auger nanoprobe.
The combination of the two proposed approaches permitted to demonstrate the effect of nanometric thinning in conversion coatings on the local reactivity at metal-oxide-polymer interface. The effect of the size and distribution of nanometric defects was also discussed.
The PhD was performed on the example of epoxy coated electrodeposited zinc-based alloy with trivalent chromium conversion coating.

KEYWORDS

Electrochemistry, Interface, Conversion coating, Surface characterization